Dedicated Carbon Scaffolds for Next Generation Hydrogenation Chemistry and H_2 Evolution



A thesis submitted to the Board of the Faculty of Physical Sciences in partial fulfilment of the requirements for the degree of
Master of Science by Research in Materials

University of Oxford
Department of Materials

Ceren Zor
St Edmund Hall, Trinity 2016

I confirm that the work presented in this Thesis is my own. Where information has been derived from other sources, I confirm that this has been indicated in the Thesis.

ABSTRACT

Dedicated Carbon Scaffolds for Next Generation Hydrogenation Chemistry and H_2 Evolution

Ceren Zor, St Edmund Hall, University of Oxford
A thesis submitted for the degree of Master of Science by Research, Trinity 2016

This Thesis is primarily concerned with developing sustainable and cost-efficient methods for applications of hydrogen (H_2-driven fine chemical synthesis) and production of hydrogen (hydrogen evolution reaction, HER). Using novel catalysts, immobilising these catalysts, and translating the conventional batch processes to flow processes are the key solutions used for both of these processes.

In the first part of this work enzymes are employed as catalysts in fine chemical synthesis. Enzymes are enantio-, regio- and stereoselective, can be used in mild reaction conditions, and can be easily produced in the laboratory. It is possible to electronically couple a hydrogenase to an NAD^+ reductase enzyme *via* conductive carbon particles for NAD^+ to NADH reduction. Thus, enzymes were immobilised on high surface area, porous and electronically conducting commercial carbon particles for H_2-driven generation of NADH, an expensive cofactor required by many enzymes to work, in batch. The commercial carbon materials which are conventionally used for metal catalysed hydrogenation reactions were shown to be suitable supports for enzymes used in H_2-driven biotransformations in batch. In this work, novel carbon nanotube columns (CNCs) were utilised as enzyme supports and flow devices for a range of H_2-driven biotransformations including ketone reduction and reductive amination reactions. This is the first demonstration of H_2-driven NADH recycling for selective biotransformations in flow.

The second part of this work focuses on HER catalysis. Here, novel WS_2 assemblies were developed as alternatives to expensive and rare platinum catalysts. WS_2 nanostructures were directly grown on multi-wall carbon nanotube (MWCNT) carpets and CNCs for the first time. Preliminary electrochemical studies showed that these assemblies are suitable to be used as HER catalysts, although they require a significant overpotential. This is a promising proof-of-concept demonstration of WS_2-MWCNT assemblies being used in HER catalysis. A possible future extension of this work would involve using these assemblies in flow.

ACKNOWLEDGEMENTS

First and foremost, I would like to thank my supervisors Prof Nicole Grobert, Prof Kylie A. Vincent, and Dr Frank C. Dillon for their support and supervision throughout my degree. I appreciate their efforts as mentors.

I am grateful to Dr Frank Dillon for his patience, helping me with TGA and BET analyses, discussing the data, reading my Thesis and making this MSc journey fun. I am thankful to Dr Holly Reeve for teaching me the mysterious ways of handling enzymes and reading my Thesis. I very much appreciate the help of Karwei So and Dr Vitaliy Babenko for TEM and EDX analyses, respectively. It was very kind of them to spend hours with me on the microscopes. I am thankful to Alistair Farley from Dixon group and Dr Phil Holdway for providing the results for GC and XRD analyses, respectively. I want to acknowledge outstanding researchers and friends, who inspired and assisted me including Dr Shayan Meysami, Dr Jonathan Quinson, Dr Arunvinay Prabakaran, Dr Ricardo Hidalgo, and Thomas H. Lonsdale.

I would like to thank all the previous and present members of Grobert group and Vincent group I worked with for being there for me and making me smile regardless of failed experiments, deadlines, drizzle, and rain. I am lucky to have Thomas H. Lonsdale both as a friend and as a colleague to share all the absurdity of life. I want to thank Dr Ricardo Hidalgo for all the gossip and his unique sense of humour. It has been an honour and privilege to get to know all the people I met and friends I made in Oxford, including Ceren Yalaz and Zhanet Zaharieva.

I am lucky to have such supportive and loving family and friends. I am thankful to my grandfather for believing in me and financially supporting me. I am grateful to Turkpetrol Foundation for their financial support as well. I am very lucky to have Prof Mehmet Somer as a mentor and, I am thankful to him for encouraging me to pursue a research degree. Special thanks to Berkay, Cemre, Erkan, and Semra for their unconditional love and support.

CONTENTS

ABSTRACT ..... **II**

ACKNOWLEDGEMENTS ..... **III**

CONTENTS ..... **IV**

ABBREVIATIONS ..... **VIII**

LIST OF FIGURES ..... **X**

LIST OF TABLES ..... **XIX**

LIST OF PUBLICATIONS ..... **XX**

1 CHAPTER 1 INTRODUCTION **1**

1.1 LITERATURE REVIEW ON HYDROGEN ECONOMY: THE PRODUCTION AND THE APPLICATIONS OF HYDROGEN 1

1.1.1 Hydrogen Economy *2*

1.1.2 The production of hydrogen *4*

1.1.2.1 Hydrogen evolution reaction (HER) 7

1.1.3 The applications of hydrogen in chemical industries *8*

1.1.3.1 Reactions catalysed by hydrogenases 10

1.1.4 Comparison of Batch and Flow Processes *13*

1.1.4.1 Hydrogen production in flow 14

1.1.4.2 Hydrogenation in flow 16

1.1.5 Catalyst immobilisation methods *17*

1.1.5.1 Carbon materials as catalyst supports 19

1.1.5.2 Enzyme immobilisation 19

1.1.5.2.1 Carrier-free enzyme immobilisation methods 21

1.1.5.2.2 Enzyme immobilisation methods on support materials 22

1.1.5.2.3 Non-carbon materials for enzyme immobilisation 23

1.1.6 Catalyst used in this Thesis *25*

1.1.6.1 WS_2, a transition metal dichalcogenide as a catalyst for HER 25

1.1.6.2 Hydrogenase, NAD^+ reductase and NADH dependant enzymes used in this Thesis to catalyse H_2-driven Biotransformations 26

1.1.6.2.1 Hydrogenase 26

1.1.6.2.2 Soluble hydrogenase – NAD^+ reductase 28

1.1.6.2.3 NADH-dependent enzymes 29

1.1.7 Cofactor regeneration methods *31*

1.1.7.1 Enzyme catalysed cofactor regeneration 33

1.1.7.2 Electrochemical NAD^+ reduction 34

1.1.7.3 H_2-driven cofactor regeneration 36

1.2 SUMMARY AND CONCLUSION 38

1.3 OUTLINE OF THE THESIS 41

2 CHAPTER 2. H_2-DRIVEN NADH GENERATION ON VARIOUS CARBON SUPPORT MATERIALS 42

2.1 INTRODUCTION 43
2.1.1 Carbon catalysis support materials 43
2.1.2 Carbon based enzyme support materials 44
2.2 EXPERIMENTAL METHODS AND ANALYSIS TECHNIQUES 46
2.2.1 Experimental Methods 47
2.2.1.1 Materials 47
2.2.1.2 Testing the adsorption of organic molecules onto the carbon particles 48
2.2.1.3 Preparation of the enzyme modified carbon particles 48
2.2.1.4 The protocol for H_2-driven NADH generation 49
2.2.2 Analysis Techniques 50
2.2.2.1 Characterisation techniques used for carbon materials 50
2.2.2.2 High-performance liquid chromatography 52
2.2.2.3 Ultraviolet-visible spectroscopy 53
2.3 RESULTS AND DISCUSSION 54
2.3.1 Characterisation of the Carbon Materials 54
2.3.1.1 SEM/TEM characterisation of the carbon materials 54
2.3.1.2 Specific surface area analysis based on Brunauer–Emmett–Teller (BET) theory 56
2.3.1.3 Determination of crystallinity of carbon materials by X-ray diffraction analysis 58
2.3.1.4 Characterisation of graphitic structure of the carbon materials by Raman spectroscopy . 58
2.3.1.5 Energy-dispersive X-ray spectroscopy of the carbon materials 60
2.3.2 Testing reactants and products on the carbon materials 62
2.3.2.1 Adsorption of the chemical used on the carbon materials 62
2.3.3 H_2-Driven NADH Production on the Carbon Materials 65
2.4 CONCLUSION 68

3 CHAPTER 3. H_2-DRIVEN FLOW BIOCATALYSIS IN CARBON NANOTUBE COLUMNS . 70

3.1 INTRODUCTION 70
3.1.1 Development of carbon nanotube assemblies 71
3.1.1.1 Basics of development and properties of carbon nanotubes 71
3.1.1.2 Towards tailored-novel carbon nanotube assemblies for applications 73
3.1.2 Carbon nanotube catalyst immobilisation materials 75
3.1.3 Carbon support based flow reactors 77
3.2 EXPERIMENTAL METHODS AND ANALYSIS TECHNIQUES 79
3.2.1 Experimental Methods 79
3.2.1.1 Materials 79
3.2.1.2 Aerosol-assisted chemical vapour deposition method for CNC synthesis 80
3.2.1.3 Evaporation rates of the reactants and products 81
3.2.1.4 Preparation of enzyme modified CNCs 82
3.2.1.5 The protocol for H_2-driven biotransformations in flow 84
3.2.1.5.1 The protocol for H_2-driven NADH generation in flow 84

3.2.1.5.2 The protocol for H_2-driven ketone reduction in flow 84
3.2.1.5.3 The protocol for H_2-driven reductive amination in flow 84
3.2.2 Analysis Techniques 85
3.2.2.1 Characterisation techniques used for CNCs 85
3.2.2.2 Ultraviolet-visible spectroscopy 85
3.2.2.3 High-performance liquid chromatography 86
3.2.2.4 Gas chromatography 86
3.3 RESULTS AND DISCUSSION 87
3.3.1 Characterisation of the CNCs 87
3.3.1.1 Scanning electron microscopy of CNCs 87
3.3.1.2 Raman spectroscopy of CNCs 89
3.3.1.3 Thermogravimetric Analysis of CNCs 90
3.3.2 Evaporation of the reactants and products under overnight H_2 flow 91
3.3.3 Biotransformations on CNCs 92
3.3.3.1 NADH generation on CNCs 92
3.3.3.2 Ketone reduction on CNCs 94
3.3.3.3 Reductive amination on CNCs 97
3.4 CONCLUSION 100

4 CHAPTER 4. HYDROGEN EVOLUTION REACTION WITH NOVEL CHALCOGENIDE ASSEMBLIES AS CATALYSTS 102

4.1 INTRODUCTION 102
4.1.1 Alternative inorganic catalysts for HER catalysis 103
4.1.2 Recent advancements in developing MX_2s as HER catalysts 104
4.2 EXPERIMENTAL METHODS AND ANALYSIS TECHNIQUES 105
4.2.1 Experimental Methods 105
4.2.1.1 Materials 105
4.2.1.2 Growth of WS_2 2D-3D nanostructures 105
4.2.2 Analysis Techniques 106
4.2.2.1 Characterisation techniques used for WS_2 assemblies 106
4.2.2.2 Electrochemical methods 107
4.3 RESULTS AND DISCUSSION 107
4.3.1 Characterisation of WS_2 assemblies 107
4.3.1.1 Scanning electron microscopy of WS_2 assemblies 107
4.3.1.2 Raman spectroscopy of the WS_2 assemblies 111
4.3.1.3 Energy-dispersive X-ray spectroscopy of WS_2 assemblies 112
4.3.1.4 X-Ray diffraction analysis of WS_2 assemblies 114
4.3.2 Electrochemical studies on WS_2 assemblies 115
4.4 CONCLUSION 118

5 CHAPTER 5. CONCLUSION AND FUTURE WORK 119

5.1 CONCLUSION 119
5.2 FUTURE WORK 122

5.2.1 Flow reactors for H_2-driven biotransformations 122
5.2.2 Optimising WS_2-MWCNT assemblies for HER catalysis 123

REFERENCES 125

APPENDICES 148

ABBREVIATIONS

AACVD	aerosol-assisted chemical vapour deposition
AADH	amino acid dehydrogenase
ACS	American Chemical Society
ADH	alcohol dehydrogenase
AES	alkaline electrolysis systems
BET	Brunauer–Emmett–Teller
BP	black pearls 2000
CE	counter electrode
CNC	carbon nanotube column
CNT	carbon nanotube
CPI	Current Policy Initiative
CSS	continuous stirred slurry reactors
CSTR	continuous flow stirred-tank reactor
CVD	chemical vapour deposition
D	particle diameter
df	degrees of freedom
e^-	charge of an electron
E.coli	*Escherichia coli*
EDX	energy-dispersive X-ray spectroscopy
ee	enantiomeric excess
EHT	extra high tension
F	Fisher–Snedecor distribution critical value
FMN	flavin mononucleotide
GC	gas chromatography
GCI	green chemistry industry

HER	hydrogen evolution reaction
HPLC	high-performance liquid chromatography
Hyd-1	*Escherichia coli* Hydrogenase 1
Hyd-2	*Escherichia coli* Hydrogenase 2
LalaDH	L-alanine dehydrogenase
LA(M)	Longitudinal acoustic phonons
MWCNT	multi-wall carbon nanotube
N-MWCNT	nitrogen-doped multi-wall carbon nanotube
NAD^+	nicotinamide adenine dinucleotide (oxidised)
NADH	nicotinamide adenine dinucleotide hydride (reduced)
PEM	polymer electrolyte membrane
PV	photovoltaic
R. eutropha	*Ralstonia eutropha* H16
RE	reference electrode
rGO	reduced graphene oxide
SH	soluble hydrogenase
slm	standard litres per minute
SWCNT	single-wall carbon nanotube
TGA	thermogravimetric analysis
TMDC	transition metal dichalcogenide
UV-Vis	ultraviolet-visible
WDX	wavelength-dispersive X-ray spectroscopy
WE	working electrode
wt %	weight percent
XRD	X-ray diffraction
ε	extinction coefficient

LIST OF FIGURES

Figure 1: Veziroglu's 2000 projection for hydrogen economy. Adapted from Reference 10, © 2000, with permission from Elsevier. 3

Figure 2: A schematic representation of electrolysis of water. H_2 is produced at the cathode. Up to date, expensive platinum/platinum coated materials are used as the most efficient catalysts for water splitting. 5

Figure 3: 2007 H_2 production cost (US$ / GJ). Sensitivity of different H_2 production technologies to energy price. Reproduced from Reference 23, © 2007, with permission from OECD/IEA. .. 5

Figure 4: A schematic representation of a photovoltaic (PV) unit for a hydrogen production system. 6

Figure 5: A schematic representation of water-gas shift reaction catalysed by immobilised enzymes (carbon monoxide dehydrogenase (CODH I), pink and hydrogenase (Hyd-2), blue) on graphite platelets (grey). Reprinted from Reference 3, © 2009, wıth permission from American Chemical Society. 12

Figure 6: Representation of the bio-inspired cathode material (middle). A nickel bisdiphosphine complex was covalently attached onto a multi-wall carbon nanotube to mimic the active site of hydrogenase enzymes. [FeFe] and [NiFe] hydrogenases in their reduced active state (left and right, respectively), and the H_2-evolving Ni catalyst modified carbon nanotube (middle). Reprinted from Reference 87 with permission from AAAS, © 2010. 13

Figure 7: A schematic representation of a serpentine design micro-channel flow reactor. The image is adopted from Reference 130, © 2010, with permission from Elsevier. 15

Figure 8: Comparison of the ee of homogeneous and heterogeneous (on silica and USY zeolite) hydrogenation of (Z)-N-acetamidocinnamic acid derivatives catalysed by rhodium complexes with a proline derived ligand.[145] 18

Figure 9: Schematic representation of preparation of CLEA. Reprinted from Reference 147, © 2007, with permission from John Wiley and Sons. 22

Figure 10: A schematic representation of [NiFe] hydrogenase. Three blocks in the subunit represent proximal (P), medial (M) and distal (D) clusters. 27

Figure 11: A cartoon representation of Hydrogenase 1 from E.coli. The enzyme used in this work, Hyd-2, is not crystallised. Thus, the structure is not in the literature. However, the arrangement of iron-sulphur clusters in the figure are same for Hyd-2. Yellow and orange spheres are iron-sulphur clusters and the blue-green-orange-pink spheres are carbon monoxide-(dicyano) iron and nickel. Figure was prepared using The PyMOL Molecular

Graphics System, Version 1.3 Schrödinger, LLC. Hyd-1 PDB code 3UQY, H_2-reduced structure of a membrane bound hydrogenase-1 from E. coli.[183] 27

Figure 12: Modular structure of the soluble hydrogenase from R. eutropha. a) The SH consists of a hydrogenase dimer (HoxHY), a diaphorase dimer (HoxFU) and two HoxI subunits. Both HoxHY and HoxFU contain one FMN. The electron conducting FeS clusters are shown in elemental colours. b) HoxFU dimer of SH which can exchange electrons with an electrode/carbon surface and reduce (oxidise) NAD(H). 28

Figure 13: Thermodynamic potential of H^+/H_2 and NAD^+/NADH couples at pH 7, 25 °C, at different concentrations. 29

Figure 14: Cartoon representation of an ADH molecule. Red chains represent NAD^+s and yellow spheres represent Zn. Figure was prepared using The PyMOL Molecular Graphics System, Version 1.3 Schrödinger, LLC. ADH PDB code 4ILK, Short Chain Alcohol Dehydrogenase from E. coli.[187] ADH molecules are represented as green cartoons in **Chapter 3**. 30

Figure 15: Cartoon representation of an L-alanine dehydrogenase crystallised with pyruvate and NAD^+. Red sticks represent NAD^+ and green sticks represent pyruvate. The enzyme used in this work is not crystallised in the literature. However, the crystal structure of L-alanine dehydrogenase from Phormidium lapideum complexed with NAD^+ was used as a representative L-alanine dehydroganese, which also uses pyruvate as a substrate. Figure was prepared using The PyMOL Molecular Graphics System, Version 1.3 Schrödinger, LLC. LalaDH PDB code 1PJC.[188] LalaDH are represented as red cartoons in **Chapter 3**. 31

Figure 16: The structure of 1,4-NADH and NAD^+. 32

Figure 17: Image showing NADH being used by an NADH-dependant enzyme (blue) to reduce a ketone to a secondary alcohol. 32

Figure 18: Schematic representations of the enzyme-based cofactor regeneration methods. a) substrate-coupled cofactor regeneration method, using one enzyme both for the synthesis of the desired product and for the cofactor regeneration. b) enzyme-coupled cofactor regeneration method, using a second enzyme for cofactor regeneration. 34

Figure 19: Schematic representations of different electrochemical NAD^+ reduction methods. a) direct NAD^+ reduction on an electrode. b) mediated NAD^+ reduction method where a mediator is used to lower the overpotential. c-d) electro-enzymatic NAD^+ reduction methods; c) uses an immobilised enzyme for NAD^+ reduction and in d) an enzyme uses electron from a mediator for NAD^+ reduction. 36

Figure 20: H_2-driven NADH regeneration by a soluble hydrogenase coupled with an NADH-dependent dehydrogenase. 37

Figure 21: A schematic representation of the co-immobilisation of enzymes on carbon support. (The enzyme molecules and the carbon particle are not shown to scale.) 49

Figure 22: A schematic representation of the batch reaction set-up. The Eppendorf tubes placed in a sealed shaker with hydrogen gas inlet and outlet. (The enzyme molecules and the carbon particles are not shown to scale.)..... 50

Figure 23: Raman spectrum of a graphitic material showing a strong G peak at 1580 cm^{-1}. Adopted from Reference 213, © 1988, with permission from Elsevier. 51

Figure 24: Sorption isotherms classified by IUPAC. 52

Figure 25: Four main hysteresis loops according to 1985 IUPAC classification. 52

Figure 26: Scanning electron micrographs of four different carbon materials taken at 1000 X (a) CC, b) CD, c) CP, d) BP). 55

Figure 27: Transmission electron micrographs of CC, CD, CP and BP. TEM image of BP was adapted from Reference 1.TEM images were obtained with the assistance of Karwei So, Grobert Group, University of Oxford. 56

Figure 28: Nitrogen adsorption (dotted black) and desorption (solid red) isotherms at 77 K for each carbon material (CC, CD, CP, and BP). The analyses were carried out with the assistance of Dr Frank Dillon, Grobert Group, University of Oxford. 57

Figure 29: XRD spectra of CC, CD, CP and BP with % crystallinity of each material. XRD analyses was carried out by Dr Philip Holdway, Oxford Materials Characterisation Service. . 58

Figure 30: Raman spectra of carbon materials (CC, CD, CP, and BP) with D peaks around 1340 cm^{-1} and G peak around 1575 cm^{-1} confirming amorphous structure with a I_D/I_G close to 1. 59

Figure 31: EDX spectra of CC along with elemental composition of the selected regions of the material. EHT = 15 kV, I Probe = 500 pA. 60

Figure 32: EDX spectra of CD along with elemental composition of the selected regions of the material. EHT = 15 kV, I Probe = 500 pA. 61

Figure 33: EDX spectra of CP along with elemental composition of the selected regions of the material. EHT = 15 kV, I Probe = 500 pA. 61

Figure 34: EDX spectra of BP along with elemental composition of the selected regions of the materials. EHT = 15 kV, I Probe = 500 pA. 61

Figure 35: HPLC chromatograms for the overnight adsorption of 350 µL 10 mM reactant (acetophenone) and 350 µL 10 mM product (1-phenylethanol) on 28 mg mL^{-1} CC, CD, CP, and BP. CC, CP and BP adsorbed more than 99 % of the starting acetophenone and 1-phenylethanol solutions. CD adsorbed 96 % and 94 % of the starting acetophenone and

1-phenylethanol solutions, respectively. High carbon loading was used to determine the extent of the adsorption of the carbon materials. 64

Figure 36: HPLC chromatograms for the overnight adsorption of the cofactors. 350 µL 1 mM NAD^+ and 350 µL 1mM NADH were tested on 28 mg mL^{-1} CC, CD, CP and, BP. CC adsorbed 92 % and 77 % of the starting NAD^+ and NADH solutions, respectively. CD adsorbed 88 % and 85 % of NAD^+ and NADH, respectively. CP and BP adsorbed 98 % of NAD^+. CP adsorbed 99 % and BP adsorbed 97 % of the starting NADH solutions. High carbon loading was used to determine of the adsorption of the carbon materials. 64

Figure 37: HPLC chromatograms for the overnight adsorption of 985 µL 10 mM 1-phenylethanol on 15 µL 10 mg mL^{-1} on CD, CP and BP. The same amount of carbon loading was used as in the NADH generation experiments. The aim was to test the potential effect of adsorption in the NADH generation system. The carbon materials adsorbed less than 1 % of the starting 1-phenylethanol solutions. 65

Figure 38: A schematic representation of the mechanism of H_2-driven NADH generation. Hydrogenase and NAD^+ reductase were co-immobilised on the selected electronically conducting carbon materials. H_2 saturated NAD^+ solution was used as the reactant. H_2 was flowing through the headspace of the reaction. (The carbon particle and the enzymes are not shown to scale.) 66

Figure 39: a) The overall UV-Vis spectra for the 1:10 diluted 1 mM NAD^+ in buffer reaction mixture and 1:10 diluted 16 hr H_2-driven NADH generation on BP. b) The A_{340} peak for NADH generation on BP with time points taken at 2, 4, and 16 hours. The peak at 340 nm shows increase in NADH concentration over time, c) NADH generation on CD, d) NADH generation on CP. 67

Figure 40: Graphene sheet is rolled up in different geometries to construct zigzag, armchair or chiral SWCNTs. Reproduced from Reference 227, © 2011, with permission from The Royal Society of Chemistry. 72

Figure 41: Examples of a) scanning electron micrograph of coiled carbon nanotubes and b) transmission electron micrograph of branched carbon nanotubes. Image a) is Reprinted from Reference 230, © 2006, with permission from Elsevier. Image b) is Reproduced from Reference 232, © 2005, with permission from Elsevier. 73

Figure 42: a) Organised and simultaneously synthesised carbon nanotube arrays on patterned silica substrates. Scale bars are 50 µm (left-side image) and 100 µm (right-side image). b) CNT-based device for recording extracellular signals. a) Adapted by permission from Macmillan Publishers Ltd: Nature from Reference 233, © 2002, b) Adapted from Reference 236, © 2014, with permission from Elsevier. 74

Figure 43: Representative TEM images of the Pd particles introduced inside the MWNT (A) and deposited on the activated charcoal (B). The particles deposited on the activated charcoal were aggregated. Thus, the dispersion of the metal on the support was highly inhomogeneous. Reprinted from Reference 246, © 2005, with permission from Elsevier. 76

Figure 44: The SEM image in Figure a1 shows the freestanding a carbon nanotube column, the scale bar is 1 mm. Figures a2 and a3 show the petroleum filtration and E.coli filtration systems, respectively. The schematic representation in b1 shows the conventional microreactor with Pt deposited channel and the novel Pt-CNT microreactor. Figures c1-c3 show Fermat's spiral type CNT microchannel reactor. The diameter of the spiral is 5 mm. Figures c2 and c3 show water flowing through the microchannels at 0.8 s and 1.2 s, respectively. Figure a1-3) Adapted from Reference 248 by permission from Macmillan Publishers Ltd: Nature, © 2014. Figure b1-2) Adapted from Reference 249 with permission of The Royal Society of Chemistry. Figure c1-3) Adapted from Reference 250, © 2009, with permission from Elsevier. 78

Figure 45: A schematic representation the AACVD set-up for CNC synthesis. 81

Figure 46: a) An image of the peristaltic pump and the tubing used in flow experiments, b) an image of a CNC connected to the tubing via Teflon adaptors. 82

Figure 47: A schematic representation of co-immobilisation of Hyd-2 (cyan) and I64A (blue) on a CNC for NADH generation. (The representation is not shown to scale.) 83

Figure 48: A schematic representation of co-immobilisation of Hyd-2 (cyan), I64A (blue), and ADH (green) on a CNC for ketone reduction. (The representation is not shown to scale.) 83

Figure 49: A schematic representation of co-immobilisation of Hyd-2 (cyan), I64A (blue), and LalaDH (red) on a CNC for reductive amination. (The representation is not shown to scale.) 83

Figure 50: a) An image of a CNC directly after the synthesis, b) an image of a CNC after cleaning the outer MWCNT deposit, ready to use as a flow device, c) a cross-section image of a CNC directly after the synthesis. 87

Figure 51: Scanning electron micrographs of CNCs under different magnifications. a) Scanning electron micrograph of a cross-section of a CNC. The MWCNT deposits can be seen inside the quartz column. The dark ring in the middle is the hollow section b) layers of MW CNTS due to interrupted aerosol flow, c) inner walls of a CNC, d-e) MWCNT deposits in CNCs. 88

Figure 52: Scanning electron micrographs of enzyme-modified CNCs after a flow experiment taken at different magnifications. When compared with the CNC images directly after CNC synthesis, these images show that there is morphology change in CNCs after the flow experiments. 89

Figure 53: Raman spectrum of CNCs showing three characteristic MWCNT peaks, D peak at around 1340 cm^{-1}, G peak at around 1570 cm^{-1},and 2D peak at around 2680 cm^{-1}. 90

Figure 54: TGA curve of the CNCs showing that the yield of carbon deposit is 88 % and the CNCs are resistant to oxidation at < 500 °C. 91

Figure 55: HPLC chromatograms for overnight evaporation of acetophenone and 1-phenylethanol under H_2 flow through the headspace. The spectra show that acetophenone concentration decreased due to evaporation caused by H_2 bubbling over the headspace. 51 % of the starting acetophenone solution evaporated overnight and concentration of 1-phenylethanol remained the same. 92

Figure 56: A schematic representation of the H_2-driven NADH generation mechanism on CNCs. Hyd-2 (cyan) and I64A (blue) were co-immobilised on the electronically conducting CNCs. H_2 was oxidised at Hyd-2 and the electrons were transferred to the I64A. Using the electrons transferred and the generated H^+, NAD^+ was reduced at I64A. 93

Figure 57: UV-Vis spectra for 5 hour long H_2-driven NADH generation in flow in a CNC. The peak at 260 nm shows that NAD^+ was consumed and the peak at 340 nm shows that NADH was generated, and the conversion was 49 %. 94

Figure 58: Reaction mechanism showing acetophenone to (S)-1-phenylethanol conversion. 94

Figure 59: A schematic representation of the H_2-driven acetophenone reduction mechanism on the electronically conducting CNCs. Hyd-2 (cyan), I64A (blue) and ADH (green) were co-immobilised on the CNCs. Acetophenone and NAD^+ in H_2 saturated buffer was used as the reaction mixture. H_2 was oxidised, acetophenone was reduced. NAD^+/H was constantly reduced/oxidised. Thus, it was recycled in the reaction mechanism. 95

Figure 60: HPCL chromatograms for starting reaction mixture (black) and the overnight solution after cycling through the CNCs (red). The peak around 2.1 minutes is the 1-phenylethanol peak and the peak around 3.4 minutes is the acetophenone peak. 96

Figure 61: Gas chromatography results for acetophenone reduction to (S)-1-phenylethanol. Traces for a) racemic 1-phenylethanol (both S and R enantiomers), b) (S)-1-phenylethanol and c) overnight acetophenone reduction with acetophenone and (S)-1-phenylethanol peaks. ... 97

Figure 62: Reaction mechanism showing pyruvate to L-alanine conversion. In the experiments sodium pyruvate was used instead of pyruvic acid and ammonium chloride was used instead of ammonia. 98

Figure 63: A schematic representation of the H_2-driven pyruvate reduction mechanism on CNCs. 98

Figure 64: HPCL chromatograms for overnight pyruvate amination in flow in CNCs. a) the HPLC curves for the overnight reaction mixture. The peak around 7.2 minutes is the pyruvate peak

and the peak around 12.5 minutes it the L-alanine peak. b) the HPLC traces for the starting reaction mixture (black) and the overnight reaction mixture (red). The traces show an increase in the peak around 12.4 minutes i.e. show overnight L-alanine production. 99

Figure 65: A schematic representation the CVD set-up for WS_2 nanoflower synthesis. 106

Figure 66: Scanning electron micrographs of WS_2 nanoflakes and nanoflowers grown on Si substrates showing effect of experiment duration on the growth. a) 5-minute long experiment, substrate 5, b) 20-minute long experiment, substrate 5. 108

Figure 67: Scanning electron micrographs of WS2 nanoflakes and nanoflowers grown on Si substrates in a 20-minute long experiment showing the effect of substrate position on the growth. a) substrate 1 at 235 mm, b) substrate 3 at 255 mm, and c) substrate 5 at 255 mm. 108

Figure 68: Scanning electron micrographs of WS_2 nanoflakes and nanoflowers grown on MWCNT carpets in a 20 minute long experiment. 109

Figure 69: Scanning electron micrographs of WS_2 nanoflakes and nanoflowers grown on CNCs in 20 minute long experiments. 110

Figure 70: Scanning electron micrographs of WS_2 structures grown on CNCs. The images a2, b2 and c2 are the Z-contrast images of a1, b1, and c1, respectively. The heavier atoms on MWCNTs are brighter in the images a2, b2, and c2. 111

Figure 71: Raman spectroscopy of WS_2 nanoflowers grown on Si substrate showing characteristic first order and second order peaks of WS_2. 112

Figure 72: Scanning electron micrographs and EDX spectra of different nanoflower morphologies on a carbon nanotube carpet. 113

Figure 73: Scanning micrograph and EDX spectra of nanoflowers and thin film on a carbon nanotube carpet. 113

Figure 74: Scanning electron micrographs and EDX spectra of prisms and nanoflowers grown on a carbon nanotube carpet. 114

Figure 75: XRD analysis of grounded product (WS_2) on CNT carpets showing characteristic peaks of crystalline WS_2 phase and other side products WO_3 and $FeWO_4$. XRD analyses was carried out by Dr Philip Holdway, Oxford Materials Characterisation Service. 115

Figure 76: a) Polarisation performance curves b) cyclic voltammograms for plain and WS_2 decorated MWCNT carpets for the first and tenth cycles. 117

Figure 77: Tafel curves for Pt, MWCNT carpets, and WS_2 on MWCNT carpets. 117

Figure 78: Alternative set-ups for using CNCs in H_2-driven biotransformations. 123

Figure 79: A schematic representation of a flow platform with a spectro-electrochemical cell (developed in Vincent group) for HER. WS_2 catalysts on MWCNT carpet substrates can be used as the working electrode (WE). 124

Figure A 1: HPLC calibration curves for acetophenone and 1-phenylethanol. R^2 value for acetophenone calibration curve is 0.994 and the line equation is $Y = 1.20 \times 10^6 X$. R^2 value for 1-phenylethanol calibration curve is 0.990 and, the line equation is $Y = 1.72 \times 10^6 X$. 149

Figure A 2: HPLC calibration curves for pyruvate and alanine. R^2 value for pyruvate calibration curve is 0.996 and the line equation is $Y = 1.15 \times 10^6 X$. R^2 value for alanine calibration curve is 0.995 and, the line equation is $Y = 2.81 \times 10^4 X$. 149

Figure A 3: A plot of $[NAD^+]/[NADH]$ vs $A_{260\ nm}/A_{340\ nm}$ that was graphed by using the calculated values with literature coefficients can be used to determine the concentration ratio of an unknown sample. 150

Figure A 4: Temperature profile of the 55 cm long single-zone horizontal tubular furnace used in CNC syntheses at 850 °C under 2.5 standard litre min^{-1} argon flow. 151

Figure A 5: HPCL curves for H_2-driven biotransformations on CNCs without enzymes. Absence of a peak around 2.1 minutes shows that the CNCs do not catalyse the reaction. Following the same procedure in **Section 3.2.1.5.2**, 3 mL of reaction mixture containing 1 mM NAD^+ and 10 mM acetophenone was cycled through the CNCs. The samples were 10 times diluted with MilliQ water for HPLC analysis. 152

Figure A 6: HPLC curves for overnight adsorption of acetophenone on MWCNTs scraped off CNCs. 30 µL of 10 mg mL^{-1} MWCNT solution was used with 500 µL 10 mM acetophenone. The dispersion was not successful. 153

Figure A 7: UV-Vis spectra for 19.5 hrs NADH generation on MWCNTs scraped off from a CNC. The same experimental conditions as NADH generation on carbon materials **Section 2.2.1.4** were used. However, the amount of the carbon used in the reaction was not the same due to the dispersion issues. a) spectra for 1:10 diluted NAD^+ starting solution and the 1:10 diluted 19.5 hrs reaction mixture. b) spectrum for 1:5 diluted 19.5 hrs reaction mixture. 153

Figure A 8: HPLC chromatogram for acetophenone to 1-phenylethanol reduction on MWCNTs scraped off CNCs. The same conditions as the highest yield ketone reduction experiment conditions were used. The samples were 10 times diluted with MilliQ water for HPLC analysis. Conversion in batch is 10 times less than the conversion in flow. MWCNTs were not dispersed prior to the experiment. 154

Figure A 9: The overall HPLC chromatograms for overnight ketone reduction in **Chapter 3**. 154

Figure A 10: The overall HPLC spectra for reductive amination in **Chapter 3**. 155

Figure A 11: Temperature profile of the 31 cm long single-zone horizontal tubular furnace used in WS_2 syntheses at 800 °C under 100 standard cubic centimetre per minute Ar flow. 155

Figure A 12: Raman spectra of a) WS_2-WO_3-CNT b) WS_2-CNT c) WO_3-CNT 156

Figure A 13: Cyclic voltammogram of a blank Si wafer 156

Figure A 14: Linear sweep voltammograms of an MWCNT carpet synthesised at 800 °C in 15 minutes (black) and an MWCNT carpet synthesised at 850 °C in 20 minutes (red). 157

LIST OF TABLES

Table 2-1 Literature extinction coefficients (ε) for cofactors NAD^+ and NADH.[215] 54

Table 2-2 Characteristics of carbon materials investigated. 57

Table 2-3 Overnight conversion of NAD^+ to NADH on the carbon materials for the optimised and final system. 67

Table 2-4 Overnight conversion of NAD+ to NADH on the carbon materials (BP,CP and CD) for all of the experiments with $p < 0.05$ 68

Table 4-1 Three possible reaction steps for HER 103

Table A 1: Correlation factor for Langmuir and BET models used for analysis of carbon materials in **Chapter 2**. 148

Table A 2 Table showing the calculated values of $[NAD^+]/[NADH]$ and $A_{260\ nm}/A_{340\ nm}$ with the method and the extinction coefficients in the literature[215] for the plot in Figure A 3. 150

Table A 3 Calculation of NAD^+/NADH ratio for 16 hr experiment in **Section 2.3.3** on carbon materials (CC, CD, CP, and BP). 151

Table A 4 Calculation of NAD^+/NADH ratio for 5 hr experiment in **Section 3.3.3.1** on CNCs. 152

LIST OF PUBLICATIONS

Papers

Zor, C., Reeve, H. A., Quinson, J., Park, H., Lonsdale, T. H., Grobert, N. & Vincent K. A. H_2-driven Biocatalysis in Flow Using Enzyme-Modified Carbon Nanotube Columns. *Ready for Submission, Awaiting IP Protection.*

Koz, C., Roßler, S., Tsirlin, A. A., Zor, C., Armagan, G., Wirth, S. & Schwarz, U. Effect of Co and Ni substitution on the two magnetostructural phase transitions in $Fe_{1.12}Te$. *Phys. Rev. B* **93,** 024504 (2016).

Talks

Zor, C., Reeve, H. A., Dillon F., Vincent, K. A. & Grobert, N. Novel scaffolds for Robust Biocatalysis. 2nd Year Talk, Oxford Materials, Oxford, UK, 2 March 2016.

Posters

Zor, C., Reeve, H. A., Vincent, K. A. & Grobert, N. Novel approach to H_2-driven biotransformations in flow systems. ICIQ Unicat Summer School, Berlin - Germany, 6-9 July 2015.

Zor, C., Prabakaran, A., Quinson, J., Dillon, F. & Grobert, N. WS_2 Nanoflowers on Carbon Nanotubes as Hydrogen Evolution Reaction Catalyst. *NanoteC 15*, Oxford - United Kingdom, 14-17 September 2015.



Naturmort Cherry Blossom – *WS_2 nanoflowers on a coiled multi-wall carbon nanotube*

(The image was shortlisted in 2015 RMS International Imaging Competition)

CHAPTER 1 INTRODUCTION

"Oui, mes amis, je crois que l'eau sera un jour employée comme combustible, que l'hydrogène et l'oxygène, qui la constituent, utilisés isolément ou simultanément, fourniront une source de chaleur et de lumière inépuisables et d'une intensité que la houille ne saurait avoir."

(L'Île Mystérieuse, Jules Verne, 1874)

1.1 Literature Review on Hydrogen Economy: The Production and the Applications of Hydrogen

This Thesis is primarily concerned with developing novel ways and materials for producing and using hydrogen gas for clean energy production and fine chemical synthesis applications. Initially, as an application of hydrogen gas, H_2-driven flow biotransformations on carbon nanotube columns (CNCs) were investigated for the production of fine chemicals including chiral amines and chiral alcohols. The novel CNC assemblies developed in the Grobert group[1] were employed as high surface area, stable, and electronically conducting supports for the enzymes used. Supporting enzymes on carbon particles is a method developed for batch chemical synthesis by Armstrong, Vincent and co-workers in recent years.[2–5] In this work, CNC assemblies enabled implementation of a novel flow system for the H_2-driven biotransformations previously studied in batch. Finally, for hydrogen production, novel transition metal dichalcogenide (TMDC) assemblies were developed to be utilised in hydrogen evolution reaction (HER) catalysis. WS_2 nanostructures were directly grown on multi-wall carbon nanotube (MWCNT) carpets and CNCs for the first time. WS_2 and improving its catalytic activities have been studied in the last decade for catalysis of HER. In this work, novel assemblies were developed to increase the electronical contact between catalysts particles and provide a platform for HER in flow.

The literature review initially focuses on hydrogen production methods and hydrogenation reactions, both in batch and flow processes. Then, catalyst immobilisation methods, including enzyme immobilisation techniques are discussed. Finally, cofactor regeneration methods are covered.

The Global Energy Challenge and Hydrogen

The global energy demand is expected to grow exponentially and by 2040 this expansion is set to increase by one-third of the demand in 2015.[6] Hydrogen is considered as one of the key answers to this increasing demand.[6–11] In a world, where climate change has become a severe issue and the abundance oil resources is uncertain, sustainable energy strategies based on renewable energy inputs and energy efficiency are extensively investigated.[7,8] The World Energy Outlook 2015 and 2015 Paris Climate Conference both report that the concept of long-term decarbonisation is vital and the core of international efforts to combat climate change should be aiming a low-carbon, high-efficiency energy sector.[6] Furthermore, global consensus on greenhouse gas emissions, decisions by United Nations Framework on Climate Change on global warming and sustainability, and policies of many inter- and intra- governmental organisations on renewable energy sources point to hydrogen as a key component in future energy systems.[6,8] Although the annual investment in low-carbon technologies is increasing, the cumulative investment in renewable energy up to 2040 represents only ~ 15 % of total investment in global energy supply.[6] Thus, there is still a substantial gap to fill in research and development, and investment regarding renewable energy sources and hydrogen as an energy vector.

1.1.1 Hydrogen Economy

The phrase “hydrogen economy” was first coined by John Bockris at General Motors in 1970.[8,9] The phrase quickly spread due to the oil crises in the 1970s.[8] It was used for mentioning hydrogen energy systems. Although the notion of hydrogen economy and the consideration of hydrogen as an energy vector have been around since the 1920s, hydrogen as a clean energy vehicle started to gain major attention in the 1970s.

In 1974, Caprioglio stated the urgent need for coupling hydrogen, as a secondary energy distribution and utilisation system, with already existing (fossil fuels *etc.*) and up-and-coming (nuclear energy) energy sources.[11] Hydrogen was considered as a suitable

energy vector due to its flexibility for the end uses, easy transportation, storability and cleanness.[11] Also, the already existing importance of hydrogen in the chemical industries as a reducing agent was also included in the bigger picture of H_2 economy. This market alone was seen well worth to take hydrogen into consideration.[11] Veziroglu's quarter century (1974 - 2000) hydrogen report (**Figure 1**) shows that until 1974 there was little or no usage and mention of hydrogen in the following: Electric power production, land vehicles, naval applications, space transportation, air transportation, aerospace planes, hydride applications, catalytic combustion appliances, and international energy programs. According to Veziroglu's 2000 hydrogen report, usage of hydrogen in these fields expanded tremendously from the 1970s to 2000.[10]

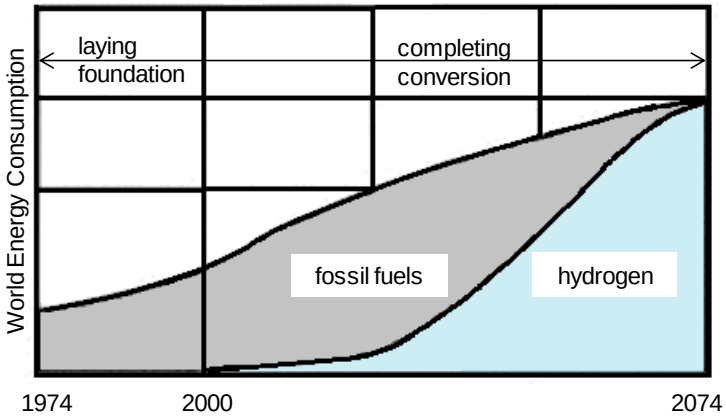


Figure 1: Veziroglu's 2000 projection for hydrogen economy. Adapted from Reference 10, © 2000, with permission from Elsevier.

The 2030 Climate and Energy Policy Framework of the European Council rekindled the notion of a hydrogen economy.[12] According to the Current Policy Initiative (CPI) scenario, the total production of hydrogen in the European Union energy systems in 2050 will be around 196 x 10^{11} L and this number will reach to 125 x 10^{12} L according to the long-term CO_2 cap scenario.[i] Overall, hydrogen is one of the top solutions for a sustainable future and is an essential part of chemical industries. Thus, more efficient methods for production of hydrogen and applications of hydrogen need to be developed.

[i] The production scales for 2050 are 250 petajoules and 1600 petajoules according to CPI and CO_2 cap scenarios, respectively. Petajoules were converted to litres by using 286 kJ $mole^{-1}$ as the heat of combustion of hydrogen and 22.4 litres as the volume of 1 mole of hydrogen.

1.1.2 The production of hydrogen

Hydrogen is a clean, non-toxic fuel[13] with a high energy density of 122 kJ g^{-1}.[14] This yield is 2.75 times greater than that of hydrocarbons.[14] Hydrogen is a flexible energy carrier and can be the backbone of a sustainable, highly-decarbonised energy system together with electricity.[8] Regarding sustainability, climate change, and pollution, the advantage of using hydrogen depends on its production method.[8]

There are numerous hydrogen production routes depending on the application it will be used and the scale of the process. These methods vary from large-scale production methods to high efficiency, small-scale, and/or proof-of-concept methods. The main large-scale hydrogen production method is steam reforming of hydrocarbons. Some of the recent small-scale methods include sorption-enhanced catalytic steam reforming of bio-oil,[15] gamma irradiation induced disintegration of waste activated sludge,[16] and CO_2 reforming of methane over $Ni/CeZrO_2/Al_2O_3$.[17]

Hydrogen can also be produced from renewable sources. Using biomass for hydrogen production is one of the environmentally friendly and sustainable methods. The methods of hydrogen production from biomass are usually collected under two major categories: thermochemical and biological.[18] Thermochemical methods such as supercritical water gasification, steam reforming of bio-oils, and pyrolysis have higher efficiency and lower cost compared to the biological methods such as photo fermentation and dark fermentation.[13,19]

One of the environmentally friendly hydrogen production methods which also makes use of renewable resources is water splitting by electrolysis (**Figure 2**).[20,21] However, commercial alkaline electrolysis systems (AES) usually consume 4.2 - 5 kWh m^{-3} electricity to produce pure hydrogen (99.5 % - 99.9998 % purity).[13,22] They have the highest cost among other large-scale, commercially available hydrogen production methods (**Figure 3**).[23] Usually in water splitting by electrolysis, cathode is coated with platinum. Thus, large-scale water electrolysis technologies are not yet cost-efficient. A key solution is employing

new catalysts in these processes. However, one of the challenges in tailoring catalysts is obtaining very low or zero overpotential. A cobalt phosphate catalyst was introduced by Kanan *et al.*[24,25] as an alternative to expensive platinum catalysts. This development made the water splitting systems a lot cheaper, since cobalt phosphate is highly abundant and cheap compared to platinum. However, the applications are not in large-scale yet. According to Ulleberg, the basic improvements needed for AES are reducing specific cell resistance, increasing process temperatures and reducing electrode overpotentials.[26]

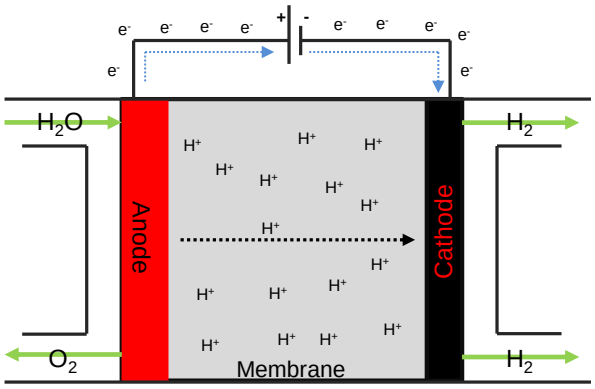


Figure 2: A schematic representation of electrolysis of water. H_2 is produced at the cathode. Up to date, expensive platinum/platinum coated materials are used as the most efficient catalysts for water splitting.

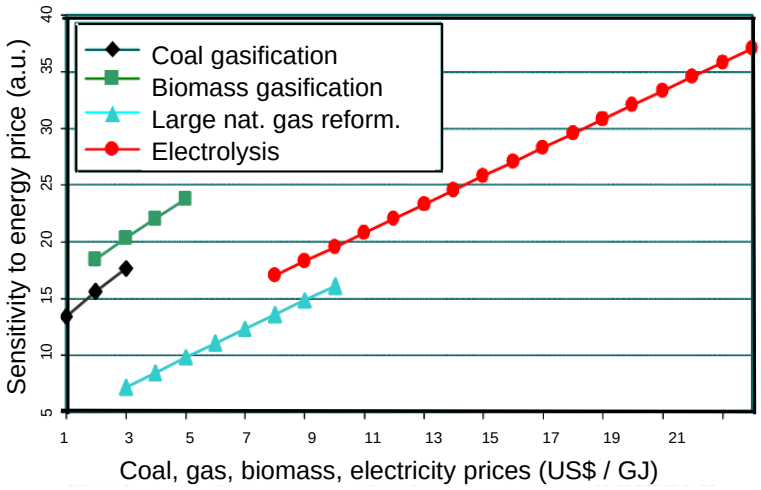


Figure 3: 2007 H_2 production cost (US$ / GJ). Sensitivity of different H_2 production technologies to energy price. Reproduced from Reference 23, © 2007, with permission from OECD/IEA.

Other clean methods for hydrogen production include utilising wind, geothermal and solar energy in electrolysis applications. Solar energy is an indirect hydrogen production method and is utilised to provide electricity for methods such as electrolysis (**Figure 4**).[27] Today,

one of the efficient hydrogen production methods utilising solar energy is coupling ultra-high temperature solar concentrators with thermochemical water splitting.[28] This method offers an opportunity to decrease the cost of solar to hydrogen systems to $ 2 - $ 4 per kg, which meets the target of the US Department of Energy.[29]

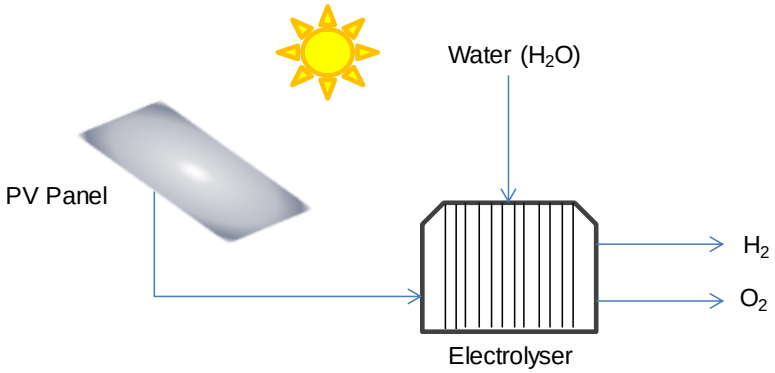


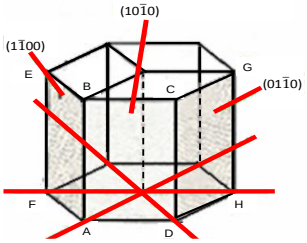
Figure 4: A schematic representation of a photovoltaic (PV) unit for a hydrogen production system.

Hydrogen evolution reaction (HER) is one of the most widely investigated reactions in electrochemistry. It is the main reaction in hydrogen production by water splitting (electrocatalytic or photoelectrocatalytic) and H_2 oxidation and, it produces highly pure hydrogen.[30–32] HER requires highly efficient, highly stable and robust catalyst materials. Noble metals are the most widely used catalysts in HER applications. They are, at present, the most active catalysts for HER. However, for large-scale applications they are limited by their elemental abundance and high cost.[33] Some of the properties of an ideal electrocatalytic cathode listed by Jaccaud *et al.*[34] are as follows: i) low hydrogen overvoltage at industrial current densities, ii) no potential drift, iii) chemical and electrochemical stability, iv) low sensitivity to short-circuit, v) high adhesion to the support, and vi) low manufacture cost. Thus, researches have been investigating materials with good catalytic activity, high stability, low overpotential and cost for HER catalysis.[30,31,35] Hence, in this Thesis, HER was chosen as a clean hydrogen production method and a transition metal dichalcogenide material (WS_2) as assembly on carbon supports was studied as a HER catalyst.

1.1.2.1 Hydrogen evolution reaction (HER)

As mentioned in ***Section 1.1.2,*** watersplitting is one of the main methods for hydrogen production and HER is the key reaction in this method. Researchers have been focusing on moving away from high cost, low abundance bulk noble metal catalysts to either nano-noble metal catalysts or earth abundant transition metal compounds. HER catalysis with nano-noble metal assemblies offers better catalytic performance due to high surface area, low density, and high reactant permeability. It also decreases the amount of precious metal used.[36,37] On the other hand, cheaper transition metals are already shown to be good catalyst materials for HER since, in nature, hydrogenase enzymes have Fe-Fe or Ni-Fe active sites.[38] Myriads of transition metal compounds, such as FeP,[39] Ni_2P,[39] CoP,[40,41] CoS_2,[42] MoP,[43] MoS_2,[44–48] and WS_2[44,49–51] have been studied and proven to catalyse HER. One of the widely studied HER catalysts are transition metal sulphides, MS_2 (M= Mo or W). Theoretical and experimental studies show that mainly the metallic edges of MS_2 are electrocatalytically active.[45–47] The origin of the high activity of these materials was thought to be due to the under coordinated sulphur atoms at the $1\ 0\ \bar{1}\ 0$ edge[ii] in 2H polymorph forms that possess a metallic character (MS_2 materials obtained by lithium exfoliation have a metastable 1T phase that is responsible for HER catalysis.).[52] Thus, tailoring the chemistry and morphology during the synthesis, such as maximising these edges, is one of the keys points to increase the electrocatalytic performance of these materials.[49] Another key factors is overcoming the poor electrical conductivity of MS_2. To eliminate this issue, conductive materials are usually used along with the MS_2 catalyst materials.[44,48,50,51]

[ii] $1\ 0\ \bar{1}\ 0$ prism plane. Miller-Bravais indices for hexagonal lattice system. In this notation system 4 indices are used (h k i l) and a plane is specified using these indices. h+k+i = 0.



However, from an electrocatalytic perspective, overpotential is still a key challenge for these catalysts.

1.1.3 The applications of hydrogen in chemical industries

The study of hydrogenation reactions goes back to the start of the 20th century. Sabatier pioneered catalysing hydrogenation reactions of alkenes and arenes by finely divided metallic nickel.[53] Hydrogenation reactions are mainly catalysed by metallic particles, colloids and mononuclear soluble complexes. Various metals and metal oxides are good heterogeneous catalysts for hydrogenation reactions. Fe, Co, Ni, Zn, and Ru, Rh, Pd, Ir, and Pt are widely used for hydrogenation reaction catalysis.[54] Raney nickel and palladium on charcoal are simple, widely used heterogeneous catalysts. Additionally, metal complexes, offer substrate-, regio-, and enantio-selectivity depending on the ligand selection.[53] Thus, the combination of the above listed metals and other elements are commonly used to alter the activity and/or the other properties of the catalyst.[55] Adding hydrogen to double bonds of unhindered alkenes was established as early as 1966. Wilkinson *et al.*[56] showed the feasibility of this addition by using rhodium phosphine complexes in homogenous phase. A rapid, practical, and homogenous system for reduction of alkenes, alkynes and other unsaturated alkenes were first conducted with the Wilkinson catalyst[a]. With the development of the resolution of optical isomers, alongside the Wilkinson catalysts, led to the discovery of asymmetric hydrogenation reactions of prochiral unsaturated substances with C=C, C=O, and C=N bonds.[53] New ligands, new metal complexes and new routes for hydrogenation were developed in the last two decades *e.g.* lanthanide catalysts[57] and transfer hydrogenations.[58]

For industrial applications, catalysts are usually used on a support material, the one exception being Raney-type catalysts. Using catalyst supports offers larger exposed surface area of the catalyst, less sensitivity towards the effect of additives and impurities and higher resistance to catalyst poisoning.[55,59–61] There are many different catalyst support materials and preparation methods for catalysts and support assemblies. These

approaches vary from impregnation of the support with the active metal catalyst to deposition of the catalysts in the microchannel of flow reactors.[55,60,62–66] In this research, the support material chosen to be used in flow applications is novel carbon nanotube columns due to their high surface area, inertness in the desired biotransformations, robustness, and electrical conductivity. Catalyst support materials and catalyst immobilisation methods will be further discussed in ***Section 1.1.5***.

Large-scale hydrogenation reactions

There are many important industrial scale hydrogenation reactions. In industry, transfer hydrogenations of unsaturated compounds are used to eliminate explosive hydrogen gas or moisture-sensitive hydride reagents in the preparation of saturated chemical products.[67–69] Furfural[b] hydrogenation plays a big part in the chemical industries in the production of lignocellulosic biofuels and value-added chemical such as furan[c], and furfuryl alcohol[d].[70] Asymmetric transfer hydrogenations of ketones are used in many industrial applications[71] such as in the production of α- and β-adrenergic blockers, agonists in the treatment of cardiovascular diseases,[72] in the synthesis of the antidepressant (*S*)-duloxentine[e],[73] and in the generation of the only stereocenter in the anti-Alzheimer drug Ladostigil. [74]

Other than large-scale fine chemicals and pharmaceutical applications, there are industrial-scale hydrogenation applications as well. Some of the main pollutants in flue gas in chemical industries are SO_x and H_2S gases. The Clauss process is one of the main sulphur recovery processes. In these processes, the main reaction taking place is hydrogenation of sulphur species and the effluent gas.[75] Nowadays, conventional hydrogenation catalysers are being replaced by low-temperature hydrogenation catalysers. They are used for larger industrial processes. [76]

Selectivity in large-scale hydrogenation reactions

One of the industrial applications of hydrogenation is hydrogenation of 1,3-butadiene. It has been investigated widely and has established production methods for large-scale applications such as production of cleaner fuels and petrochemical intermediates.[77–79] Continuous stirred slurry and fixed bed reactors are some of the reactors used in large

scale production of 1,3-butadiene.[77] These reactors all have pros and cons depending on the scale of the production and the reaction conditions. For example, continuously stirred slurry reactors (CSS) have better temperature control, lower external mass transfer resistance, and pressure drop compared to fixed bed type reactors. On the other hand, CSS give lower conversion and are more difficult to scale up. Some studies use packed trickle-bed reactors for 1,3 butadiene production due to their good liquid distribution, tolerance to wide range of reactions conditions, and high conversion. However, they do not perform well with small catalyst particles and result in large pressures in the stream.[77] Overall, there has been much research on optimising the reaction conditions (reactor type, size, feed stream composition, catalyst size *etc.*) for higher yield and selectivity in different reactors.[79–82]

1.1.3.1 Reactions catalysed by hydrogenases

The current processes for generating hydrogen and using hydrogen either require harsh reaction conditions or employ toxic and/or expensive catalysts and reactants.[83] Thus, there has been intensive research on developing sustainable hydrogen production methods as mentioned in ***Section 1.1.2.*** One of these methods is concentrating on the catalysis methods of nature, which consist of mild and sustainable mechanisms. These mechanisms employ enzymes as catalysts. Enzymes are protein molecules that act as macromolecular biological catalysts. As discussed in ***Section 1.1.3,*** many metals and metal complexes are able to active hydrogen. In this section, the focus moves away from ability of metals to activate hydrogen to ability of micro-organisms to activate hydrogen, thus to enzymes that activate hydrogen.[84]

In nature, enzymes are used as modular catalysts to combine redox half reactions in biological cells for specific mechanisms.[83] Hydrogenases are enzymes that catalyse reversible oxidation of hydrogen.[85] Hydrogenases have been widely investigated for the last decade as immobilised electrocatalysts and in numerous applications such as hydrogen fuel cells, light-driven hydrogen production, and H_2-driven chemical synthesis in

small-scale.[86] There are different families of hydrogenases found in nature: [FeFe], [NiFe], and [Fe] hydrogenases.[83,87] The consideration of using hydrogen for possible future biotechnology applications go back to the 1980s. In 1986, van Berkel-Arts pointed out some of these applications such as using hydrogenase at electrode surfaces, photochemical production of H_2 by hydrogenase, and the production of fine chemicals by a system containing specific enzymes, hydrogenase, and H_2.[88]

Today, the applications of hydrogenases are much more closely investigated. One of the main fields that hydrogenases are used in is electrocatalysis. These enzymes can be isolated from cells and put on electrode surfaces to be used as electrocatalysts. The activity of the enzyme is linked with the current produced. Thus, with the hydrogenases adsorbed or covalently attached onto electrodes, results show the immediate catalytic behaviour over a given potential under specified reaction conditions such as pH, temperature, and partial pressure of H_2 or O_2.[86] Another area of research is photoelectrochemical cells. Hambourger *et al*.[89,90] worked on the development of photoelectrochemical biofuel cells. They observed similar H_2 production rates both for platinum catalyst and [FeFe]-hydrogenase on carbon.[90] One of the possible areas is biofuel cells and Ciaccafava *et al.*[91] designed H_2/O_2 biofuel cells where hyperthermophilic O_2-tolerant hydrogenase and bilirubin oxidase were immobilised on functionalised CNTs. Although the power densities that they reached were low, they showed that the biofuel cell was stable up to 24 h continuous usage and point out that the development of this cell can offer an alternative power supply for portable devices.[91]

One of the focuses of this Thesis is using enzymes (including hydrogenase) for catalysis of chemical transformations and methods for making the system suitable for chemical industries (such as implementation of a flow device). There have been proof-of-concept demonstrations of using immobilised hydrogenases for fine chemical synthesis.[86] Vincent *et al.*[2] showed that by co-immobilising hydrogenase and nitrate reductase reduction of nitrate[f] to nitrite[g] can be catalysed. Armstrong and co-workers demonstrated water gas shift reaction on hydrogenase and carbon monoxide dehydrogenase modified graphite platelets

(**Figure 5**).[3] In 2012, Vincent and co-workers developed a modular heterogeneous catalyst system for recycling of the biological cofactor NADH on pyrolytic graphite particles modified with *R. eutropha* NAD^+ reductase and *E. coli* Hyd-I.[4] Following this development, a recent publication by Vincent and co-workers further investigated the novel selective H_2-driven hydrogenation system with cofactor recycling mechanism. A greater than 98 % conversion of acetophenone[h] to 1-phenylethanol[i] was achieved on carbon black modified with alcohol dehydrogenase, hydrogenase and an NAD^+ reductase with high enzyme stability.[5]

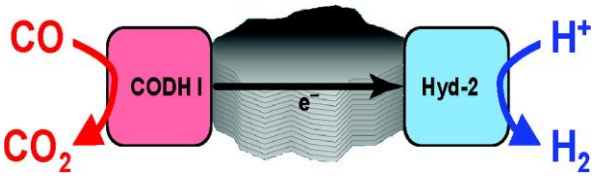


Figure 5: A schematic representation of water-gas shift reaction catalysed by immobilised enzymes (carbon monoxide dehydrogenase (CODH I), pink and hydrogenase (Hyd-2), blue) on graphite platelets (grey). Reprinted from Reference 3, © 2009, with permission from American Chemical Society.

There is also various research going on mimicking the active sites and the working mechanisms of hydrogenases and replicating their behaviour *in vitro* (**Figure 6**).[87] The earliest research which focuses on synthesising complexes of Group VIII metals with ligands to activate molecular hydrogen like hydrogenases do goes back to the 1970s.[84] Metal complexes that mimic hydrogenases are aimed to be inexpensive, efficient (*i.e.* work at low overpotentials and have high moles of H_2 produced per mole of catalyst used), robust[92] and derived from non-precious metals.[38,93]

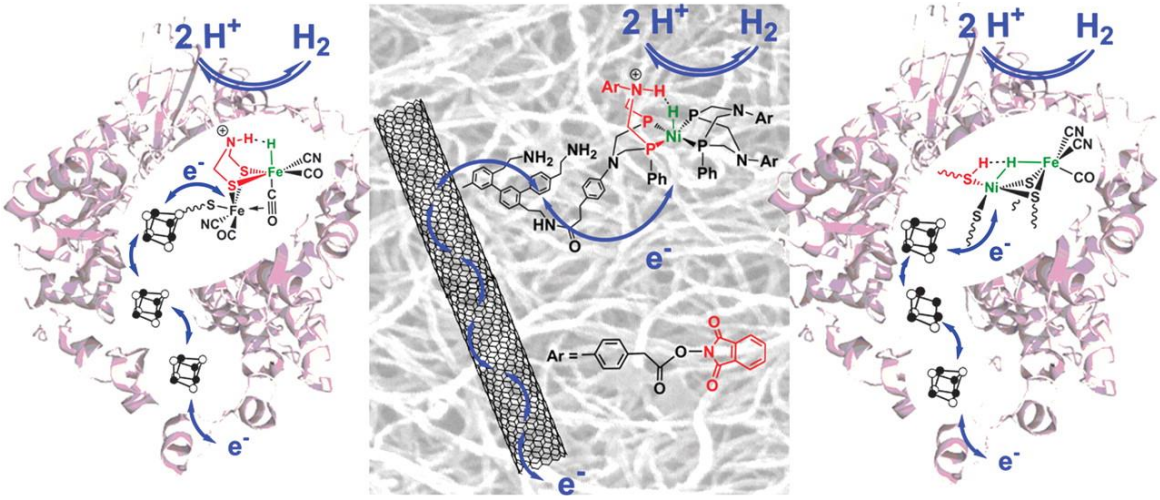


Figure 6: Representation of the bio-inspired cathode material (middle). A nickel bisdiphosphine complex was covalently attached onto a multi-wall carbon nanotube to mimic the active site of hydrogenase enzymes. [FeFe] and [NiFe] hydrogenases in their reduced active state (left and right, respectively), and the H_2-evolving Ni catalyst modified carbon nanotube (middle). Reprinted from Reference 87 with permission from AAAS, © 2010.

1.1.4 Comparison of Batch and Flow Processes

Pharmaceutical, fine chemical, and nanomaterials industries have been working on developing millimetre or submillimetre flow synthesis systems for the last decade.[94–102] In 2005, the American Chemical Society (ACS), Green Chemistry Institute (GCI), and some global pharmaceutical companies, such as AstraZeneca, Merck and GlaxoSmithKline, founded the ACS GCI Pharmaceutical Roundtable.[103] Their aim is to develop and encourage green chemistry, engineering, and green industry. In 2007, ACS GCI Pharmaceutical Roundtable agreed on several key chemical research areas and engineering process conditions.[104] Some of the key research points are as follows: amide formation avoiding poor atom economy reagents, aldehyde or ketone + NH_3 + ‘‘X’’ to give a chiral amine, asymmetric synthesis of amines from prochiral ketones and, solvent-less reactor cleaning.[104] Continuous processing and bioprocesses were listed as the top two green engineering areas to be focused on.[103]

Fine chemical and pharmaceutical substance (active pharmaceutical ingredient or the formulated drug) production usually involve many steps and require quality and uniformity control at several points during the process. Conventionally, these processes are done in

several consecutive batch reactors. The limiting factor in the batch processing is usually the equipment itself, whereas continuous processing is only constrained by process parameters such as flow rate and temperature.[103] Continuous processes have many advantages over batch processing. Thus, the chemical industries are focusing on replacing the already existing batch reactors with suitable and feasible continuous flow reactors and developing novel production processes for novel reaction sets.

In the fine chemical industry, continuous processing offers cost-efficient, environmentally friendly, safe, and high quality production compared to batch processing. It reduces costs, the size of the equipment, solvent utilisation, energy consumption, and waste generated.[99,103,105–108] In continuous processing, actuators, automated fluid handling, automated optimisation, and process analytical tools enhances synthesis applications.[98,109–112] Continuous processing has many advantages especially in small-scale production. Small-scale flow reactions usually offer better heat and mass transfer and enable highly exothermic reactions to run safely.[109,113] Additionally, since the headspace issue is eliminated in flow reactors, accumulation of toxic or dangerous reactants such as hydrogen is avoided.[114] Overall, flow chemistry offers sustainable, environmentally friendly, and more efficient processes.

1.1.4.1 Hydrogen production in flow

Many hydrogen production processes are conducted either fully or partially in flow. One of the bio-hydrogen production methods is fermentation using anaerobic bacteria. The continuous flow stirred-tank reactors (CSTRs) have been widely used in this production method.[115,116] When the hydraulic retention time is the same with the retention time of the bacteria, the bacteria may be washed out.[116–118] In these cases, granule-based and biofilm based reactors, which require cell immobilisation can be alternatives to traditional CSTR.[116,117] They maintain high biomass concentration without biomass washout. Bio-hydrogen is also produced from sludge from plants such as wastewater treatment plants (*e.g.* rice winery, potato processing)[119] and from waste materials such as municipal

solid wastes.[120] CSTRs (typically used reactors which represent suspended-cell systems) and up-flow reactors (which can maintain higher levels of fermentative biomass and higher hydrogen production rates compared to the conventional CSTRs) are some of the flow reactors used for the bio-hydrogen production.[121]

Water splitting by photocatalysis is a popular hydrogen production method conducted under mild conditions with no harmful by-products and has a possibility to be combined with solar energy systems.[122–124] The first example of water splitting for hydrogen production, which mimicked natural photosynthesis was conducted in batch mode by Sayama *et al.*[125] The latest reactors developed for large-scale, cost efficient industrial applications are twin membrane flow reactors.[122,126,127] Another hydrogen production method is steam reforming of methanol. Usually, two dimensional flow microreactors such as packed-bed reactors[128] are used in hydrogen production from steam reforming of methanol for small-scale applications.[129] Three dimensional reactor designing also led to development and utilisation of novel small-scale reactors for hydrogen production such as serpentine flow reactors (**Figure 7**)[130]

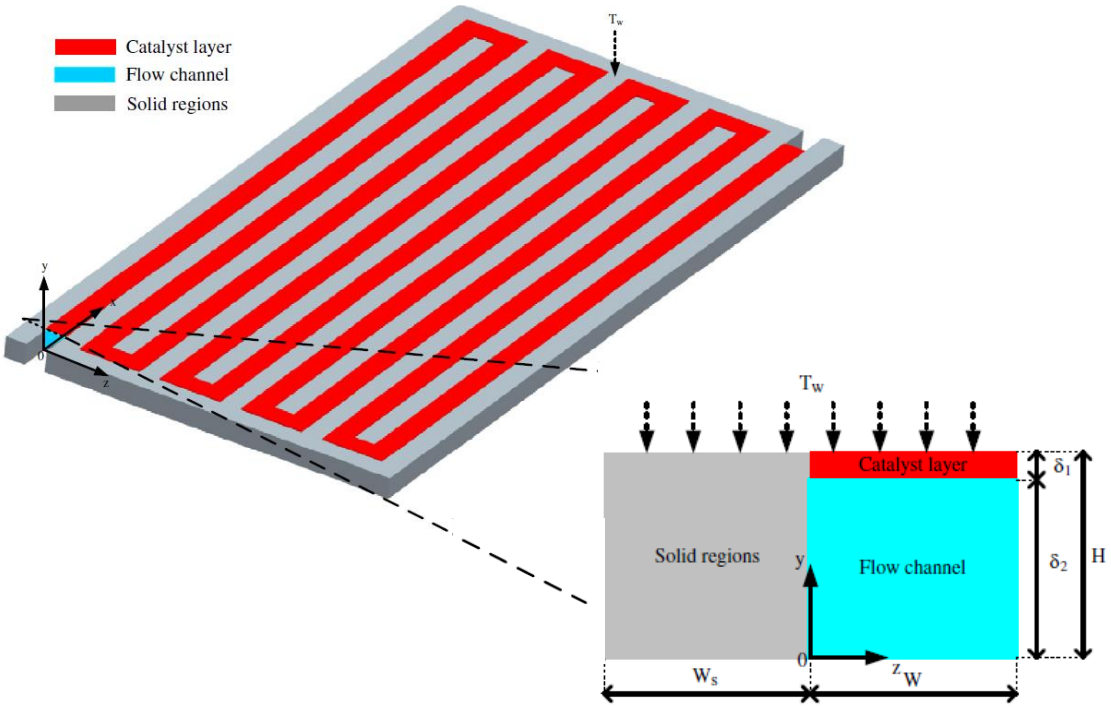


Figure 7: A schematic representation of a serpentine design micro-channel flow reactor. The image is adopted from Reference 130, © 2010, with permission from Elsevier.

1.1.4.2 Hydrogenation in flow

Hydrogenation reactions are an essential part of the chemical industry. One of the up-and-coming methods for hydrogenation reactions in industry is using heterogeneous catalyst in continuous flow systems. Since, conventional batch processes for hydrogenation reactions are usually hazardous and tedious, due to the handling and separation of reactants and solid precious metal catalysts, novel continuous flow systems have been investigated.[106,131]

There has been commercially available hydrogenation flow reactors developed in the last decade. Some of these reactors are H-Cube® of ThalesNano,[132] Coflore ACR stirred flow reactor of AM Technology and Robinson Brothers Ltd.,[133] Integrated Lab Solutions' fixed bed and slurry selective hydrogenation reactors, and 5500 HP compact reactors of Parr Instrument Company.[134] In 2005, ThalesNano marketed the H-Cube® flow hydrogenation instrument, which is a high pressure hydrogenator with a HPLC-like substrate delivery platform.[55,132] In H-Cube® the substrate/hydrogen mixture runs through a packed catalyst bed. This results in a very high ratio of the active area catalyst to the amount of hydrogen/substrate.[55,135,136] Ley and co-workers showed the efficiency of a H-Cube® reactor is due to higher interfacial area between phases *via* the hydrogenation reaction to produce spatially desymmetrised butane-2,3-diacetal protected *meso* tartrate[j]. The reaction is challenging in batch and requires multiple days at 80 bar of H_2, whereas in an H-Cube® reactor, the reaction time was shortened to 4 hours and the pressure was reduced to 60 bar. The processes also offered recycling and high local concentration of the catalyst.[137]

Other than commercially available reactors, myriads of reactors ranging from industrially well-established reactors such as packed-bed flow reactors to custom-made flow reactors are also utilised for hydrogenation reactions.[55] In hydrogenation reactions, packed-bed micro reactors usually make use of immobilised organometallic materials in flow. Thus,

they eliminate the problems homogenous catalyst face such as downstream catalyst separation and catalyst recycling.[109,138]

Homogeneous catalysis has many advantages compared to heterogeneous catalysis, even though continuous flow heterogeneous hydrogenation catalysis is much more established. Homogeneous catalysis offers increased selectivity of the product and better activity.[131] Also, the mechanism for the homogeneous catalysis is more easily comprehended than that of heterogeneous catalysis. However, separating the homogeneous catalyst from the product is a major setback for large-scale applications.[131,139] Researchers have been focusing on making homogeneous catalysis as practical as heterogeneous catalysis for the last decade. There has been much investigation on immobilising homogeneous catalysts on solid support materials.[66,140–144]

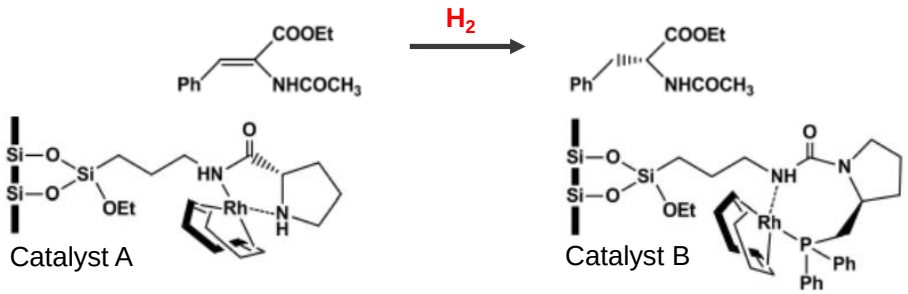
1.1.5 Catalyst immobilisation methods

One of the aims of catalyst research is achieving catalyst and catalyst support assemblies that display the advantages of both homogeneous and heterogeneous catalysis. Homogeneous catalysis offers highly active and selective mechanisms and heterogeneous catalysis consists of robust catalysts, which can be easily removed from the reaction solution and are readily implemented in flow reactors.[145,146] As mentioned in ***Section 1.1.3***, the use of a support material usually offers larger exposed catalyst surface area, and often makes the catalyst less sensitive towards additives and impurities.[55,59–61] Support material and catalyst assemblies are prepared using numerous different methods, depending on the properties of the catalyst, the support material, and the nature of the desired application.[55,59–61,140–142,146–150]

Precious metals have been the main catalysts used in the chemical industries for decades. Metal catalyst particles may be immobilised on various support materials.[55] Alumina[k], silica[l], zeolites, activated carbon, and carbon based materials are some of the commonly used support materials for metal catalysts.[55] Carbon materials are preferred in some applications over alumina and silica due to their stability.[141] For example, activated carbons

are stable both under acidic and basic conditions, whereas alumina and silica are dissolved at high pHs. Alumina is also attacked at very low pHs.[141] In this work, carbon support materials were used not only due to their electronic conductivity, but also due to their stability and inertness in H_2-driven biotransformations. However, as stated before, the selection of the support materials depends on the components of the desired application.

Immobilising homogenous catalysts is one of the most widely investigated areas due to the unique selectivity and versatility of chiral homogenous catalysts, especially for asymmetric catalysis.[145,151–153] One of the studies on this shows increased enantiomeric excess for two different catalysts on two different supports for hydrogenation of (*Z*)-N-acetamidocinnamic acid derivatives (**Figure 8**).[145] Thus, the results show that it is possible to achieve higher selectivity when homogenous catalysts are immobilised. However, many reports show reduced activity, accessibility or the stability of the immobilised/supported catalyst, hence intense research is going on to unify both homogenous and heterogeneous catalysis.[146]



	Homogenous	Heterogeneous	Heterogeneous
		On silica	On USY zeolite
Catalyst A	54 % ee	58 % ee	94 % ee
Catalyst B	34 % ee	84 % ee	53 % ee

Figure 8: Comparison of the ee of homogeneous and heterogeneous (on silica and USY zeolite) hydrogenation of (Z)-N-acetamidocinnamic acid derivatives catalysed by rhodium complexes with a proline derived ligand.[145]

Anchoring catalyst particles (organometallic catalysts, metal nanoparticle catalysts, enzymes *etc*.) on support materials *via* different physical and chemical approaches is one of the main focus points of industrial-scale fine chemical and biochemical research. This section briefly pointed out that catalysts and support materials have been developed and tailored for specific applications in numerous ways. Overall, the chemical industries initially

aim developing catalyst immobilisation to achieve better yield and higher selectivity and, make the final chemical process environmentally friendly. Then, it is aimed to implement these developments to economically feasible large-scale applications with low cost of catalyst per product.

1.1.5.1 Carbon materials as catalyst supports

According to Auer *et al.*,[141] until the development of nano-carbons in the mid-1990s, three carbon materials (activated carbons, carbon black and graphitised materials) were used and modified as precious metal catalyst supports. These support materials were developed to optimise catalyst properties and performance in the chemical industries.[141] Metal catalysts are preferably supported on materials, which allow the stabilisation of small particles and fine particle dispersions. The use of small catalyst particles allows access to larger numbers of catalytically active atoms than in a bulk metal. Thus, fine dispersions of carbon supports make the catalyst accessible.[141] Due to the possibility of easy tailoring of morphology of carbon and its surface properties, carbon based support materials have been investigated as catalysts support materials for several decades. Overall, carbon is a cheap, easily manipulated and functionalised and, electronically conductive support material with high surface area and porosity. In this work, commercial carbon materials (amorphous carbons such activated carbon) and carbon nanotube assemblies are used as catalyst support materials. Properties of carbon support materials will be further discussed in ***Chapter 2*** and ***Chapter 3***.

1.1.5.2 Enzyme immobilisation

Researchers in both academia and industry have been moving towards more environmentally friendly and sustainable processes of chemical synthesis. The use of enzymes in chemical synthesis has gained importance in the last decade because enzymatic processes usually involve fewer steps, generate less waste (as they are often more selective) and can be more energy efficient than conventional catalysis. In addition,

the enzymatic reaction conditions are milder, *e.g*. close to ambient pressure, ambient temperature and physiological pH, compared to the synthetic routes. Enzyme immobilisation has been widely investigated since it can enable the enzymatic processes to be reproducible, cost-effective, and make them practical for large-scale applications. Regarding the chemical and physical properties, immobilised enzymes are preferred to free enzymes mainly due to the improved stability and recyclability of the biocatalysts, and the lowered risk of contaminating the product with enzyme residues.[147]

Enzyme immobilisation was first reported in 1916 by Nelson and Griffin, who showed that the adsorbed enzyme, invertase on charcoal retains its activity.[154] Later, immobilisation of invertase (on commercial supports such as cellulose[m] supports or divinylbenzene[n] polystyrene[o] derivative resins) started to be used in industrial applications and became one of the important processes in sugar industry for hydrolysis of sucrose[p].[155] Although the immobilised enzymes have been investigated since the mid-1910s, they were only used in small-scale applications until the development of improved immobilisation techniques in the 1960s.[156]

The first industrial application of immobilised enzymes was demonstrated in 1969 by Tanane Seiyaku Co. Aminoacylase was physically adsorbed on polymer DEAE-Sephadex and used for production of L-methionine[q] in a packed bed reactor. This process overcame issues such as separation of the product, reusability of the enzyme and, high cost-low yield batch process.[156]

Some industrial scale enzyme immobilisation approaches

One of the common enzyme classes used in industrial applications is lipases. These lipases have been used to catalyse many chemical reactions such as ester synthesis,[157] polymerisation,[158] and solvent-free amidation of lauric acid[r].[159] Although most of the applications remain small scale, there is much on-going research to develop cost-efficient large scale processes.[160,161]

One industrial application of lipase B from *Candida antarctica* is production of myristyl myristate.[162] Evonik Industries have been producing several hundred metric tons of myristyl

myristate[s] per year using *Candida antarctica* lipase B. They run their biocatalytic esterification reactions at around 60 °C, whereas the temperature of the traditional esterification of long-chain fatty acids and alcohols can go up to 240 °C.[162] Tufvesson *et al.*[161] investigated the immobilisation and stability of lipase B from *Candida antarctica* for developing industrial-scale applications, since the cost and the enzyme stability are the major setbacks of these applications. They achieved complete stability for five consecutive batches of amidation reactions, each for 10 hours at 70 °C, in a packed bed reactor-loop set-up.[161]

1.1.5.2.1 Carrier-free enzyme immobilisation methods

Carrier free enzyme immobilisation started in the 1960s. Initially, dissolved enzymes were cross-linked with a bi-functional chemical cross-linker and the resulting immobilised enzymes were called cross-linked enzymes (CLEs).[147] This method had many drawbacks such as low activity, low mechanical stability, difficult in handling the gelatinous CLEs and poor reproducibility. In the 1990s cross-linked enzyme crystals (CLECs) started to be used for commercialised and industrial applications. CLECs were robust, highly active and enabled the control of particle size. On the other hand, the enzyme had to be crystallised. This was a major drawback since crystallisation is a difficult process and requires high purity enzymes. As a result, the CLECs were replaced by cross-linked enzyme aggregates (CLEAs).[147] Preparation of CLEAs involves precipitation of enzymes, as physical aggregates by addition of salts, non-ionic polymers or water miscible organic solvents, and cross-linking. CLEAs can be prepared from crude enzyme preparations, are cost-efficient and robust, exhibit high facile recovery and recyclability (**Figure 9**). Today, CLEAs are commercially available and employed in myriads of biocatalytic applications.[147]

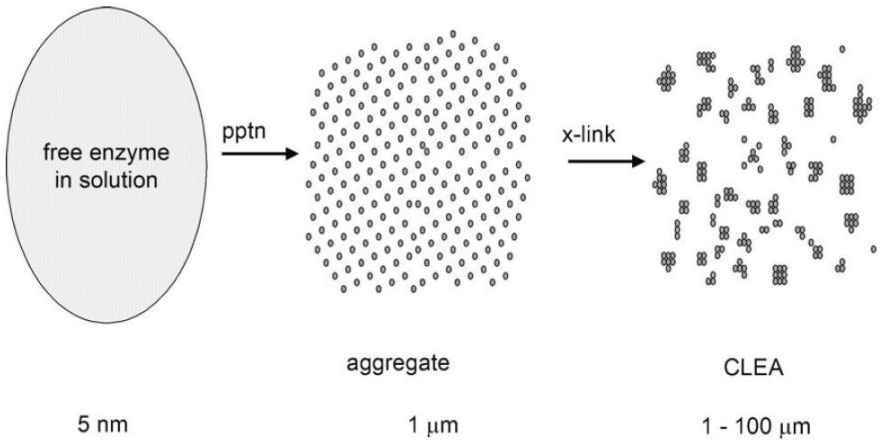


Figure 9: Schematic representation of preparation of CLEA. Reprinted from Reference 147, © 2007, with permission from John Wiley and Sons.

1.1.5.2.2 Enzyme immobilisation methods on support materials

As mentioned in ***Section 1.1.5***, there are numerous catalyst support materials and numerous methods for immobilising catalysts (*e.g.* metals or enzymes) on these support materials. Enzyme immobilisation methods can be collected under three main categories, binding enzymes to a prefabricated support, encapsulation and cross-linking. The binding method can have ionic, covalent or physical (*e.g.* hydrophobic and van der Waals interactions) nature.

The encapsulation method comprises the inclusion of an enzyme in a polymer network, such as silica sol-gel or polyacrylamide[t], or in membrane device such as a hollow fibre or a microcapsule. The cross-linking method is a carrier free method where enzyme surface groups interact with bi-functional chemical cross–linkers.[147]

Binding enzymes to a prefabricated support is a widely used enzyme immobilisation method. It allows implementation of enzymes as heterogeneous catalysts, offers easy automated control in flow systems, allows almost instant separation and, is cheaper than other immobilisation methods.[163] Direct physical adsorption of the enzyme on a support surface is an easy and time saving method, which does not involve complex chemical steps. However, the forces keeping the support and enzyme together (*e.g*. hydrophobic interactions, van der Waals forces) may not be strong enough to prevent enzyme leakage. To overcome leaching, covalent attachment to surface functionalised acrylic resins, such

as Eupergit® C, is used.[147] Eupergit® C is widely used in many industrial applications and allows enzymes to retain most of their activity after many cycles.[163] However, in many of the presented immobilisation methods, the effects of mass transfer and enzyme kinetics are not taken into account.

One of the drawbacks of the encapsulation method is the enzyme leakage, which is usually due to the weakness of the polymer network. Thus, an extra covalent attachment is usually required. Sol-gels are the most commonly used networks for encapsulation. In a study, Reetz *et al.*[164] showed that a porous support added to the sol-gel process resulted in materials with "double immobilisation", higher thermal stability and enzymatic activity. Overall, the encapsulation process may result in the leakage of the enzyme, but with additional modifications in the immobilisation process the enzymatic activity may be higher than other immobilisation processes.

Overall, the benefits of all immobilisation approaches discussed above depend on the chosen enzyme and support/gel/cross-linker, nature and the scale of the process. It is difficult to pick one universal one method and catalyst support. In this Thesis, adsorption on a prefabricated support was chosen as the enzyme immobilisation method. This method is easy and does not require complex chemical steps. It is applicable to the enzymes used in this work. In addition, enzymatic properties are not affected in this method. Thus, the selectivity of the enzymes used for this work remains unaffected. Most importantly, the carbon support provides an electronically conducting network for enzymes which is crucial for the reactions in this work.

1.1.5.2.3 Non-carbon materials for enzyme immobilisation

There are many different enzyme support materials, since there is not one well-established immobilisation method suitable for all the novel applications of enzymes. Porous silica supports are one of the most widely used enzyme support materials due to their large surface area, narrow pore size distribution, well-defined pore geometry and toxicological safety. They also offer thermal and mechanical stability and, the possibility of modifying

their surface with various functional groups.[149] However, there are not any industrial applications making use of the tailor-made silica supports yet. Other materials used as enzyme supports include zeolites, organic compounds, apatite and magnetic nanoparticles.[148,149] However, zeolites, due to their small pore size (< 1.3 nm), are not suitable to be used as large enzyme (molecular size 3 - 30 nm) support materials.[148] Organic compounds such as polystyrene polymers and polyacrylamide are also used as enzyme support materials. But their stability in organic solvents is low and some of them have low resistance to microbial attack.[165] Although the enzymes may maintain high activity, the support itself usually lacks thermal and chemical stability. Organic solid materials usually have relatively high toxicity to enzymes as well.[166] Thus, inorganic solid supports such as silica, zeolite, activated carbon based supports, have advantages over organic supports.

One of the inorganic solid support materials that has gained a lot of attention in the last couple of years is the group of clay based support materials. They can have large surface areas, demonstrate swelling and ion exhangeability.[167,168] They also possess different surface functional groups. Thus, the modified clay supports with increased adhesion area, hydrophobicity, lowered steric hindrance and additional functional groups have been investigated for biosensor and biocatalysis applications.[166,169–171]

One of the latest developments in enzyme immobilisation research involves employing nanomaterials as supports. The unique and adaptable chemical, physical, optical and electrical properties of nanomaterials allow them to be used with many enzymes with different catalytic properties. The high surface-to-volume ratio also increases the efficiency of the immobilisation. Following the trend in immobilisation methods, the immobilisation on nanoparticles offers higher thermal stability and broader working conditions compared to free enzymes. Additionally, compared to other immobilisation methods, it is easier to control the particle size. Enzymes have been reported to be immobilised on many different nanostructures such as on silica nanotubes,[172] gold nanoparticles,[173,174] iron oxide nanoparticles,[175,176] and selenium nanospheres[177] for biotechnological applications.

1.1.6 Catalyst used in this Thesis

1.1.6.1 WS_2, a transition metal dichalcogenide as a catalyst for HER

MX_2s (M: transition metal, X: chalcogen) belong to the family of transition metal chalcogenides (TMCs).These compounds are formed when a transition metal (group IV-X) combines with a chalcogen (Group XVI: S, Se, and Te). Transition metal dichalcogenides (TMDCs) are one of the most investigated inorganic materials due to their layered graphene like structure and electronical properties. WS_2, an anisotrophic semiconductor from the TMDC family, is one of the most investigated inorganic compounds. It can be synthesised in different ways to produce thin films, inorganic fullerene-like structures (0D),[178] inorganic nanotubes (1D),[178] inorganic graphene analogues (2D),[179] and nanoflowers (3D).[178] The properties of the materials changes according to its structure. Thus, the applications of WS_2 changes accordingly.

In the last decade, following the developments in using MoS_2 in HER, WS_2 has been studied as a HER catalyst as well. The catalytic activity of WS_2 is attributed to the edge sites of 2D nanostructures. More specifically, it is due to the unsaturated sulphur atoms along the edges. This is true for the bulk WS_2, which mainly consists of 2H phase. Thus, the basal surfaces in these materials are mostly catalytically inactive. More recently, the lithium exfoliated WS_2 structure have been studied. These materials consist of 1T phase and the catalytic activity is due this metastable phase.

These materials are investigated as alternatives to expensive and comparatively rare platinum as HER catalysts. Platinum has near zero overpotential and is the most electroactive material for HER up to date. The main challenge with WS_2 materials are lowering the overpotential, increasing the amount and reactivity of active sites, poor electronical contact between the catalyst and its support.[50,180]

In ***Chapter 4***, WS_2 nanoflowers and nanoflakes were directly grown on MWCNT structures for the first time as HER catalysts to increase the stability and the electronic contact

between nanostructures. The developments in this field is further discussed in ***Section 4.1.2***.

1.1.6.2 Hydrogenase, NAD^+ reductase and NADH dependant enzymes used in this Thesis to catalyse H_2-driven Biotransformations

1.1.6.2.1 Hydrogenase

Hydrogenases are enzymes used for H_2 activation. They catalyse oxidation of H_2 (yield protons and electrons) or reduction of protons to generate H_2. They can catalyse these reactions with high efficiency and activity under mild conditions. Hydrogenases are present in a variety of archaebacteria, bacteria and in some eukaryotes such as green algae.[181]

These enzymes have different classes depending on the metal in their active site. They either have [Fe], [FeFe] or [NiFe] active sites. In biology, [NiFe] hydrogenases are mainly used for H_2 oxidation and [FeFe] hydroganases for H_2 production. This Thesis uses a [NiFe] hydrogenase, which is natively attached to a protein membrane, but can be separated from the membrane and isolated from the cell. [NiFe] hydrogenases usually consist of a large and a small protein subunit. The large subunit contains the active site. The small unit contains iron-sulphur clusters that take part in electron transfer. The closest cluster to nickel is termed the proximal cluster and is a $[Fe_4S_4(cys^{iii\ u})_3]^{2-/3-}$ cluster. The medial cluster is a $[Fe_3S_4(cys)_3]^{2-/3-}$ and the distal cluster is a $[Fe_4S_4(cys)_3(his^{iv\ v})]^{1-/2-}$ cluster. The structures also contain a channel for H_2 gas to reach the nickel ion of the [NiFe] active site and a H-bonded network to carry protons in solution (**Figure 10**).[181]

Some hydrogenases are bound to a membrane that plays an important part in the electron transfer. These hydrogenases can exchange electrons with an electrode without a mediator and can be used as electrocatalysts for $2H^+/H_2$ cycling. Other hydrogenases

[iii] Cysteine (cys) is an amino acid with a thiol side chain. This thiol is nucleophilic and can easily be oxidised. Sulfide in FeS clusters are derived from cysteines.
[iv] Histidine (his) is an amino acid as well. It has an amino group, carboxylic acid group and imidazole side chain.

which do not have a membrane anchor are called soluble hydrogenases and they transfer electrons to a soluble electron acceptor or a redox partner protein.

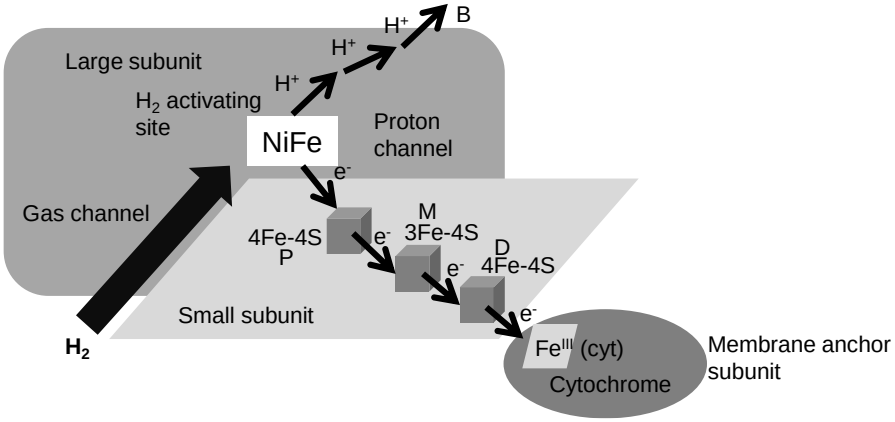


Figure 10: A schematic representation of [NiFe] hydrogenase. Three blocks in the subunit represent proximal (P), medial (M), and distal (D) clusters.

The [NiFe] membrane bound hydrogenase used in this Thesis is a hydrogenase-2 from *E.coli* (Hyd-2) (**Figure 11**). It was isolated and purified following published protocols.[182] It does not exhibit an overpotential requirement for H_2 oxidation, meaning it operates at the thermodynamic potential of the $2H^+/H_2$ couple.

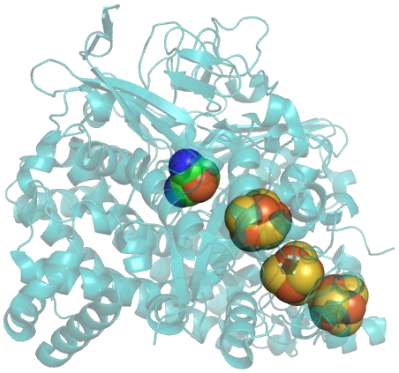


Figure 11: A cartoon representation of Hydrogenase 1 from E.coli. The enzyme used in this work, Hyd-2, is not crystallised. Thus, the structure is not in the literature. However, the arrangement of iron-sulphur clusters in the figure are same for Hyd-2. Yellow and orange spheres are iron-sulphur clusters and the blue-green-orange-pink spheres are carbon monoxide-(dicyano) iron and nickel. Figure was prepared using The PyMOL Molecular Graphics System, Version 1.3 Schrödinger, LLC. Hyd-1 PDB code 3UQY, H_2-reduced structure of a membrane bound hydrogenase-1 from E. coli.[183]

1.1.6.2.2 Soluble hydrogenase – NAD⁺ reductase

The NAD^+-reducing soluble hydrogenase (SH) from *R. eutropha* H16 can catalyse both the H_2-driven reduction of NAD^+ and electron transfer from NADH to H^+. It can function under an O_2 atmosphere. The SH consists of six subunits (HoxY, HoxH, HoxU, HoxF, and 2 HoxI) (**Figure 12 a**) which can be grouped together into two catalytic moieties (HoxHY and HoxFU).[184] HoxHY can be considered as the hydrogen cycling moiety and HoxFU as the NAD^+/NADH cycling moiety. The [NiFe] H^+/H_2 cycling catalytic centre is again close to an iron-sulphur cluster relay for electron transfer, and there is also a non-covalently bound flavin mononucleiotide (FMN) in HoxHY.

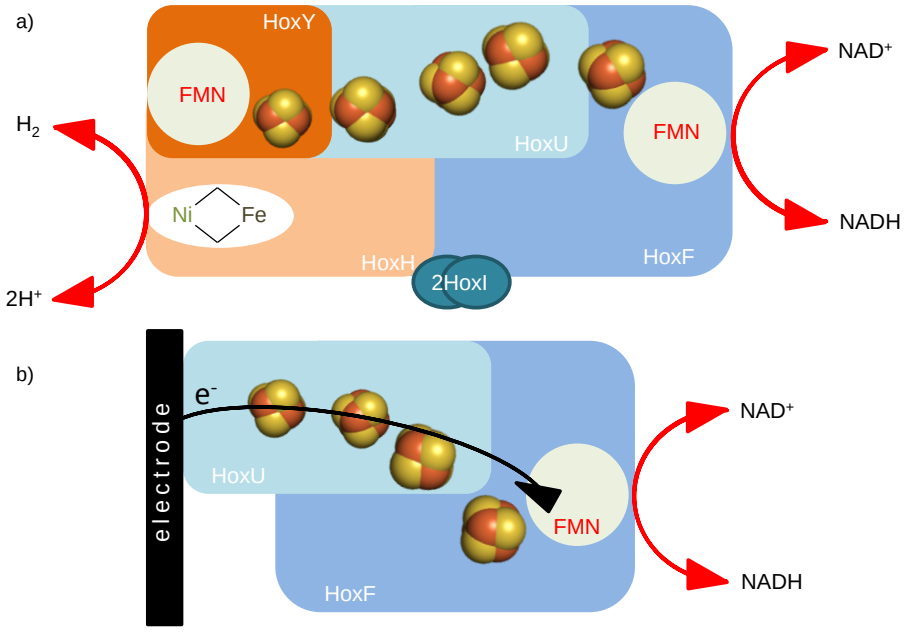


Figure 12: Modular structure of the soluble hydrogenase from R. eutropha. a) The SH consists of a hydrogenase dimer (HoxHY), a diaphorase dimer (HoxFU) and two HoxI subunits. Both HoxHY and HoxFU contain one FMN. The electron conducting FeS clusters are shown in elemental colours. b) HoxFU dimer of SH which can exchange electrons with an electrode/carbon surface and reduce (oxidise) NAD(H).

I64A, a variant of the soluble hydrogenase from *R. eutropha*, in which the inherent hydrogenase moiety is inactivated - due to the inability of the hydrogenase domain, was used as the NAD^+ reductase in this Thesis (**Figure 12 b**). Vincent and co-workers showed that HoxFU shows electrocatalytic activity for both NAD^+ reduction and NADH oxidation with minimal overpotential relative to the potential of the NAD^+/NADH couple. This is an

important point for this work since the difference between H^+/H_2 and NAD^+/NADH thermodynamic potentials is very small. **Figure 13** shows that at low concentrations of NADH and under high H_2 concentration, it is thermodynamically favourable to couple to NAD^+ reduction.

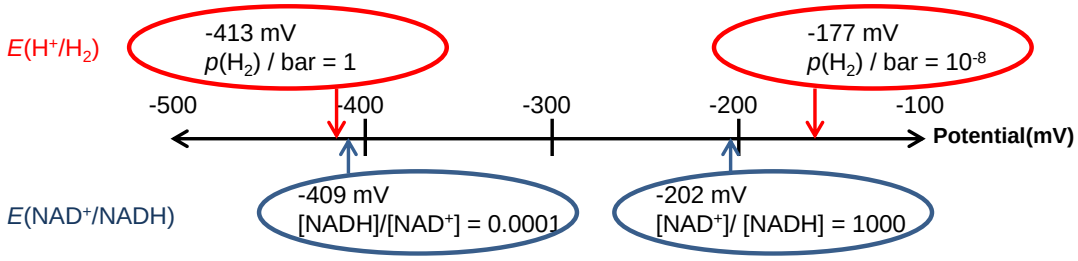


Figure 13: Thermodynamic potential of H^+/H_2 and NAD^+/NADH couples at pH 7, 25 °C, at different concentrations.

1.1.6.2.3 NADH-dependent enzymes

The reduction mode of oxidoreductases is very important for fine chemical synthesis, as it yields chiral compounds. Most of the known oxidoreductases require NADH or NADPH as a cofactor.[185] Thus, cofactor recycling is very important in the applications using these enzymes. Dehydrogenases belong to the oxidoreductase family and alcohol dehydrogenases and amino acid dehydrogenases (AADH) are two of the most commonly used enzymes in this family.

Alcohol dehydrogenase

This Thesis uses alcohol dehydrogenase (ADH) for ketone reduction (**Figure 14**). ADHs -also called ketoreductases, KREDs- transfer a hydrogen ion and two electrons from their NADH moieties to an acceptor molecule, a ketone in this case. In most of the cases, this is a highly stereoselective process. The hydride from the ADH is delivered either to the *re-* or *si-* face of the carbonyl.[185] Thus, the product is either (*R*) or (*S*). Alcohol dehydrogenase, ADH 105, used in this Thesis for ketone (acetophenone) reduction to secondary alcohol ((*S*)-1-phenylethanol) in ***Section 3.2.1.5.2*** was provided by Johnson Matthey Catalysis and Chiral Technologies. It belongs to the zinc-containing ADH family and is a recombinant enzyme produced in *E.coli.* It is (*S*)-selective towards acetophenone

and described to be compatible with several cofactor regeneration methods such as isopropanol/ADH and glucose/GDH methods.[186]

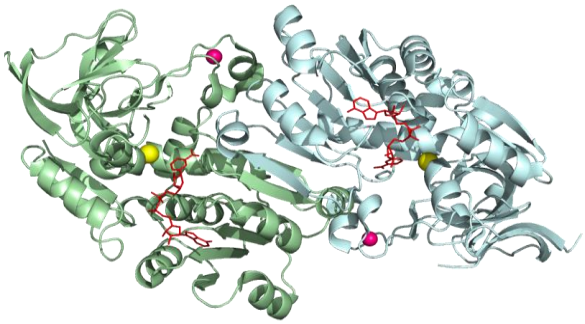


Figure 14: Cartoon representation of an ADH molecule. Red chains represent NAD$^+$s and yellow spheres represent Zn. Figure was prepared using The PyMOL Molecular Graphics System, Version 1.3 Schrödinger, LLC. ADH PDB code 4ILK, Short Chain Alcohol Dehydrogenase from E. coli.[187] ADH molecules are represented as green cartoons in ***Chapter 3****.*

L-alanine dehydrogenase

Alanine dehydrogenase (LalaDH) is the AADH used in this Thesis for α-keto acid (pyruvate[w]) conversion to α-amino acid (L-alanine[x]) (**Figure 15**). One of the main routes for chiral amino acid (α-amino carboxylic acid) production is kinetic resolution of racemates.[185] However, one of the desired methods of amino acid synthesis is enzymatic synthesis from prochiral precursors. AADHs are used for reductive amination and L-amino acids are the products, with only few exceptions. However, there is a limited number of AADHs used in chemical applications. Although the variation of the sequences of AADHs is high, the residues active in catalysis are highly similar. The LalaDH used in this Thesis is derived from *Bacillus cereus* and is a recombinant from *E.coli.* It stabilizes the α-keto acid when ammonia reacts with the acid and forms an imine. Then, water is produced as a side product and hydride from NADH is transferred for the production of the α-amino acid.

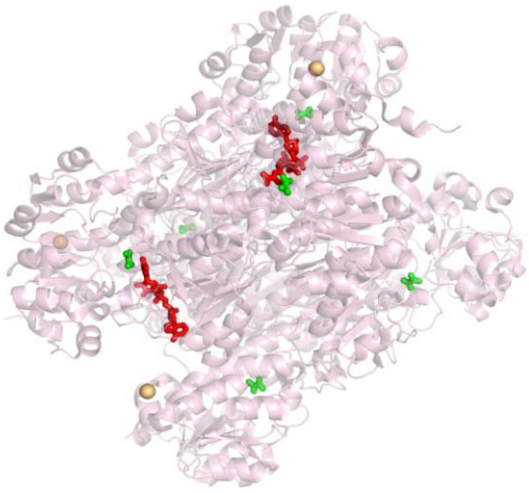


Figure 15: Cartoon representation of an L-alanine dehydrogenase crystallised with pyruvate and NAD^+. Red sticks represent NAD^+ and green sticks represent pyruvate. The enzyme used in this work is not crystallised in the literature. However, the crystal structure of L-alanine dehydrogenase from Phormidium lapideum complexed with NAD^+ was used as a representative L-alanine dehydroganese, which also uses pyruvate as a substrate. Figure was prepared using The PyMOL Molecular Graphics System, Version 1.3 Schrödinger, LLC. LalaDH PDB code 1PJC.[188] LalaDH are represented as red cartoons in ***Chapter 3****.*

1.1.7 Cofactor regeneration methods

Most of the enzymes that are desirable for redox reactions require additional chemical components to function. These helper components are either cofactors –one or more inorganic ions, such as Fe^{2+}, Mg^{2+}, Mn^{2+}, Zn^{2+} *etc.*- or coenzymes –complex organic or metalloorganic molecules, such as tetrahydrofolate[y], lipoate[z] *etc*.[189] Some proteins require both one or more metal ions and a coenzyme. One of the most common cofactors used by redox enzymes –and by the redox enzymes in this Thesis- is nicotinamide adenine dinucleotide NAD(H). There are around 700 enzymes known to use NAD(H) as a cofactor.[190] In redox reactions, this cofactor acts a proton and two electron (H^-) transporter. Thus, the cofactor is found in two forms: an oxidised form, NAD^+, and a reduced form, NADH (**Figure 16**). In industry, NAD(H) plays an important role in enzyme biocatalysed chiral compound synthesis[190] and in synthetic reactions where conventional chemical catalysts fail.[191] NAD(H) is also used in Alzheimer's and Parkinson treatments, biosensors, as well as the synthesis of new high-value-added compounds such as pharmaceuticals, food additives, perfumes, insecticides-pesticides.[190]

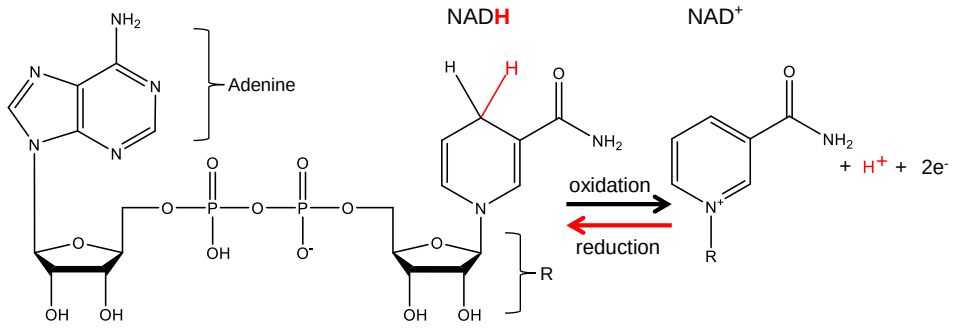


Figure 16: The structure of 1,4-NADH and NAD$^+$.

The cofactor, especially the reduced form, NADH, is very expensive. Because of its high cost, its usage in industrial processes is limited. Also, it is critical to provide stoichiometric amounts of NADH to the redox mechanism. Thus, the regeneration of NADH from the oxidised form, NAD$^+$, is a crucial step in chemical industries (**Figure 17**). However, as mentioned above, these cofactors are too expensive to use in stoichiometric quantities for industrial scale applications. Cofactor regeneration does not only decrease the cost associated with the cofactor by allowing it to be used in catalytic quantities (< 0.1 mol %), but can also simplify the product isolation and drive thermodynamically unfavourable transformations by coupling them with favourable regeneration reactions.[192]

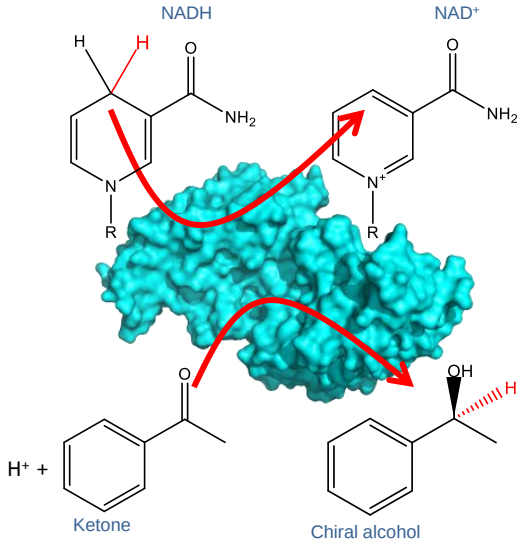


Figure 17: Image showing NADH being used by an NADH-dependant enzyme (blue) to reduce a ketone to a secondary alcohol.

There are several cofactor regeneration methods. The industrial-scale methods are enzyme-based or whole-cell based and the lab-scale methods include electrochemical,

photochemical and H_2-driven approaches. The main challenge is to implement cofactor regeneration methods and processes with immobilised enzymes and to flow processes. Ideally, a cofactor generation method should allow the cofactor to be cycled 1000 - 10000 times.[193] It should not complicate the purification of the final product and should not inhibit process.

1.1.7.1 Enzyme catalysed cofactor regeneration

There two pathways for the enzyme catalysed cofactor regeneration. One of them is using substrate-coupled systems and the other one is using a second enzyme to regenerate the cofactor.[193] The substrate-coupled mechanisms (**Figure 18 a**) use one enzyme and two substrates. The enzyme catalyses both the product synthesis and the cofactor regeneration. Thus, it uses both the oxidised and the reduced form of the cofactor. One of the substrates is used for product synthesis and the other one for cofactor recycling. It is quite difficult to achieve thermodynamically favourable conditions for both reactions simultaneously, since one enzyme is catalysing both. The enzyme-coupled methods (**Figure 18 b**), which require a second enzyme, are the most common cofactor regeneration methods in industry. Two enzymes and two substrates are used in these mechanisms. One of the enzyme-substrate couple is employed in catalysing the desired product synthesis, whereas the other couple is used for the cofactor regeneration.

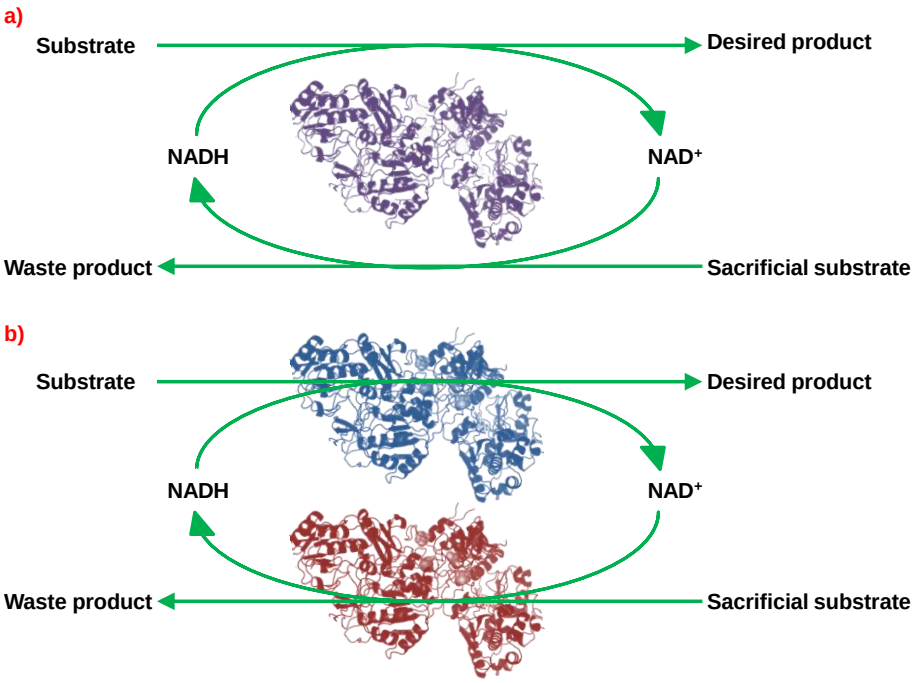


Figure 18: Schematic representations of the enzyme-based cofactor regeneration methods. a) substrate-coupled cofactor regeneration method, using one enzyme both for the synthesis of the desired product and for the cofactor regeneration. b) enzyme-coupled cofactor regeneration method, using a second enzyme for cofactor regeneration.

Overall, in both methods, a sacrificial substrate is used and waste product is generated. Ideally, the additional substrate should yield a value-added product or should not be expensive. It would be also ideal to regenerate the additional substrate to be reused. The waste generated is usually carbon based and burnt at the end of the process. These complicate the final product and impair the environmental benefits of using enzymes for chemical transformations. In both of the enzyme-catalysed methods, it is difficult to obtain the optimum conditions to drive both of the reactions *i.e.* product synthesis and cofactor regeneration.

1.1.7.2 Electrochemical NAD^+ reduction

Electrochemical methods for NAD^+ reduction have gained attention because they do not require additional reducing reagents, allow easy product purification and are potentially low cost methods.[190] The main electrochemical NAD^+ reduction methods can be collected under three groups: direct, mediated and electro-enzymatic NAD^+ reduction (**Figure 19**).

However, these current electrochemical NAD^+ reduction methods are all in lab-scale. Also, there are several setbacks of these methods. In these methods, a counter electrode is needed to complete the circuit. Thus, there is also an additional oxidation reaction occurring at the counter electrode. In addition, the reactions occur only in the close proximity of the electrodes. Usually a potential is applied across the electrodes and this increases the potential low cost of these methods. One of the major set-backs in the direct NAD^+ reduction methods is the synthesis of the desired form of NADH.1,4 NADH is the only form used as the cofactor and the electrochemical methods can lead to formation of NAD_2 dimer or the proton addition may lead to different configurations of NADH.[190]

In most of the direct reduction approaches, there is an energy barrier that requires an overpotential to drive the reaction at the desired rate. Mediators are used to overcome this problem (**Figure 19 b**). Mediators usually are more active then NAD(H) on electrodes, regarding the electrochemical reaction. They also have lower thermodynamic potentials than the substrate for the desired reduction reaction. Overall, they provide higher reaction rates and require smaller overpotentials.[193,194] Although the mediated approaches require smaller overpotentials, these overpotentials are a significant challenge for industrial-scale applications. Similar to direct electrochemical methods, the mediated NAD^+ reductions methods are not very selective as well.

There are several studies on electro-enzymatic NAD^+ reduction methods (**Figure 19 c, d**). The idea behind these methods are combining the practicality of electrochemical NAD^+ reduction and the selectivity of enzymes. The first report on electro-enzymatic methods are by Durliat *et al.*[195] where they used cytoplasmic hydrogenase to regenerate NAD(H) by electrolysis on a Pt electrode. However, further studies showed that the enzyme is too unstable to be used in a reactor device[196] and there are no large-scale applications using this method. In a more recent study on characterisation of NAD^+-reducing soluble hydrogenase from *R. eutropha*, Vincent *et al.*[184] reported direct electron transfer between the electrode and the immobilised enzyme for NAD^+ reduction (**Figure 19 c**).

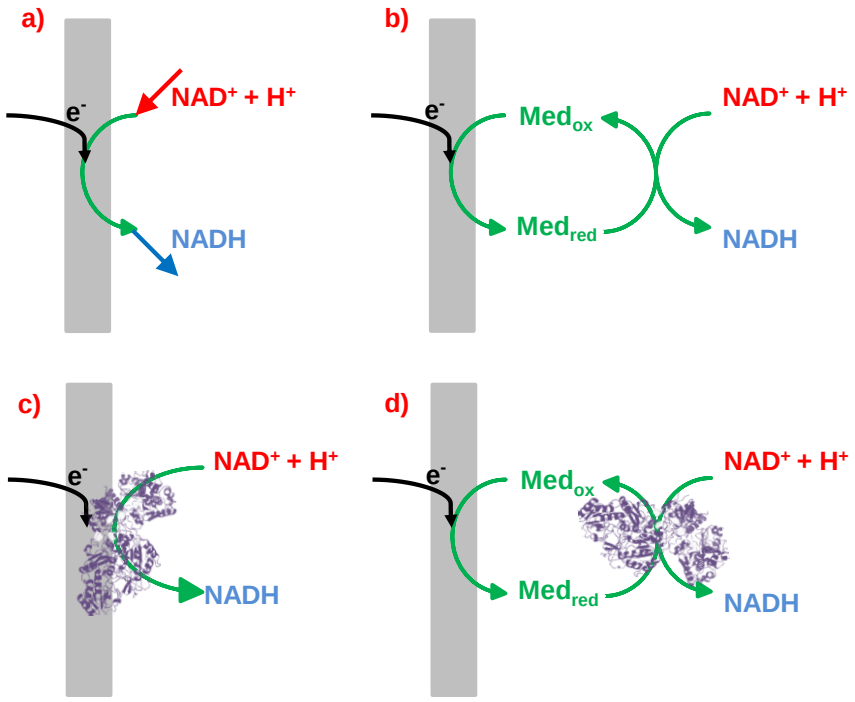


Figure 19: Schematic representations of different electrochemical NAD^+ reduction methods. a) direct NAD^+ reduction on an electrode. b) mediated NAD^+ reduction method where a mediator is used to lower the overpotential. c-d) electro-enzymatic NAD^+ reduction methods; c) uses an immobilised enzyme for NAD^+ reduction and in d) an enzyme uses electron from a mediator for NAD^+ reduction.

1.1.7.3 H_2-driven cofactor regeneration

In nature, some of the organisms produce enzymes that can couple oxidation of H_2 (producing two protons and two electrons) to the reduction of NAD^+. Enzymes such as hydrogenase I from *Pyrococcus furiosus*[197] and soluble hydrogenase from *R. eutropa*[198] have been studied for H_2-driven NADH regeneration. In 2013, Lauterbach *et al*.[199] studied a range of hydrogenases for NAD^+ regeneration. O_2-tolerant NAD^+-reducing hydrogenase from *R. eutropa* was found to be a promising enzyme for NADH regeneration.

H_2-driven NAD(H) regeneration methods (**Figure 20**) are 100 % atom efficient. Thus, they are environmentally friendly. Another benefit of these methods is that they use a cheap reducing agent, H_2. However, solubility of hydrogen gas in solution is an important limiting factor for these methods. The catalytic activity and stability of the soluble hydrogenases also limit the efficiency of the process. Currently, there are no industrial-scale H_2-driven NADH regeneration systems. However, the catalytic properties of the enzymes used, such as soluble hydrogenase, can be improved for the desired applications. There are some

methods using whole cells that contain both a soluble hydrogenase and an NADH-dependant dehydrogenase, but these methods are not scalable either.

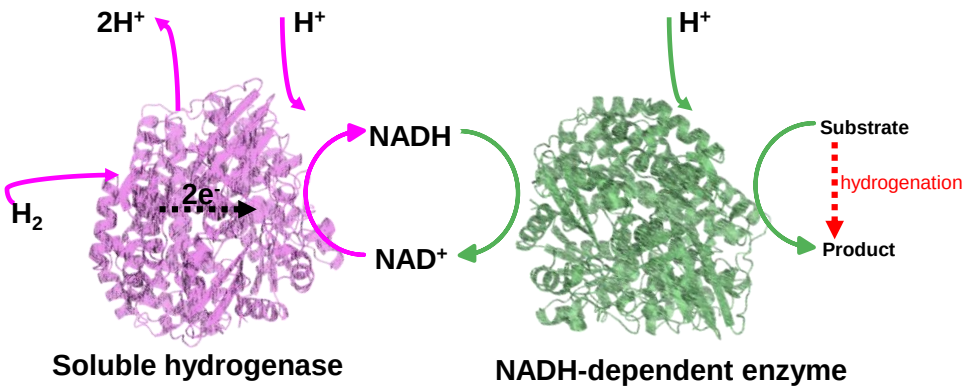


Figure 20: H_2-driven NADH regeneration by a soluble hydrogenase coupled with an NADH-dependent dehydrogenase.

In **Chapter 2**, the NAD^+-reductase (I64A) is coupled to a hydrogenase (Hyd-2) *via* different electronically conducting carbon materials to study a modular system for H_2-driven NADH generation. In ***Chapter 3***, this modular NADH generation is coupled with NADH-dependent enzymes for further biotransformations. Thus, NAD(H) recycling will be coupled to a NAD(H) dependent synthesis.

1.2 Summary and Conclusion

This Thesis, in a broad sense, focuses on i) developing novel methods and materials for using hydrogen in catalytic biotransformations and ii) novel materials for catalysing hydrogen production. Regarding the usage of hydrogen in chemical research and industry, H_2-driven biotransformations in flow on novel carbon nanotube columns were investigated. The new science includes utilising carbon nanotube columns as enzyme support materials and catalysing H_2-driven biotransformations (ketone reduction and reductive amination) in flow. On the aspect of hydrogen production, novel WS_2 catalyst assemblies for hydrogen evolution catalysis were studied. WS_2 nanostructures were directly grown on multi-wall carbon nanotube carpets and carbon nanotube columns for the first time as the new science.

This Introduction initially underlines the importance of hydrogen as an energy vector and briefly explains what hydrogen economy is. The current hydrogen production methods, what they lack and, the desired properties for novel hydrogen production processes are discussed. Consequently, the trends hydrogen evolution reaction are briefly introduced. Then, the applications of hydrogen in industry and the importance of hydrogenation chemistry for industrial applications and research is covered. Regarding the sustainability and low cost, hydrogenation reactions catalysed by hydrogenase enzymes are discussed. One of the key points in hydrogen economy and in chemical industry in general is translating current batch processes to flow applications. Thus, the Introduction then discusses the pros and cons of batch and flow processes both in hydrogen production and in hydrogenation reactions. In both batch and flow processes, using low cost, earth-abundant, environmentally friendly and, selective catalysts is a crucial point. For this, immobilising novel catalysts (non-precious metals or enzymes) on novel support materials is an important step. Hence, the Introduction also discusses the catalyst immobilisation methods and focuses on enzyme immobilisation.

Finally, the catalysts used in this Thesis are introduced. These catalysts involve transition metal dichalcogenide WS_2 for HER catalysis and enzymes, hydrogenase -NAD^+ reductase-NADH dependant enzymes, for H_2-driven biocatalysis. These enzymes use an expensive cofactor NAD(H). Thus, cofactor recycling mechanisms in the literature and this work are discussed as well.

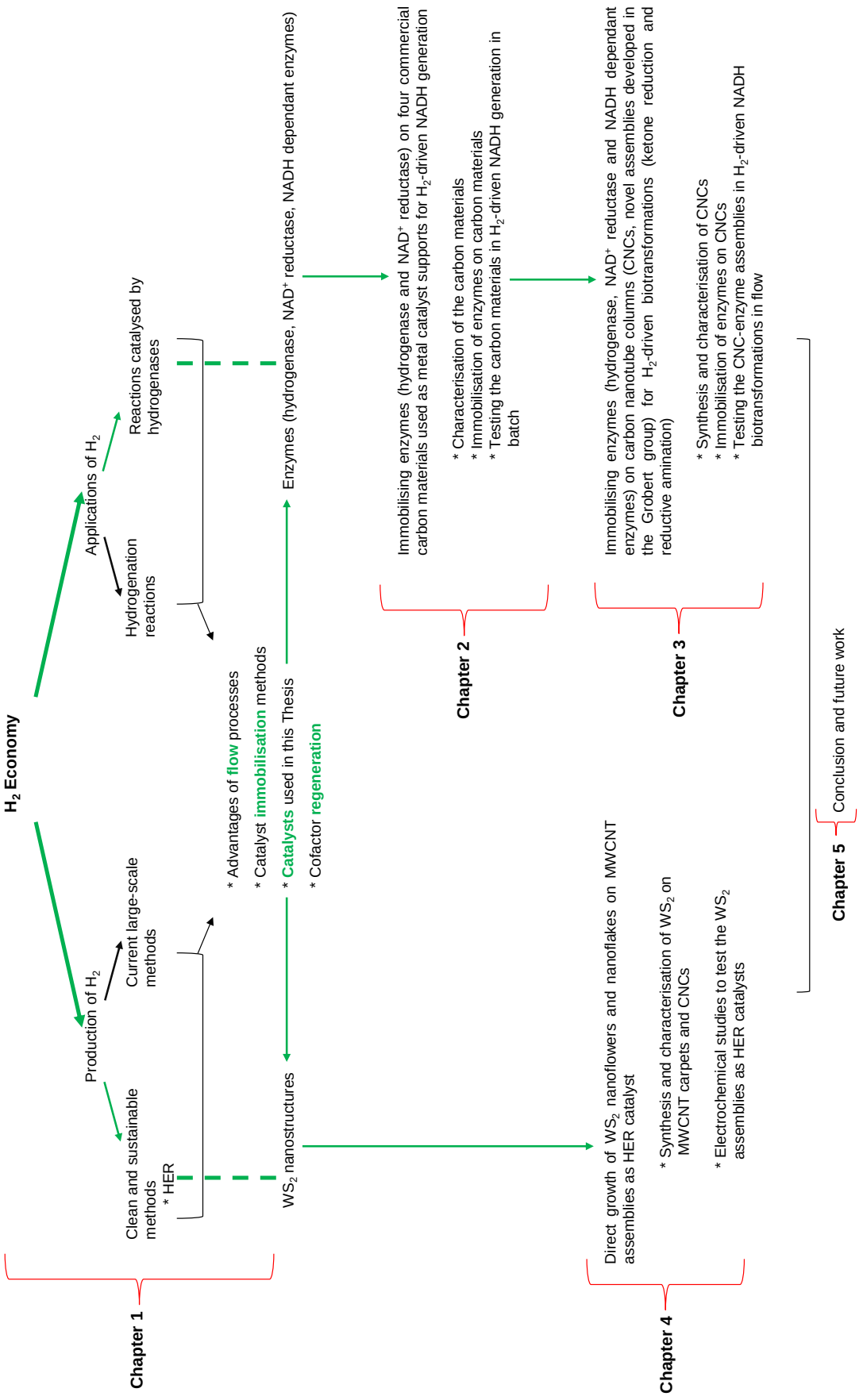
Overall, this Chapter shows that hydrogen is a key element for a green and sustainable future. It both plays a role in novel environmentally friendly energy applications and synthesis of both bulk and fine chemicals. Accordingly, the key points in hydrogen production and applications are pointed out. These are focusing on hydrogen evolution reaction and reactions catalysed by hydrogenases, implementing flow set-ups for these reactions and, developing sustainable and low cost catalysts. Thus, the aim of this Thesis is developing flow methods to improve hydrogen usage (H_2-driven fine chemical synthesis) and production (HER catalysis) for sustainable and cost-efficient applications.

Aims

- Referring to hydrogen economy for a sustainable and clean future
- Using environmentally friendly, cheap and simple routes for hydrogenation reactions (hydrogen in chemical and pharmaceutical industries) and for hydrogen evolution reaction (hydrogen as an energy vector).
- Employing enzymes as catalysts in hydrogenation reactions and related H_2-driven biotransformations instead of using precious metal catalysts.
- Making use of selectivity of enzymes for the synthesis of expensive and enantiomerically pure chemicals.
- Using carbon as a cheap, electronically conducting and stable catalyst support for enzymes.
- Immobilising enzymes on carbon materials for easy handling, to reuse enzymes and, to simplify the product purification steps.
- Translating current batch H_2-driven biotransformations to flow reactions.

- Investigating the suitability of the chosen commercial carbon supports for commercial hydrogenation reactors.
- Utilising carbon nanotube columns as mini flow devices for H_2-driven biotransformations.
- Using WS_2 as a HER catalyst instead of expensive and rare Pt catalysts.
- Growing WS_2 nanostructures on carbon nanomaterials for better electronical contact and stability.

1.3 Outline of the Thesis



CHAPTER 2. H_2-DRIVEN NADH GENERATION ON VARIOUS CARBON SUPPORT MATERIALS

This Chapter focuses on assessing the suitability of using different commercial carbon materials as enzyme supports for H_2-driven NADH generation in a batch set-up. The key points are testing the suitability of the four commercial carbon materials as electronically conducting supports for enzymes and using H_2 for NADH generation. Conventionally, these commercial carbon materials have been used as supports in metal catalysed hydrogenation reactions. In this Chapter, these materials are investigated for enzyme catalysed hydrogenation reactions. The Vincent group have demonstrated a H_2-driven system for NADH generation using carbon particles (initially pyrolytic graphite particles, then carbon black particles, Black Pearls 2000 (BP)) modified with hydrogenase and NAD^+ reductase enzymes.[4,5] In these batch processes, maintaining the activity and selectivity of enzymes and decreasing the cost of cofactors by regeneration methods are key points. The next step is translating these H_2-driven reactions into flow processes for safer and cheaper routes. However, these small size particles or particles with similar size and surface area are undesirable for translating the approach to flow processes due to particle size and pressure limitations. The development of a system for H_2-driven biotransformations in flow under high pressures with large surface area catalyst support materials is one of the aims of fine chemical industries. Challenges in this field include finding suitable high surface area support materials, growing tailored enzymes, decreasing the cost of cofactor/cofactor recycling and implementing these in a flow system under high-pressure.

This Chapter focuses on comparing BP and other commercially available carbon materials for enzyme immobilisation and H_2-driven biotransformations. Thus, the methods and results for investigating H_2-driven NADH generation using the enzyme-modified carbon system are presented in ***Section 2.2*** and ***Section 2.3***, as well as the characterisation of

these carbon materials for potential H_2-driven biotransformations in flow using hydrogenation reactors filled with these carbon materials.

2.1 Introduction

In this Chapter, the suitability carbon supports that are used for transition metal catalysed hydrogenation reactions are investigated for enzyme immobilisation for H_2-driven biocatalysis. Thus, their suitability for the H_2-driven cofactor (NADH) generation system is studied. The introduction, following the catalyst immobilisation methods in ***Section 1.1.5***, briefly discusses different carbon and nano-carbon support materials in catalysis and then focuses on carbon based enzyme support materials.

2.1.1 Carbon catalysis support materials

Carbon materials (initially bulk carbon materials, then nano-carbon materials) have been widely studied as metal catalyst supports as discussed in ***Section 1.1.5.1***. The surface of carbon materials can be easily modified and therefore manipulated for the desired applications. These surface modifications can make the surfaces more hydrophilic and enhance the dispersion of the carbons in the polar solvents required for the catalyst loading processes. There are various methods for functionalising and tailoring the carbon surfaces, such as acid treatment, base treatment, vacuum-ultraviolet photochemical reactions, oxidation and plasma treatment and microwave procedures.[200] However, acid and base treatments are the cheapest and most effective processes in the surface modification. Doping hybrid atoms into the nanostructures of carbons can also be used to alter the hydrophilicity and electrical conductivity of the materials.

Activated carbons are one of the popular catalyst support materials, especially in the purification of water and air, and in the separation of gas mixtures.[201] There are hundreds of commercially available activated carbons with different porosity for specific applications. These different activated carbons can be made from the same source. Usually coals,

peats, woods and some synthetic organic polymers are used as the resource. One of the industrial applications of using activated carbons and carbon blacks as catalyst supports is generating liquid fuels. They are widely used in the Fischer-Tropsch synthesis and higher alcohol synthesis to convert syngas to hydrocarbons and alcohols, respectively. [200]

In the last decade, nano-carbons have been used as catalyst support materials as well. Initially, carbon nanotubes (CNTs) were utilised in catalysis. Advancements in the synthesis and characterisation of CNTs and their lowered cost have allowed major progress in their usage as catalyst support materials.[202] One of the areas opened up due to the fast development of the synthesis and tailoring methods of CNTs and novel nano-carbon materials such as graphene is research on designing novel catalyst supports from these materials. The development of nano-carbon materials will be further discussed in ***Section 3.1***.

2.1.2 Carbon based enzyme support materials

For several decades, carbon electrodes have been used for direct electron transfer between enzymes and electrodes. Compared to the other electrodes used in electro-enzymatic studies such as Au,[203] Pt,[203] and metal oxides such as RuO_2 and IrO_2,[204] carbonaceous electrodes (glassy carbon, pyrolytic graphite) are cheaper, offer large surface area and suitable pore size for enzymes, and can easily be modified.[205] Pyrolytic graphite started to be used widely as an electrode material for multi-centred redox enzymes. Léger *et al.*[206] showed that protein film voltammetry, which then was a relatively new approach to study redox enzymes, could even be used to observe transient states in redox reactions when spectroscopic methods were not sufficient.[206] High catalytic activity was achieved and useful information could be obtained even when the electrode coverage (redox protein was configured as a film on the electrode) was low.

Following the research trend in electrocatalysis and redox enzymes, carbon materials started to be used directly as support materials for enzymes. As mentioned in ***Section 1.1.3.1***, first, Vincent *et al.*[2] demonstrated that electronically conducting graphite particles

modified with hydrogenase and another electron-acceptor enzyme could catalyse selective reduction reactions of nitrate or fumarate. Similarly, Armstrong *et al.*[3] immobilised a carbon monoxide dehydrogenase and a hydrogenase on graphite platelets to catalyse CO_2 reduction and Reeve *et al.*[4] immobilised a hydrogenase and an NAD^+-reductase for H_2-driven NAD^+ reduction.[4]

There are several studies on using carbon materials as support materials for hydrogenases. Armstrong and co-workers covalently linked a hydrogenase to 1-pyrenebutyric acid[aa] on CNT coated graphite for an enzymatic H_2/O_2 fuel cell.[207] Quinson *et al*.[208] showed that various carbon materials ranging from pyrolytic graphite to MWCNTs could adsorb hydrogenase I (obtained from *E.coli*). These materials could be used as enzyme electrodes to perform electrocatalysis. A wide scope of carbon materials were used and they all showed electrocatalytic activity with redox enzymes immobilised. They used various commercialised carbon powders, graphite flakes, micron–sized graphite particles, graphite platelet nanofibers, MWCNTs and nitrogen-doped MWCNTs (N-MWCNT). This study points out that the choice of carbon support for enzymatic applications can be very broad and there are many novel structures and enzymatic applications to investigate. Overall, enzyme immobilisation on different carbon materials allows researchers to incorporate the fascinating properties of carbon materials in to the biological applications. Carbon material immobilised enzymes are very important for the future advancements in biosensors and biofuel cells.[209]

2.2 Experimental Methods and Analysis Techniques

Three commercial carbon samples, Carbon Support Batch M08176 (CC), Activated Carbon Darco Batch 33896CJ (CD), and Carbon Support Batch M06241 (CP) were obtained from Thales Nano and Black Pearls 2000 (BP) was obtained from Cabot Corporation. These commercial materials were already used as metal catalyst supports. In this work, these carbon materials were used in the H_2-driven NADH generation. The aim, in a broad sense, was to test the suitability of these materials for batch H_2-driven biotransformations and asses their chemical and physical properties for flow chemistry. These materials were used in chemical and surface analyses without any chemical treatment. BP was previously shown to adsorb biological and metal catalysts and its performance is well-known to the Vincent Group[5,210,211]. Thus, it was, mainly, used as a reference point with which to compare the other commercial carbon supports.

In the Experimental Methods section, protocols and methods for testing carbon materials and carbon-enzyme assemblies are introduced. Initially, adsorption of reactants and products on carbon materials were tested to see the effect of adsorption on the concentration of these compounds. Then, methods for immobilising enzymes on these carbon materials and the batch H_2-driven NADH generation were presented.

In the Analysis Methods section, initially, the analysis techniques used for the characterisation of carbon materials were explained. These techniques were chosen to study the morphology, particle size, porosity and graphitisation of these materials. In addition, the impurities in these commercial carbon materials were investigated. Then, high-pressure liquid chromatography methods used to study the concentration of reactants and products adsorbed on carbon materials were presented. Finally, ultra-violet (UV-Vis) spectroscopy methods used to detect the NADH generation were introduced.

2.2.1 Experimental Methods

The H_2-driven NADH generation experiments were performed anaerobically, under a N_2 (BOC) atmosphere, < 1 ppm O_2, in a glovebox. These experiments consist of using enzyme modified carbon particles in desired reaction mixtures in a batch reaction set-up with hydrogen gas (BOC) flowing through the headspace of the reaction vial. Thus, the main parts of the experimental steps include, enzyme modified carbon particle preparation, buffered reaction mixture preparation and building the batch reaction set-up.

2.2.1.1 Materials

Enzymes: As mentioned in ***Section 1.1.6.2***, hydrogenase (*E. coli* hydrogenase 2, Hyd-2) and NAD^+ reductase (I64A, variant of the soluble hydrogenase from *R. eutropha)* were used in the NADH generation experiments. The enzymes were isolated and purified by Ms. Elena Nomerotskaia, Fraser Armstrong group, University of Oxford and Dr Oliver Lenz, TU Berlin, following the previously published protocols.[182,212]

Chemicals: NAD^+ (Prozomix, 97.5 %), acetophenone (Sigma-Aldrich, 99 %), 1-phenylethanol (Sigma-Aldrich, 98 %), acetonitrile[bb] (Sigma-Aldrich, ≥ 99.9 %), concentrated HCl (Fisher-Scientific, concentrated) and Bis-Tris (Sigma- Aldrich, ≥ 98 %) were used as received without further purification. Ethanol (Sigma- Aldrich, ≥ 99.8 %) was used for cleaning the equipment used and for TEM sample preparation. Milli-Q water was used in specified dilutions, buffer preparations and rinsing the equipment used.

Buffer: Bis-Tris pH 6 buffer solution was used in all of the experiments to maintain the pH of the reaction mixture within a particular range. This is essential for the enzymes and the processes, since enzymes usually work in certain pH values and the thermodynamic potential of the $2H^+/H_2$ and NAD^+/NADH couples are related to the pH of the solution they occur in.

50 mM Bis-Tris[cc] buffer solution was prepared at 20 °C by dissolving the appropriate mass of Bis-Tris in MilliQ water. This buffer solution was then titrated to the desired pH by using

concentrated HCl. The titration was performed by using a Ag/AgCl pH electrode (Fisher-Scientific) at 20 °C.

2.2.1.2 Testing the adsorption of organic molecules onto the carbon particles

Carbon materials were all tested for acetophenone, 1-phenylethanol, NAD^+ and NADH adsorption. This was done to investigate whether the concentration of the reactants and products are affected by adsorption onto carbon materials. Two sets of adsorption analysis were done: i) For each test, a 10 mg sample of each carbon particle material was weighed and put into Eppendorf tubes. 10 mM acetophenone, 10 mM 1-phenylethanol, 1 mM NAD^+ and 1 mM NADH solutions were prepared, 350 µL of each solution were mixed with each 10 mg carbon particle separately and left overnight for adsorption and ii) A suspension of 5 mg of each carbon material in 0.5 mL buffer was prepared and sonicated for 40 minutes to aid uniform dispersion. 15 µL of each dispersion was mixed with 985 µL of 10 mM 1-phenylethanol overnight for overnight adsorption. The final concentrations were studied with high-pressure liquid chromatography analysis.

2.2.1.3 Preparation of the enzyme modified carbon particles

Carbon materials were chosen as catalyst support materials due to electronically conductivity, high surface area, porosity and inertness of carbon materials in general. The chosen carbon materials were used as metal catalysts supports commercially. In this section, they were tested as enzyme support materials. Stock suspensions of CC, CD, CP, and BP particles were each prepared at 10 mg mL^{-1} in 0.5 mL buffer and sonicated for 40 minutes to aid uniform dispersion. Fair dispersions of CD, CP and BP were obtained after sonication. CC could not be dispersed due to its bulky structure. Since the particles were used without any modification, CC was not grounded to follow the general procedure. Thus, CC had to be eliminated from H_2-driven NADH generation experiments. However, it was used in all other analyses as it is.

15 µL from each dispersion was pipetted into Eppendorf tubes. 30 µL Hyd-2 (4 mg mL^{-1}) and 30 µL I64A (1.6 mg mL^{-1}) were mixed together and 20 µL from this mixture were added to the Eppendorf tubes. The carbon particle dispersion-enzyme mixtures were gently mixed by flicking the Eppendorf tubes to obtain a homogenous mixture of the particles and enzymes. The carbon-enzyme mixture was left in the glovebox fridge at 4 °C for 60 minutes for enzymes to immobilise on these carbon materials. The enzyme concentration for the reactions was determined for the specific reaction conditions after varying the concentration of each enzyme in multiple trials for BP.

2.2.1.4 The protocol for H_2-driven NADH generation

After the adsorption and co-immobilisation of enzymes on carbon materials (**Figure 21**), the unadsorbed enzyme supernatant was pipetted out. The remaining carbon-enzyme assemblies were washed by addition of 1 mL buffer solution. The mixture was sonicated and liquid contents were pipetted out. Then, 965 µL of the H_2 saturated reaction mixture that contains 1 mM NAD^+ was added to each enzyme-modified carbon containing Eppendorf tube. The reaction mixture was prepared by dissolving an appropriate amount of NAD^+ in Bis-Tris pH 6 buffer solution and flowing H_2 gas into the mixture for 30 minutes. The Eppendorf tubes with enzyme modified carbons and reaction mixtures were placed with their lids open in a shaker that allows H_2 gas to flow over the headspace (**Figure 22**). The H_2 gas was first passed through a water containing bubbler to wet the gas and then was passed to the shaker set-up. The Eppendorf tubes were left for 2 hours under H_2 gas flow in the shaker.

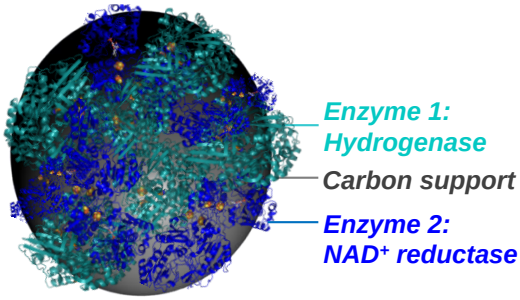


Figure 21: A schematic representation of the co-immobilisation of enzymes on carbon support. (The enzyme molecules and the carbon particle are not shown to scale.)

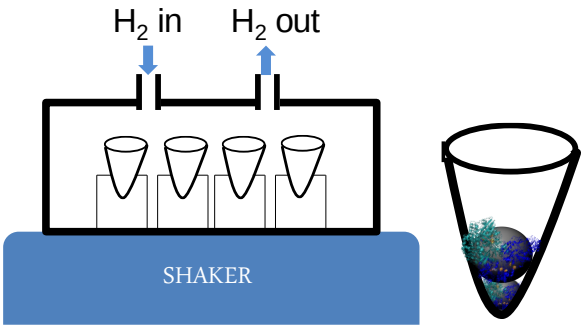


Figure 22: A schematic representation of the batch reaction set-up. The Eppendorf tubes placed in a sealed shaker with hydrogen gas inlet and outlet. (The enzyme molecules and the carbon particles are not shown to scale.)

2.2.2 Analysis Techniques

2.2.2.1 Characterisation techniques used for carbon materials

The carbon materials were used as received in all of the analysis techniques used; they were not grounded into fine powders.

Overall, size and shape (morphology) of CC, CD, CP, and BP, their degree of graphitisation, surface area and porosity and, impurities were investigated. Size, surface area and porosity are characteristic that directly affect the efficiency of enzyme adsorption on these materials. The degree of graphitisation was studied because associated with protein adsorption and, the impurities were analysed because they could affect the investigated H_2-driven biotransformations.

The morphology of the carbon materials were analysed by scanning electron microscopy (SEM), transmission electron microscopy (TEM), and Raman spectroscopy. SEM images were obtained using a JEOL 840F microscope. The secondary electron detector was operated at 5 kV acceleration voltage. For TEM analysis, the carbon materials were dispersed in ethanol by using a sonic tip for 2 minutes. A JEOL 2100 microscope was operated at 200 kV acceleration voltage to obtain TEM images.

Powder X-ray diffraction (XRD) analysis was used to determine the degree of crystallinity of the carbon samples. The analysis was carried out on a Siemens D5000 X-ray powder spectrometer with a 10° - 80° 2Θ range and a step size of 0.0195°. Additionally, Raman spectroscopy was used to study the graphitisation of the samples by using JY Horiba

Labram Aramis imaging confocal Raman microscope at 532 nm green laser excitation. Carbon materials with graphitic structures have exposed “edge-like” structures. These edges of platelets are related with adsorption of protein molecules on these surfaces.[208] Raman spectra of graphitic materials have a strong G peak around 1580 cm^{-1} and a smaller D peak around 1340 cm^{-1} (**Figure 23**)[213], whereas in amorphous materials the ratio of these peaks are close to one.

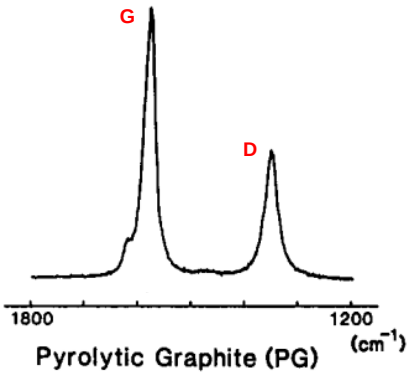


Figure 23: Raman spectrum of a graphitic material showing a strong G peak at 1580 cm-1. Adopted from Reference 213, © 1988, with permission from Elsevier.

The specific surface area and porosity of these samples were investigated by nitrogen adsorption measurements. These analyses were conducted using a Micromeritics Gemini V BET surface area analyser (nitrogen adsorption at 77 K). The samples were left at 200 °C under dinitrogen flow for 12 hours before the adsorption measurements. The results were determined according to the models defined by Brunauer, Emmett, and Teller (BET). The sorption isotherms are plots of amount of gas adsorbed/desorbed versus relative pressure. These are isotherms are standardised by IUPAC (**Figure 24**).[214] Type I isotherms usually belong to microporous materials and, types IV and V are characteristic of mesoporous materials. Hysteresis loops can also be observed in these isotherms due to the pressure difference between the pressure at which capillary condensation and capillary evolution take place (**Figure 25**).[214] In cases where BET model does not fit to the materials, Langmuir models are used. The Langmuir model is usually used for microporous materials.[208]

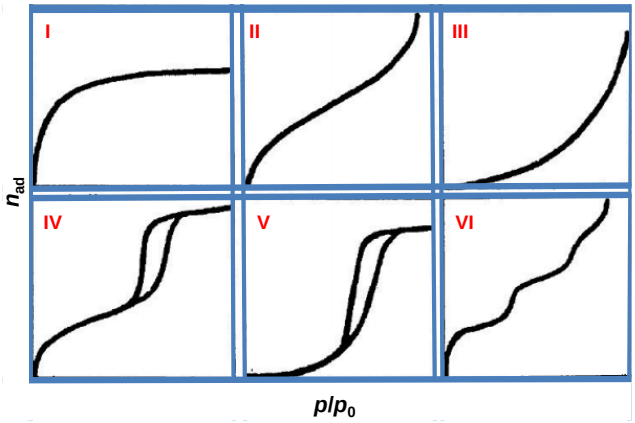


Figure 24: Sorption isotherms classified by IUPAC.

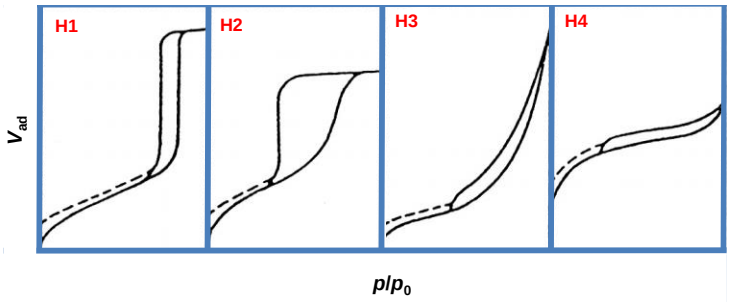


Figure 25: Four main hysteresis loops according to 1985 IUPAC classification.

Energy dispersive X-ray spectroscopy (EDX) was used to identify and determine the atomic proportions of the elements and impurities present in the carbon materials. EDX mapping was obtained using Zeiss Merlin EDX SEM. This technique was chosen over wavelength-dispersive X-ray spectroscopy (WDX), because EDX detects the elements in an unknown sample faster. In EDX, detector measures all of the energies of incident characteristic X-rays simultaneously. The entire spectrum is measured at once and rapidly. WDX can be used as a complementary technique to WDX, after detection of elements in a sample. WDX measures single wavelength at a time and the detector records number of X-ray photons at the given wavelength. However, WDX has higher resolution and is more precise than EDX.

2.2.2.2 High-performance liquid chromatography

In this Chapter high-performance liquid chromatography (HPLC) is used to determine the initial and final concentrations of the cofactors (NAD^+ and NADH) and some of the organic chemicals (acetophenone and 1-phenylethanol), which are either reagents or products in

this Thesis, after adsorbing them on the carbon materials. HPLC is both a qualitative and a quantitative analysis method, which works similar to simple column chromatography. The compounds are separated by their affinity towards a mobile and stationary phase. The compounds are characterised by their retention times and the concentration is worked out by the comparison of the peak areas of the known standards. In reverse phase HPLC, which is used in this Thesis, the stationary phase is non-polar and the mobile phase is moderately polar. Thus, analytes with higher hydrophobic surface area have higher retention times. In this Thesis, a Shimadzu Prominence HPLC equipped with a CBM-20 system controller, LC-20AD superior solvent delivery system, SIL-20A high-throughput autosampler, CTO-10AS column oven and SPD-20A UV-Vis absorbance detector was used. The results were collected using LabSolutions software. The absorbance at 210 nm and 260 nm were recorded. Chromolith® Performance, 100 - 3 mm column (Merck) is the only HPLC column used in this Chapter for the detection of NAD^+, NADH, acetophenone and 1-phenylethanol. A mobile phase consisting of 80 % MilliQ water and 20 % acetonitrile was used in the analyses. The flow rate of the mobile phase was 1 mL min^{-1} and the column was maintained at 40 °C.

2.2.2.3 Ultraviolet-visible spectroscopy

Ultraviolet-visible spectroscopy was used to monitor the conversion of NAD^+ to NADH. A Cary 60, Agilent UV-Vis spectrometer was used with samples in a UV-Vis cuvette (Hellma Analytics) of well-defined path length (l) (1 cm). This system allowed using Beer-Lambert Law, Eq- 1, to calculate the concentration (c) of the samples. A baseline measurement with the buffer solution as the analyte was taken before each analysis since the buffer absorbs strongly below *ca* 210 nm. The subsequent sample measurements were analysed by subtracting this baseline. Absorbance (A) below 1.5 A was used for quantitative analysis. NAD^+ was detected at 260 nm and NADH was detected at 340 nm. The extinction coefficients (ε) for NAD^+ and NADH were taken from literature to be used in Beer-Lambert

Law to monitor the NADH concentration (**Table 2-1**).[215] A plot of [NAD^+]/[NADH] vs $A_{260\ nm}/A_{340\ nm}$ is used to determine the concentration ratio of an unknown sample. The details are in ***Appendix 4.***

Eq- 1

$$A = \varepsilon\ l\ c$$

Table 2-1 Literature extinction coefficients (ε) for cofactors NAD^+ and NADH.[215]

Sample	$\varepsilon_{260\ nm}$ ($mM^{-1}\ cm^{-1}$)	$\varepsilon_{340\ nm}$ ($mM^{-1}\ cm^{-1}$)
NAD^+	17.4	N/A
NADH	14.1	6.22

2.3 Results and Discussion

2.3.1 Characterisation of the Carbon Materials

2.3.1.1 SEM/TEM characterisation of the carbon materials

The SEM (**Figure 26**) and TEM images (**Figure 27**) give an estimation of the particle size and the morphology of the carbon materials, CC, CD, CP, and BP. SEM images show that CC, CD, and CP mostly have agglomerates inhomogeneous particles size, whereas BP has well defined particle size. All of the materials mostly consist of particle-like structure. Additionally, CC and CP have plate-like structures observed in SEM images.

CC: CC consists of plate-like structures (length ranging from 8.5 µm to 15 µm and thickness ranging from 3.5 µm to 6.5 µm) and particle-like structures (diameter: 0.2 µm to 15 µm) (**Figure 26**). Macropores with diameters bigger than 50 nm[216] can also be observed.

CD: CD appears to have particle-like morphology with particle diameter ranging from 0.2 µm to 20 µm (**Figure 26**). There are also few plate-like structures up to 20 µm in length and up to 3 µm in thickness.

CP: According to the SEM images taken at 1000 X (**Figure 26**), CP has both particle-like and plate-like structures. The particle diameter is between 0.15 µm - 2 µm and the plate-like structures have length up to 40 µm with thickness up to 4 µm length.

BP: BP consists of particles with diameter ranging between from 0.2 µm to 20 µm according to the SEM image (**Figure 26**).

TEM images of the carbon materials give more information about the particle size since the materials were dispersed and individual particles could be observed. The TEM images of CC, CD, and CP mainly show that these materials are not homogenous in size and shape. TEM images taken at different magnification and from the different regions of the TEM grids show that the materials, after 2 minutes of dispersion with a sonic tip in ethanol, still consist of agglomerates. CC, CD, CP, and BP all show characteristics of amorphous carbon structure (**Figure 27**). Additional to the amorphous carbon background, TEM images of CC and CD consisted of both sheet-like structures and particle-like structures, whereas in TEM micrographs of CP and BP there are only particle-like structures (**Figure 27**). Overall, CC, CD, and CP do not have homogenous particle size or structure. CC has particle diameter ranging from 40 nm to 65 nm. CD has particles with diameter between 15 nm to 30 nm. CP has particle diameter ranging from 20 nm to 43 nm, and BP has more well-defined shaped sphere-like particles with diameter between 17 nm to 31 nm.

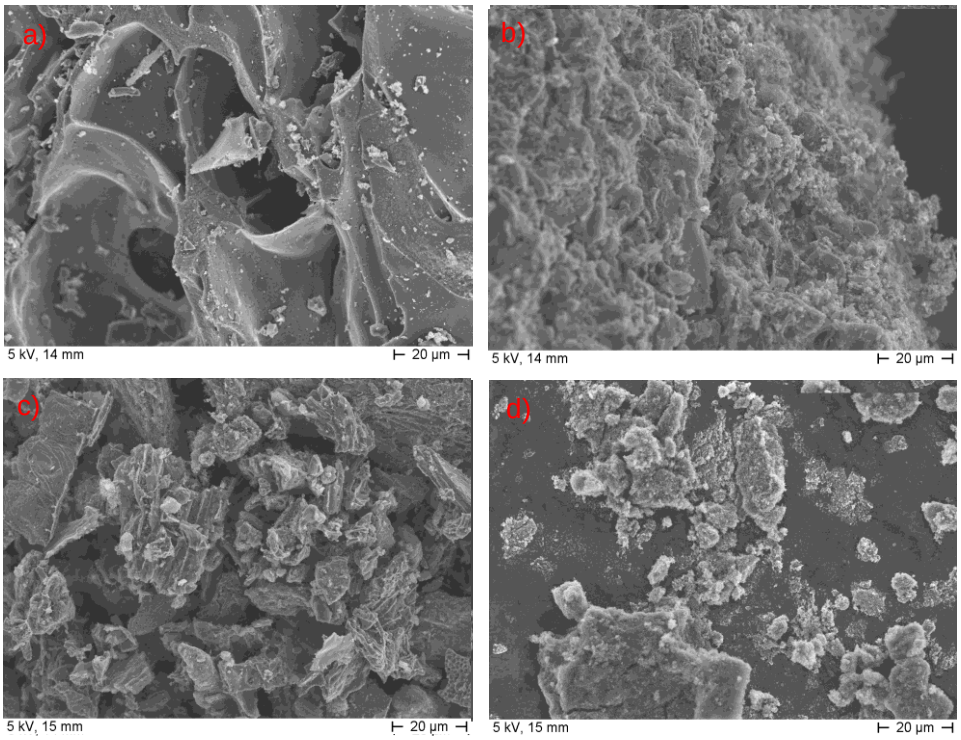


Figure 26: Scanning electron micrographs of four different carbon materials taken at 1000 X (a) CC, b) CD, c) CP, and d) BP).

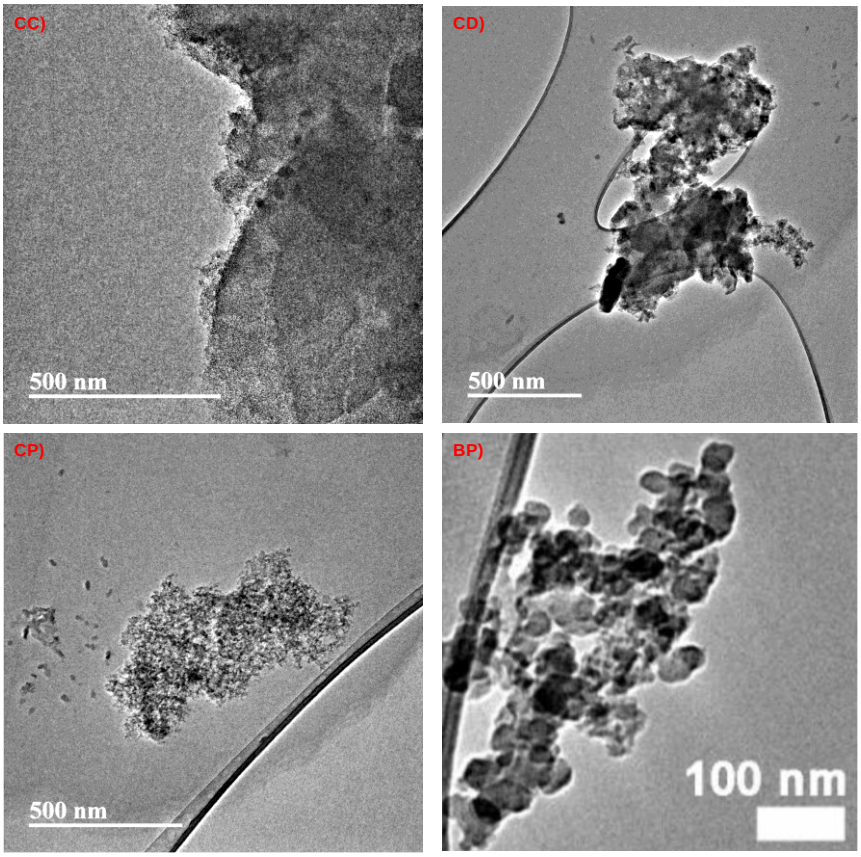


Figure 27: Transmission electron micrographs of CC, CD, CP, and BP. TEM image of BP was adapted from Reference 1.TEM images were obtained with the assistance of Karwei So, Grobert Group, University of Oxford.

2.3.1.2 Specific surface area analysis based on Brunauer–Emmett–Teller (BET) theory

The estimated specific surface area, pore diameter and pore volume are as given in **Table 2-2**. The surface area the size characteristics were determined using the BET models[217] and the nitrogen adsorption/desorption curves (**Figure 28**) were studied using the IUPAC characterisation.[218] CC, CD, and CP are mesoporous materials and display type IV isotherms with H3 hysteresis (**Figure 24** and **Figure 25**). BP has a slightly different isotherm compared to CC, CD, and CP. A bit more well-defined plateau at high relative pressures is indicative of a type I isotherm. This suggests the presence of micropores (pore size < 2 nm). This is in agreement with the fact that the Langmuir model for surface area estimation gives a better fit than the BET model. The correlation factor for Langmuir model (**Table A 1**) is close to that of BET model in CC and CP as well as BP. For these carbon materials, the specific surface area according to the Langmuir model is also included in

Table 2-2. The samples have high pore population density at less than 2 nm pore diameter which would make them microporous but a high pore population peak above 2 nm pore diameter is observed as well. Thus, the results yield to mesoporous type IV H3 hysteresis isotherms. According to the BET results, the samples do not have a uniform pore distribution to conclude that they are strictly microporous or mesoporous. Overall, the pore sizes of these materials are suitable for enzymes which have diameters ranging from 3 nm to 5 nm.

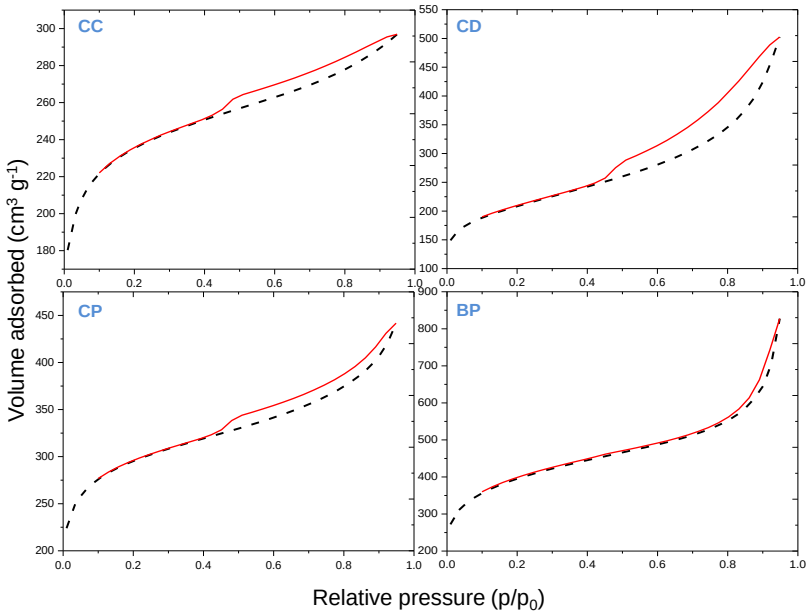


Figure 28: Nitrogen adsorption (dotted black) and desorption (solid red) isotherms at 77 K for each carbon material (CC, CD, CP, and BP). The analyses were carried out with the assistance of Dr Frank Dillon, Grobert Group, University of Oxford.

Table 2-2 Characteristics of carbon materials investigated.

Material	Abbreviation	Source	Estimated typical size (nm)	Model used for specific surface area	Specific surface area ($m^2\ g^{-1}$)	Estimated pore diameter* (nm)	Estimated pore volume** ($cm^3\ g^{-1}$)
Carbon Support Batch M08176	CC	Cabot Corporation	D: 40-65	BET Langmuir	732.31 ± 15.85 1107.16 ± 6.17	3.23	0.46
Activated Carbon Darco Batch 33896CJ	CD	Cabot Corporation	D: 15-30	BET Langmuir	685.75 ± 9.13 1059.86 ± 16.70	5.18	0.78
Carbon Support Batch M06241	CP	Cabot Corporation	D: 20-43	BET	927.70 ± 18.83 1407.93 ± 10.09	3.94	0.68
Black Pearls 2000	BP	Cabot Corporation	D: 17-31	BET Langmuir	1287.24 ± 21.37 1986.14 ± 24.53	4.62	1.28

* BJH Adsorption average pore diameter (4V/A), ** Single point adsorption total pore volume of pores less than 39.69 nm diameter at relative pressure 0.949. *D*: diameter. Specific surface areas obtained using Langmuir model were also given in cases where Langmuir model fit better than BET model

2.3.1.3 Determination of crystallinity of carbon materials by X-ray diffraction analysis

XRD analyses was used to determine the crystallinity of the commercial carbon samples that are provided by the manufacturers as amorphous materials. The results show that the materials are mostly amorphous. CD, activated carbon has the highest % crystallinity that is 18.9 %. The peaks in the spectra which does not belong to carbon is due to SiO_2 impurities in the commercial carbon samples. The structure of the materials was also investigated using Raman spectra.

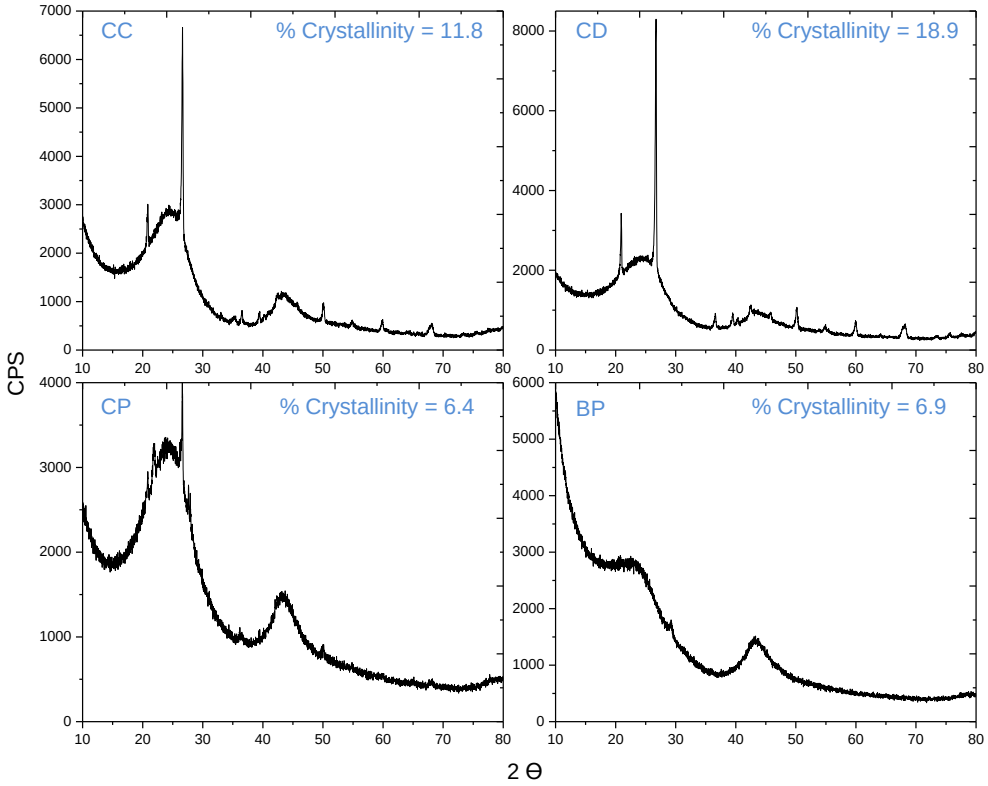


Figure 29: XRD spectra of CC, CD, CP and BP with % crystallinity of each material. XRD analyses was carried out by Dr Philip Holdway, Oxford Materials Characterisation Service.

2.3.1.4 Characterisation of graphitic structure of the carbon materials by Raman spectroscopy

The peaks identified for Raman spectroscopy of the carbon materials are D band (around 1340 cm^{-1}), G band (around 1575 cm^{-1}) and 2D peak (also referred as G', around 2675 cm^{-1}). The main point of doing Raman spectroscopy on these carbon materials is to investigate the degree of graphitisation of the samples. As mentioned in ***Section 2.2.2.1***, the "edge-like" structures in exposed edges of platelets in graphitic materials are

associated with protein adsorption. The D peak intensity is used to correlate the defects/disorder in the carbon lattice and is linked to the degree of sp^3 hybridisation. The G peak is linked to the degree of sp^2 hybridisation, in other words it is a result of the graphitic network in the material.[208,219] Lastly, the presence of a 2D peak contributes to the graphitic content of the material and is related to the interactions between graphene-like planes.[208] All of the carbon materials investigated (CC, CD, CP, and BP) have I_D/I_G ratios close to 1 and lack 2D peaks. Raman spectra of these materials (**Figure 30**) suggest that they have amorphous structures and do not have well-defined crystalline domains. The spectra confirm the findings of the XRD analysis, which also suggest that these carbon materials mainly have amorphous structure. Although "edge-like" structures are move favourable for protein adsorption and the commercial carbon materials studied here lack those structures, the high surface area of these amorphous materials compensate this.

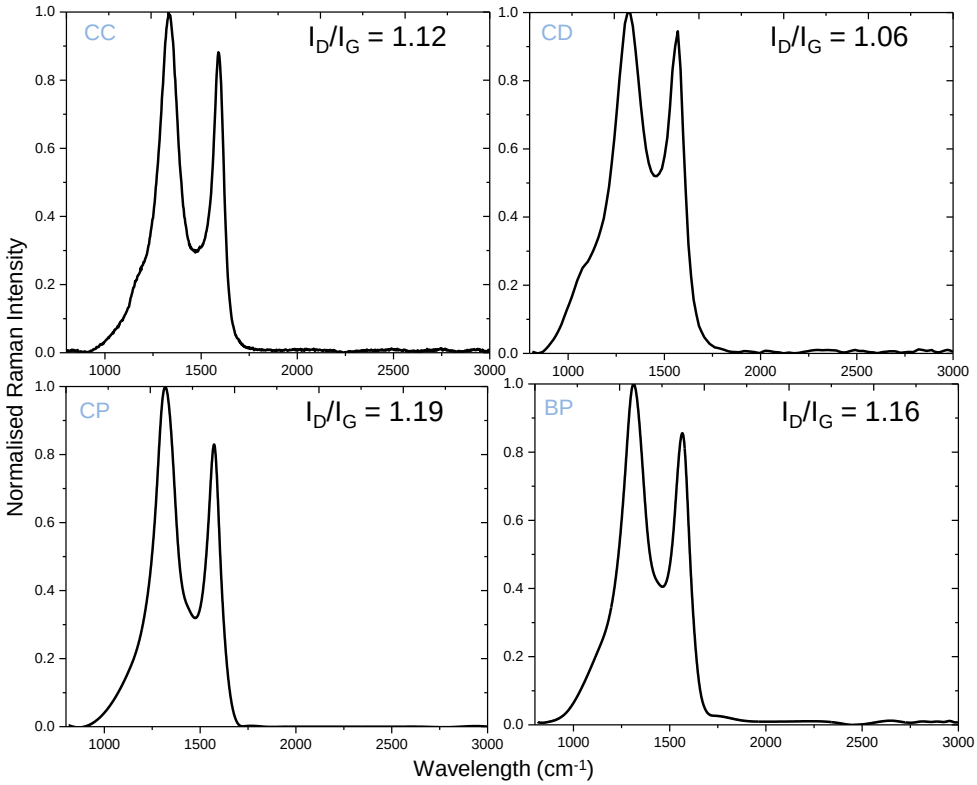


Figure 30: Raman spectra of carbon materials (CC, CD, CP, and BP) with D peaks around 1340 cm^{-1} and G peak around 1575 cm^{-1} confirming amorphous structure with a I_D/I_G close to 1.

2.3.1.5 Energy-dispersive X-ray spectroscopy of the carbon materials

EDX analysis was done to detect the elemental compositions of the carbon materials, CC, CD, CP, and BP. Since the materials are to be used as enzyme support materials, the elemental composition could affect the activity of the enzyme or contribute to the catalytic activity. After using the materials as received in EDX analysis, it was detected that the carbon amount in each carbon materials was more than 88 % and the impurities other than oxygen were all ≤ 1 %. Thus, the carbon materials were not grinded for a further EDX analysis to avoid introducing impurities from the powdering process. The figures, **Figure 31**, **Figure 32**, **Figure 33**, and **Figure 34** obtained with the assistance of Dr Vitaliy Babenko, show the elemental composition of the different areas of the materials and give an estimate of the distribution of the impurities in the carbon materials. BP has the most homogenous elemental distribution among the investigated carbon materials. It can be a support material for applications very sensitive to impurities. All of the materials have oxygen as the highest percentage impurity. Oxygen is likely to be present as acidic or basic oxygen groups and can be present due to the synthetic routes, the precursor used in manufacturing and the oxidation methods.[220] The common impurities in all of the carbon materials are sulphur and silicon. Sulphur can be present in the carbon materials as elemental sulphur, organo-sulphur compounds or inorganic species.[220] Other impurities such as calcium and sodium can arise from trace metals in water treatments, acid and base treatments during the manufacturing process of these commercial carbon materials.

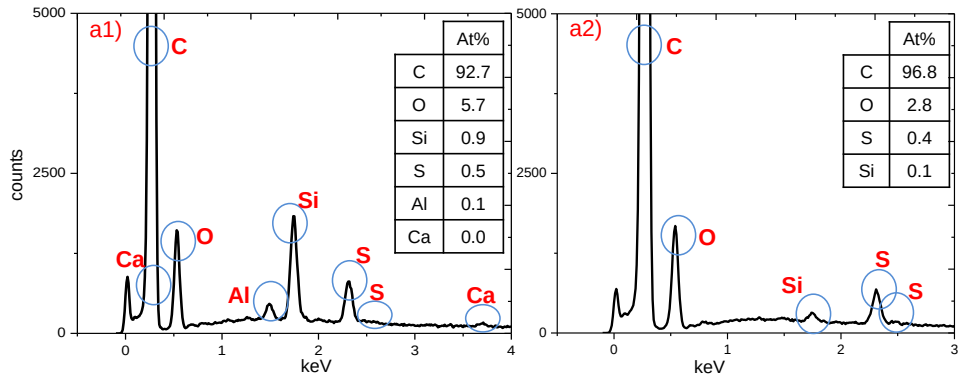


Figure 31: EDX spectra of CC along with elemental composition of the selected regions of the material. EHT = 15 kV, I Probe = 500 pA.

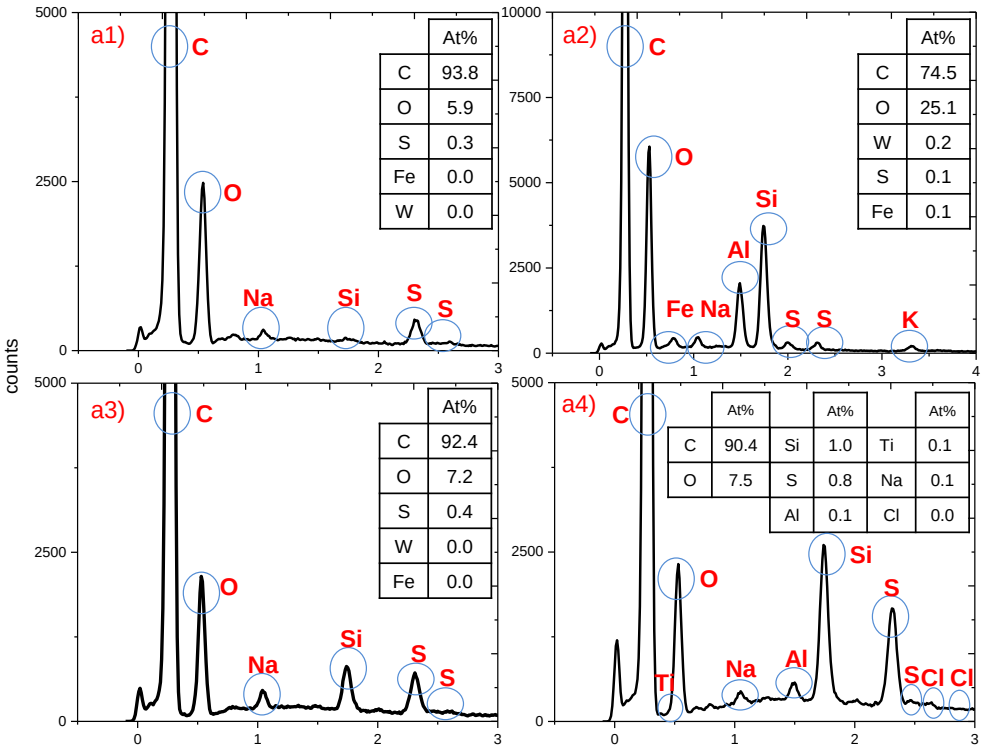


Figure 32: EDX spectra of CD along with elemental composition of the selected regions of the material. EHT = 15 kV, I Probe = 500 pA.

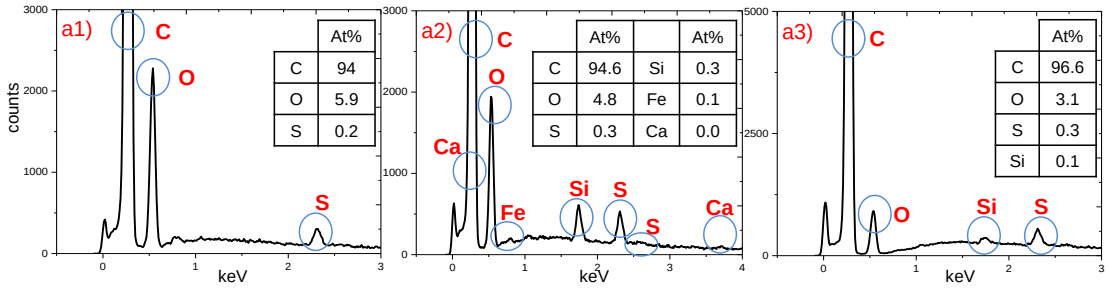


Figure 33: EDX spectra of CP along with elemental composition of the selected regions of the material. EHT = 15 kV, I Probe = 500 pA.

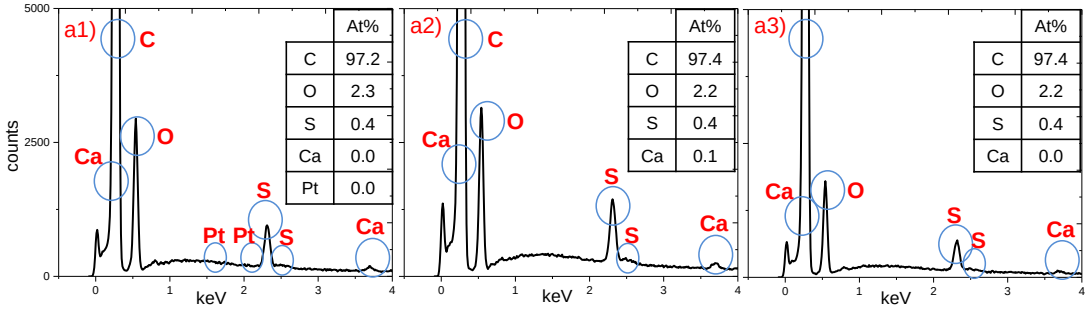


Figure 34: EDX spectra of BP along with elemental composition of the selected regions of the materials. EHT = 15 kV, I Probe = 500 pA.

2.3.2 Testing reactants and products on the carbon materials

2.3.2.1 Adsorption of the chemical used on the carbon materials

The nitrogen physisorption analysis show that all of the carbon materials (CC, CD, CP, and BP) have high surface area (> 1000 $m^2 g^{-1}$) and are porous materials. Carbon blacks and activated carbons have been used in several applications, including industrial-scale applications, to adsorb organic or inorganic materials due to their high surface area and porosity. They are usually used in pollution treatment systems. Thus, there is a tendency to use cheap natural resources or waste materials in the making of carbon adsorbents.[221] Peat, coal in the making, has been used as a commercial adsorbent and some of the pollutants it adsorbs are heavy metals such as Hg, Cd, and Ni. Activated carbons, due to their high surface area and rigid internal pore structures, have been widely used in water treatment systems to remove organic and inorganic pollutants.[221]

In this work, the carbon is used as a support to immobilise enzymes to catalyse H_2-driven biotransformations. It is desired for the enzymes to be fully adsorbed on the carbon materials and adsorption is mostly due to hydrophobic interactions. The commercial carbon materials used in this work mainly consist of micro- and mesopores. The average pore size changes between 3 nm to 5 nm. The enzymes used in this work also have diameters around 3 nm to 5 nm. Thus, enzymes can be surrounded by the carbon surface and have good electronic contact. However, the diffusion into the mesoporous network is slow and the sufficient time for equilibration should be provided for the immobilisation. On the other hand, it is not desirable for the organic reactants and products of the H_2-driven biotransformations to adsorb onto the carbon materials. This would affect the concentration of the reactants and the products and, could lower the yield. In this section, the absorption of acetophenone (the reactant in ***Section 3.2.1.5.2***), 1-phenylethanol (the product in ***Section 3.2.1.5.2***) and NAD^+/NADH (cofactors used in H_2-driven biotransformations in this Thesis) were analysed on all of the carbon materials.

Initially, a high loading of carbon was used to rank the adsorption of the acetophenone, 1-phenylethanol, NAD^+ and NADH on the carbon materials (**Figure 35** and **Figure 36**). The HPLC chromatograms (**Figure 35** and **Figure 36**) show loss of the molecule of interest, most likely due to adsorption onto the carbon materials; the absence of any additional peaks in the HPLC provides evidence that no products were formed. A large drop in peak intensity, therefore, equates to strong adsorption. The HPLC spectra show that acetophenone, 1-phenylethanol and NAD(H) adsorb most strongly on CP, BP, CC, and CD, in a decreasing order. CP and BP have similar adsorption results for all of the chemicals tested. CD and CC have similar adsorption results for NAD(H) and, CD has the least adsorption for acetophenone and 1-phenylethanol. CD adsorbed 96 % of the starting acetophenone and 94 % of 1-phenyethanol. The results are quite similar. However, higher adsorption of acetophenone is an expected result due to its lower polarity compared to 1-phenylethanol, when non-polar interactions between non-polar carbon materials and the solvents are taken into account. The difference between carbons is quite minor compared to the fact that all of the carbon samples adsorb organic molecules very strongly at the given concentrations.

Then, to observe the effect of the adsorption on the reactions, the same amount of carbon was used in the adsorption experiments (**Figure 37**) as in the H_2-driven biotransformations. The results in **Figure 37** are for the second set of adsorption experiments with low carbon loading. The amount of carbon loading used was the same as the amount of carbon loading in the H_2-driven biotransformations in this Thesis. The HPLC chromatograms indicate that the adsorption of reactants and products on carbon materials is negligible when they are used in H_2-driven biotransformations. This shows that the final conversion is not significantly affected by the sticking of the reactants/products on the carbon support.

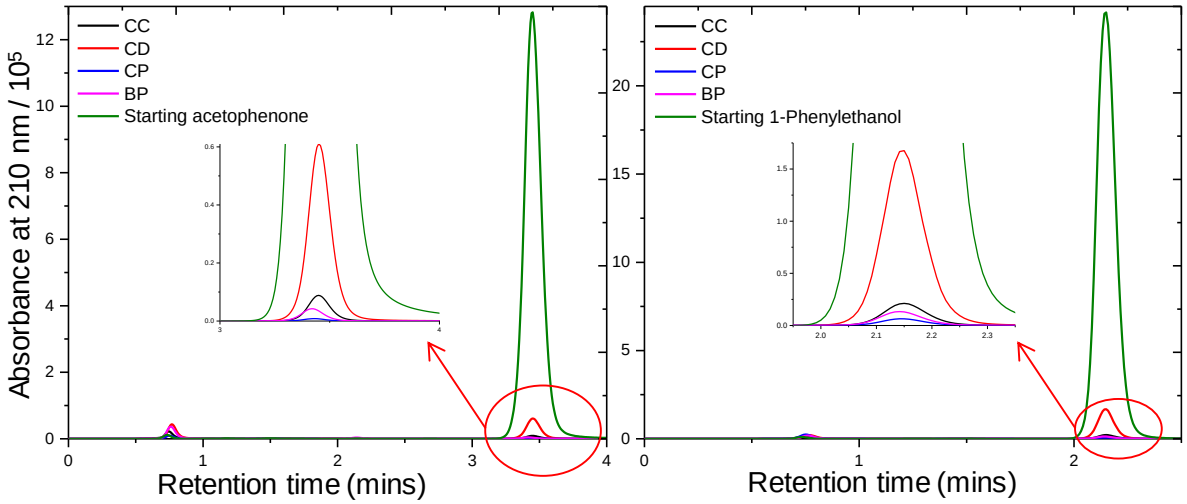


Figure 35: HPLC chromatograms for the overnight adsorption of 350 µL 10 mM reactant (acetophenone) and 350 µL 10 mM product (1-phenylethanol) on 28 mg mL^{-1} CC, CD, CP, and BP. CC, CP and BP adsorbed more than 99 % of the starting acetophenone and 1-phenylethanol solutions. CD adsorbed 96 % and 94 % of the starting acetophenone and 1-phenylethanol solutions, respectively. High carbon loading was used to determine the extent of the adsorption of the carbon materials.

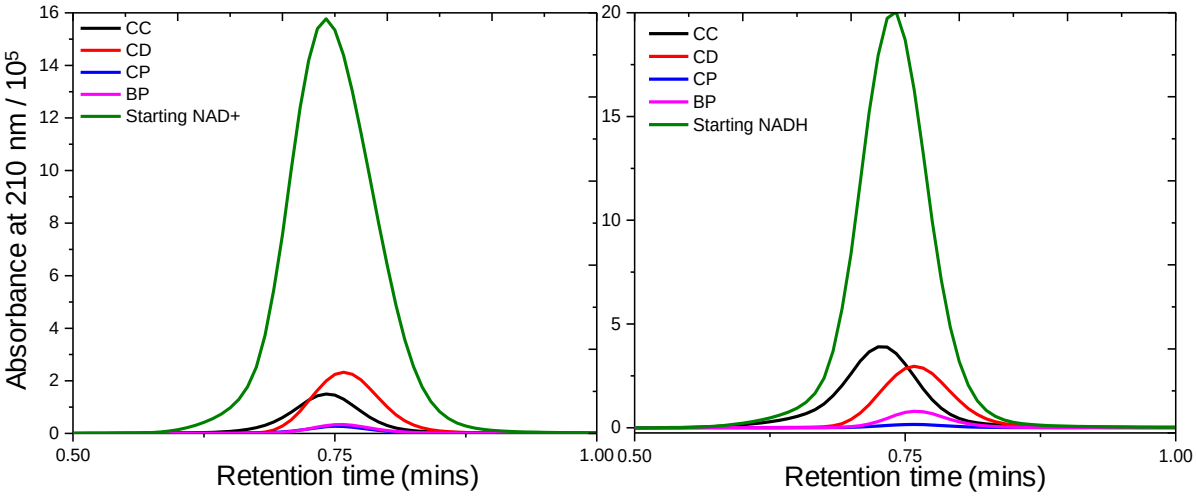


Figure 36: HPLC chromatograms for the overnight adsorption of the cofactors. 350 µL 1 mM NAD$^+$ and 350 µL 1mM NADH were tested on 28 mg mL^{-1} CC, CD, CP and, BP. CC adsorbed 92 % and 77 % of the starting NAD$^+$ and NADH solutions, respectively. CD adsorbed 88 % and 85 % of NAD$^+$ and NADH, respectively. CP and BP adsorbed 98 % of NAD$^+$. CP adsorbed 99 % and BP adsorbed 97 % of the starting NADH solutions. High carbon loading was used to determine of the adsorption of the carbon materials.

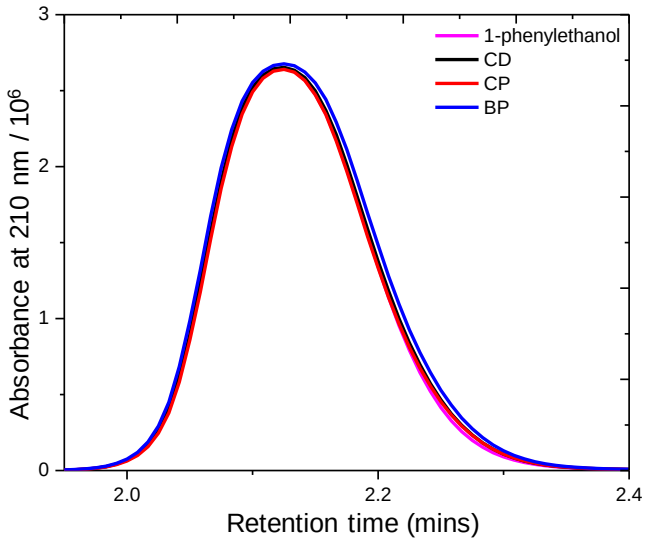


Figure 37: HPLC chromatograms for the overnight adsorption of 985 µL 10 mM 1-phenylethanol on 15 µL 10 mg mL^{-1} on CD, CP and BP. The same amount of carbon loading was used as in the NADH generation experiments. The aim was to test the potential effect of adsorption in the NADH generation system. The carbon materials adsorbed less than 1 % of the starting 1-phenylethanol solutions.

2.3.3 H_2-Driven NADH Production on the Carbon Materials

As explained in a detailed way in the experimental section, ***Section 2.2.1.3*** , both enzymes hydrogenase (Hyd-2) and NAD^+ reductase (I64A) were co-immobilised on the selected electronically conducting carbon materials (CC, CD, CP, and BP). Briefly, H_2 oxidation by a hydrogenase puts electrons into a carbon particle, which can be used for NAD^+ reduction by the NAD^+ reductase (**Figure 38**). This has been demonstrated for BP particles previously.[5] The reactions were run in a H_2 saturated NAD^+ solution in buffer and analysed using UV-Vis spectroscopy to determine the extent of conversion of NAD^+ to NADH. The UV-Vis results in **Figure 39** show that in the carbon material (CD, CP, and BP)-enzyme assemblies NAD^+ was converted to NADH, each with a different conversion, in 16 hours.

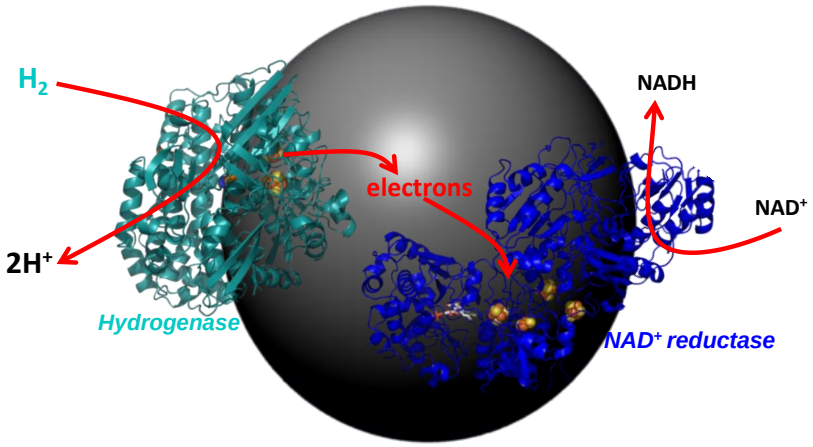


Figure 38: A schematic representation of the mechanism of H_2-driven NADH generation. Hydrogenase and NAD^+ reductase were co-immobilised on the selected electronically conducting carbon materials. H_2 saturated NAD^+ solution was used as the reactant. H_2 was flowing through the headspace of the reaction. (The carbon particle and the enzymes are not shown to scale.)

The UV-Vis spectra in **Figure 39** show the NADH generation for each experiment and therefore confirm that the enzymes were immobilised on the carbon materials and were able to exchange electrons. Otherwise, without the electrons supplied, the I64A would not be able to reduce NAD^+ to NADH.

The UV-Vis curves show that all of the enzyme-modified carbon materials (CD, CP, and BP)[v] had led to NADH generation after 16 hours. The decreasing peak at 260 nm shows that NAD^+ was being used up and the increasing peak at 340 nm shows that NADH was being formed. The highest conversion, with BP, was 84 % in 16 hours (**Table 2-3**). The initial experiments to make the biotransformations work on commercial carbon materials and optimise the reaction conditions have lower conversion (**Table 2-4**). The concentration of the final solution and the conversion are calculated in ***Appendix 4***. CD and CP have similar NADH generation results (19.9 % and 17.7 % conversion) and these results are lower than the BP result. BP has higher surface area then both CD and CP but this big difference is most likely due to the dispersion issues. CD and CP were dispersed by sonicating in buffer for 40 minutes, the same method with BP. A clear dispersion was obtained for all of the carbon materials. However, the dispersion of CD and CP were only

[v] The results for CC are not included in **Figure 39** because they are not comparative due to the fact that the material has particles around 2 mm diameter and can not be dispersed in the same conditions.

stable for a couple of hours whereas the dispersion for BP stayed stable overnight. Poor dispersion is likely to impair the mass transport of NAD^+ and H_2 to the enzymes; therefore, resulting in a low conversion for CD and CP. Overall, the results show that CD, CP and BP can all be used as carbon support materials for H_2-driven biotransformations. However, the system should be further developed for CC and CP if they were to be packed in hydrogenation reactors and the gas-liquid-solid contact should be increased.

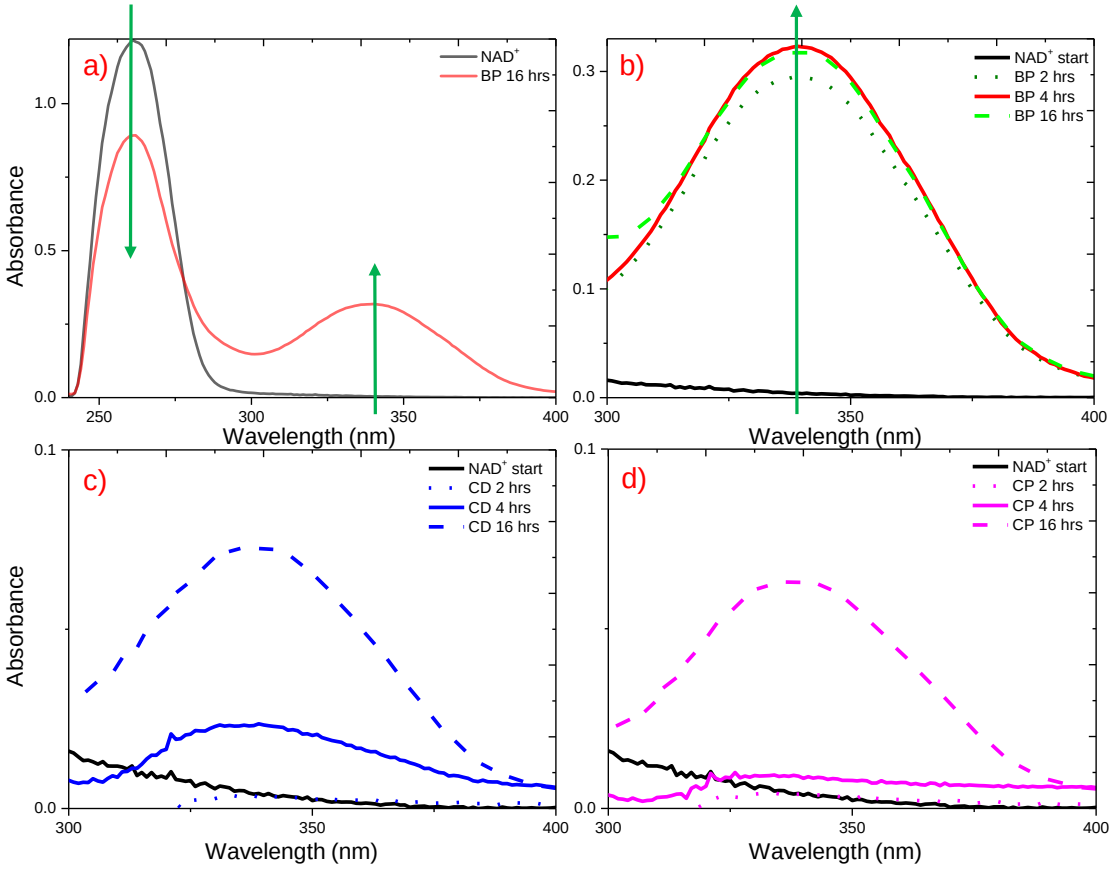


Figure 39: a) The overall UV-Vis spectra for the 1:10 diluted 1 mM NAD^+ in buffer reaction mixture and 1:10 diluted 16 hr H_2-driven NADH generation on BP. b) The A_{340} peak for NADH generation on BP with time points taken at 2, 4, and 16 hours. The peak at 340 nm shows increase in NADH concentration over time, c) NADH generation on CD, d) NADH generation on CP.

Table 2-3 Overnight conversion of NAD^+ to NADH on the carbon materials for the optimised and final system.

Carbon Material	% Conversion
BP	84
CP	17
CD	20

Table 2-4 Overnight conversion of NAD+ to NADH on the carbon materials (BP, CP, and CD) for all of the experiments with $p < 0.05$

	BP	CP	CD
Mean % conversion	75.26	13.15	12.28
Standard deviation	6.46	2.75	4.98
df_1	2	2	2
df_2	15	15	15
F	3.6823	3.6823	3.6823

2.4 Conclusion

This Chapter concentrates on immobilising enzymes (hydrogenase, Hyd-2 and NAD^+ reductase, I64A) on electrically conducting and high surface area carbon materials for H_2-driven fine chemical synthesis (reduction of NAD^+ to NADH). The commercial carbon materials (carbon blacks and activated carbons, CC, CD, CP, and BP) which, conventionally, have been used as supports for metal catalysts were tested as enzyme (Hyd-2 and I64A) supports. Carbon materials were chosen as supports due their high surface area, stability and electronic conductivity. It is important for the support to be electronically conducting in this work, because electrons need to be transferred between enzymes for the chosen biotransformations.

BP was previously used in the Vincent group for H_2-driven NADH generation in batch.[5] Here, three other commercial carbon materials (CC, CD, and CP) were investigated following the same methods and compared with BP. The feasibility of using different carbon materials with suitable size and surface area in flow hydrogenation reactors (***Section 1.1.4.2***) is one of the key points in fine chemical industry. BP is not suitable for these type of high pressure reactors due to its fine particle size. Thus, the characteristics of other three carbon materials such as particle diameter, pore size and surface area were also studied. The characterisation results show that the carbon materials have amorphous structure, high surface area (> 1000 $m^2\ g^{-1}$) and low amount of impurity with different particle size

and shapes. Although they do not have graphitic structure, which would increase the adsorption of enzymes, their high surface areas make them suitable support materials. Their average pore size is 3 nm to 5 nm (mesopores), which is similar to the size of the enzymes and means that enzymes in the pores are in good electronical contact with the support. However, these mesoporous materials require longer equilibrium times for diffusion of the enzymes through the pores. Thus, it is important to provide the minimum amount of time for enzymes to immobilise on these carbon materials.

After the characterisation, the commercial carbon samples were used as supports for co-immobilisation of Hyd-2 and I64A. H_2-driven NADH generation was achieved under specified reaction conditions (***Section 2.2.1.3*** and ***2.2.1.4***). UV-Vis investigation showed that CD, CP, and BP all worked as supports for the desired biotransformation. BP had the highest conversion. This is most likely due to the dispersion issues with the other carbon samples. However, when these batch processes are translated into flow processes *via* filling them into hydrogenation reactors, dispersion of these materials will not matter.

Overall, this Chapter shows that the commercial carbon materials used in metal catalysed hydrogenations can be used as enzyme support materials for H_2-driven NADH generation under further optimised conditions for each support-enzyme assembly. They have suitable pore sizes and high surface area. They provide the electronically conductive background for enzymes to exchange electrons. H_2-driven NADH generation in batch was successful on these materials and the reaction conditions can to be optimised for each carbon material due to their different characteristics. Potentially, these materials can be used in hydrogenation reactors.

CHAPTER 3. H_2-DRIVEN FLOW BIOCATALYSIS IN CARBON NANOTUBE COLUMNS

In the last decade, there has been a growing interest in converting metal-catalysed batch hydrogenation processes to continuous flow processes. In view of this, this Chapter focuses on using carbon nanotube columns (CNCs) in H_2-driven biotransformations and is the first demonstration of H_2-driven ketone reduction and reductive amination in flow. Continuous hydrogenation offers safer H_2 handling, enables automated process control and usually decreases the cost of the operation. Another up-and-coming key point in fine chemical and pharmaceutical industries is using enzymes as catalysts in hydrogenation reactions. Enzymes are cheaper compared to precious metal catalysts, can be grown in laboratories, require milder reaction conditions and most importantly offer stereo-, regio-, and enantioselectivity.

Following the batch H_2-driven NADH generation on carbon supports in ***Chapter 2***, in this Chapter CNCs were used as the catalyst (enzyme) supports for H_2-driven biotransformations. H_2-driven NADH generation is coupled with further biotransformations: i) ketone reduction (acetophenone to (*S*)-1-phenylethanol conversion) and ii) reductive amination (pyruvate to L-alanine conversion). NADH dependent enzymes are co-immobilised with hydrogenase and NAD^+ reductase on CNCs for these biotransformations. In these H_2-driven reactions, CNCs are not only used as enzyme support materials but also as flow reactors. Also, in these processes, NAD(H) is being continuously reduced (oxidised). Thus, this flow system also has a cofactor recycling mechanism (***Section 1.1.7***).

3.1 Introduction

In this Chapter, utilising carbon nanotube columns both as the catalyst (enzyme) support materials and as the flow reactors in H_2-driven biotransformations is investigated. The key points of this Chapter, i) enzyme immobilisation and ii) cofactor recycling were discussed

in ***Section 1.1.5.2*** and ***2.1.2***, and ***Section 1.1.7***, respectively. Thus, the introduction initially focuses on the development of novel carbon nanotube assemblies, their usage as catalysts support materials and some of the novel microflow devices build using carbon nanotubes.

3.1.1 Development of carbon nanotube assemblies

3.1.1.1 Basics of development and properties of carbon nanotubes

Carbon nanotubes (CNTs) were first observed and reported by Radushkevisch and Lukyanovich in 1952.[222] However, microscopy was not developed enough to investigate these materials.[223] Thus, the breakthrough and the increasing interest in the field started with the Iijima's description of multi-wall carbon nanotube (MWCNT).[224] He observed these novel structures, during arc discharge synthesis of fullerenes. There was a deposit of these materials, CNTs, at the negative end of the electrode used Then, in 1993, Iijima *et al.*[225] and Bethune *et al.*[226] reported the growth process of single-wall carbon nanotubes (SWCNTs).

SWCNTs are structurally similar to rolled-up, one atom thick layer of graphite (graphene). The SWCNTs can have different constructions due to the way the graphene is rolled-up. The way of wrapping is indicated by a chiral vector $\vec{C}$, which is a result of two graphene vectors $\vec{a}_1$ and $\vec{a}_2$ and, corresponding pair of integers (*n, m*) (**Figure 40**).[227] The resulting SWCNT can have zigzag, armchair or chiral structure. When SWCNTs with different diameter are concentric, the resulting structure is a MWCNT CNTs, according to their structural properties (number of walls, inner-outer diameter, length, chiral angle *etc.*) have unique properties such as mechanical, optical, electrical and thermal. Since their re-discovery in 1991, they have been developed to be used in numerous applications due to their unique, fascinating and tailor-made properties. CNTs can be synthesised in several ways including, bottom-up organic approach, laser ablation, arc discharge and, a range of low temperature chemical vapour deposition (CVD) methods.[227]

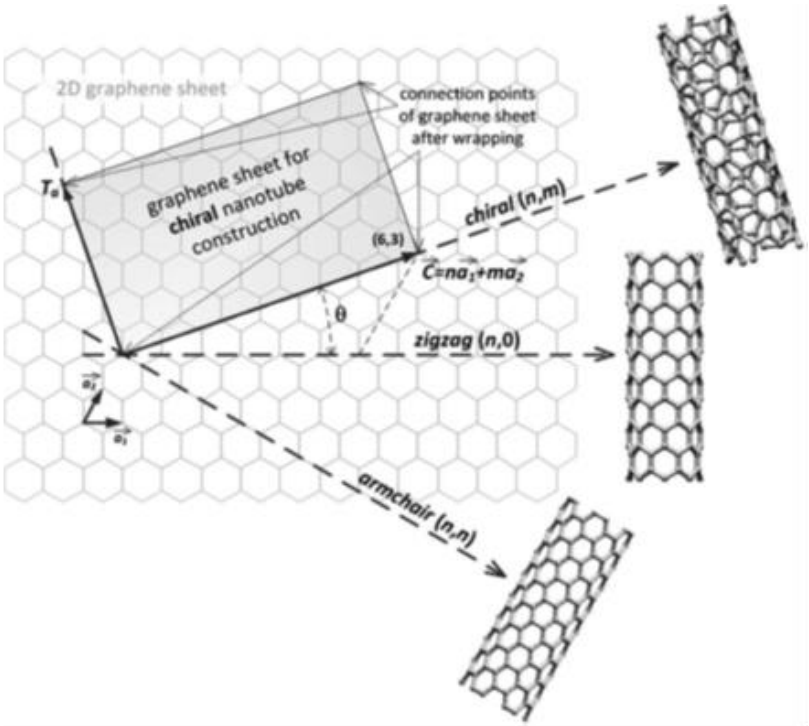


Figure 40: Graphene sheet is rolled up in different geometries to construct zigzag, armchair or chiral SWCNTs. Reproduced from Reference 227, © 2011, with permission from The Royal Society of Chemistry.

CVD method is the standard manufacturing method for CNTs due to its versatility.[227] There are many CVD methods and, the main ones include catalytic chemical vapour deposition -either plasma-enhanced chemical vapour deposition or spray-pyrolysis chemical vapour deposition, and aerosol-assisted chemical vapour deposition (AACVD). CVD methods, in general, allow easy monitoring of reactions and implementation of various recipes with different precursors, offer high purity materials and need lower reaction temperatures compared to methods such as laser ablation and arc discharge. Most importantly, CVD methods allow large-scale CNT synthesis.

In this Thesis, AACVD was chosen as the synthesis method for MWCNTs. In all CVD methods, a carbon source and a catalyst is present. The reactants (precursors) are in gas phase and they react on the surface of the substrates. A carrier gas at a monitored flow rate is used to carry unreacted precursor and by-products away from the reactor. In AACVD, liquid carbon precursor is used and it is atomised using an ultrasonic aerosol generator.[228] MWCNTs are generated *via* pyrolysis of hydrocarbons in the presence of metal catalysts. AACVD allows simultaneous injection of catalysts and carbon source and,

does not require additional catalyst preparation. It depends on the solubility of the precursor, the solubility of the metal salts and, complexes in the organic solvent, not the volatility of the precursor.[229] Thus, a wide range of carbon precursors can be used in AACVD. However, production of uniform CNTs is still a challenge.

3.1.1.2 Towards tailored-novel carbon nanotube assemblies for applications

CNTs do not always grow in a straight, well-aligned way. Due to the defects, non-hexagonal rings in the network and local mechanical deformations waved, coiled, bent or branched CNTs can be formed (**Figure 41**).[230–232] These different types of CNTs can be further tailored for specific applications. For example, coiled CNTs generate an inductive magnetic field when electricity is conducted through them and, they can act as resonating elements due to their 3D structures. Thus, some of the potential application areas they are investigated for are high-performance electromagnetic absorbers and circuit connections.[231]

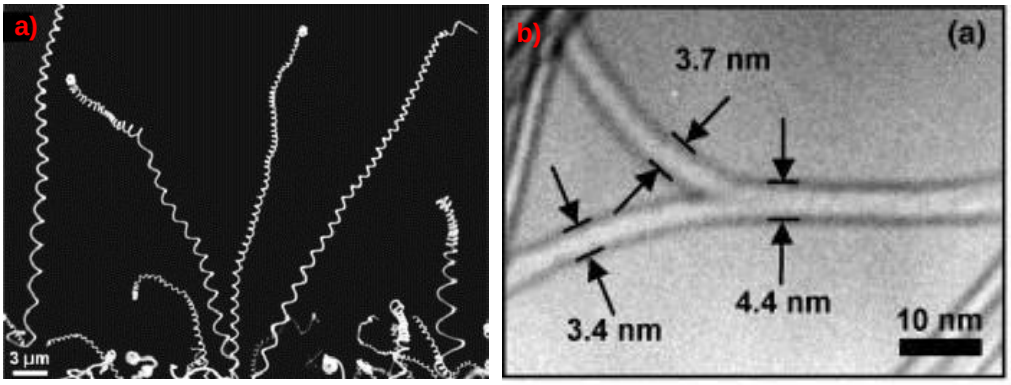


Figure 41: Examples of a) scanning electron micrograph of coiled carbon nanotubes and b) transmission electron micrograph of branched carbon nanotubes. Image a) is Reprinted from Reference 230, © 2006, with permission from Elsevier. Image b) is Reproduced from Reference 232, © 2005, with permission from Elsevier.

CNTs gained a lot of importance due to their unique properties such as high surface area, high electronic conductivity and porosity. One of the main points that draws attention to these nanomaterials is the extensive possibility of tailoring them. Not only the structure of the individual CNTs, but also the structure of their assemblies are studied. There is an intense research on building smart architectures, novel 3D structures of CNTs for

numerous applications such as batteries, magnetic devices, electrical probes, actuators, cell growth and biosensors. As an example, Ajayan and co-workers showed that CNTs could be grown simultaneously grown on a single substrate in a multiply oriented way which could be used for building electromechanical devices (**Figure 42 a**).[233] In another work, they have grown CNTs imitating the structure of a real electronical device.[234] They also showed that by depositing tungsten electrodes on CNTs, they could develop an assembly with a better nanotube-metal line contact and carry the current simultaneously on several layers of nanotubes. In 2015, Kang *et al.*[235] showed multi-stacked 3D CNTs could be used as anode materials in lithium-ion batteries. They obtained three times higher areal density and higher average volume capacity than state-of-the-art graphitic anodes. Another example of CNT architectures is on CNT based electrodes to study extracellular signals (**Figure 42 b**).[236] Chemically durable and bio-compatible CNT islands were grown on lithographically patterned titanium nitride traces. They achieved higher signal-to-noise ratio of extracellular signals with these architectures compared to plain titanium nitride electrodes.[236,237]

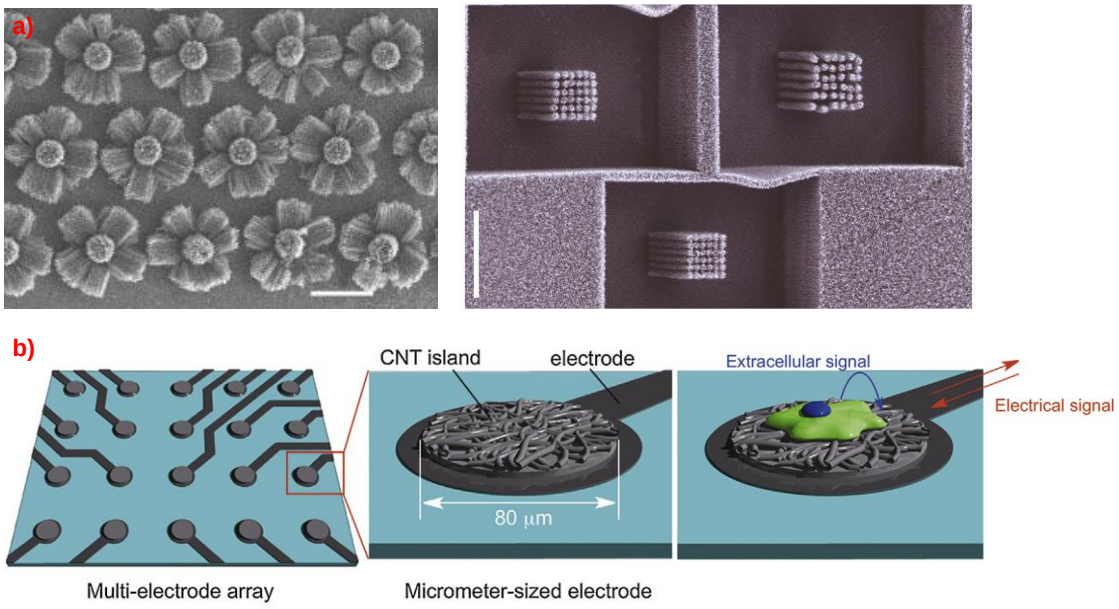


Figure 42: a) Organised and simultaneously synthesised carbon nanotube arrays on patterned silica substrates. Scale bars are 50 µm (left-side image) and 100 µm (right-side image). b) CNT-based device for recording extracellular signals. a) Adapted by permission from Macmillan Publishers Ltd: Nature from Reference 233, © 2002, b) Adapted from Reference 236, © 2014, with permission from Elsevier.

3.1.2 Carbon nanotube catalyst immobilisation materials

CNTs have gained much attention as supports for heterogeneous catalysts due their chemical and physical properties, such as high surface area, unique morphologies and, hollow geometries. The development of numerous methods for tailoring them for specific applications also plays an important role in their popularity in catalysis applications.[238] Today, there are many electrochemical, chemical and physical methods to decorate CNTs with metal catalyst particles. These methods all result in different CNT-catalyst assemblies that can be used in many different applications.[238]

Electrochemical deposition is a fast and facile method of decorating CNTs with metal particles. Although it enables easy control of nucleation and growth of metal catalysts on CNTs, the variety of metals that have been deposited with this method are usually limited to Pd, Pt, Au, Ag, and bimetallic Pt–Ru. The main disadvantage of the electrochemical deposition method is the low quantity of the product.[238] Deposition of metal vapour on CNTs is an alternative method to electrodeposition. This method may include processes such as simultaneous CVD,[239–241] simultaneous arc discharge,[242] incorporating the metal nanoparticle to the catalyst used to grow CNTs,[238] and thermal decomposition.[243] Some of the other methods for decorating CNTs include employing hydrophobic/hydrogen-bonding interactions, using quantum dots, and using metal salt adsorption. The metal nanoparticles used to decorate CNTs with these methods are not limited to common metal nanoparticles such as Pd, Pt, Au, Ag, and Ni. The metal nanoparticles used in these deposition methods include compounds such as TiC, TaC, NbC,[238] Pt-Ru, CdSe, and CdTe.[244]

Selective hydrogenation is the one of the common catalytic steps conducted with CNT supported metal nanoparticles. Selective hydrogenation is a crucial reaction in petrochemical and fine chemical industries.[238] One of the studies that investigate the selectivity of the CNT-catalyst assemblies is on Co doped CNTs by Zhang *et al.*[245] They showed that Co nanoparticles on CNTs are highly active and regioselective (with a ratio of 81.23 % normal C^9-aldehyde to isomer-C^9-aldehyde) in hydroformylation of 1-octene. In

another study, Tessonier *et al.*[246] observed the selective hydrogenation of cinnamaldehyde[dd] by Pd nanoparticles immobilised on CNTs. The activity of Pd dispersed on high surface area activated carbon support was higher than that of Pd-MWCNT, but Pd-MWCNT showed a significant increase in selectivity (> 80 % hydrocinnamaldehyde[ee] being the major product instead of phenyl propanol[ff]) (**Figure 43**).[246]

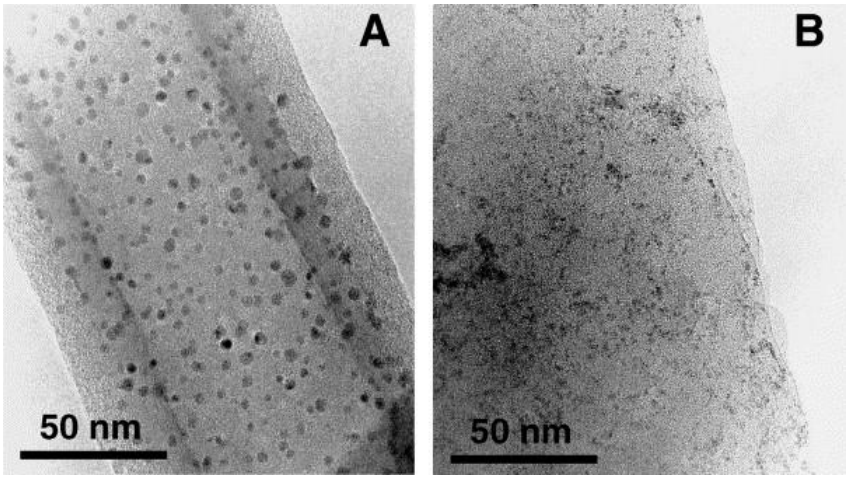


Figure 43: Representative TEM images of the Pd particles introduced inside the MWNT (A) and deposited on the activated charcoal (B). The particles deposited on the activated charcoal were aggregated. Thus, the dispersion of the metal on the support was highly inhomogeneous. Reprinted from Reference 246, © 2005, with permission from Elsevier.

CNT supported metal catalysts are also used in hydrogen storage and sensing, energy storage, optical and electronic applications, and several biological applications.[238] According to Trogadas *et al.*[247] utilisation of CNTs as catalyst supports offers high conductivity, stability and high rates of mass/charge transport.[247] Although CNTs are one of the most promising candidates to support metal catalyst for industrial applications, there are still challenges in the commercialisation of these assemblies for industrial applications. The main challenges are long-term stability and development of cost-effective synthesis techniques for mass-scale production. Still, CNTs make excellent nanoparticle/catalyst support due to their unique geometries and properties and the applications of CNTs functionalised with metals, alloys, metal oxides, compound semiconductors and other nanoparticles are likely to grow.[238]

3.1.3 Carbon support based flow reactors

Flow processes, including catalysis in flow, have gained a lot of attention in the last decade. The benefits of continuous flow processes such as low cost, easy process control and small reactor sizing and, the increasing interest in flow hydrogenation are discussed in ***Section 1.1.4***. CNT support and catalyst assemblies have been used in numerous applications in batch as discussed in ***Section 3.1.2***. CNTs have been also synthesised in different architectures as discussed in ***Section 3.1.1.2***. However, there are not many examples of microflow systems using CNT assemblies directly as the flow reactors or both as the catalysts support and the reactors. In this Chapter, CNT assemblies are used as the catalyst (enzyme) supports in H_2-driven biotransformations. Furthermore, these CNT assemblies also act as the flow device in which these biotransformations take place. In this section, some CNT assemblies manufactured as flow devices for potential applications such as heterogeneous catalysis are discussed.

One of the CNT assemblies used as flow device is synthesised by Ajayan and co-workers.[248] They synthesised freestanding monolithic carbon nanotube columns with dimensions up to several centimetres (**Figure 44 a1**). They developed flow filtration systems with these columns for filtering heavier hydrocarbons from petroleum and filtering *E.coli* from water (**Figure 44 a2** and **a3**). These CNT filters could also be cleaned up repeatedly, which is a major improvement over conventional filters. One of the intriguing designs was developed by Ishigami *et al*.[249], which utilises vertically-aligned CNTs grown in micro-channels both as the catalyst support and the reactor. They synthesised CNTs on channelled Si substrates and decorated these assemblies with Pt (**Figure 44 b1**). The microreactor (**Figure 44 b2**) was used for hydrosilylation of an olefin (1-octene) with a total flow rate of 1 μL min^{-1}. They achieved higher catalytic activity and lifetime using these Pt-CNT microreactors than the conventional microreactors. Another CNT flow device was developed by Kinoshita *et al.*[250] They have grown CNTs to make Y-junction and Fermat's spiral shaped (**Figure 44 c1-3**) flow devices. Silicon oxide was used in the channels to

create hydrophilic regions for water flow. They stated that the reactions between gasses and fluids are possible applications of these flow devices.

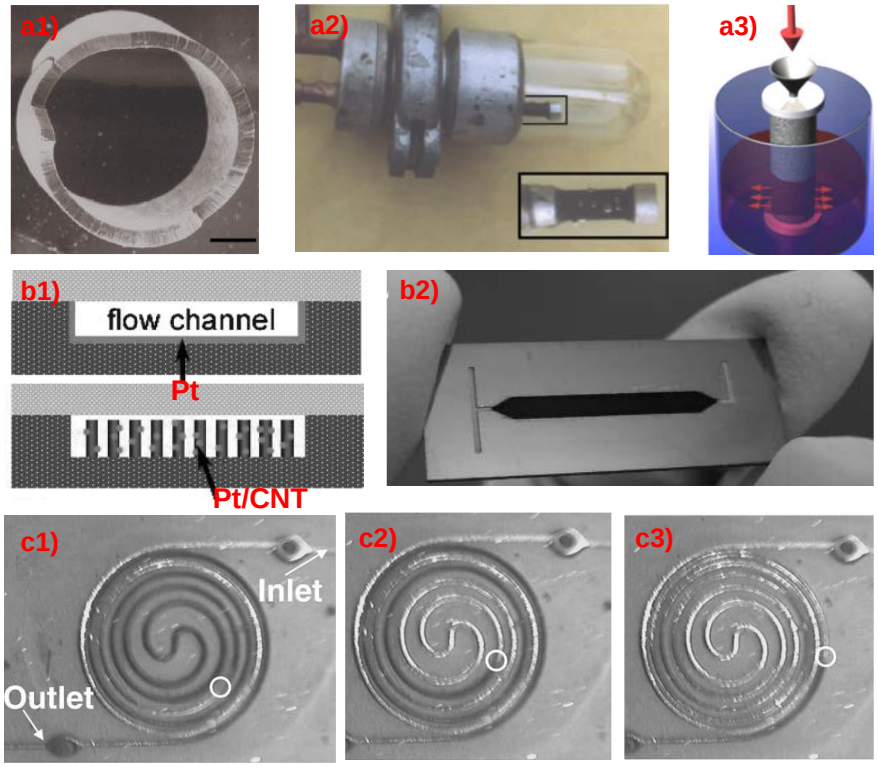


Figure 44: The SEM image in Figure a1 shows the freestanding a carbon nanotube column, the scale bar is 1 mm. Figures a2 and a3 show the petroleum filtration and E.coli filtration systems, respectively. The schematic representation in b1 shows the conventional microreactor with Pt deposited channel and the novel Pt-CNT microreactor. Figures c1-c3 show Fermat's spiral type CNT microchannel reactor. The diameter of the spiral is 5 mm. Figures c2 and c3 show water flowing through the microchannels at 0.8 s and 1.2 s, respectively. Figure a1-3) Adapted from Reference 248 by permission from Macmillan Publishers Ltd: Nature, © 2014. Figure b1-2) Adapted from Reference 249 with permission of The Royal Society of Chemistry. Figure c1-3) Adapted from Reference 250, © 2009, with permission from Elsevier.

3.2 Experimental Methods and Analysis Techniques

This experimental section initially focuses on the production method of CNCs. Then, provides the techniques for immobilising enzymes (hydrogenase (Hyd-2), NAD^+ reductase (I64A), and NADH dependent enzymes (alcohol dehydrogenase (ADH) and L-alanine dehydrogenase (LalaDH), see ***Section 1.1.6.2***) on CNCs. Finally, it details out the methods for H_2-driven biotransformations in flow catalysed by the immobilised enzymes.

The analysis section provides the characterisation methods used for CNCs and then focuses on determination of products of the described biotransformations.

3.2.1 Experimental Methods

3.2.1.1 Materials

Chemicals used in H_2-driven biotransformations:

The H_2-driven biotransformations and enzyme immobilisations were performed anaerobically, under N_2 (BOC) atmosphere, <1 ppm O_2), in a glovebox.

The chemicals used in H_2-driven biotransformations are the same chemicals mentioned in ***Section 2.2.1.1.*** Additionally, for reductive amination sodium pyruvate (Sigma-Aldrich, ≥ 99 %), L-alanine (Alfa-Aesar, 99 %), and ammonium chloride (Fisher Scientific, > 99 %) were used in the reaction mixtures in the flow system. In gas chromatography, for the analysis of chiral ketone reduction products, (*S*) - (—) 1-phenylethanol (Sigma-Aldrich, ≥ 98.5 %) was used as the chiral standard.

Enzymes:

In addition to the enzymes, Hyd-2 (4 mg mL^{-1}) and I64A (1.6 mg mL^{-1}), ADH and LalaDH were also used in this Chapter. Johnson Matthey Catalysis and Chiral Technologies provided ADH, commercially sold as ADH 105. The enzyme was used as supplied, without any further purification. The activity of ADH is 2.73 U when 1 mM substrate (acetophenone) and 1 mM cofactor (NADH) was used to test the activity (***Appendix 1***). 1 U corresponds to the amount of ADH which converts 1 µmol acetophenone per minute at pH 6.0 and 20 °C.

LalaDH is commercially available from Sigma-Aldrich and was used as received, without any further purification. The activity of LalaDH is 1929 µmol mL^{-1} min^{-1} when 5 mM substrate (pyruvate), 10 mM ammonia source (ammonium chloride) and 0.2 mM cofactor (NADH) was used to test the activity at pH 6.0 and 20 °C.

Chemicals used in CNC synthesis:

The chemicals used in CNC synthesis are toluene[gg] (Sigma-Aldrich, 99.9 %) and ferrocene[hh] (Sigma-Aldrich 98 %, further purified by sublimation at 95 °C). The cleaning of the aerosol units were done with toluene and ethanol (Fisher Scientific, 99.99 %). Ethanol was also used in the cleaning of the quartz reaction tubes and quartz tube substrates. Acetone (Fisher Scientific, > 99 %) was used as the solvent in the bubbler.

3.2.1.2 Aerosol-assisted chemical vapour deposition method for CNC synthesis

All CNCs were synthesised with AACVD method and following the synthesis procedure developed in the Grobert group.[1] A system consisting of a piezo electric transducer amplifier (Central Electronics Group, Oxford Physics) connected to an aerosol unit with a piezo-electric at the bottom (RBI Pyrosol 7901) and a quartz tube (Robson Scientific; 800 mm long, 21 mm inner diameter, 1.5 mm thick with B19/26 socket and cone connections) placed inside a single-zone horizontal tubular furnace (Elite Thermal Systems; 550 mm long; 40 mm inner diameter; N-type (Nicrosil/Nisil) thermocouple; Eurotherm 2216e temperature controller). The temperature profile of the furnace was measured before the synthesis using a K-type (Chromel/Alumel) thermocouple at 850 °C under 2.5 L min^{-1} (Brooks mass flow controller) argon (BOC, 99.999 %) flow (**Figure A 4**). Quartz tubes (Robson Scientific: 2 mm inner diameter, 4 mm outer diameter) were cut in to 20 mm long pieces with a diamond pen and used as substrates (columns).

16 quartz columns were cut for each experiment. 8 of them were placed at 230 mm from the start of the ethanol cleaned reaction tube. The remaining columns were placed at 290 mm from the start of the tube. At both points, the columns were stacked on each other

(**Figure 45**). The quartz reaction tube was placed inside the tubular furnace carefully, avoiding column roll off. The precursor solution for CNC synthesis was prepared by dissolving 5 wt % ferrocene in 95 wt % toluene. The aerosol unit was filled with 400 mL precursor solution. The aerosol unit and the acetone bubbler were connected to the reaction tube as shown in **Figure 45.** The first 50 mm of the gap between the furnace and the quartz reaction tube were sealed with glass wool. The aerosol unit was connected to the piezo electric device. The aerosol unit-quartz tube assembly was sealed and purged with Ar (flow rate 2.5 slm) for 5 minutes. Ar flow to the aerosol unit was switched off. Therefore, the flow was only allowed through the quartz reaction tube. The temperature controller was set to 850 °C. When the furnace temperature reached 850 °C, the aerosol unit was connected to the piezo electric device. The amplitude and frequency were set to provide a dense aerosol to the system and the Ar flow was let into the aerosol unit (**Figure 45**). The duration of the experiments were 90 minutes. After 90 minutes the heating was turned off. The aerosol unit was blocked to Ar flow. The flow was let only through the quartz reaction tube and the flow rate was decreased to 1 slm. The quartz tube was left inside the furnace to cool down.

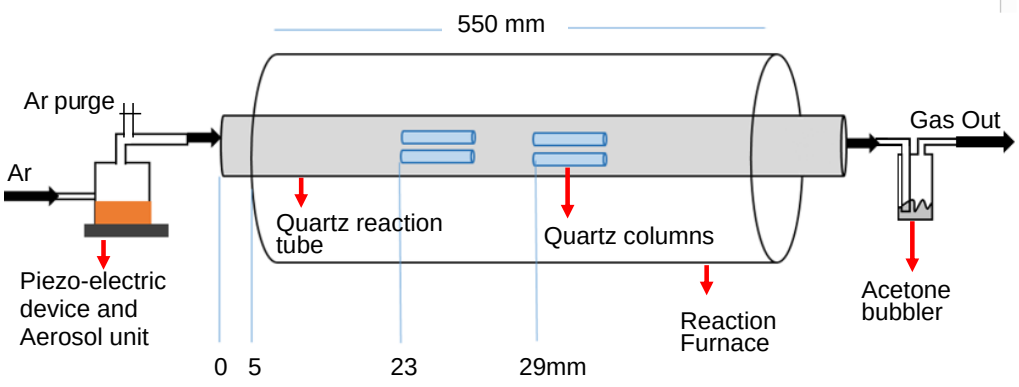


Figure 45: A schematic representation the AACVD set-up for CNC synthesis.

3.2.1.3 Evaporation rates of the reactants and products

Amongst the main starting materials (acetophenone and sodium pyruvate) and the products (1-phenylethanol and alanine) of the chosen biotransformations, acetophenone was detected to evaporate significantly. Thus, acetophenone and 1-phenylethanol were

tested for their evaporation rates. 1 mL of 10 mM acetophenone and 1-phenylethanol were kept in sealed vials with H_2 flowing through the headspace overnight. The initial and final concentrations were tested with HPLC.

3.2.1.4 Preparation of enzyme modified CNCs

The co-immobilisation of three enzymes, Hyd-2, I64A, and an NADH dependant enzyme (ADH or LalaDH) on CNCs was carried out with a similar approach to the method in ***Section 2.2.1.3***. A mixture of the three enzymes was passed slowly through CNC columns back and forth several times *via* a peristaltic pump (**Figure 46**). After making sure that the CNCs were all wet with the enzyme solution, the solution was left inside the CNCs. The CNC-enzyme solution assemblies were maintained at 4 °C for 90 minutes.

The amount of enzyme mixtures were optimised by varying the amounts of each enzyme (Hyd-2: 20 µL - 40 µL, I64A: 15 µL - 30 µL, 20 µL ADH: 30 mg mL^{-1} - 50 mg mL^{-1} and, LalaDH: 30 µL - 40 µL) and running experiments at specific reaction conditions. The reactions conditions (*e.g.* H_2 flow rate and flow rate of the reaction mixture) were also optimised for the amount of enzyme mixture and *vice versa*.

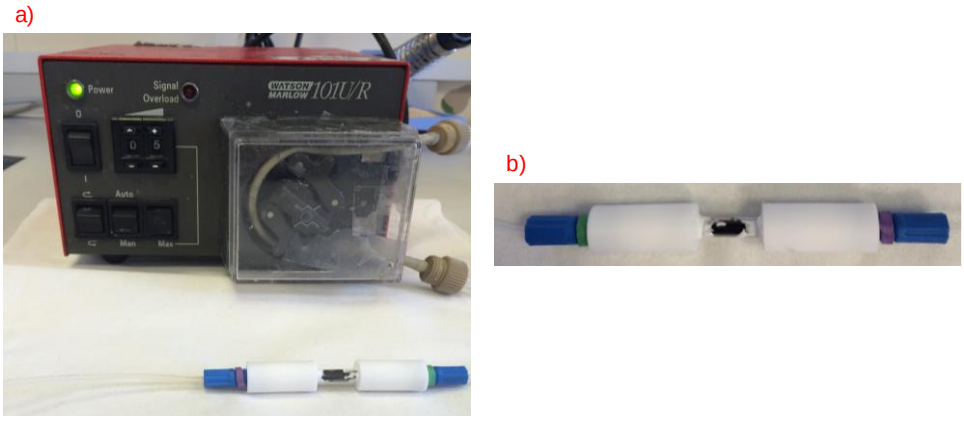


Figure 46: a) An image of the peristaltic pump and the tubing used in flow experiments, b) an image of a CNC connected to the tubing via Teflon adaptors.

For NADH generation, Hyd-2 and I64A were co-immobilised on the CNCs (**Figure 47**). The obtained optimum amounts of the enzymes used were 40 µL Hyd-2 and 20 µL I64A.

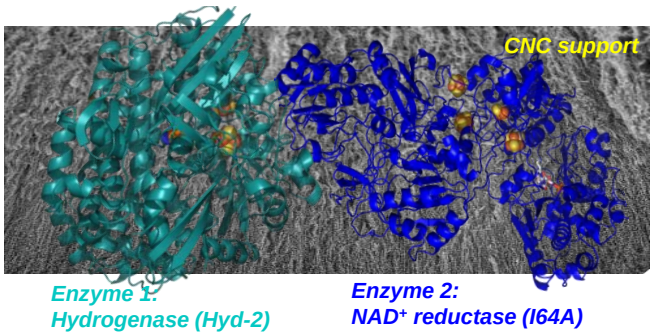


Figure 47: A schematic representation of co-immobilisation of Hyd-2 (cyan) and I64A (blue) on a CNC for NADH generation. (The representation is not shown to scale.)

ADH was used as the NADH dependant enzyme for ketone reduction. Thus, Hyd-2, I64A and ADH were co-immobilised on the CNCs**.** The obtained optimum amounts of the enzymes used were 30 µL Hyd-2, 40 µL I64A and 20 µL ADH from a fresh 50 mg mL^{-1} ADH stock solution (**Figure 48**).

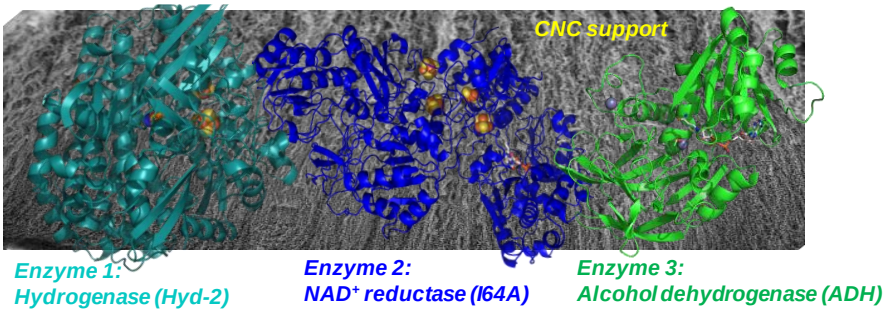


Figure 48: A schematic representation of co-immobilisation of Hyd-2 (cyan), I64A (blue), and ADH (green) on a CNC for ketone reduction. (The representation is not shown to scale.)

LalaDH was used as the NADH dependant enzyme for reductive amination. Hyd-2, I64A and LalaDH were co-immobilised on the CNCs. The obtained optimum amounts of the enzymes used were 40 µL Hyd-2, 30 µL I64A and 30 µL LalaDH (**Figure 49**).

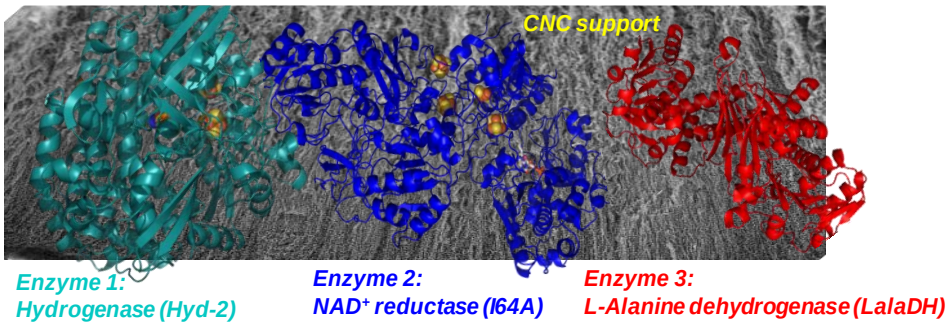


Figure 49: A schematic representation of co-immobilisation of Hyd-2 (cyan), I64A (blue), and LalaDH (red) on a CNC for reductive amination. (The representation is not shown to scale.)

3.2.1.5 The protocol for H_2-driven biotransformations in flow

Before the biotransformations, CNC-enzyme assemblies were taken out of the 4 °C fridge and the remaining solution in the CNC was pumped out. The CNC-tubing set-up was washed with 1 mL of buffer to remove any free enzyme left in the CNCs.

After the reaction mixtures and the CNCs were prepared, the vessels containing the reaction mixture was the CNC-tubing-pump set-up in the **Figure 46** with syringe needles. H_2 gas lines and a water bubbler were also connected to the reaction vessel *via* syringe needles. Hydrogen gas was flowed into the solution for the initial 30 minutes. Then, it was flowed through the headspace until the end of the experiment.

3.2.1.5.1 The protocol for H_2-driven NADH generation in flow

A reaction mixture containing 1 mM NAD^+ was prepared in buffer. 3 mL of the reaction mixture was used in the flow experiments and the remaining solution was kept for further analysis. 3 mL reaction mixture was transferred into a sealed vessel and hydrogen saturated by bubbling H_2 into the solution for 30 minutes. Then, the procedure in ***Section 3.2.1.5*** was followed for the flow experiment.

3.2.1.5.2 The protocol for H_2-driven ketone reduction in flow

Initially, 1 mM NAD^+ solution was prepared in buffer and hydrogen saturated by flowing hydrogen gas through the solution for 30 minutes. For the preparation of the 10 mM acetophenone reaction mixture, the required amount of acetophenone was added to the H_2 saturated 1 mM NAD^+ solution. 3 mL of reaction mixture was used in the flow experiments. The reaction mixture was transferred into a sealed vessel and the same procedure in ***Section 3.2.1.5*** was followed for the flow experiment.

3.2.1.5.3 The protocol for H_2-driven reductive amination in flow

A reaction mixture containing 1 mM NAD^+, 100 mM ammonium chloride, and 10 mM sodium pyruvate was prepared in buffer solution. The reaction mixture was hydrogen saturated by flowing hydrogen gas through the solution for 30 minutes. 3 mL of reaction

mixture was used in the flow experiments. The reaction mixture was transferred into a sealed vessel and the same procedure in ***Section 3.2.1.5*** was followed for the flow experiment.

3.2.2 Analysis Techniques

3.2.2.1 Characterisation techniques used for CNCs

A similar approach to characterisation of carbon materials in ***Chapter 2*** was followed for the characterisation of CNCs.

The morphology of the CNCs were investigated by scanning electron microscopy. JEOL 840F microscope was used for the analysis and the secondary electron detector was operated at 5 kV acceleration voltage. Complementary information was obtained by Raman spectroscopy. Raman spectroscopy was done by using JY Horiba Labram Aramis imaging confocal Raman microscope at 532 nm green laser excitation. Thermogravimetric measurements were performed using a Perkin Elmer Pyris Thermogravimetric Analyser to detect the amount Fe catalysts in the MWCNT network. The temperature range was from 50 °C to 1000 °C and the heating rate was 10 °C min^{-1}. Energy-dispersive X-ray spectroscopy was used to detect the elemental difference between CNCs before and after the flow experiments.

3.2.2.2 Ultraviolet-visible spectroscopy

The ultraviolet-visible spectra were recorded following the protocol in ***Section 2.2.2.3***. A Cary 60, Agilent UV-Vis spectrometer was used with samples in a UV-Vis cuvette (Hellma Analytics) of well-defined path length (1 cm). Literature extinction coefficient values in **Table 2-1** were used along with the plot of $[NAD^+]/[NADH]$ vs $A_{260\ nm}/A_{340\ nm}$ in ***Appendix 4*** for final NAD(H) concentration calculations in ***Appendix 8***.

3.2.2.3 High-performance liquid chromatography

The high-performance liquid chromatography protocol for ketone reduction was described in ***Section 2.2.2.2***. A ZIC®-HILIC column was used for the detection of pyruvate and alanine in reductive amination mechanism. A > 20 minutes gradient mobile phase starting with 95 % acetonitrile and 5 % water and ending with 20 % acetonitrile 80 % water was used. The flow rate of the mobile phase was 0.75 mL min^{-1} and the column was maintained at 40 °C.

3.2.2.4 Gas chromatography

Chiral gas chromatography (GC) was used to confirm the chirality of the alcohol in ***Section 3.2.1.5.2*** (ketone reduction product, 1-phenylethanol). A racemic mixture of 1-phenylethanol, (*S*)-1-phenylethanol and a final reaction mixture were analysed by GC. A Supelco β-dexTM 325 column (30 m, 0.25 mm, and 0.25 μm) was used with He as the carrier gas (flow rate 21.5 cm s^{-1}). The column temperature was maintained constant at 120 °C.

3.3 Results and Discussion

3.3.1 Characterisation of the CNCs

CNCs were synthesised with an established method in the Grobert group[1] as described in ***Section 3.2.1.2***. The properties of the CNCs in this Thesis were investigated with scanning electron microscopy (SEM) and Raman spectroscopy to make sure that these materials are in fact following the characteristics reported before. Thermogravimetric analysis (TGA) and energy-dispersive X-Ray analysis (EDX) were used to study the amount of iron in CNCs and enzyme immobilised CNCs, respectively.

The images in **Figure 50** show how CNCs look to the naked eye. Image a) is an image of a CNC directly after synthesis. The quartz column is covered with carbon deposit on the outside. Image c) shows the cross-section of this CNC. The carbon deposit on the outside and in the inside of the quartz column can be seen. Image b) belongs to the same CNC after the deposit on the outside is scraped off. It can be seen that there are no gaps inside the quartz column and it is filled with carbon deposit.



Figure 50: a) An image of a CNC directly after the synthesis, b) an image of a CNC after cleaning the outer MWCNT deposit, ready to use as a flow device, c) a cross-section image of a CNC directly after the synthesis.

3.3.1.1 Scanning electron microscopy of CNCs

Scanning electron microscopy (SEM) was used to study the morphology of the CNCs. The deposit inside the quartz columns follow the characteristic morphology of forests of aligned MWCNTs.[251] A representative cross-section image of a CNC in **Figure 51 a** shows the MWCNT deposit inside the quartz tube. The dark area in the middle is the hollow part of the CNC. This shows that MWCNTs were not long enough to fill the column. The length of MWCNT deposits range from 0.55 mm to 0.85 mm according to the **Figure 51 a.** The

images taken at higher magnifications (**Figure 51 b-e**) show the detailed geometry of CNCs and are in agreement with the morphology of aligned MWCNTs in the literature.[251]

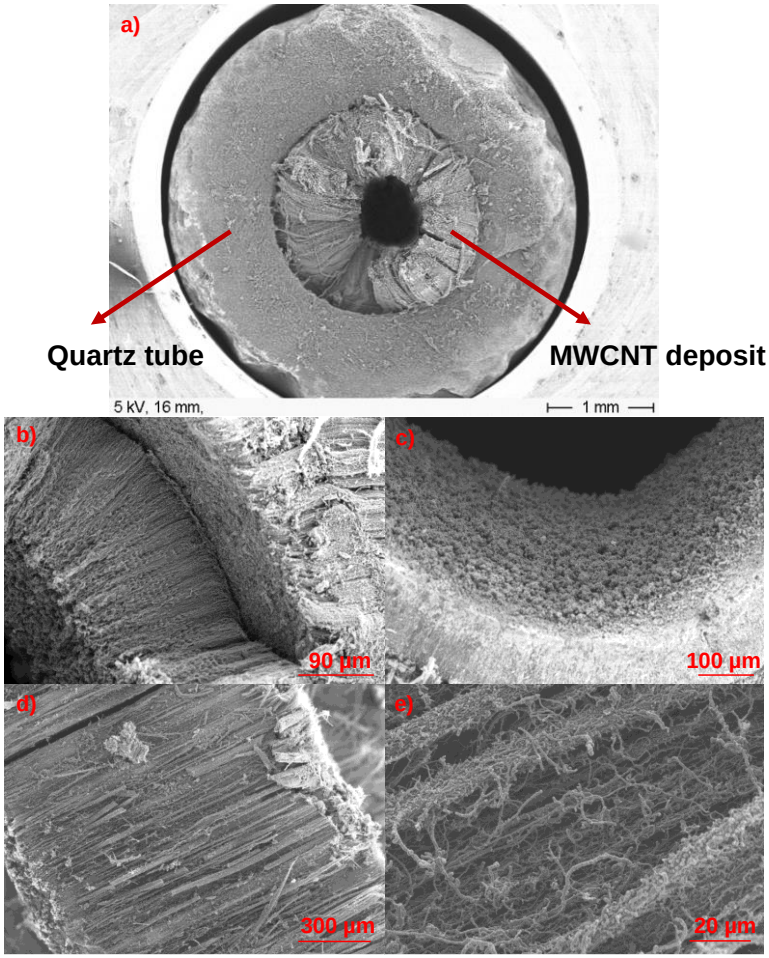


Figure 51: Scanning electron micrographs of CNCs under different magnifications. a) Scanning electron micrograph of a cross-section of a CNC. The MWCNT deposits can be seen inside the quartz column. The dark ring in the middle is the hollow section b) layers of MW CNTS due to interrupted aerosol flow, c) inner walls of a CNC, d-e) MWCNT deposits in CNCs.

These CNCs were directly used in H_2-driven flow biotransformations. As explained in ***Section 3.2.1.4***, they were connected to Teflon adaptor and plastic tubing without any chemical or geometrical modification. SEM images of CNCs were also taken after the flow experiments to detect possible morphological changes in CNC structures. The images in **Figure 52**, taken after the flow experiments, show that the MWCNT deposits are thicker and some of the bundles are tangled together. The MWCNTs are also seen to be coated with a new material. This is probably due to the overnight flow of buffer solution,

immobilised enzymes on CNCs and adsorption of any chemicals in the reaction mixture on CNCs.

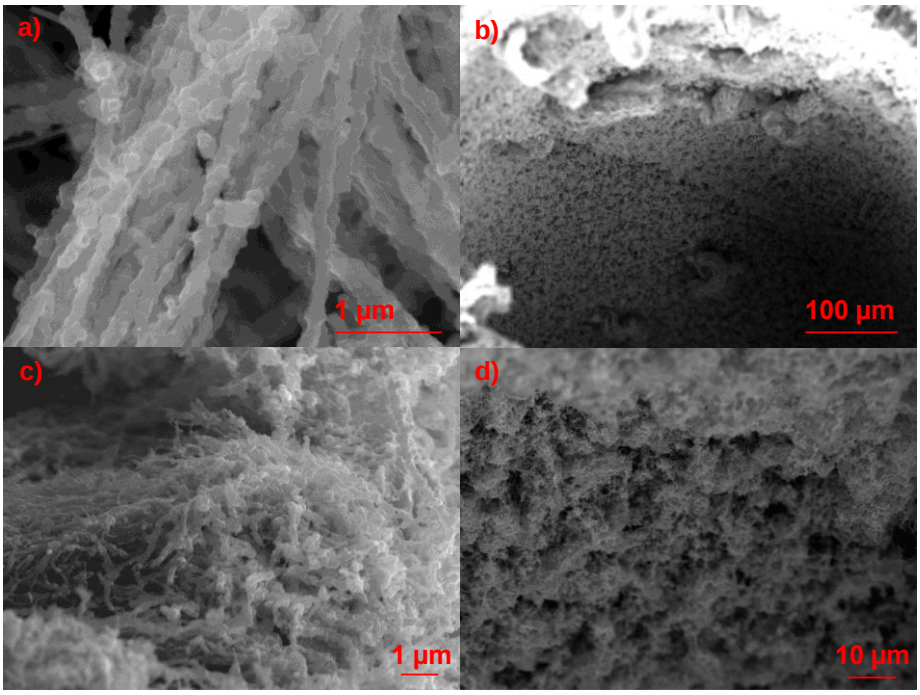


Figure 52: Scanning electron micrographs of enzyme-modified CNCs after a flow experiment taken at different magnifications. When compared with the CNC images directly after CNC synthesis, these images show that there is morphology change in CNCs after the flow experiments.

3.3.1.2 Raman spectroscopy of CNCs

Raman spectroscopy was used to investigate the degree of graphitisation and support the findings of the SEM study. Raman spectrum of CNCs in **Figure 53** shows the intensity of the energy shifts in the incident photons. Three Raman bands are observed in the spectrum: two first-order bands and one second-order band. The first-order peaks are at around 1340 cm^{-1} and 1570 cm^{-1} are D and G peaks, respectively. The peak at around 2680 cm^{-1} is the second-order 2D peak. D band is attributed to the extent of sp^3 hybridisation in the carbon network. The intensity of this band is linked with defects in the carbon lattice. G band is attributed to the sp^2 hybridisation in carbon network and the intensity of it is an indicative of the degree of graphitisation.[252] I_D/I_G ratio is used to study the extent of graphitic character and purity of CNTs. The spectrum in **Figure 53** is in agreement with the literature spectra for MWCNTs and has a I_D/I_G ratio less than 1.[252]

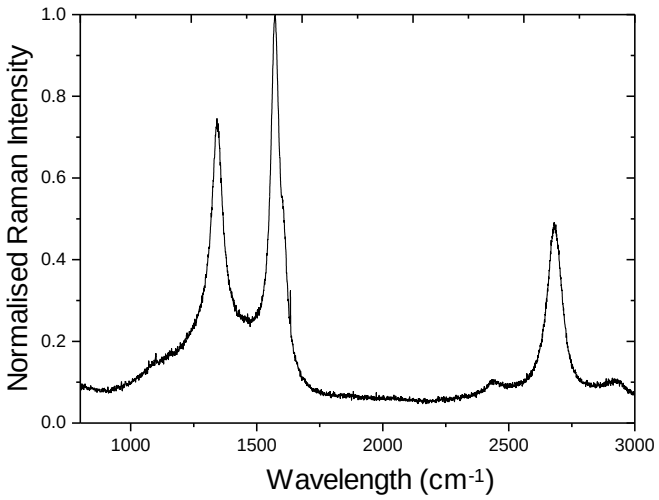


Figure 53: Raman spectrum of CNCs showing three characteristic MWCNT peaks, D peak at around 1340 cm^{-1}, G peak at around 1570 cm^{-1}, and 2D peak at around 2680 cm^{-1}.

3.3.1.3 Thermogravimetric Analysis of CNCs

TGA was used to investigate the thermal stability of the CNCs and the amount of metal catalyst in the CNCs. The weight loss during the analysis is due to the oxidation of carbon into carbon dioxide. Thus, the final weight percentage shows the ratio of metal catalyst in the CNC sample. Any weight gain during the heating process can be due to oxidation of trace metal impurities into solid oxides.[252] **Figure 54** shows that the yield of carbon deposit is 88 wt % and CNCs are thermally stable at temperatures < 500 °C.

The amount of catalyst, ferrocene, used in the precursor was 5 wt %. However, the TGA shows that the amount of metal catalyst is 12 wt %. This is due to constant supply of the atomised precursor in 90 minute long AACVD experiments. The oxidation resistance is < 500 °C, which is important for the high temperature catalysis applications. This shows that CNCs can be used as support materials not only in biocatalysis but also in high-temperature catalysis applications.

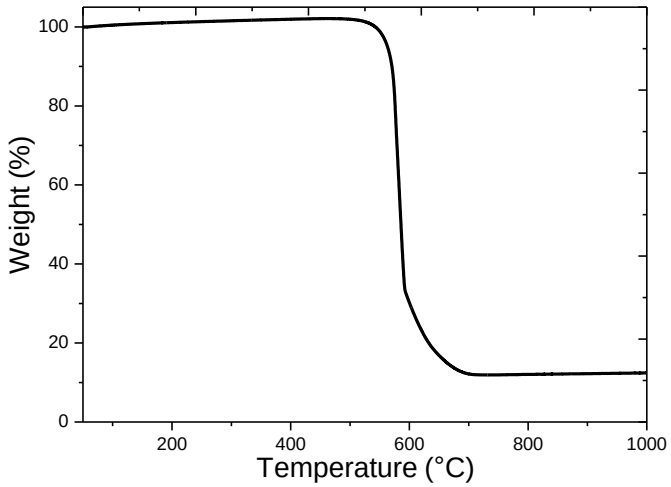


Figure 54: TGA curve of the CNCs showing that the yield of carbon deposit is 88 % and the CNCs are resistant to oxidation at < 500 °C.

3.3.2 Evaporation of the reactants and products under overnight H_2 flow

The reactants and the products in the H_2-driven biotransformations in this Chapter are acetophenone, 1-phenylethanol, pyruvate, ammonium chloride, and L-alanine. During the H_2-driven biotransformation experiments, significant loss of reactant was observed in acetophenone to 1-phenylethanol reduction. The loss of acetophenone and the potential loss of 1-phenylethanol was investigated. The adsorption of the chemicals on CNCs and the evaporation of the chemicals under H_2 were considered as the possible causes of this loss. Adsorptions of acetophenone and 1-phenylethanol on carbon materials were investigated in ***Section 2.2.1.2*** and it was shown that the adsorption was negligible under the experimental conditions. Adsorption on the MWCNTs of CNCs was also investigated and the adsorption of acetophenone on MWCNTs was negligible. H_2 was bubbled in different methods during the experiments: i) directly into the reaction mixture overnight, ii) into the reaction mixture for 2 hours and over the headspace overnight, iii) over the headspace overnight, and iv) over the headspace for 2 hours. It was seen that acetophenone was lost due to the evaporation under H_2. To conclude that the loss of acetophenone and potential loss of 1-phenylethanol was due to the evaporation under H_2, 1 mL 10 mM of each chemical was left overnight with H_2 bubbling over the headspace. The final solutions were tested with HPLC. The HPLC results (**Figure 55**) showed that

acetophenone evaporated under the experimental conditions but the concentration of 1-phenylethanol remained the same.

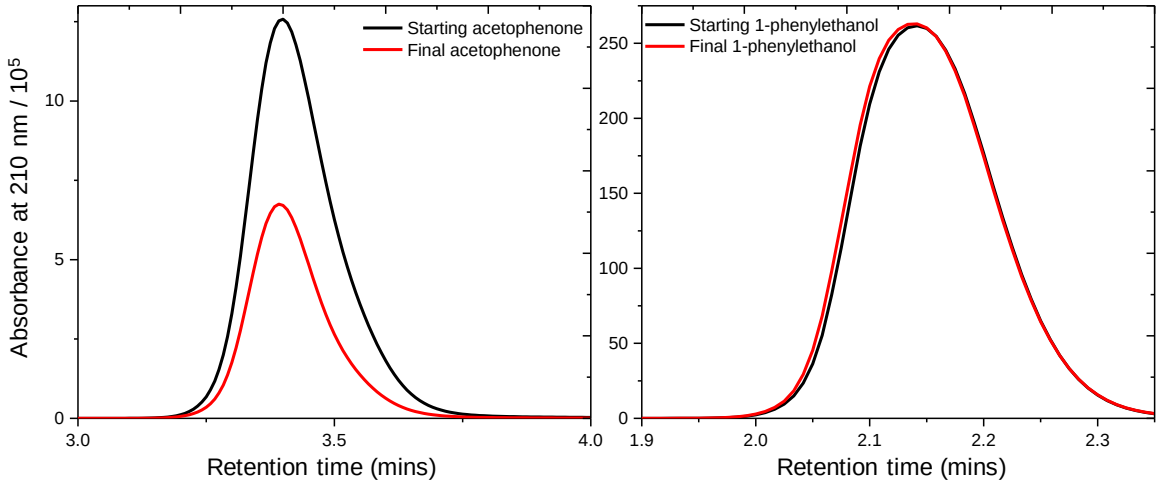


Figure 55: HPLC chromatograms for overnight evaporation of acetophenone and 1-phenylethanol under H_2 flow through the headspace. The spectra show that acetophenone concentration decreased due to evaporation caused by H_2 bubbling over the headspace. 51 % of the starting acetophenone solution evaporated overnight and concentration of 1-phenylethanol remained the same.

3.3.3 Biotransformations on CNCs

3.3.3.1 NADH generation on CNCs

Initially, the first part of the reaction mechanism, H_2-driven NADH generation, was investigated using hydrogenase (Hyd-2) and NAD^+ reductase (I64A) immobilised on the CNCs to make sure that the flow system is suitable for the H_2-driven biotransformations. This system requires that the two enzymes are electronically linked and therefore immobilised on the CNT network.

The mechanism for NADH generation on CNCs in flow is shown in **Figure 56**. Hydrogen was oxidised to $2H^+$ and was released into the buffer. Since CNCs are electronically conducting, electrons were transferred to NAD^+ reductase. NAD^+ was reduced to NADH at NAD^+ reductase.

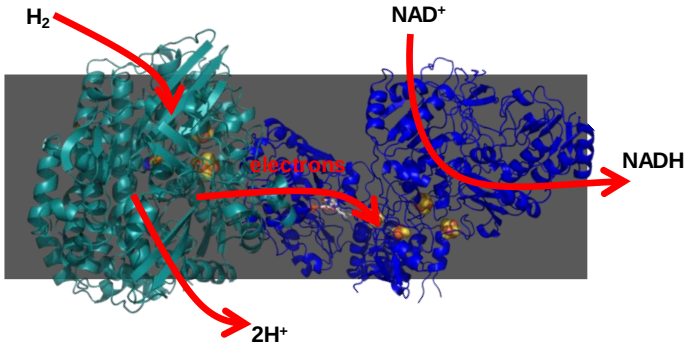


Figure 56: A schematic representation of the H_2-driven NADH generation mechanism on CNCs. Hyd-2 (cyan) and I64A (blue) were co-immobilised on the electronically conducting CNCs. H_2 was oxidised at Hyd-2 and the electrons were transferred to the I64A. Using the electrons transferred and the generated H^+, NAD^+ was reduced at I64A.

The NADH generation was monitored by UV-Vis spectroscopy, following the protocol for batch NADH generation, and the extent of conversion was calculated using $A_{260\ nm}/A_{340\ nm}$ as shown in ***Appendix 8***. A typical 5 hour long experiment showed 49 % conversion. In **Figure 57**, the decreasing peak at 260 nm shows that NAD^+ was being used up and the increasing peak at 340 nm shows that NADH was being generated. This result shows that the two enzymes can be immobilised on the CNCs and they are in electronic contact, which is essential for these biotransformations.

Blank flow experiments were run under the same reaction conditions with the optimised experiments (***Appendix 7***). These experiments had blank CNCs *i.e.* CNCs without enzymes. The blank experiments showed that there was no NADH generation without enzymes and iron in CNCs does not catalyse the NADH generation. Overall, these experiments support the conclusion that the chosen biotransformations in flow are catalysed by immobilised enzymes.

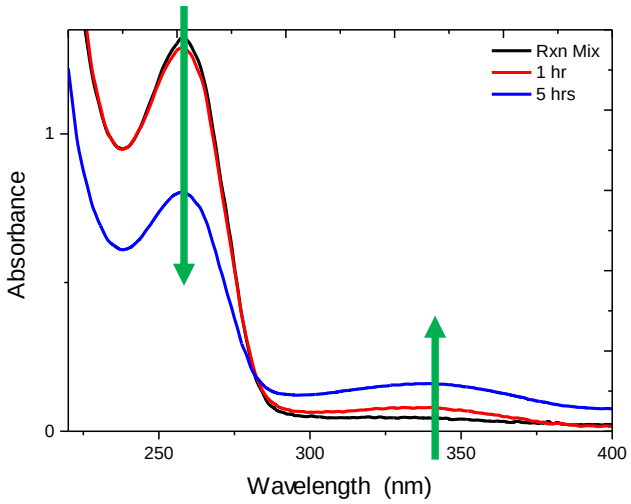


Figure 57: UV-Vis spectra for 5 hour long H_2-driven NADH generation in flow in a CNC. The peak at 260 nm shows that NAD^+ was consumed and the peak at 340 nm shows that NADH was generated, and the conversion was 49 %.

3.3.3.2 Ketone reduction on CNCs

After showing that CNC-enzyme assemblies work in a flow system for NADH production, a different biotransformation requiring an additional enzyme was investigated. Alcohol dehydrogenase, was co-immobilised with Hyd-2 and I64A for ketone reduction to secondary alcohol (**Figure 58**). In this system, NADH was generated the same way as explained above in ***Section 3.2.1.5.1***. The NADH generated was then used by alcohol dehydrogenase (ADH). In this process, NADH is oxidised to NAD^+ and acetophenone was reduced to 1-phenylethanol (**Figure 59**). The NAD^+ was used by I64A for NADH generation. Thus, NAD^+/NADH was constantly recycled in the system without any by-product or sacrificial substrate generation.

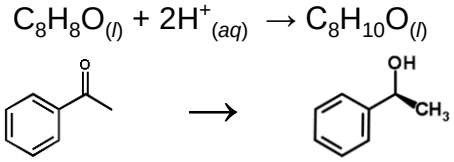


Figure 58: Reaction mechanism showing acetophenone to (S)-1-phenylethanol conversion.

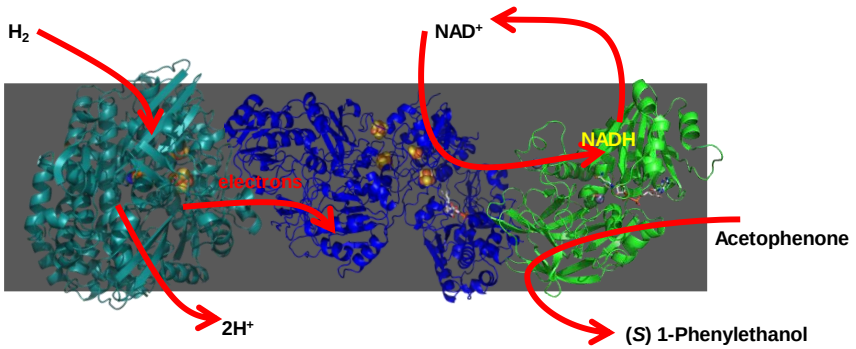


Figure 59: A schematic representation of the H_2-driven acetophenone reduction mechanism on the electronically conducting CNCs. Hyd-2 (cyan), I64A (blue) and ADH (green) were co-immobilised on the CNCs. Acetophenone and NAD^+ in H_2 saturated buffer was used as the reaction mixture. H_2 was oxidised, acetophenone was reduced. NAD^+/H was constantly reduced/oxidised. Thus, it was recycled in the reaction mechanism.

The 1-phenylethanol production was confirmed by HPLC (**Figure 60**) and the chirality of it was confirmed by GC (**Figure 61**). The conversion was calculated using the standard HPLC curves and the line equations in ***Appendix 3***.

The HPLC peak around 2.1 minutes is the 1-phenylethanol peak and the peak around 3.4 minutes is the acetophenone peak. It can be seen in the **Figure 60** that the starting solution (black) does not have any peaks at 2.1 minutes and the overnight solution (red) has a peak at 2.1 minutes. Thus, this peak formation shows that 1-phenylethanol was formed. The conversion is 11.4 % according to the standard HPLC curves and the line equation obtained from these curves. However, the HPLC trace in **Figure 60** shows that the acetophenone concentration dropped significantly. The final acetophenone concentration dropped to ~ 0.9 mM from ~ 8.5 mM starting concentration. This is most likely due to the evaporation of acetophenone. In **Figure A 6** and **Figure 35**, it is shown that under these experimental conditions adsorption of acetophenone on CNCs and carbon materials, respectively, was insignificant.

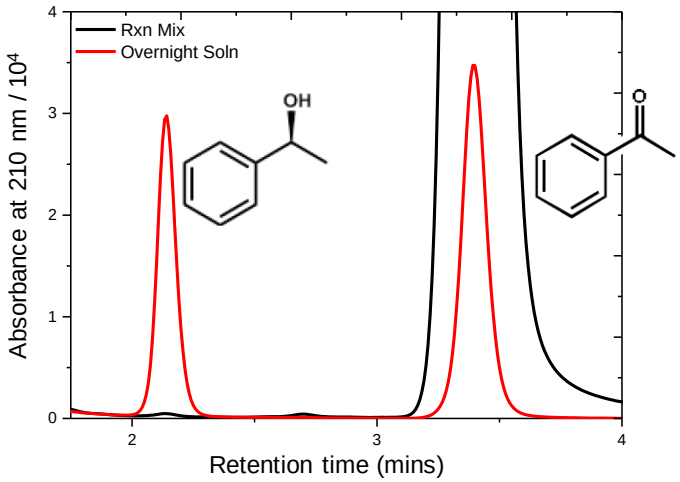


Figure 60: HPCL chromatograms for starting reaction mixture (black) and the overnight solution after cycling through the CNCs (red). The peak around 2.1 minutes is the 1-phenylethanol peak and the peak around 3.4 minutes is the acetophenone peak.

ADH 105 used is known to reduce acetophenone to (*S*)-1-phenylethanol. As discussed in ***Section 1.1.5.2***, one of the main concern with immobilising enzymes and hydrogenation catalyst is maintaining the stereoselectivity. In this study, the chirality of the product was tested with GC to show that the enzyme is in fact producing the *S* enantiomer and the immobilisation did not affect the stereoselectivity of the enzyme. The GC trace in **Figure 61** show the peaks for both for racemic acetophenone mixture (*i.e.* both the *S* and *R* enantiomers), *S* enantiomer, and the overnight reaction mixture. When the racemic mixture and *S* enantiomer traces are compared, it is seen that the peak after 13.7 minutes belongs to the *S* enantiomer and the peak around 13.4 minutes belongs to the *R* enantiomer. The overnight reaction mixture contains unreacted acetophenone and 1-phenylethanol. The first peak around 10 minutes is the acetophenone peak. There is only one peak for the product showing that the product is not a racemic mixture of 1-phenylethanol. The position of the product peak confirms that the product is *S*-1-phenylethanol, as expected. This shows that although the conversion is low, the result is important since the enantiomerically pure product is expensive[vi] compared to the racemic mixture. Also, it is shown that the immobilisation does not change the stereoselectivity of the ADH 105.

[vi] According to data taken from http://www.sigmaaldrich.com on 23.06.15, 25 g of 1-phenylethanol is £24.60 and 1.012 grams of (S)-(—)-1-phenylethanol is £110.5.

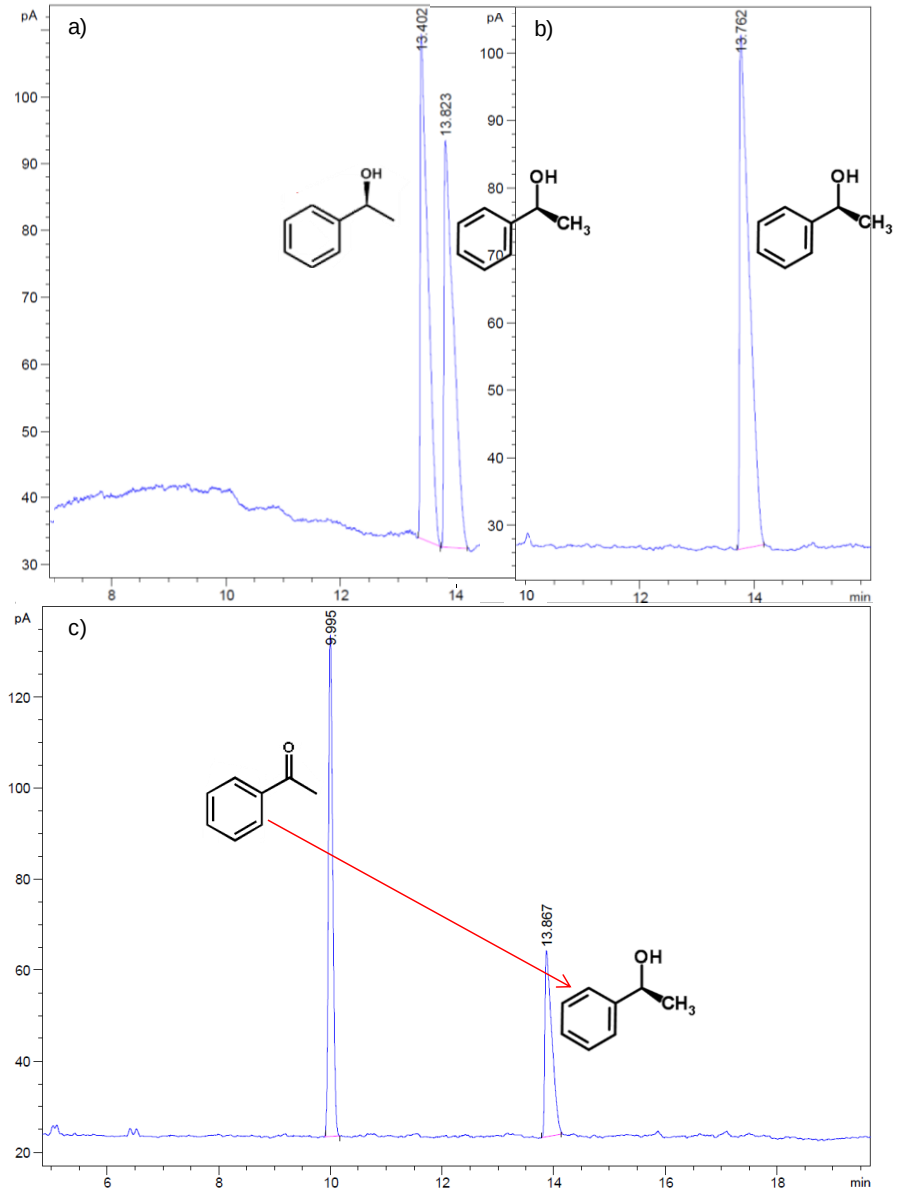


Figure 61: Gas chromatography results for acetophenone reduction to (S)-1-phenylethanol. Traces for a) racemic 1-phenylethanol (both S and R enantiomers), b) (S)-1-phenylethanol and c) overnight acetophenone reduction with acetophenone and (S)-1-phenylethanol peaks.

3.3.3.3 Reductive amination on CNCs

Initially, it was shown that the flow system with the CNCs is suitable for H_2-driven NADH generation (co-immobilising Hyd-2 and I64A on the CNCs). Then, an NADH dependant enzyme (alcohol dehydrogenase) was co-immobilised with Hyd-2 and I64A for further biotransformations requiring the cofactor, NAD^+/H. It was shown that the CNC-enzyme flow assemblies are suitable to be used for H_2-driven ketone reduction. To show that this H_2-driven biotransformation system with NAD/H recycling is applicable for a range of

NADH-dependant enzymes, a different NADH dependent enzyme was co-immobilised with Hyd-2 and I64A. A reductive amination biotransformation was studied using L-alanine dehydrogenase (LalaDH) as the NADH dependent enzyme and pyruvate (α-keto acid) as the reactant to produce L-alanine (α-amino acid).

For the reductive amination (**Figure 62**) (production of L-alanine), Hyd-2, I64A, and LalaDH were co-immobilised on the CNCs and a H_2 saturated reaction mixture containing NAD^+, sodium pyruvate and ammonium chloride (the ammonia source) in buffer was cycled through the CNCs (**Figure 63**). According to a similar reaction mechanism proposed for amino acid dehydrogenases by Ohshima and Soda, initially amination takes places with an α-keto acid and NH_3 where an imine is the main product and water is the by-product. Then, imine is reduced with a hydride from NADH.[253]

$$C_3H_3NaO_{3(aq)} + NH_4Cl_{(aq)} + 2H^+_{(aq)} \rightarrow C_3H_7NO_{2(l)} + H_2O_{(l)} + Na^+_{(aq)} + Cl^-_{(aq)}$$

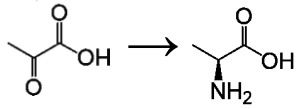


Figure 62: Reaction mechanism showing pyruvate to L-alanine conversion. In the experiments sodium pyruvate was used instead of pyruvic acid and ammonium chloride was used instead of ammonia.

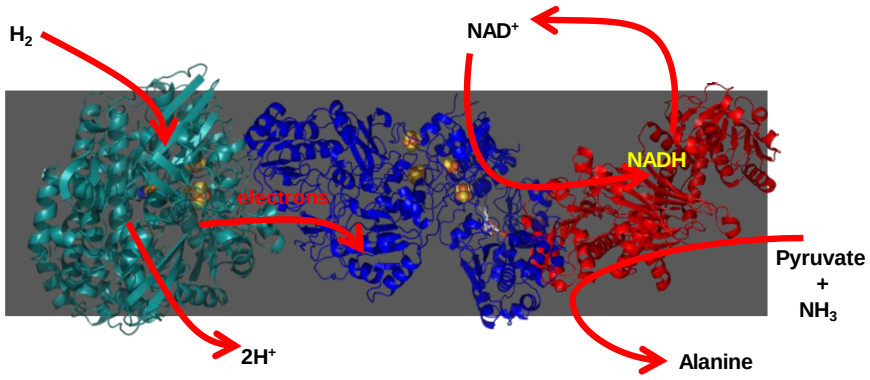


Figure 63: A schematic representation of the H_2-driven pyruvate reduction mechanism on CNCs.

HPLC traces in **Figure 64** show L-alanine production overnight. The peak around 7.2 minutes is the pyruvate peak and the peak around 12.5 minutes is the L-alanine peak. According to the standard HPLC traces for pyruvate and L-alanine, the overnight conversion is 89.9 %. In **Figure 64 b** the L-alanine peak is small compared to the pyruvate peak, making it difficult to understand the extent of the conversion without assessing the

standard spectra. However, the L-alanine peak high is smaller compared to the pyruvate peak height at the same concentration, according to the standard solutions. According to the time points taken, the immobilised enzymes were active in flow catalysis after > 21 hours.

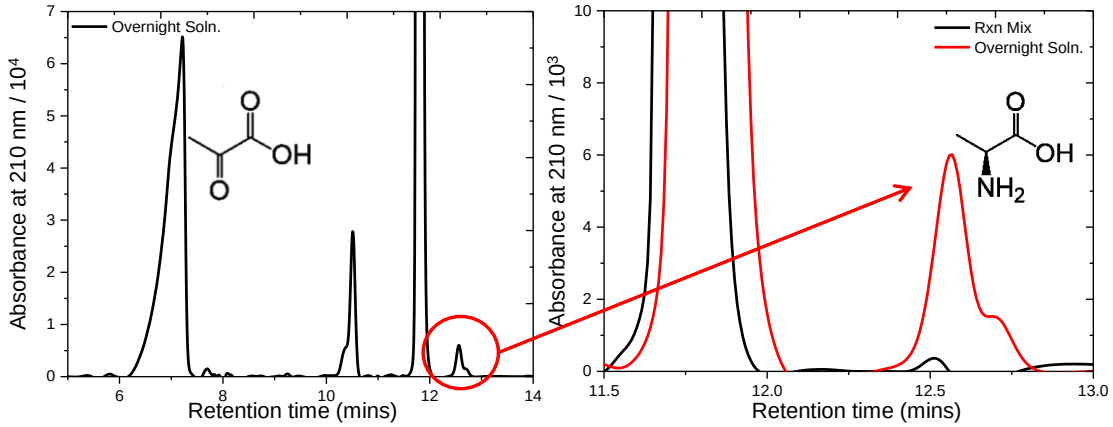


Figure 64: HPCL chromatograms for overnight pyruvate amination in flow in CNCs. a) the HPLC curves for the overnight reaction mixture. The peak around 7.2 minutes is the pyruvate peak and the peak around 12.5 minutes it the L-alanine peak. b) the HPLC traces for the starting reaction mixture (black) and the overnight reaction mixture (red). The traces show an increase in the peak around 12.4 minutes i.e. show overnight L-alanine production.

3.4 Conclusion

This Chapter focuses on H_2-driven biocatalytic transformations in flow. Following some of the main areas in catalysis research in the last decade such as using enzymes as catalyst, cofactor recycling and continuous processing, enzymes were used to catalyse hydrogenation reactions (ketone reduction and reductive amination) in flow.

Various carbon support materials were investigated in ***Chapter 2*** for H_2-driven NADH generation. In this Chapter, novel carbon nanotube columns (CNCs) are used as enzyme support materials. Following a similar method to batch H_2-driven NADH generation on carbon materials in ***Chapter 2***, initially continuous H_2-driven NADH generation in CNCs was investigated. Hydrogenase (Hyd-2) and NAD^+ reductase (I64A) were co-immobilised on CNCs and the reaction mixture was cycled in the CNC flow system with H_2 supplied to the headspace at atmospheric pressure. NADH generation in flow was successful. Thus, the enzymes were successfully immobilised on CNCs and they were in electronic contact. Co-immobilising an NADH-dependent enzymes with Hyd-2 and I64A creates a modular biotransformation platform. Thus, alcohol dehydrogenase (ADH) and L-alanine dehydrogenase (LalaDH) were used as NADH-dependent enzymes for ketone reduction and reductive amination, respectively. The conversion was 11.4 % for the ketone reduction and 89.9 % for the reductive amination. Gas chromatography results showed that the product for ketone reduction was *S*-(1)-phenylethanol with enantiomeric excess > 99.9 %.

This Chapter presents the first demonstration of H_2-driven biocatalytic hydrogenation reactions (ketone reduction and reductive amination) in flow. Electronically conductive and robust carbon assemblies, CNCs, were used for the first time as enzyme support materials. The cofactor (NAD(H)) recycling/regenerating issue was addressed. High conversion (89.9 %) was achieved in the reductive amination reaction. 99.9 % chiral product was produced in the ketone reduction reaction. It was shown that the selectivity of the enzyme was not affected due to the immobilisation, which can be a problem in catalyst

immobilisation. Overall, the ketone reduction was 100 % atom efficient and, both of the processes neither required sacrificial substrates nor generated waste.

CHAPTER 4. HYDROGEN EVOLUTION REACTION WITH NOVEL CHALCOGENIDE ASSEMBLIES AS CATALYSTS

This Chapter focuses on developing novel WS_2 assemblies as hydrogen evolution reaction (HER) catalysts. Hydrogen is an energy vector, which has gained a lot of attention due to the increasing energy demand, sustainability and climate change. One of the important steps in environmentally friendly and high purity hydrogen production is HER. Up to date, precious metals, especially platinum, have been used as the most active and efficient catalysts with very low overpotentials for HER. In the last decade, however, low-cost, earth-abundant, non-precious metal catalysts have been studied to catalyse HER. The general challenges in these studies are lowering the overpotential, increasing the stability of the catalyst, developing assemblies and devices with desired structures for the applications and, scaling up the synthesis of these materials.

Transition metal dichalcogenide (TMDC, especially MoS_2 and WS_2) nanostructures have been shown to catalyse HER. In this Chapter, novel WS_2 assemblies are studied and preliminary results are presented for their applications in HER catalysis. WS_2 nanoflakes and nanoflowers were successfully grown on MWCNT carpets and CNCs. Preliminary electrochemical studies showed that these novel assemblies catalyse HER.

4.1 Introduction

This introduction briefly focuses on the challenges in HER catalysis and describes the novel TMDCs developed as catalysts for HER. Initially, the current trends and needs in HER and basics of HER are briefly described. Then, the increasing interest in TMDCs and how and why MX_2s have been extensively studied as catalysts for HER are explained.

4.1.1 Alternative inorganic catalysts for HER catalysis

One of the environmentally-friendly and desired methods for hydrogen production is water splitting. Hydrogen evolution reaction (HER) is the main reaction in water splitting process. It is also the main reaction in hydrogen-based fuel cells. Usually Pt-based materials are used as HER catalysts. These materials are highly electroactive and provide very low overpotentials and high reaction yields. The problems with the established HER methods are that they use precious metal catalysts, which have very high cost and are not abundant. One of the main focus in HER research is developing earth-abundant, inexpensive and efficient catalysts for viable hydrogen production.

HER can occur following two different mechanisms, using either Volmer-Heyrowsky or Volmer-Tafel mechanism (**Table** 4-1).[254] In both of the mechanisms, hydrogen atoms are adsorbed onto electrode surface. The rate of the reaction is affected by the free energy of hydrogen adsorption. Thus, the surface properties of the catalysts are very important. The binding of hydrogen should be neither too strong nor too weak.

Table 4-1 Three possible reaction steps for HER

1	Volmer step	$H^+ + e^- \rightarrow H_{ad}$
2	Heyrovsky step	$H^+ + H_{ad} \rightarrow H_2$
3	Tafel step	$2H_{ad} \rightarrow H_2$

In the last decade, transition metal dichalcogenides have gained attention as earth-abundant and inexpensive catalysts for HER. These materials have a similar layered structure to graphite. After the discovery of graphene, 2D materials have gained attention and inorganic graphene analogues (2D) were synthesised from these transition metal dichalcogenides.[179] These transition metals in bulk have varying properties *e.g.* MoS_2 and WS_2 are semiconductors and $NbSe_2$ and TaS_2 exhibit low temperature phenomena such as superconductivity.[255] Although, these materials in bulk limit the possibility of developing different morphologies and tailoring the chemical and physical properties of these materials, the 2D heterostructures can play an important role in these applications such as

electronic, optoelectronic, catalysis, electrochemical and sensing.[254,256–258] For catalysis applications hierarchical nanostructures are reported to offer large surface area, mechanical integrity and allow easy access to reaction sites.[259] Thus, recently, MoS_2 and WS_2 assemblies have been investigated for HER applications.[254] Although MoS_2 has been studied widely, other MX_2 materials such as WS_2 has not been studied extensively.

4.1.2 Recent advancements in developing MX_2s as HER catalysts

The identification of the active sites in MoS_2 speeded-up the research on using MX_2 as catalysts. The research of Hinneman and co-workers, influenced by the catalytic properties of nitrogenases and hydrogenases, showed that MoS_2 nanoparticles supported on graphite are promising catalysts for HER with an overpotential around 0.1 V – 0.2 V.[47] In 2007, Jaramillo *et al.*[260] showed that MoS_2 edge sites are active catalysts for HER. Since then, MoS_2 have been widely studied to decrease the overpotential of these materials in HER, increase the catalytic activity, develop different size and shape structures for HER relevant devices and overcome the low conductivity of these materials. Other than the properties that affect the rate and efficiency of the catalysis, scaling up the catalyst synthesis is one of the aspects that has been studied. Up to day, these materials have been produced only in small scale. Monolayer MoS_2 materials as HER catalysts are usually prepared either by exfoliation (physical ("scotch-tape" method) or chemical (using solvents and/or surfactants)) or by substrate-growth or by colloidal synthesis.[261] One of the studies contributing on large-scale synthesis of MoS_2 catalysts is using organolithium compounds to intercalate and exfoliate MoS_2.[262] A study on improving the catalytic properties of MoS_2 is on growing MoS_2 on Au foil to benefit from the good electron coupling between these two materials.[263] In another study, theoretical calculations showed that doping some transition metals such as Fe, Ni, and Co increase the catalytic activity of MoS_2.[264] Another approach in increasing the electrochemical activity, stability and decreasing the overpotential is combining MX_2 materials with reduced graphene oxide paper.[50,265] In a study, a solvothermal method was used to synthesize MoS_2 nanoflowers on reduced

graphene oxide (rGO) paper and the catalysts showed good stability (over 300 cycles) with negligible current loss.[265] A hydrothermal synthesis method was used to fabricate WS_2/rGO by Shin *et al.* [50] for rapid electron transfer from the electrode to WS_2.

4.2 Experimental Methods and Analysis Techniques

4.2.1 Experimental Methods

4.2.1.1 Materials

The chemicals used in WS_2 synthesis are tungsten (VI) chloride (WCl_6) (Sigma-Aldrich, ≥ 99.9 %) and colloidal sulphur (S) (Sigma-Aldrich, 80 %). Acetone (Fisher Scientific, > 99 %) was used for the cleaning of the quartz reaction tube, alumina boats and silicon substrates (Silicon wafer, IC Prime Grade, thickness: 625 ± 25 µm, Orientation: (100)). Acetone was also used in the bubbler. Silicon substrates, MWCNT carpets and CNCs (***Section 3.2.1.2***) were used as substrates.

4.2.1.2 Growth of WS_2 2D-3D nanostructures

All tungsten-disulphide (WS_2) nanomaterials were synthesised by chemical vapour deposition (CVD) method, following the experimental steps in the literature.[258] In all WS_2 syntheses, an assembly of a quartz tube (Robson Scientific; 800 mm long, 21 mm inner diameter, 1.5 mm thick with B19/26 socket and cone connections), a horizontal tube furnace (Instron SSL furnace, 310 mm, Severn Science Limited) with Eurotherm 2216e temperature controller (ICL-167) and an acetone bubbler (**Figure 65**) were used in a N_2 (BOC, > 99.998 %) atmosphere enclosure. Prior to the syntheses, the temperature profile of the furnace was measured using a K-type (Chromel/Alumel) thermocouple at 800 °C under 0.1 L min^{-1} (Brooks mass flow controller) argon (BOC, 99.999 %) flow (**Figure A 11**). All of the WS_2 syntheses were conducted at 800 °C under 0.1 L min^{-1} Ar flow. 20 mmol sulphur and 2 mmol WCl_6 were placed in alumina boats as precursors. The precursors, S and WCl_6 were placed at 135 mm and 185 mm from one of the quartz tube (beginning of

the quartz tube), respectively. The length of the quartz reaction tube coming out of the horizontal tube furnace was kept constant at 70 mm. Silicon substrates, MWCNT carpets and CNCs were placed in the quartz reaction tube as substrates. The positions of the substrates were altered between 235 mm to 325 mm from the beginning of the quartz tube. The heating started with the quartz reaction tube in place. The duration of the reaction was either 5 or 10 or 20 minutes, after the furnace reached 800 °C. The quartz reaction tube was left inside the furnace, still under 0.1 L min^{-1} Ar flow, during the cooling down.

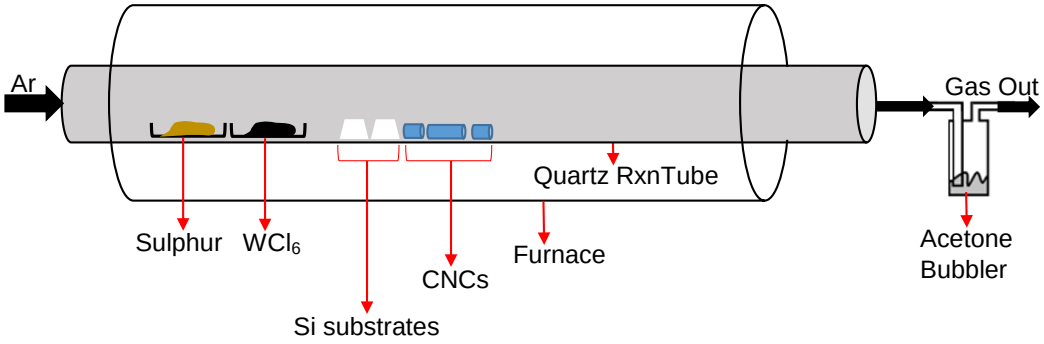


Figure 65: A schematic representation the CVD set-up for WS_2 nanoflower synthesis.

4.2.2 Analysis Techniques

4.2.2.1 Characterisation techniques used for WS_2 assemblies

The morphology of the WS_2 structures were investigated with scanning electron microscopy (SEM). A JEOL 840F microscope was used and the secondary electron detector was operated at 5 kV to obtain the SEM images. The Raman spectroscopy was carried out on a JY Horiba Labram Aramis imaging confocal Raman microscope with a 532 nm green laser using as grown samples. Energy dispersive X-ray spectroscopy (EDX) was performed to identify and determine the atomic proportions of the elements present in the materials. EDX mapping was obtained using Zeiss Merlin EDX SEM. Powder X-ray diffraction analysis was carried out on a Siemens D5000 X-ray powder diffractometer. The range of 2θ used was 10°- 80° with a step size of 0.0195°.

4.2.2.2 Electrochemical methods

All of the WS_2 catalysts were tested in an electrochemical cell filled with 0.5 M deaerated H_2SO_4 electrolyte. The cell was kept at 25 °C *via* a water jacket. A three-electrode set-up was used. The WS_2 catalyst assemblies were used as the working electrode (WE). Pt mesh was used as the counter electrode (CE) and a saturated calomel electrode (E(RHE) = E(SCE) + 0.2412 V)) was used as the reference electrode (RE). Linear sweep voltammetry and cyclic voltammetry were recorded using Autolab PGstat128N potentiostat with ECD module running on GPES software, EcoChemie, The Netherlands. The voltammetry measurements were run at a scan rate of 5 mV s^{-1}.

4.3 Results and Discussion

4.3.1 Characterisation of WS_2 assemblies

4.3.1.1 Scanning electron microscopy of WS_2 assemblies

Morphology of WS_2 structures were investigated using SEM. The SEM images obtained for WS_2 structures (**Figure 66-69**) follow the literature structures of WS_2 flakes and nanoflowers.[258] The SEM images in **Figure 66** show that the growth of WS_2 nanostructures are affected by the duration of the experiment, more flower-like structures are observed on Si substrates as the duration of the experiment increases from 5 to 20 minutes. The growth of the structures are also affected by the position of the substrate. The SEM images in **Figure 67** show that denser flower-like structures occur as the position of the substrates change from 235 mm (**Figure 67 a**) to 255 mm (**Figure 67 b**) and to 275 mm (**Figure 67 c**) within the furnace.

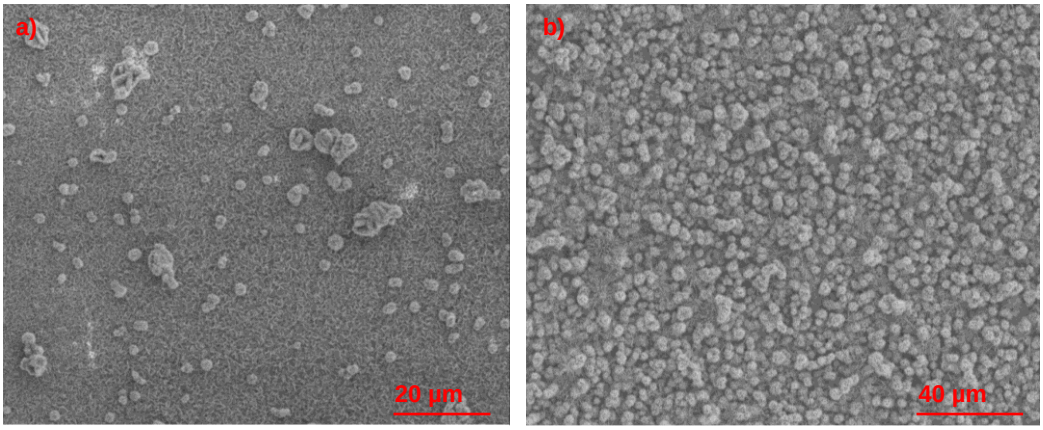


Figure 66: Scanning electron micrographs of WS_2 nanoflakes and nanoflowers grown on Si substrates showing effect of experiment duration on the growth. a) 5-minute long experiment, substrate 5, b) 20-minute long experiment, substrate 5.

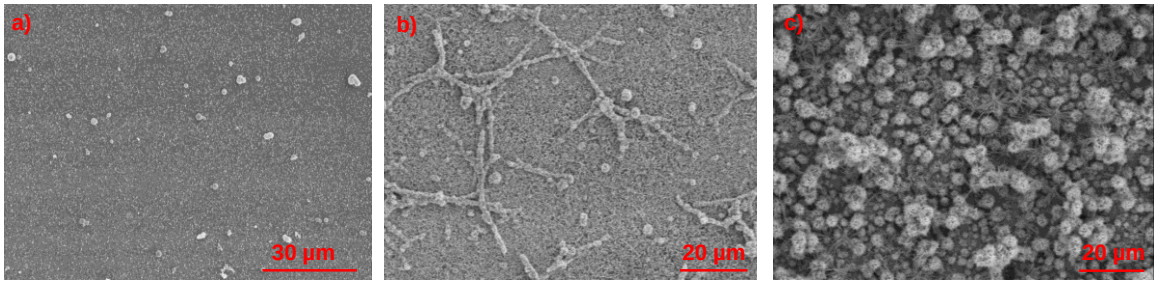


Figure 67: Scanning electron micrographs of WS2 nanoflakes and nanoflowers grown on Si substrates in a 20-minute long experiment showing the effect of substrate position on the growth. a) substrate 1 at 235 mm, b) substrate 3 at 255 mm, and c) substrate 5 at 255 mm.

The direct growth of WS_2 structures on carbon nanotubes were first investigated by growing them on MWCNT carpets. The SEM images in **Figure 68** show that the carpets look like as there is another materials deposited on them. As the magnification is increased from **Figure 68 a** to **Figure 68 d** WS_2 flakes and nanoflowers can be seen on carbon nanotubes. These images suggest that the direct growth of WS_2 nanoflakes and nanoflowers on carbon nanotube carpets was successful.

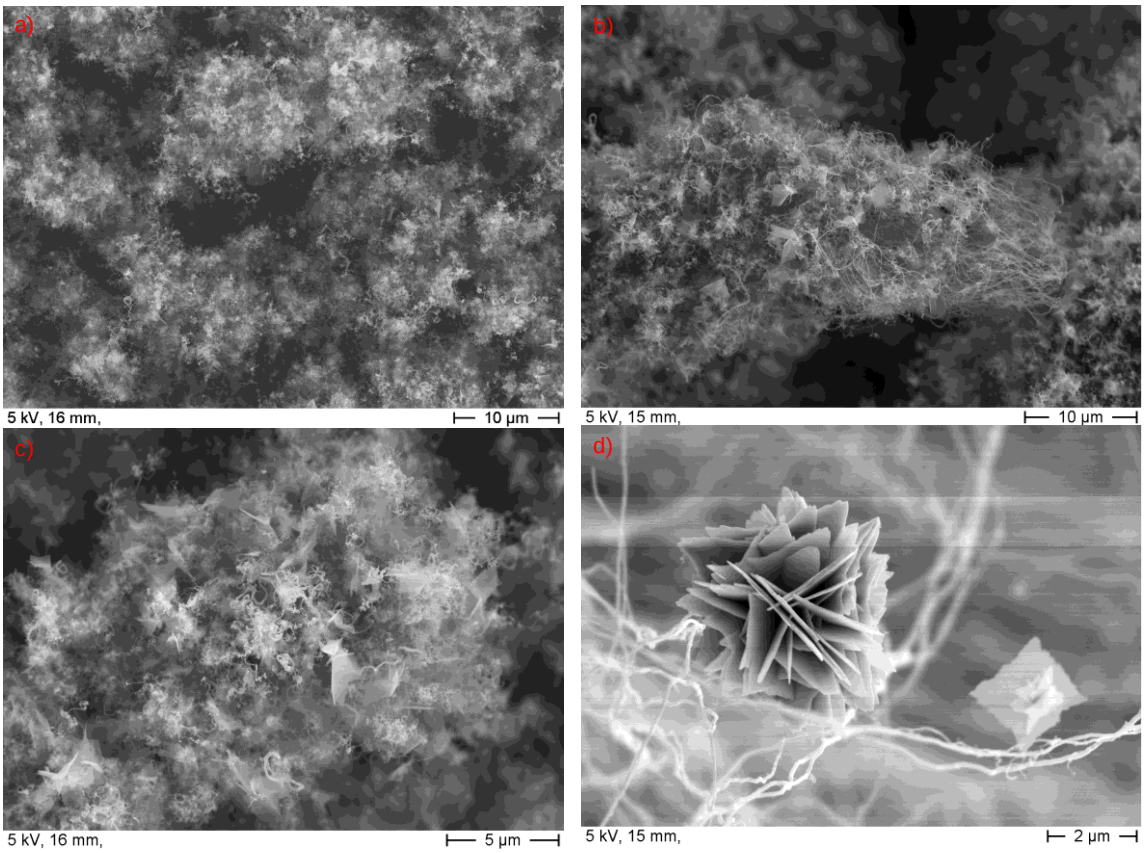


Figure 68: Scanning electron micrographs of WS_2 nanoflakes and nanoflowers grown on MWCNT carpets in a 20 minute long experiment.

Finally, WS_2 were grown on CNCs to obtain novel WS_2-MWCNT assemblies. **Figure 69** shows WS_2 nanoflakes, nanoflowers grown on MWCNTs. **Figure 69 d** belongs to the end of the CNC not facing the flow and faceted cubic crystals were observed as well as nanoflakes. These structures were further investigated with EDX and XRD to detect their elemental composition. SEM images in **Figure 70** also belong to WS_2s grown on CNCs. Images a1, b1 and c1 are regular SEM images whereas images a2, b2, and c2 are the same images taken with Z-contrast to see the elemental composition differences. Particularly, **Figure 70 a1** and **a2** show that the unusual appearance of the carbon carpet is due to a heavier material on carbon surface. It can be seen that there are many small flakes integrated in the MWCNT network. WS_2 nanoflowers have radii ranging from 2 µm to 6 µm when grown on Si substrate. However, nanoflowers grown on MWCNTs of CNCs have smaller radii. The nanoflowers in CNCs –the ones not sticking out of the tube, *i.e.* the

ones towards the inside of the tube, imaged when the sample was tilted inside the microscope- have radii ranging from 400 nm to 3 μm.

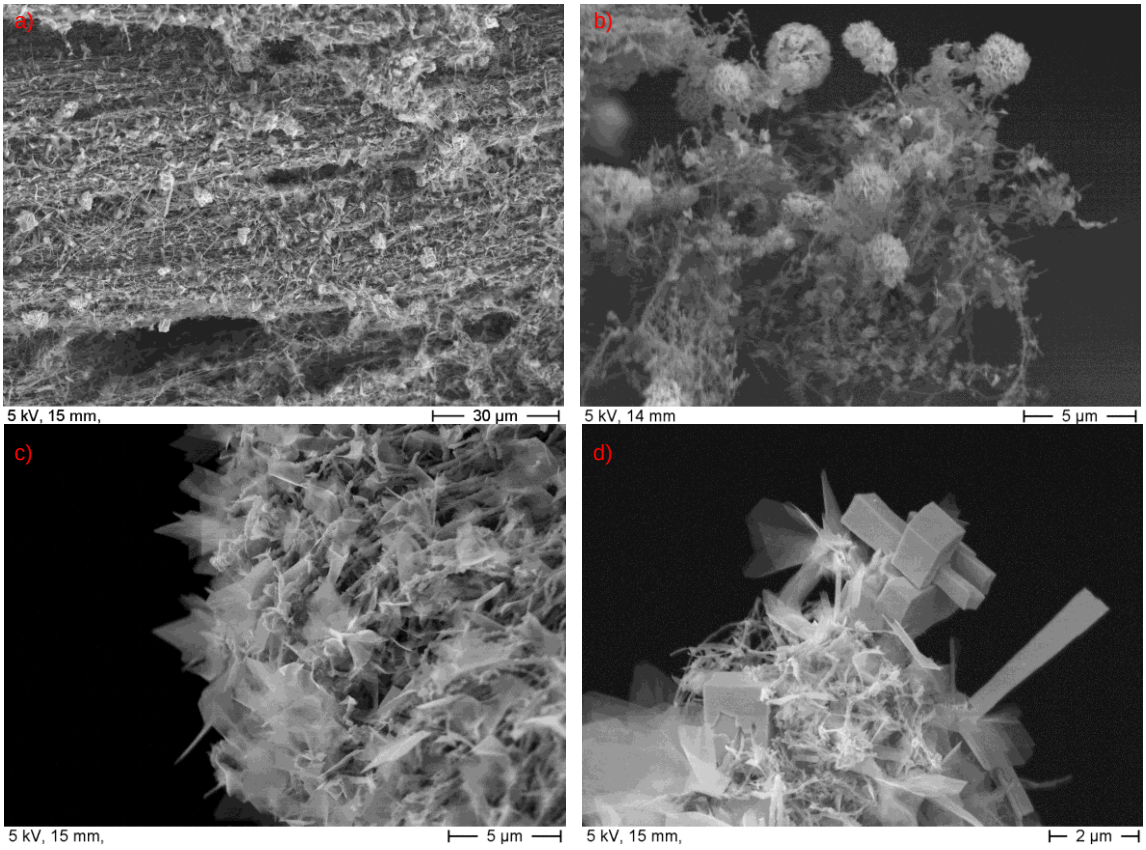


Figure 69: Scanning electron micrographs of WS_2 nanoflakes and nanoflowers grown on CNCs in 20 minute long experiments.

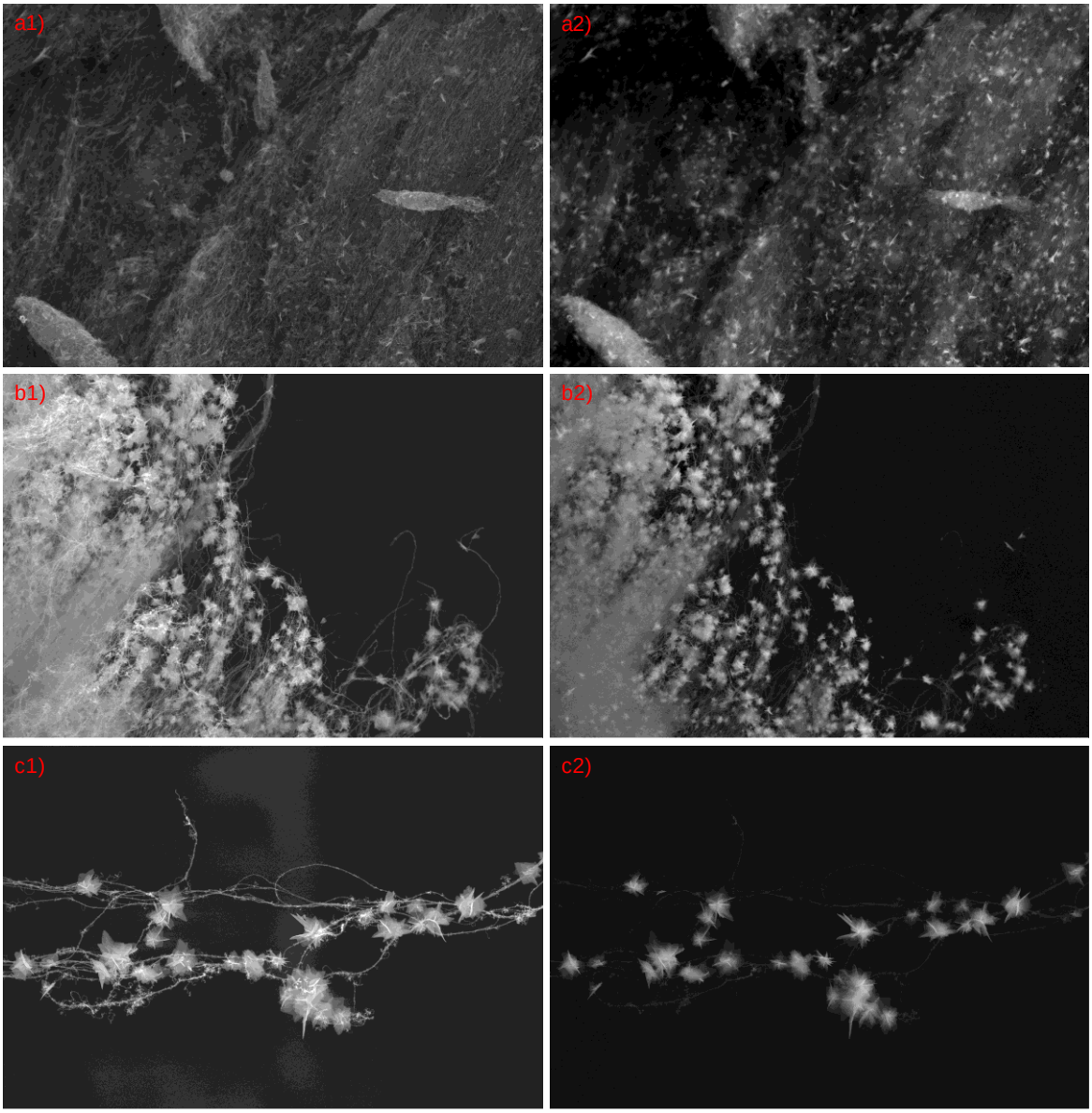


Figure 70: Scanning electron micrographs of WS_2 structures grown on CNCs. The images a2, b2, and c2 are the Z-contrast images of a1, b1, and c1, respectively. The heavier atoms on MWCNTs are brighter in the images a2, b2, and c2.

4.3.1.2 Raman spectroscopy of the WS_2 assemblies

Bulk WS_2 belongs to the symmetry space group $P6_3/mmc$ and point group D_{6h}. Odd and even layered WS_2 belong to $P6m2$ (D_{3h}) and $P3m1$ (D_{3d}) space groups, respectively. Both of the systems have two characteristic Raman active modes. These are $E_2{}^1{}_g$ and A_{1g} (E´-A´$_1$ and E_g-A_{1g} for odd and even layered materials, respectively.[266] $E_2{}^1{}_g$ first-order mode is at 356 cm^{-1} and A_{1g} first-order mode is at 418 cm^{-1}.[267] The Raman spectroscopy in **Figure 71** shows the characteristic Raman modes for WS_2 with second order modes. For 532 nm

laser-excitation, the second order peak, 2LA(M) mode at 352 cm^{-1} is observed the strongest.[267]

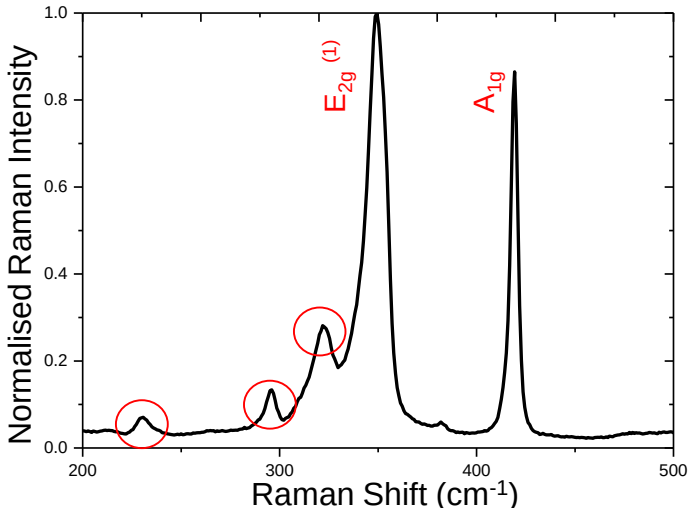


Figure 71: Raman spectroscopy of WS_2 nanoflowers grown on Si substrate showing characteristic first order and second order peaks of WS_2.

4.3.1.3 Energy-dispersive X-ray spectroscopy of WS_2 assemblies

The different morphologies observed in SEM images, such as different shaped nanoflakes, nanoflowers, thin films, and prisms were further investigated with EDX to determine the composition of the elements in these structures. The morphologies of the deposits and their elemental structure are in SEM images and EDX spectra (obtained with the assistance of Dr Vitaliy Babenko, Grobert Group, University of Oxford) in **Figure 72-Figure 74**. The EDX results of these structures have C, Fe and Si as well as W, S, and O, which are the predicted elements in the nanoflowers, nanoflakes, and prisms. The C and Fe peaks in EDX spectra are due to the strong signal coming from the MWCNTs and the Si peak is due to the substrate from the regions where the MWCNT and WS_2 deposition are thin.

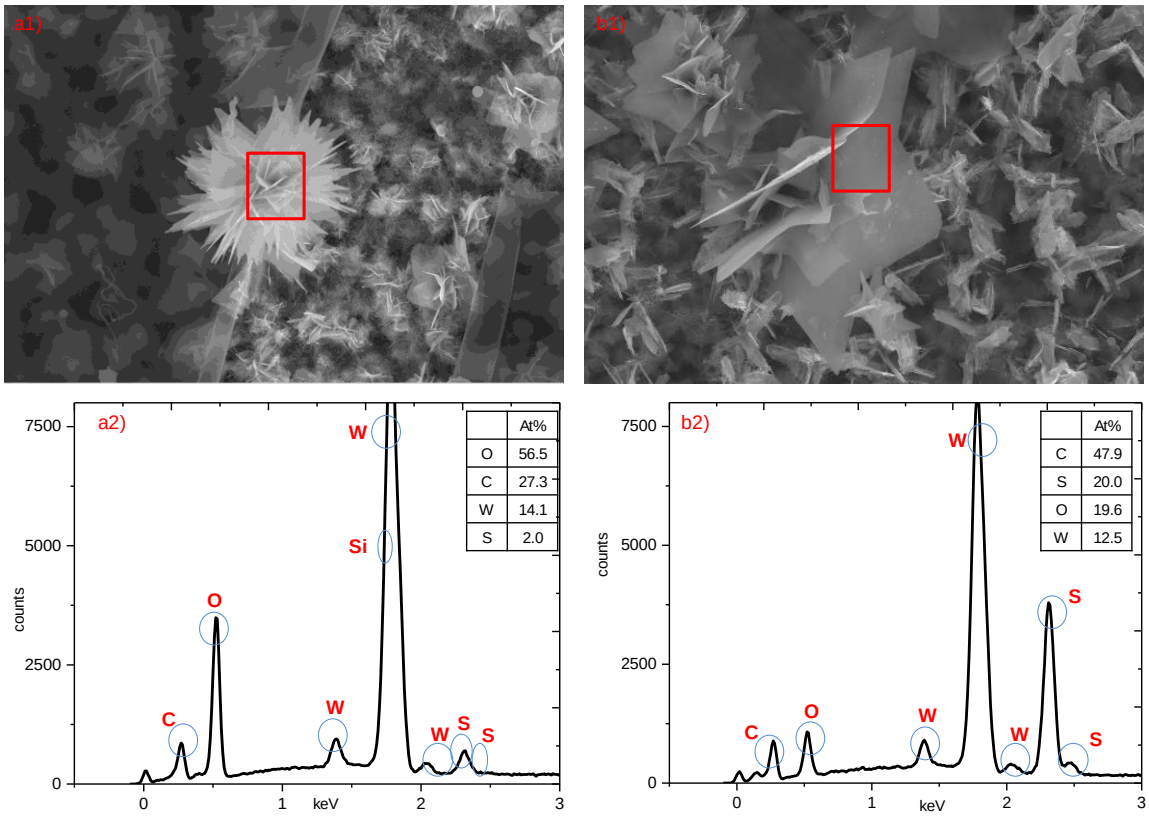


Figure 72: Scanning electron micrographs and EDX spectra of different nanoflower morphologies on a carbon nanotube carpet.

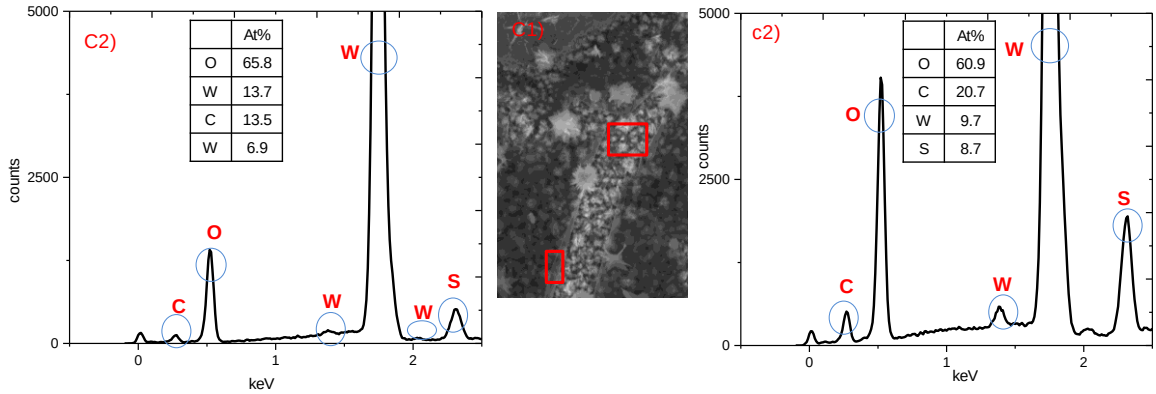


Figure 73: Scanning micrograph and EDX spectra of nanoflowers and thin film on a carbon nanotube carpet.

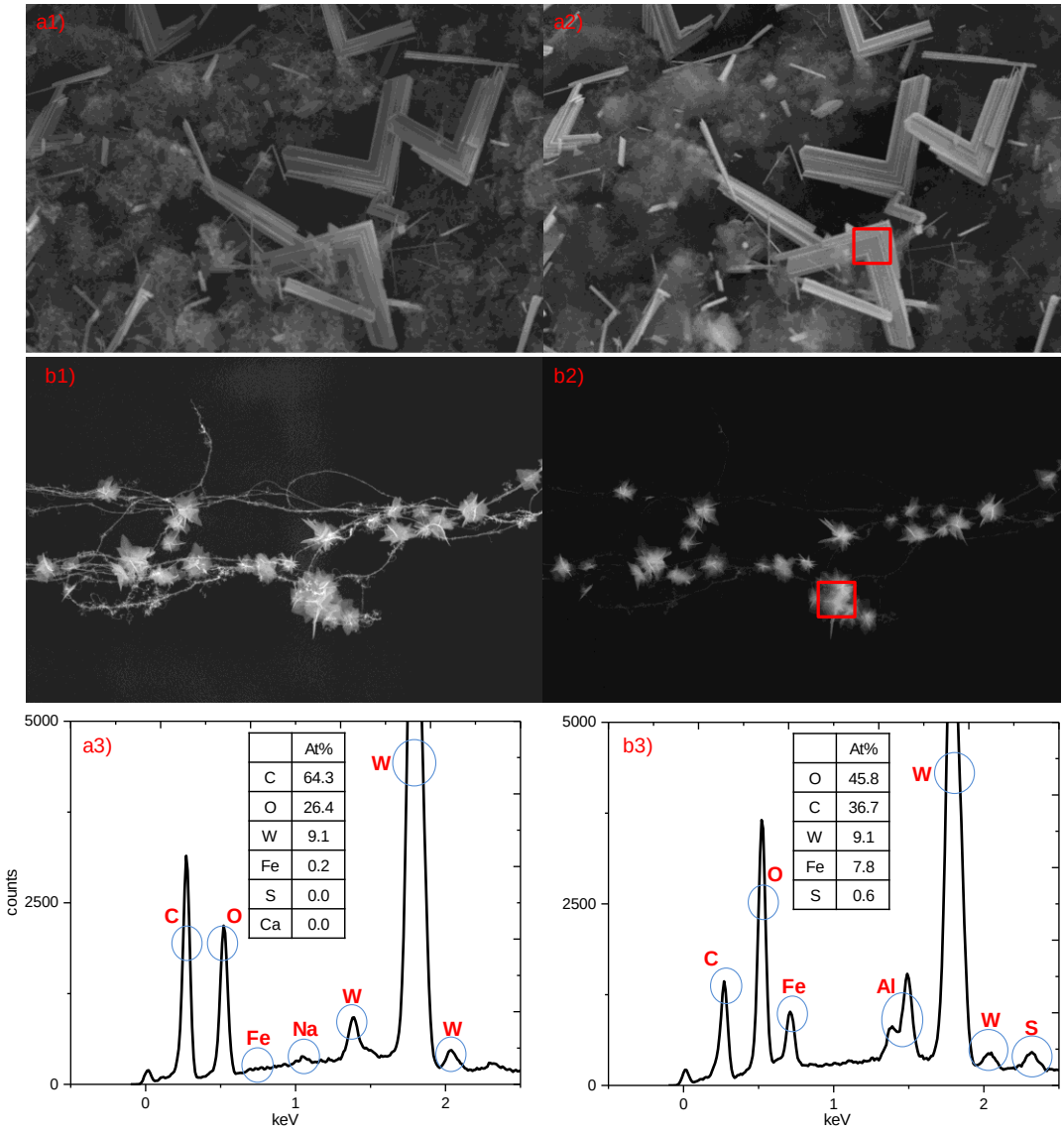


Figure 74: Scanning electron micrographs and EDX spectra of prisms and nanoflowers grown on a carbon nanotube carpet.

4.3.1.4 X-Ray diffraction analysis of WS_2 assemblies

XRD analysis was used for phase identification. The nanoflowers and nanoflakes observed in SEM follow the literature morphology of WS_2 nanoflowers and nanoflakes. However, there are different shaped nanoflowers and prism. EDX analysis showed that the structures are not containing only W and S but O as well. The XRD analysis showed that the deposit on MWCNTs consists of WS_2, $FeWO_4$ and WO_3 (**Figure 75**). Combining the EDX and XRD data, it can be concluded that “regular” nanoflowers and nanoflakes are WS_2 structures, spiky nanoflowers, thin films, and corner-shaped prisms are WO_3 structures and, cubic prisms are $FeWO_4$ structures.

The syntheses were conducted under Ar atmosphere in a N_2 enclosure. However, reactant preparations were done in ambient conditions. The reactant WCl_6 is a very air-sensitive compound and oxidises fast. Most of the oxidised in the product either should be coming from the oxidation of WCl_6 during the preparation or from already oxidised WCl_6 from the bulk material. The oxide groups from impurities on CNTs can also play a role in the formation of WO_3. $FeWO_x$ materials are synthesised using FeO and WO_3 on Pt or Pd in the literature.[268,269] $FeWO_4$ has potential applications in photocatalysis, photoluminescence, magnetism and battery applications.[268,270]

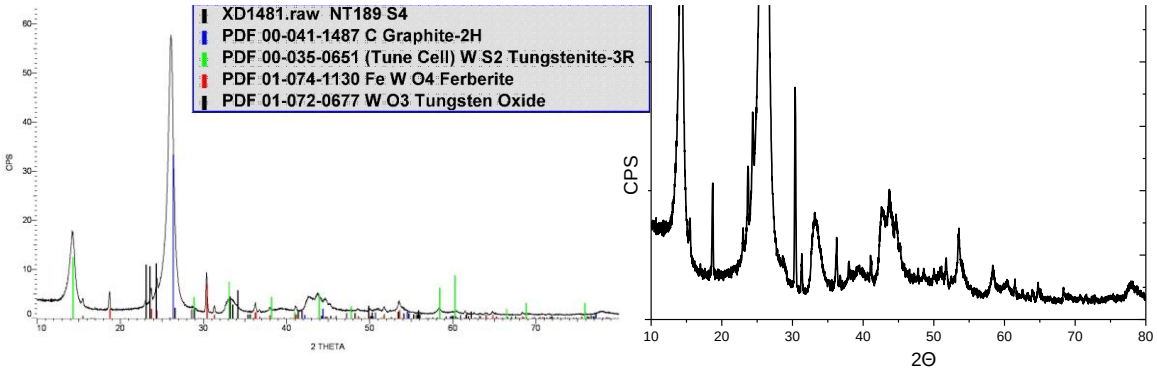


Figure 75: XRD analysis of grounded product (WS_2) on CNT carpets showing characteristic peaks of crystalline WS_2 phase and other side products WO_3 and $FeWO_4$. XRD analyses was carried out by Dr Philip Holdway, Oxford Materials Characterisation Service.

4.3.2 Electrochemical studies on WS_2 assemblies

One of the limitations of WS_2 catalysts for HER is their low conductivity. One of the approaches to overcome this problem, increase the contact between WS_2 nanostructures and lower the overpotential is integrating carbon materials with WS_2 nanostructures. Shin *et al.*[50] synthesised WS_2/rGO nanosheets by hydrothermal reaction of WCl_6 in graphene oxide solution to improve the WS_2 catalyst efficiency in HER. Another study on bringing carbon and WS_2 structures together for HER catalysis is on synthesising WS_2 wrapped carbon nanofibers using S and $(NH_4)_2WS_4$ contained electrospun polyacrylonitrile nanofibers as precursors.[180] There are several studies in literature, which does not directly focus on using WS_2 in HER but investigate its electronical and mechanical properties. These studies include making SWCNT/WS_2-NT and MWCNT/WS_2-NP hybrid films by

filtering suspensions of these materials[271] and making MWCNT hybrids with WS_2 nanoparticles by mixing and refluxing a $H_3PW_{12}O_{40}$ and MWCNT mixture.[272] In this Chapter, a simple direct CVD growth of WS_2 nanoflowers on MWCNT carpet substrates is investigated for the first time. WS_2 were grown on MWCNT carpets and CNCs to have increased contact between nanoflakes and nanoflowers, increase the catalyst performance and have assemblies that can be directly used in flow applications, which will be further discussed in ***Section 5.2.2***.

The catalytic performance of WS_2 grown on MWCNTs were studied by polarisation curves and Tafel plots (**Figure 76** and **Figure 77**). Platinum is the most commonly used catalyst for HER with near zero overpotential. Thus, a platinum wire (Superpure Chemetals, 99.95 %, 0.4 mm diameter) was used as the catalyst under the same conditions for comparison. From **Figure 76 a**, the overpotential for WS_2 decorated MWCNT was calculated as 220 mV with a Tafel slop 174 mV dec^{-1}. The most promising studies on using WS_2 nanostructures for HER catalysis have overpotential between 150 mV – 200 mV.[50,273] Tafel plots are also tools to study the electrochemical kinetics of electrode materials. Tafel slops are used to calculate the additional voltage needed to increase the catalytic current by an order of magnitude.[254] Other than overpotential, the Tafel slope would also show whether a catalyst is suitable for the desired application. Two catalysts with the same overpotential can perform differently in the same application. The Tafel slope can show whether the catalyst performs better in low current devices or in high current devices *i.e.* for applications such as water electrolysis, materials with low Tafel slope are desireable.[254] Platinum, the best catalyst for HER, has a very small Tafel slope, 30 mV dec^{-1}.[274] Thus, WS_2 assemblies with Tafel slops close to that of platinum is preferred.

Cyclic voltammograms for WS_2 on MWCNT carpets show that the currents both for the carpet and the assembly are increasing overtime (**Figure 76 b**). The current produced by the plain MWCNT carpets suggest that excess Fe in MWCNT carpets can be catalysing HER as well. The increase in the current over time can be due to the carpets absorbing electrolyte solution overtime reaching both to more WS_2 nanoflakes and more Fe. The

effect was also observed when thicker MWCNT carpets (synthesised at 850 °C in 20 minutes) are compared with the thinner carpets (synthesised at 800 °C in 15 minutes).

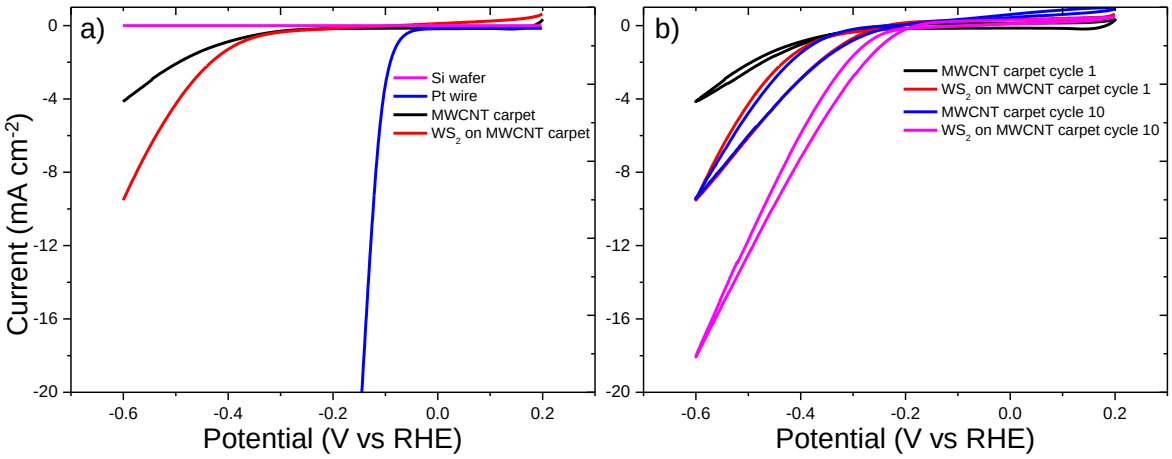


Figure 76: a) Polarisation performance curves b) cyclic voltammograms for plain and WS_2 decorated MWCNT carpets for the first and tenth cycles.

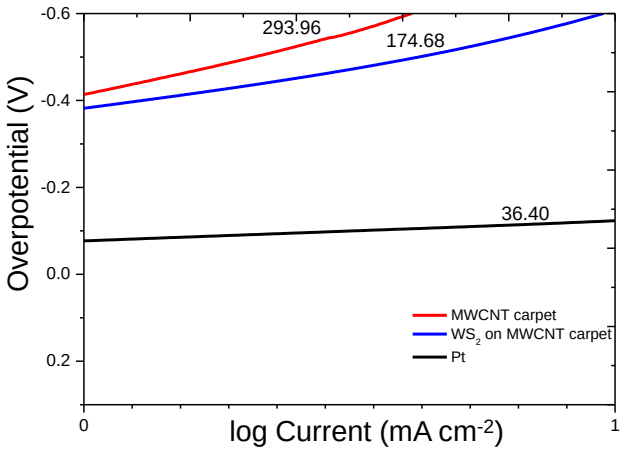


Figure 77: Tafel curves for Pt, MWCNT carpets, and WS_2 on MWCNT carpets.

4.4 Conclusion

One of the clean, sustainable and high quality hydrogen production methods is HER. Up to day, platinum is the most effective catalyst for HER with very low overpotential (near zero) and low Tafel slope (30 mV dec^{-1}). However, platinum is very expensive and not earth-abundant. One of the areas of research in improving the efficiency of HER is developing novel catalysts/catalyst assemblies. Catalysts with low cost, high activity and stability and low overpotential are desired for HER applications.

WS_2 nanostructures are one of the catalysts studied for this. In this study, WS_2 were directly grown on MWCNTs (carpets and CNCs) by a simple CVD method to increase the stability and the electronical contact between the nanoflowers and the electrode set-up. The growth of WS_2s on MWCNTs was successful and the materials were analysed by using SEM, Raman, EDX, and XRD. The results confirm and follow the characteristics of WS_2 in literature. One of the aims behind creating WS_2 nanostructures on carbon based substrates was to create assemblies that can be directly used in flow applications.

Preliminary electrochemical studies showed that WS_2 assemblies catalyse HER with overpotentials and Tafel slops close to the studies in the literature. Although the results do not show an improvement in electrochemical properties of WS_2, these assemblies, which offer stability, intimate electronical contact and implementation of flow configurations can be further improved. Optimising the reaction conditions for increasing the density of WS_2 nanoflakes on thinner MWCNT carpets can be one of the approaches to obtain better electrochemical properties for these assemblies to be used in HER applications. However comparing catalyst assemblies does not always give perfect results. The definition of onset potential is ambiguous. The activity is not directly related with the mass loading of the catalyst but is associated with the actives sites present. Measuring the total catalysts surface area (with methods such as BET, electrochemical probe molecule adsorption *etc*.) are not perfect as well.[254]

CHAPTER 5. CONCLUSION AND FUTURE WORK

5.1 Conclusion

Increasing population, depletion of fossil fuels, irreversible climate change and dangerous levels of pollution triggered the research on sustainable, clean and cost-efficient energy technologies. Hydrogen is one of the top alternative solutions to this energy problem. Thus, in this Thesis, in a broad sense, applications of hydrogen (H_2-driven biotransformations) and production of hydrogen (hydrogen evolution reaction) were studied. Using non-precious metal catalysts (enzymes and a transition metal dichalcogenide, WS_2), immobilising catalysts, and translating batch processes to flow processes are some of the key points of this work. ***Chapter 2*** and ***Chapter 3*** focus on using carbon based support materials for H_2-driven biotransformations, and ***Chapter 4*** focuses on using WS_2 assemblies for HER catalysis.

Carbon materials act as cheap, stable, electronically conductive, and high surface area catalyst supports. Especially, for the enzymes used in this work, it is important for the supports to be electronically conducting. In Chapter 2, commercial carbon materials were used as supports in H_2-driven NADH generation in batch. In Chapter 3, carbon nanotube columns (CNCs) were used as supports in H_2-driven ketone reduction and H_2-driven reduction amination, both in flow. Some key points of these two chapters are using enzymes as alternatives to expensive precious metal catalysts and, immobilising them for stability, easy product purification, and practicality for large-scale and/or flow applications. Another important point is using cofactor recycling mechanisms to decrease the cost of product purification and expensive cofactors and, create no sacrificial carbon waste.

In ***Chapter 2***, commercial carbon materials (CC, CD, CP, and BP) were studied as enzyme support materials for H_2-driven NADH generation. These materials have been commercially used as supports for metal catalysed hydrogenation reactions. The important characteristics of these materials for immobilisation such as pore volume, pore size, and

surface area were investigated. TEM analysis and Raman spectroscopy results indicated that the materials have amorphous structure. The nitrogen adsorption results showed that these materials have high surface area (> 1000 m^2 g^{-1}) and average pore sizes between 3 nm to 5 nm (mesoporous). The distribution of pore sizes show that the enzymes were in good electronic contact with the carbon supports when diffused into the pores, since the diameters of the enzymes also change between 3 nm to 5 nm. Even though the materials are amorphous (graphitic structure is associated with protein adsorption), their high surface areas make them suitable support materials for enzymes. The carbon materials were also tested for their adsorption of the reactants and products. In this work, the adsorption of the reactants/products on carbon supports is not desired. However, since carbon materials are used as adsorbents in industry, they are expected to adsorb the chemicals used in the reactions. Thus, it is important to detect the effect of the adsorption on the reactant/product concentration. At the given experimental conditions, the adsorption of the reactants/products are insignificant, which shows that they can be used as suitable support materials at the given carbon/reactant-product ratio. Then, enzymes were co-immobilised on carbon materials and used in H_2-driven NADH generation in batch. No sacrificial reactants were needed and the cofactor, NAD^+, used was less than the stoichiometric amount. This is an important economic aspect of this system, because NAD(H) is very expensive and, both by-products, waste and NAD(H) have to be removed from the final product. The UV-Vis spectroscopy results showed that all of the carbon materials that are conventionally used as metal catalysed hydrogenations work as electronically conducting support materials for enzymes in H_2-driven NADH generation. The main disadvantage for the tested carbon materials other than BP is dispersion under the given experimental conditions. These materials can be used in batch NADH generation successfully given that the experimental conditions are optimised. In addition, the dispersion will not matter, if these materials are used in hydrogenation reactors for NADH generation in flow. This system, overall, offers a 100 % atom efficient modular platform (plugging in and

immobilising any desired enzyme) for biotransformations with cofactor recycling and zero sacrificial carbon waste.

In ***Chapter 3***, CNCs were used as enzyme support materials for H_2-driven biotransformations in flow. Initially the chemical and physical properties of CNCs were tested for their suitability as enzyme support materials. Thermogravimetric analysis showed that CNCs consisted of 12 % of Fe catalyst and were stable up to 500 °C, which shows that they can be used in high temperature catalysis applications. Then, CNCs were tested as enzyme support materials and used in H_2-driven biotransformation. EDX analysis done on CNCs used in biotransformations showed an increase in Fe content. This is likely to be due to FeS clusters in enzymes (Hyd-2 and I64A). Thus, it confirms that the enzymes were successfully immobilised on CNCs. Initially, H_2-driven NADH generation in flow was tested. UV-Vis spectroscopy showed that CNCs and the flow set-up are suitable for this biotransformation. Then, three enzymes (Hyd-2, I64A, and NADH dependant enzyme) were co-immobilised on CNCs for further biotransformations. Alcohol dehydrogenase was used as the NADH dependant enzyme for ketone reduction. The HPLC results showed that the reaction has 11 % conversion. However, the product was further analysed by GC and the results show that the reduction is enantioselective and the product is > 99.9 % *S* enantiomer. Finally, L-alanine dehydrogenase was used as the NADH dependant enzyme for reductive amination. HPLC analysis showed 89.9 % conversion was achieved with this system. The only by-product is water. The turnover number, which shows how many times the NAD^+ reductase was used/cycled is greater than 54000. This number shows that the enzyme is highly stable and active. Overall, this is the first demonstration of enzyme catalysed H_2-driven ketone reduction and reductive amination in flow. This system offer a modular platform for H_2-driven biotransformations, since any NADH dependant enzyme can be immobilised for the desired application. The system shows that immobilised enzymes retain their selectivity. Both of the systems showed stability and enzymatic activity for > 20 hours. Recycling of NAD(H) in flow with no sacrificial reactant and waste was achieved.

Chapter 4 focuses on developing novel catalysts assemblies for clean and economically feasible methods to produce high purity hydrogen *via* HER. WS_2 assemblies were studied as an alternative to expensive platinum catalysts. In this work, WS_2 nanoflowers were grown on MWCNT assemblies (MWCNT carpets and CNCs) to increase their stability and the electronic contact. Previously, WS_2 nanostructures have been integrated with carbon materials *via* various methods. However, a simple and direct growth of WS_2 structures has not been studied before. Other than increasing the conductivity of the catalyst, these novel WS_2-MWCNT assemblies act as novel designs that may be directly used in flow applications. Preliminary linear and cyclic voltammetry results showed that the materials catalyse HER with an overpotential around 220 mV.

5.2 Future Work

5.2.1 Flow reactors for H_2-driven biotransformations

The H_2-driven biotransformation system in this work is a modular platform. The system consists of hydrogenase, NAD^+ reductase and an NADH dependant enzyme. Various NADH dependant enzymes can be co-immobilised with hydrogenase and NAD^+ reductase and, different biotransformations can be run. Thus, the system can be used to produce not only (*S*)-1-phenylethanol and L-alanine but also different chiral and expensive fine chemicals.

The main limiting factor for biotransformations studied in this Thesis is solubility of hydrogen. In batch set-ups used in ***Chapter 2***, this problem was overcome by flowing hydrogen over the large headspace. However, since hydrogen is explosive, this is a safety issue for industrial applications. In addition, the trend in fine chemical synthesis is translating batch processes to automatised, cost-efficient flow processes. In flow processes, it is difficult to provide necessary hydrogen in the same way as batch processes. Thus, high-pressure systems are desired. There are commercial flow hydrogenation reactors used in metal catalysed reactions. A similar approach can be used

for H_2-driven biotransformations. Thus, the columns of hydrogenation reactors can be packed with carbon materials for immobilisation of enzymes and, high conversion synthesis can be achieved safely under appropriate pressures for enzymes. On the other hand, CNCs can be modified for high-pressure applications. Quartz columns with large diameter can be used as substrates and longer reaction times can yield thicker MWCNT deposit. In addition, these columns can have tailored-made connectors along the column for connecting hydrogen lines (**Figure 78 a**). Alternatively, multiple CNCs can be used and hydrogen can be supplied to the connection points between these CNCs (**Figure 78 b**).

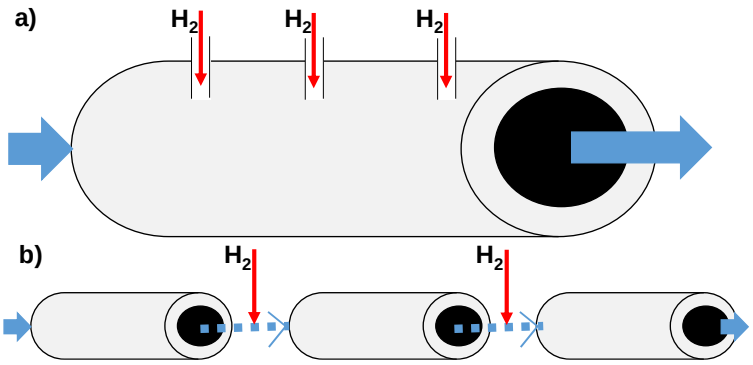


Figure 78: Alternative set-ups for using CNCs in H_2-driven biotransformations.

5.2.2 Optimising WS_2-MWCNT assemblies for HER catalysis

The WS_2-MWCNT assemblies can be optimised further for lower overpotential and higher current density. The plain MWCNT carpets showed activity for HER as well as carpets decorated with WS_2. This may be due to the excess Fe in the MWCNT network. This can be investigated further by changing the density of the deposit (synthesising thicker carpets) on the substrates with the same size. The thickness of the carpets may not only affect the current obtained due to presence of Fe but may also effect the growth of the WS_2 nanostructures. The density of the WS_2 flakes can be increased by changing the position of the MWCNT substrate in CVD furnace, altering the duration of the experiment and having carpets with optimum thickness. Also, having a two stage furnace and sublimating the precursors in the first chamber and carrying out the deposition in the second chamber may increase the yield. Another issue with the transition metal dichalcogenide based HER

catalysts is that their production is not in large-scale. Large diameter furnaces and large substrates can be used for large-scale synthesis. Overall, WS_2-MWCNT assemblies with better electronical contact, lower overpotential, and higher activity towards HER can be developed. WS_2-CNC structures can be used in electrochemical studies with tailor made electrodes that can be connected to CNCs. Then, the assemblies can be optimised for HER catalysis in a similar way with the optimisation of WS_2-MWCNT carpet assemblies.

One of the aims of developing WS_2-MWCNT carpet and WS_2-CNC structures was to develop assemblies that can directly be used in flow applications. In the literature, WS_2 materials have been mixed with carbon based materials to increase the electronical contact between WS_2 nanostructures. However, these studies have not focused on HER catalysis in flow applications. The WS_2-MWCNT carpets can be directly used as the working electrode in a spectro-electrochemical cell (**Figure 79**). This set-up allows the electrolyte solution to in and out when connected to a pump and, having all three electrodes in the same chamber. The circulation of the electrolyte can also prevent the build-up of bubble on the electrode surface. A flow set-up can also be prepared for WS_2-CNC assemblies. CNCs with an inner diameter bigger than 2 mm can be connected to custom-made Teflon connectors with holes for electrodes and tubing for flow. Overall, these two approaches can to be used for HER catalysis in flow and may be coupled with small-scale H_2-driven chemical synthesis. These approaches can decrease the cost of catalyst and the cost of process by translating the current batch methods to flow processes.

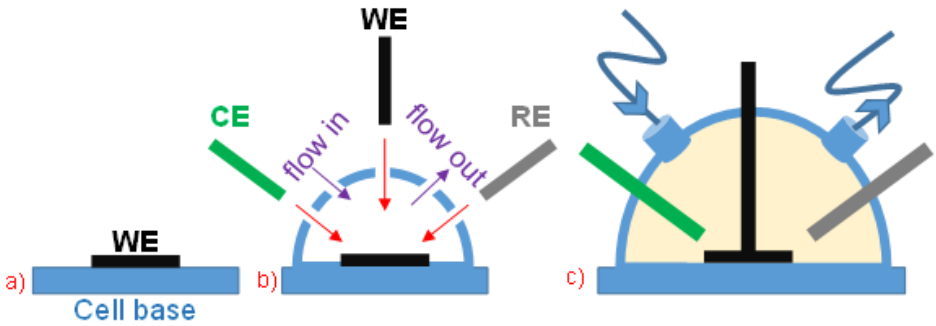


Figure 79: A schematic representation of a flow platform with a spectro-electrochemical cell (developed in Vincent group) for HER. WS_2 catalysts on MWCNT carpet substrates can be used as the working electrode (WE).

REFERENCES

1. Quinson, J. Tailored Carbon-based Nanomaterials for Biological Energy Electrocatalysis. (DPhil Thesis, University of Oxford, 2015).

2. Vincent, K. A. *et al.* Enzymatic catalysis on conducting graphite particles. *Nat. Chem. Biol.* **3,** 761–762 (2007).

3. Lazarus, O. *et al.* Water-gas shift reaction catalyzed by redox enzymes on conducting graphite platelets. *J. Am. Chem. Soc.* **131,** 14154–14155 (2009).

4. Reeve, H. A., Lauterbach, L., Ash, P. A., Lenz, O. & Vincent, K. A. A modular system for regeneration of NAD cofactors using graphite particles modified with hydrogenase and diaphorase moieties. *Chem. Commun.* **48,** 1589–1591 (2012).

5. Reeve, H. A., Lauterbach, L., Lenz, O. & Vincent, K. A. Enzyme-Modified Particles for Selective Biocatalytic Hydrogenation by Hydrogen-Driven NADH Recycling. *ChemCatChem* **7,** 3480–3487 (2015).

6. IEA. Energy and climate change. *World Energy Outlook Spec. Rep.* 1–200 (2015). doi:10.1038/479267b

7. Andrews, J. & Shabani, B. Where does hydrogen fit in a sustainable energy economy? *Procedia Eng.* **49,** 15–25 (2012).

8. Ball, M. & Weeda, M. The hydrogen economy - Vision or reality? *Int. J. Hydrogen Energy* **40,** 7903–7919 (2015).

9. Veziroglu, T. N. John O'M Bockris (1923–2013). *Int. J. Hydrogen Energy* **38,** 13133–13134 (2013).

10. Veziroglu, T. N. Quarter century of hydrogen movement 1974 – 2000. *Int. J. Hydrogen Energy* **25,** 1143–1150 (2000).

11. Caprioglio, P. Prospects for a hydrogen economy. *Energy Policy* **2,** 244–245 (1974).

12. European Commission. 2030 climate and energy goals for a competitive , secure and low-carbon EU economy. *Press Release* (2014). at <http://ec.europa.eu/clima/policies/2030/documentation_en.htm>

13. Hosseini, S. E. & Wahid, M. A. Hydrogen production from renewable and sustainable energy resources: Promising green energy carrier for clean development. *Renew. Sustain. Energy Rev.* **57,** 850–866 (2016).

14. Kapdan, I. K. & Kargi, F. Bio-hydrogen production from waste materials. *Enzym.*

Microb. Technol. **38,** 569–582 (2006).

15. Xie, H. *et al.* Hydrogen production via sorption-enhanced catalytic steam reforming of bio-oil. *Int. J. Hydrogen Energy* **41,** 2345–2353 (2016).

16. Yin, Y. & Wang, J. Gamma irradiation induced disintegration of waste activated sludge for biological hydrogen production. *Radiat. Phys. Chem.* **121,** 110–114 (2016).

17. Faria, E. C., Neto, R. C. R., Colman, R. C. & Noronha, F. B. Hydrogen production through CO_2 reforming of methane over Ni/$CeZrO_2$/Al_2O_3 catalysts. *Catal. Today* **228,** 138–144 (2014).

18. Milne, T. A, Elam, C. C. & Evans, R. J. Hydrogen from Biomass State of the Art Research Challenges, (Technical report, 1 Feb 2002). doi:10.2172/792221

19. Wang, D., Czernik, S., Montane, D., Mann, M. & Chornet, E. Biomass to hydrogen via fast pyrolysis and catalytic steam reforming of the pyrolysis oil or its fractions. *Ind. Eng. Chem. Res.* **36,** 1507–1518 (1997).

20. Barbaro, P. & Bianchini, C. *Catalysis for Sustainable Energy Production*. *Catalysis for Sustainable Energy Production,* 235-269 (2009). doi:10.1002/9783527625413

21. Abdin, Z., Webb, C. J. & Gray, E. M. Solar hydrogen hybrid energy systems for off-grid electricity supply: A critical review. *Renew. Sustain. Energy Rev.* **52,** 1791–1808 (2015).

22. Bertuccioli, L. *et al. Development of Water Electrolysis in the European Union - Fuel Cells and Hydrogen Joint Undertaking*. (2014). at <http://www.fch.europa.eu/sites/default/files/study electrolyser_0-Logos_0.pdf>

23. Simbolotti, G. *IEA Energy Technology Essentials - Hydrogen Production & Distribution*. at <https://www.iea.org/publications/freepublications/publication/essentials5.pdf>

24. Kanan, M. W. & Nocera, D. G. In situ formation of an oxygen-evolving catalyst in neutral water containing phosphate and Co^{2+}. *Science* **321,** 1072–1075 (2008).

25. Kanan, M. W., Surendranath, Y. & Nocera, D. G. Cobalt-phosphate oxygen-evolving compound. *Chem. Soc. Rev.* **38,** 109–114 (2009).

26. Ulleberg, Ø. Modeling of advanced alkaline electrolyzers: A system simulation approach. *Int. J. Hydrogen Energy* **28,** 21–33 (2003).

27. Agrafiotis, C., Roeb, M. & Sattler, C. A review on solar thermal syngas production via redox pair-based water/carbon dioxide splitting thermochemical cycles. *Renew. Sustain. Energy Rev.* **42,** 254–285 (2015).

28. Duigou, A. *et al.* HYTHEC: An EC funded search for a long term massive hydrogen production route using solar and nuclear technologies. *Int. J. Hydrogen Energy* **32,** 1516–1529 (2007).

29. Pinaud, B. A. *et al.* Technical and economic feasibility of centralized facilities for solar hydrogen production via photocatalysis and photoelectrochemistry. *Energy Environ. Sci.* **6,** 1983 (2013).

30. Cabán-Acevedo, M. *et al.* Efficient hydrogen evolution catalysis using ternary pyrite-type cobalt phosphosulphide. *Nat. Mater.* **14,** 1245–51 (2015).

31. Safizadeh, F., Ghali, E. & Houlachi, G. Electrocatalysis developments for hydrogen evolution reaction in alkaline solutions - A Review. *Int. J. Hydrogen Energy* **40,** 256–274 (2015).

32. Nocera, D. G. The artificial leaf. *Acc. Chem. Res.* **45,** 767–776 (2012).

33. Turner, J. A. Sustainable hydrogen production. *Science* **305,** 972–974 (2004).

34. Jaccaud, M., Leroux, F. & Millet, J. C. New chlor-alkali activated cathodes. *Mater. Chem. Phys.* **22,** 105–119 (1989).

35. Faber, M. S. & Jin, S. Earth-abundant inorganic electrocatalysts and their nanostructures for energy conversion applications. *Energy Environ. Sci.* **7,** 3519–3542 (2014).

36. Naga Mahesh, K., Balaji, R. & Dhathathreyan, K. S. Palladium nanoparticles as hydrogen evolution reaction (HER) electrocatalyst in electrochemical methanol reformer. *Int. J. Hydrogen Energy* **41,** 46–51 (2016).

37. Xu, G. R., Hui, J. J., Huang, T., Chen, Y. & Lee, J. M. Platinum nanocuboids supported on reduced graphene oxide as efficient electrocatalyst for the hydrogen evolution reaction. *J. Power Sources* **285,** 393–399 (2015).

38. Le Goff, A. *et al.* From Hydrogenases to Noble Metal–Free Catalytic Nanomaterials for H_2 Production and Uptake. *Science* **326,** 1384–1387 (2009).

39. Callejas, J. F. *et al.* Electrocatalytic and photocatalytic hydrogen production from acidic and neutral-pH aqueous solutions using iron phosphide nanoparticles. *ACS Nano* **8,** 11101–11107 (2014).

40. Popczun, E. J., Read, C. G., Roske, C. W., Lewis, N. S. & Schaak, R. E. Highly active electrocatalysis of the hydrogen evolution reaction by cobalt phosphide nanoparticles. *Angew. Chem. Int. Ed.* **53,** 5427–5430 (2014).

41. Liu, Q. *et al.* Carbon nanotubes decorated with CoP nanocrystals: A highly active non-noble-metal nanohybrid electrocatalyst for hydrogen evolution. *Angew. Chem. Int. Ed.* **53,** 6710–6714 (2014).

42. Faber, M. S. *et al.* High-performance electrocatalysis using metallic cobalt pyrite (CoS_2) micro- and nanostructures. *J. Am. Chem. Soc.* **136,** 10053–10061 (2014).

43. McEnaney, J. M. *et al.* Amorphous molybdenum phosphide nanoparticles for electrocatalytic hydrogen evolution. *Chem. Mater.* **26,** 4826–4831 (2014).

44. Yan, Y. *et al.* Vertically oriented MoS_2 and WS_2 nanosheets directly grown on carbon cloth as efficient and stable 3-dimensional hydrogen-evolving cathodes. *J. Mater. Chem. A* **3,** 131–135 (2015).

45. Bollinger, M. V *et al.* One-dimensional metallic edge states in MoS_2. *Phys. Rev. Lett.* **87,** 196803 (2001).

46. Fan, X.-L., Yang, Y., Xiao, P. & Lau, W.-M. Site-specific catalytic activity in exfoliated MoS_2 single-layer polytypes for hydrogen evolution: basal plane and edges. *J. Mater. Chem. A* **2,** 20545–20551 (2014).

47. Hinnemann, B. *et al.* Biomimetic hydrogen evolution: MoS_2 nanoparticies as catalyst for hydrogen evolution. *J. Am. Chem. Soc.* **127,** 5308–5309 (2005).

48. Liu, N. *et al.* Ultrathin MoS_2 nanosheets growing within an in-situ-formed template as efficient electrocatalysts for hydrogen evolution. *J. Power Sources* **275,** 588–594 (2015).

49. Wen, Y., Xia, Y. & Zhang, S. Tungsten disulphide nanorattle: A new type of high performance electrocatalyst for hydrogen evolution reaction. *J. Power Sources* **307,** 593–598 (2016).

50. Yang, J. *et al.* Two-dimensional hybrid nanosheets of tungsten disulfide and reduced graphene oxide as catalysts for enhanced hydrogen evolution. *Angew. Chem. Int. Ed.* **52,** 13751–13754 (2013).

51. Kim, J., Byun, S., Smith, A. J., Yu, J. & Huang, J. Enhanced electrocatalytic properties of transition-metal dichalcogenides sheets by spontaneous gold nanoparticle decoration. *J. Phys. Chem. Lett.* **4,** 1227–1232 (2013).

52. He, Z. & Que, W. Molybdenum disulfide nanomaterials: Structures, properties, synthesis and recent progress on hydrogen evolution reaction. *Appl. Mater. Today* **3,** 23–56 (2016).

53. Cotton, F. A., Wilkinson, G. & Murillo, C.A.Bochman, M. *Advanced Inorganic Chemistry*. (Wiley-Interscience, 1999).

54. Nishimura, S. *Handbook of Heterogeneous Catalytic Hydrogenation for Organic Synthesis*. (Wiley-Interscience, 2001).

55. Irfan, M., Glasnov, T. N. & Kappe, C. O. Heterogeneous catalytic hydrogenation reactions in continuous-flow reactors. *ChemSusChem* **4,** 300–316 (2011).

56. Osborn, J. A., Jardine, F. H., Young, J. F. & Wilkinson, G. The preparation and properties of tris(triphenylphosphine)halogenorhodium(I) and some reactions thereof including catalytic homogeneous hydrogenation of olefins and acetylenes and their derivatives. *J. Chem. Soc. A Inorg. Phys. Theor.* 1711 (1966).

57. Rothwell, I. P. A new generation of homogeneous arene hydrogenation catalysts. *Chem. Commun.* 1331–1338 (1997).

58. Uematsu, N., Fujii, A., Hashiguchi, S., Ikariya, T. & Noyori, R. Asymmetric Transfer Hydrogenation of Imines. *J. Am. Chem. Soc.* **118,** 4916–4917 (1996).

59. Maxted, E. B., Moon, K. L. & Overgage, E. The relationship between sensitivity to poisoning and catalytic surface. *Discuss. Faraday Soc.* **8,** 135 (1950).

60. Munirathinam, R., Huskens, J. & Verboom, W. Supported Catalysis in Continuous-Flow Microreactors. *Adv. Synth. Catal.* **357,** 1093–1123 (2015).

61. Ehrburger, P., Mahajan, O. P. & Walker, P. L. Carbon as a support for catalysis—effect of surface heterogeneity of carbon on dispersion of platinum. *Carbon N. Y.* **14,** 295 (1976).

62. Madarász, J. *et al.* A Continuous-Flow System for Asymmetric Hydrogenation Using Supported Chiral Catalysts. *J. Flow Chem.* **1,** 62–67 (2011).

63. Kiwi-Minsker, L. & Renken, A. Microstructured reactors for catalytic reactions. *Catal. Today* **110,** 2–14 (2005).

64. Radovic, L. R., Mora-Vilches, C. & Salgado-Casanova, A. J. a. Catalysis: An old but new challenge for graphene-based materials. *Chin. J. Catal.* **35,** 792–797 (2014).

65. de Lecea, C. S.-M., Linares-Solano, A. & Vannice, M. . Carbon black and activated

carbon as supports in catalysts prepared from $Fe_3(CO)_{12}$ and $Mn_2(CO)_{10}$ clusters. *Carbon N. Y.* **28,** 467–476 (1990).

66. Kaftan, A. *et al.* Supported homogeneous catalyst makes its own liquid phase. *J. Catal.* **321,** 32–38 (2015).

67. Ito, J. I. & Nishiyama, H. Recent topics of transfer hydrogenation. *Tetrahedron Lett.* **55,** 3153–3166 (2014).

68. Bartoszewicz, A., Ahlsten, N. & Martín-Matute, B. Enantioselective synthesis of alcohols and amines by iridium-catalyzed hydrogenation, transfer hydrogenation, and related processes. *Chem. Eur. J.* **19,** 7274–7302 (2013).

69. Ikariya, T. & Blacker, A. J. Asymm Transfer Hydrogenation Ketone with Bifunctional Transition Metal-Based Cat. *Acc. Chem. Res.* **40 ,** 1300–1308 (2007).

70. Yan, K., Wu, G., Lafleur, T. & Jarvis, C. Production, properties and catalytic hydrogenation of furfural to fuel additives and value-added chemicals. *Renew. and Sustainable Energy Rev.* **38,** 663–676 (2014).

71. Foubelo, F., Nájera, C. & Yus, M. Catalytic asymmetric transfer hydrogenation of ketones: recent advances. *Tetrahedron: Asymmetry* **26,** 769–790 (2015).

72. Cortez, N. A., Aguirre, G., Parra-Hake, M. & Somanathan, R. Synthesis of (R)-tembamide and (R)-aegeline via asymmetric transfer hydrogenation in water. *Tetrahedron Asymmetry* **24,** 1297–1302 (2013).

73. He, S. Z., Li, X. M., Dai, J. & Yan, M. Synthesis of antidepressant duloxetine via asymmetric transfer hydrogenation. *Chin. Chem. Lett.* **19,** 23–25 (2008).

74. Luo, Z., Qin, F., Yan, S. & Li, X. An efficient and promising method to prepare Ladostigil (TV3326) via asymmetric transfer hydrogenation catalyzed by Ru-Cs-DPEN in an HCOONa-H_2O-surfactant system. *Tetrahedron: Asymmetry* **23,** 333–338 (2012).

75. Al Wahedi, Y. *et al.* Economic assessment of Temperature Swing Adsorption systems as Claus Tail Gas Clean Up Units. *Chem. Eng. Sci.* **126,** 186–195 (2015).

76. Chang, H. *et al.* Development and industrial application of catalyzer for low-temperature hydrogenation hydrolysis of Claus tail gas. *Nat. Gas Ind. B* **2,** 368–373 (2015).

77. Pérez, D., Olivera-Fuentes, C., Curbelo, S., Rodríguez, M. J. & Zeppieri, S. Study of the selective hydrogenation of 1,3-butadiene in three types of industrial reactors.

Fuel **149,** 34–45 (2015).

78. Axens IFP Group Technologies. at <http://www.axens.net/product/technology-licensing/10065/butadiene-hydrogenation.html>

79. Tohidian, T., Dehghani, O. & Rahimpour, M. R. Modeling and simulation of an industrial three phase trickle bed reactor responsible for the hydrogenation of 1,3-butadiene: A case study. *Chem. Eng. J.* **275,** 391–404 (2015).

80. Alves, J. A., Bressa, S. P., Martínez, O. M. & Barreto, G. F. Selective hydrogenation of 1,3-butadiene: Improvement of selectivity by using additives. *Chem. Eng. J.* **99,** 45–51 (2004).

81. Bressa, S. P., Alves, J. A., Mariani, N. J., Martínez, O. M. & Barreto, G. F. Analysis of operating variables on the performance of a reactor for total hydrogenation of olefins in a C_3-C_4-stream. *Chem. Eng. J.* **92,** 41–54 (2003).

82. Tailleur, R. G., Hernandez, J. & Alejandra Rojas. Selective hydrogenation of olefins with mass transfer control in a structured packed bed reactor. *Fuel* **87,** 3694–3705 (2008).

83. Shafaat, H. S., Rüdiger, O., Ogata, H. & Lubitz, W. [NiFe] hydrogenases: A common active site for hydrogen metabolism under diverse conditions. *Biochimic. Biophysic. Acta - Bioenergetics* **1827,** 986–1002 (2013).

84. Henrici-Olivé, G. & Olivé, S. Hydrogenation catalysts: A synthetic hydrogenase model. *J. Mol. Catal.* **1,** 121–135 (1976).

85. Fontecilla-Camps, J. C., Volbeda, A., Cavazza, C. & Nicolet, Y. Structure/function relationships of [NiFe]- and [FeFe]-hydrogenases. *Chemical Reviews* **107,** 4273–4303 (2007).

86. Mcpherson, I. J. & Vincent, K. A. Electrocatalysis by Hydrogenases: Lessons for Building Bio-Inspired Devices. *J. Braz. Chem. Soc.* **25,** 1–15 (2014).

87. Barton, B. E., Olsen, M. T. & Rauchfuss, T. B. Artificial hydrogenases. *Curr. Opin. Biotechnol.* **21,** 292–297 (2010).

88. Van Berkel-Arts, A. *et al.* Application of hydrogenase in biotechnological conversions. *Biochimie* **68,** 201–209 (1986).

89. Woolerton, T. W., Sheard, S., Chaudhary, Y. S. & Armstrong, F. A. Enzymes and bio-inspired electrocatalysts in solar fuel devices. *Energy Environ. Sci.* **5,** 7470 (2012).

90. Hambourger, M. *et al.* [FeFe]-hydrogenase-catalyzed H2 production in a photoelectrochemical biofuel cell. *J. Am. Chem. Soc.* **130,** 2015–2022 (2008).

91. Ciaccafava, A. *et al.* An innovative powerful and mediatorless H2/O2 biofuel cell based on an outstanding bioanode. *Electrochem. commun.* **23,** 25–28 (2012).

92. Artero, V. & Fontecave, M. Some general principles for designing electrocatalysts with hydrogenase activity. *Coordin. Chem. Rev.* **249,** 1518–1535 (2005).

93. Ogo, S. Electrons from hydrogen. *Chem. Commun. (Camb).* **7345,** 3317–3325 (2009).

94. Marre, S. & Jensen, K. F. Synthesis of micro and nanostructures in microfluidic systems. *Chem. Soc. Rev.* **39,** 1183 (2010).

95. Hessel, V., Renken, A., Schouten, J. C. & Yoshida, J. I. *Micro Process Engineering: A Comprehensive Handbook*. *Micro Process Engineering: A Comprehensive Handbook* **1,** (2013).

96. Hartman, R. L., McMullen, J. P. & Jensen, K. F. Deciding whether to go with the flow: Evaluating the merits of flow reactors for synthesis. *Angew. Chem. - Int. Ed.* **50,** 7502–7519 (2011).

97. Hessel, V., Vural Gursel, I., Wang, Q., Noel, T. & Lang, J. Potential Analysis of Smart Flow Processing and Micro Process Technology for Fastening Process Development: Use of Chemistry and Process Design as Intensification Fields. *Chem. Eng. and Technol.* **35,** 1184–1204 (2012).

98. Ley, S. V. On being green: Can flow chemistry help? *Chem. Rec.* **12,** 378–390 (2012).

99. Malet-Sanz, L. & Susanne, F. Continuous flow synthesis. a pharma perspective. *J. of Med. Chem.* **55,** 4062–4098 (2012).

100. Webb, D. & Jamison, T. F. Continuous flow multi-step organic synthesis. *Chem. Sci.* **1,** 675 (2010).

101. Wegner, J., Ceylan, S. & Kirschning, A. Flow chemistry - A key enabling technology for (multistep) organic synthesis. *Adv. Synth. and Catal.* **354,** 17–57 (2012).

102. Wiles, C. & Watts, P. Recent advances in micro reaction technology. *Chem. Commun. (Camb).* **47,** 6512–6535 (2011).

103. Jiménez-Gonzalez, C. *et al.* Key green engineering research areas for sustainable

manufacturing: A perspective from pharmaceutical and fine chemicals manufacturers. *Org. Process Res. Dev.* **15,** 900–911 (2011).

104. Constable, D. J. C. *et al.* Key green chemistry research areas-a perspective from pharmaceutical manufacturers. *Green Chem.* **9,** 411–420 (2007).

105. Yoshida, J. I., Kim, H. & Nagaki, A. Green and sustainable chemical synthesis using flow microreactors. *ChemSusChem* **4,** 331–340 (2011).

106. Wiles, C. & Watts, P. Continuous flow reactors: a perspective. *Green Chem.* **14,** 38 (2012).

107. Hessel, V., Kralisch, D., Kockmann, N., Noël, T. & Wang, Q. Novel process windows for enabling, accelerating, and uplifting flow chemistry. *ChemSusChem* **6,** 746–789 (2013).

108. Zhang, Y. T., Arancon, R. a D., Lam, L. Y. F. & Luque, R. Flow nanocatalysis: Innovative methodologies towards green chemical syntheses. *Chim. Oggi* **32,** 36–39 (2014).

109. Born, S., O'Neal, E. & Jensen, K. F. *Organic Synthesis in Small Scale Continuous Flow: Flow Chemistry*. *Comprehensive Organic Synthesis* **9,** (Elsevier Ltd., 2014).

110. Mozharov, S. *et al.* Improved method for kinetic studies in microreactors using flow manipulation and noninvasive raman spectrometry. *J. Am. Chem. Soc.* **133,** 3601–3608 (2011).

111. Floyd, T. M., Schmidt, M. A. & Jensen, K. F. Silicon micromixers with infrared detection for studies of liquid-phase reactions. *Ind. Eng. Chem. Res.* **44,** 2351–2358 (2005).

112. Silva, B. V., Violante, F. A., Pinto, A. C. & Santos, L. S. The mechanism of Sandmeyer's cyclization reaction by electrospray ionization mass spectrometry. *Rapid Commun. Mass Spectrom.* **25,** 423–428 (2011).

113. Gutmann, B., Roduit, J. P., Kappe, C. O. & Roberge, D. Synthesis of 5-substituted lH-tetrazoles from nitriles and hydrazoic acid by using a safe and scalable high-temperature microreactor approach. *Angew. Chemie - Int. Ed.* **49,** 7101–7105 (2010).

114. Marre, S., Adamo, A., Basak, S., Aymonier, C. & Jensen, K. F. Design and Packaging of Microreactors for High Pressure and High Temperature Applications. *Ind. Eng. Chem. Res.* **49,** 11310–11320 (2010).

115. Xia, A. *et al.* Fermentative hydrogen production using algal biomass as feedstock. *Renew. and Sustainable Energy Rev.* **51,** 209–230 (2015).

116. Ren, N., Guo, W., Liu, B., Cao, G. & Ding, J. Biological hydrogen production by dark fermentation: Challenges and prospects towards scaled-up production. *Curr. Opin. Biotechnol.* **22,** 365–370 (2011).

117. Wang, J. & Wan, W. Factors influencing fermentative hydrogen production: A review. *Int. J. Hydrogen Energy* **34,** 799–811 (2009).

118. Gavala, H. N., Skiadas, I. V. & Ahring, B. K. Biological hydrogen production in suspended and attached growth anaerobic reactor systems. *Int. J. Hydrogen Energy* **31,** 1164–1175 (2006).

119. Yu, H., Zhu, Z., Hu, W. & Zhang, H. Hydrogen production from rice winery wastewater in an upflow anaerobic reactor by using mixed anaerobic cultures. *Int. J. Hydrogen Energy* **27,** 1359–1365 (2002).

120. Alzate-Gaviria, L. M., Sebastian, P. J., Pérez-Hernández, A. & Eapen, D. Comparison of two anaerobic systems for hydrogen production from the organic fraction of municipal solid waste and synthetic wastewater. *Int. J. Hydrogen Energy* **32,** 3141–3146 (2007).

121. Das, D. & Veziroglu, T. N. Advances in biological hydrogen production processes. *Int. J. Hydrogen Energy* **33,** 6046–6057 (2008).

122. Molinari, R., Marino, T. & Argurio, P. Photocatalytic membrane reactors for hydrogen production from water. *Int. J. Hydrogen Energy* **39,** 7247–7261 (2014).

123. Chaubey, R., Sahu, S., James, O. O. & Maity, S. A review on development of industrial processes and emerging techniques for production of hydrogen from renewable and sustainable sources. *Renew. Sustainable Energy Rev.* **23,** 443–462 (2013).

124. Maeda, K. Photocatalytic water splitting using semiconductor particles: History and recent developments. *J.Photochem. Photobiol. C.* **12,** 237–268 (2011).

125. Sayama, K., Mukasa, K., Abe, R., Abe, Y. & Arakawa, H. Stoichiometric water splitting into H2 and O2 using a mixture of two different photocatalysts and an IO3-/I- shuttle redox mediator under visible light irradiation. *Chem. Commun.* 2416–2417 (2001). doi:10.1039/b107673f

126. Fujihara, K., Ohno, T. & Matsumura, M. Splitting of water by electrochemical

combination of two photocatalytic reactions on TiO2 particles. *J. Chem. Soc. Faraday Trans.* **94,** 3705–3709 (1998).

127. Yu, S.-C. *et al.* A novel membrane reactor for separating hydrogen and oxygen in photocatalytic water splitting. *J. Memb. Sci.* **382,** 291–299 (2011).

128. Karim, A., Bravo, J., Gorm, D., Conant, T. & Datye, A. Comparison of wall-coated and packed-bed reactors for steam reforming of methanol. *Catal. Today* **110,** 86–91 (2005).

129. Holladay, J. D. & Wang, Y. A review of recent advances in numerical simulations of microscale fuel processor for hydrogen production. *J. Power Sources* **282,** 602–621 (2015).

130. Hsueh, C. Y., Chu, H. Sen, Yan, W. M. & Chen, C. H. Transport phenomena and performance of a plate methanol steam micro-reformer with serpentine flow field design. *Appl. Energy* **87,** 3137–3147 (2010).

131. Newman, S. G. & Jensen, K. F. The role of flow in green chemistry and engineering. *Green Chem.* **15,** 1456–1472 (2013).

132. ThalesNano Nanotechology Inc. at <http://www.thalesnano.com/>

133. AM Technology. *Hydrogenation: Batch to Continous* at <http://www.amtechuk.com/getattachment/SpecialPages/Logon/TN1310v2-Hydrogenation.pdf.aspx>

134. Parr Instument Company. *Series 5500 HP Compact Reactors* at <http://www.parrinst.com/products/stirred-reactors/series-5500-hp-compact-reactors/>

135. Jones, R. V. *et al.* Continuous-Flow High Pressure Hydrogenation Reactor for Optimization and High-Throughput Synthesis. *J. Comb. Chem.* **8,** 110–116 (2006).

136. Clapham, B. *et al.* Construction and Validation of an Automated Flow Hydrogenation Instrument for Application in High-Throughput Organic Chemistry. *J. Comb. Chem.* **10,** 88–93 (2008).

137. Carter, C. F., Baxendale, I. R., O'Brien, M., Pavey, J. B. J. & Ley, S. V. Synthesis of acetal protected building blocks using flow chemistry with flow I.R. analysis: preparation of butane-2,3-diacetal tartrates. *Org. Biomol. Chem.* **7,** 4594–7 (2009).

138. Frost, C. G. & Mutton, L. Heterogeneous catalytic synthesis using microreactor technology. *Green Chem.* **12,** 1687 (2010).

139. de Bellefon, C., Tanchoux, N. & Caravieilhes, S. New reactors and methods for the investigation of homogeneous catalysis. *J. Organomet. Chem.* **567,** 143–150 (1998).

140. McMorn, P. & Hutchings, G. J. Heterogeneous enantioselective catalysts: strategies for the immobilisation of homogeneous catalysts. *Chem. Soc. Rev.* **33,** 108–22 (2004).

141. Auer, E., Freund, a., Pietsch, J. & Tacke, T. Carbons as supports for industrial precious metal catalysts. *Appl. Catal. A Gen.* **173,** 259–271 (1998).

142. Králik, M. & Biffis, A. Catalysis by metal nanoparticles supported on functional organic polymers. *J. Mol. Catal. A Chem.* **177,** 113–138 (2001).

143. Vitulli, G. *et al.* Supported rhodium nanoparticles in catalysis: the role of stabilizers on catalytic activity and structural features. *J. Organomet. Chem.* **681,** 37–50 (2003).

144. Tsang, S. C., Yu, K. M. K., Steele, A. M., Zhu, J. & Fu, Q. J. Solid supported micellar catalysis: some syntheses and characterisations. *Catal. Today* **81,** 573–581 (2003).

145. Chaudhari, R. V. 'Heterogenized Homogeneous Catalysts for Fine Chemicals Production: Materials and Processes'. *Platin. Met. Rev.* **55,** 180–185 (2011).

146. Fernandes, A. E., Jonas, A. M. & Riant, O. Application of CuAAC for the covalent immobilization of homogeneous catalysts. *Tetrahedron* **70,** 1709–1731 (2014).

147. Sheldon, R. a & van Pelt, S. Enzyme immobilisation in biocatalysis: why, what and how. *Chem. Soc. Rev.* **42,** 6223–35 (2013).

148. Hanefeld, U., Gardossi, L. & Magner, E. Understanding enzyme immobilisation. *Chem. Soc. Rev.* **38,** 453–468 (2009).

149. Hartmann, M. & Kostrov, X. Immobilization of enzymes on porous silicas--benefits and challenges. *Chem. Soc. Rev.* **42,** 6277–89 (2013).

150. Cang-Rong, J. T. & Pastorin, G. The influence of carbon nanotubes on enzyme activity and structure: investigation of different immobilization procedures through enzyme kinetics and circular dichroism studies. *Nanotechnology* **20,** 255102 (2009).

151. Fraile, J. M., Pérez, I. & Mayoral, J. A. Comparison of immobilized Box and azaBox-Cu(II) complexes as catalysts for enantioselective Mukaiyama aldol reactions. *J. Catal.* **252,** 303–311 (2007).

152. Heitbaum, M., Glorius, F. & Escher, I. Asymmetric heterogeneous catalysis. *Angew.*

Chem. Int.Ed. **45,** 4732–4762 (2006).

153. Fan, Q. H., Li, Y. M. & Chan, A. S. C. Recoverable catalysts for asymmetric organic synthesis. *Chem. Rev.* **102,** 3385–3466 (2002).

154. Nelson, J. M. & Griffin, E. G. Adsorption of Invertase. *J. Am. Chem. Soc.* **38,** 1109–1115 (1916).

155. Tomotani, E. J. & Vitolo, M. Method for immobilizing invertase by adsorption on Dowex® anionic exchange resin. *Rev. Bras. Ciências Farm.* **42,** 2–6 (2006).

156. Liese, A. & Seelbach, K. *Industrial Biotransformations*. *Biocatalysis* (2006).

157. Hari Krishna, S. & Karanth, N. G. Lipases and Lipase-Catalyzed Esterification Reactions in Nonaqueous Media. *Catal. Rev.* **44,** 499–591 (2002).

158. Anderson, E. M., Larsson, K. M. & Kirk, O. One Biocatalyst–Many Applications: The Use of Candida Antarctica B-Lipase in Organic Synthesis. *Biocatal. Biotransform.* **16,** 181–204 (1998).

159. Tufvesson, P., Annerling, A., Hatti-Kaul, R. & Adlercreutz, D. Solvent-free enzymatic synthesis of fatty alkanolamides. *Biotechnol. Bioeng.* **97,** 447–453 (2007).

160. Guldhe, A., Singh, B., Mutanda, T., Permaul, K. & Bux, F. Advances in synthesis of biodiesel via enzyme catalysis: Novel and sustainable approaches. *Renew. Sustainable Energy Rev.* **41,** 1447–1464 (2015).

161. Tufvesson, P., Tornvall, U., Carvalho, J., Karlsson, A. J. & Hatti-Kaul, R. Towards a cost-effective immobilized lipase for the synthesis of specialty chemicals. *J. Mol. Catal. B Enzym.* **68,** 200–205 (2011).

162. elements 25 Cosmetic Esters: Sustainability That Gets Under the Skin With Metabolic Pathways to Sustainable Chemistry. *Evonik Innovation Magazine* (2008). at <http://corporate.evonik.com/sites/dc/Downloadcenter/Evonik/Global/en/Magazines/elements/elements-25.pdf>

163. Katchalski-Katzir, E. & Kraemer, D. M. Eupergit® C, a carrier for immobilization of enzymes of industrial potential. *J. Mol. Catal. - B Enzym.* **10,** 157–176 (2000).

164. Reetz, M. T., Tielmann, P., Wiesenhofer, W., Konen, W. & Zonta, A. Second generation sol-gel encapsulated lipases: Robust heterogeneous biocatalysts. *Adv. Synth. Catal.* **345,** 717–728 (2003).

165. Hudson, S., Cooney, J. & Magner, E. Proteins in Mesoporous Silicates. *Angew. Chem. Int. Ed.* **47,** 8582–8594 (2008).

166. An, N., Zhou, C. H., Zhuang, X. Y., Tong, D. S. & Yu, W. H. Immobilization of enzymes on clay minerals for biocatalysts and biosensors. *Appl. Clay Sci.* **114,** 283–296 (2015).

167. Zhao, X., Mai, Z., Kang, X. & Zou, X. Direct electrochemistry and electrocatalysis of horseradish peroxidase based on clay–chitosan-gold nanoparticle nanocomposite. *Biosens. Bioelectron.* **23,** 1032–1038 (2008).

168. Yu, W. H. *et al.* Adsorption of proteins and nucleic acids on clay minerals and their interactions: A review. *Appl. Clay Sci.* **80-81,** 443–452 (2013).

169. Tzialla, A. A. *et al.* Lipase immobilization on smectite nanoclays: Characterization and application to the epoxidation of α-pinene. *Bioresour. Technol.* **101,** 1587–1594 (2010).

170. You, Q., Yin, X., Zhao, Y. & Zhang, Y. Biodiesel production from jatropha oil catalyzed by immobilized Burkholderia cepacia lipase on modified attapulgite. *Bioresour. Technol.* **148,** 202–207 (2013).

171. Sanjay, G. & Sugunan, S. Invertase immobilised on montmorillonite: reusability enhancement and reduction in leaching. *Catal. Commun.* **6,** 81–86 (2005).

172. Mitchell, D. T. *et al.* Smart nanotubes for bioseparations and biocatalysis. *J. Am. Chem. Soc.* **124,** 11864–11865 (2002).

173. Yang, M., Yang, Y., Liu, Y., Shen, G. & Yu, R. Platinum nanoparticles-doped sol-gel/carbon nanotubes composite electrochemical sensors and biosensors. *Biosens. Bioelectron.* **21,** 1125–1131 (2006).

174. Zhao, K. *et al.* Amperometric glucose biosensor based on platinum nanoparticles combined aligned carbon nanotubes electrode. *Electroanalysis* **19,** 1069–1074 (2007).

175. Kouassi, G. K., Irudayaraj, J. & McCarty, G. Examination of Cholesterol oxidase attachment to magnetic nanoparticles. *J. Nanobiotechnology* **3,** 1 (2005).

176. Konwarh, R., Karak, N., Rai, S. K. & Mukherjee, A. K. Polymer-assisted iron oxide magnetic nanoparticle immobilized keratinase. *Nanotechnology* **20,** 225107 (2009).

177. Dhanjal, S. & Cameotra, S. Aerobic biogenesis of selenium nanospheres by Bacillus cereus isolated from coalmine soil. *Microb. Cell Fact.* **9,** 52 (2010).

178. Li, X. L., Ge, J. P. & Li, Y. D. Atmospheric pressure chemical vapor deposition: An alternative route to large-scale MoS_2 and WS_2 inorganic fullerene-like nanostructures and nanoflowers. *Chem. - A Eur. J.* **10,** 6163–6171 (2004).

179. Rao, C. N. R. & Nag, A. Inorganic analogues of graphene. *Eur. J. Inorg. Chem.* 4244–4250 (2010). doi:10.1002/ejic.201000408

180. Zou, M. *et al.* Controlled morphology evolution of electrospun carbon nanofiber templated tungsten disulfide nanostructures. *Electrochim. Acta* **176,** 255–264 (2015).

181. Kraatz, H.-B. & Metzler-Nolte, N. *Concepts and Models in Bioinorganic Chemistry*. (Wiley-VCH, 2006).

182. Lukey, M. J. *et al.* How Escherichia coli is equipped to oxidize hydrogen under different redox conditions. *J. Biol. Chem.* **285,** 3928–3938 (2010).

183. Volbeda, A. *et al.* X-ray crystallographic and computational studies of the O_2-tolerant [NiFe]-hydrogenase 1 from Escherichia coli. *Proc.Natl.Acad.Sci.USA* **109,** 5305–5310 (2012).

184. Lauterbach, L., Idris, Z., Vincent, K. A. & Lenz, O. Catalytic Properties of the Isolated Diaphorase Fragment of the NAD+-Reducing [NiFe]-Hydrogenase from Ralstonia eutropha. *PLoS One* **6,** e25939 (2011).

185. Buchholz, K., Kasche, V. & Bornscheuer, U. *Biocatalysts and Enzyme Technology*. (Wiley-VCH, 2005).

186. Alcohol Dehydrogenase 105. at <http://jmcct.com/products-services/product_p548.html>

187. Wichelecki, S., Lukk, T., Imker, H. ., Nair, S. . & Gerlt, J. A. Crystal structure of short chain alcohol dehydrogenase (rspB) from E. coli CFT073 (EFI TARGET EFI-506413) complexed with cofactor NADH. *To be Publ.* doi:10.2210/pdb4ilk/pdb

188. Tripathi, S. . & Ramachandran, R. Crystal Structures of the Mycobacterium Tuberculosis Secretory Antigen Alanine Dehydrogenase (Rv2780) in Apo and Ternary Complex Forms Captures. *Proteins: Struct., Funct., Bioinf.* **72,** 1089–1095 (2008).

189. Nelson, D. & Cox, M. *Lehninger Principles of Biochemistry*. (W. H. Freeman and Company).

190. Ali, I., Gill, A. & Omanovic, S. Direct electrochemical regeneration of the enzymatic

cofactor 1,4-NADH employing nano-patterned glassy carbon/Pt and glassy carbon/Ni electrodes. *Chem. Eng. J.* **188,** 173–180 (2012).

191. Lee, S. H., Ryu, J., Nam, D. H. & Park, C. B. Photoenzymatic synthesis through sustainable NADH regeneration by SiO_2-supported quantum dots. *Chem. Commun.* **47,** 4643–4645 (2011).

192. Van Der Donk, W. A. & Zhao, H. Recent developments in pyridine nucleotide regeneration. *Curr. Opin. in Biotechnol.* **14,** 421–426 (2003).

193. Liu, W. & Wang, P. Cofactor regeneration for sustainable enzymatic biosynthesis. *Biotechnology Advances* **25,** 369–384 (2007).

194. Höllrigl, V., Otto, K. & Schmid, A. Electroenzymatic Asymmetric Reduction ofrac-3-Methylcyclohexanone to (1S,3S)-3-Methylcyclohexanol in Organic/Aqueous Media Catalyzed by a Thermophilic Alcohol Dehydrogenase. *Adv. Synth. Catal.* **349,** 1337–1340 (2007).

195. Durliat, H., Comtat, M. & Séris, J.-L. Cytoplasmic hydrogenase. *Pat. number US 5528867 A* (1988). at <https://www.google.com/patents/US5538867?dq=1988+cytoplasmic+hydrogenase+NADH&hl=en&sa=X&ei=vuWWU6GcF4jfOeaHgIAD&ved=0CCgQ6AEwAA>

196. Cantet, J., Bergel, A. & Comtat, M. Coupling of the electroenzymatic reduction of NAD^+ with a synthesis reaction. *Enzyme Microb. Technol.* **18,** 72–79 (1996).

197. Mertens, R., Greiner, L., Van Den Ban, E. C. D., Haaker, H. B. C. M. & Liese, A. Practical applications of hydrogenase I from Pyrococcus furiosus for NADPH generation and regeneration. *J. Mol. Catal. B Enzym.* **24-25,** 39–52 (2003).

198. Ratzka, J., Lauterbach, L., Lenz, O. & Ansorge-Schumacher, M. B. Systematic evaluation of the dihydrogen-oxidising and NAD^+-reducing soluble [NiFe]-hydrogenase from Ralstonia eutropha H16 as a cofactor regeneration catalyst. *Biocatal. Biotransform.* **29,** 246–252 (2011).

199. Lauterbach, L., Lenz, O. & Vincent, K. A. H 2 -driven cofactor regeneration with $NAD(P)^+$ -reducing hydrogenases. *FEBS J.* **280,** 3058–3068 (2013).

200. Xiong, H., Jewell, L. L. & Coville, N. J. Shaped Carbons As Supports for the Catalytic Conversion of Syngas to Clean Fuels. *ACS Catal.* **5,** 2640–2658 (2015).

201. Chen, D., Holmen, A., Sui, Z. & Zhou, X. Carbon mediated catalysis: A review on oxidative dehydrogenation. *Chin. J. Catal.* **35,** 824–841 (2014).

202. Su, D. S., Perathoner, S. & Centi, G. Catalysis on nano-carbon materials: Going where to? *Catal. Today* **186,** 1–6 (2012).

203. Khan, G. F., Shinohara, H., Ikariyama, Y. & Aizawa, M. Electrochemical behaviour of monolayer quinoprotein adsorbed on the electrode surface. *J. Electroanal. Chem.* **315,** 263–273 (1991).

204. Harmer, M. A., Allen, H. & Hill, O. The direct electrochemistry of redox proteins at metal oxide electrodes. *J. Electroanal. Chem.* **189,** 229–246 (1985).

205. Blanford, C. F. & Armstrong, F. A. The pyrolytic graphite surface as an enzyme substrate: Microscopic and spectroscopic studies. *J. Solid State Electrochem.* **10,** 826–832 (2006).

206. Léger, C. *et al.* Enzyme electrokinetics: Using protein film voltammetry to investigate redox enzymes and their mechanisms. *Biochemistry* **42,** 8653–8662 (2003).

207. Krishnan, S. & Armstrong, F. a. Order-of-magnitude enhancement of an enzymatic hydrogen-air fuel cell based on pyrenyl carbon nanostructures. *Chem. Sci.* **3,** 1015 (2012).

208. Quinson, J. *et al.* Comparison of carbon materials as electrodes for enzyme electrocatalysis: hydrogenase as a case study. *Faraday Discuss.* **172,** 473–496 (2014).

209. Feng, W. & Ji, P. Enzymes immobilized on carbon nanotubes. *Biotechnol. Adv.* **29,** 889–895 (2011).

210. Duca, M., Weeks, J. R., Fedor, J. G., Weiner, J. H. & Vincent, K. A. Combining Noble Metals and Enzymes for Relay Cascade Electrocatalysis of Nitrate Reduction to Ammonia at Neutral pH. *ChemElectroChem* **2,** 1086–1089 (2015).

211. Hidalgo, R., Ash, P. A., Healy, A. J. & Vincent, K. A. Infrared Spectroscopy During Electrocatalytic Turnover Reveals the Ni-L Active Site State During H_2 Oxidation by a NiFe Hydrogenase. *Angew. Chem. Int. Ed.* **54,** 7110–7113 (2015).

212. Lauterbach, L. & Lenz, O. Catalytic Production of Hydrogen Peroxide and Water by Oxygen-Tolerant [NiFe]-Hydrogenase during H_2 Cycling in the Presence of O_2. *J. Am. Chem. Soc.* **135,** 17897–17905 (2013).

213. Katagiri, G., Ishida, H. & Ishitani, A. Raman spectra of graphite edge planes. *Carbon N. Y.* **26,** 565–571 (1988).

214. Webb, P. A. & Orr, C. Analytical Methods in Fine Particle Technology. *Micromeritics*

1–325 (1997). doi:10.1016/j.carbon.2013.08.031

215. Hald, E., Lehmann, P. & Zeigenhorn, J. Molar Absorptivities of beta-NADH and beta-NAD at 260 nm. *Clin. Chem.* **21,** 884–887 (1975).

216. Rouquerol, J. *et al.* Recommendations for the characterization of porous solids (Technical Report). *Pure Appl. Chem.* **66,** 36–49 (1994).

217. Brunauer, S., Emmett, P. H. & Teller, E. Gases in Multimolecular Layers. *J. Am. Chem. Soc.* **60,** 309–319 (1938).

218. Thommes, M. *et al.* Physisorption of gases, with special reference to the evaluation of surface area and pore size distribution (IUPAC Technical Report). *Pure Appl. Chem.* **87,** 131–141 (2015).

219. Qian, W. Quantitative Raman characterization of the mixed samples of the single and multi-wall carbon nanotubes. *Carbon N. Y.* **41,** 1851–1854 (2003).

220. *Green Carbon Materials: Advances and Applications*. (Pan Stanford Publishing, 2014).

221. Dias, J. M., Alvim-Ferraz, M. C. M., Almeida, M. F., Rivera-Utrilla, J. & Sanchez-Polo, M. Waste materials for activated carbon preparation and its use in aqueous-phase treatment: A review. *Journal of Environ. Manage.* **85,** 833–846 (2007).

222. Radushkevich, L. O strukture ugleroda, obrazujucegosja pri termiceskom razlozenii okisi ugleroda na zeleznom kontakte. *Zurn Fisic Chim* **26,** 88–95 (1952).

223. Monthioux, M. & Kuznetsov, V. L. Who should be given the credit for the discovery of carbon nanotubes? *Carbon* **44,** 1621–1623 (2006).

224. Iijima, S. Helical microtubules of graphitic carbon. *Nature* **354,** 56–58 (1991).

225. Iijima, S. & Ichihashi, T. Single-shell carbon nanotubes of 1-nm diameter. *Nature* **363,** 603–605 (1993).

226. Bethune, D. S. *et al.* Cobalt-catalysed growth of carbon nanotubes with single-atomic-layer walls. *Nature* **363,** 605–607 (1993).

227. Prasek, J. *et al.* Methods for carbon nanotubes synthesis—review. *J. Mater. Chem.* **21,** 15872 (2011).

228. Marchand, P., Hassan, I. a, Parkin, I. P. & Carmalt, C. J. Aerosol-assisted delivery of precursors for chemical vapour deposition: expanding the scope of CVD for materials fabrication. *Dalton Trans.* **42,** 9406–22 (2013).

229. Glerup, M., Kanzow, H., Almairac, R., Castignolles, M. & Bernier, P. Synthesis of multi-walled carbon nanotubes and nano-fibres using the aerosol method with metal-ions as the catalyst precursors. *Chem. Phys. Lett.* **377,** 293–298 (2003).

230. Zhang, M. & Li, J. Carbon nanotube in different shapes. *Mater. Today* **12,** 12–18 (2009).

231. Lau, K. T., Lu, M. & Hui, D. Coiled carbon nanotubes: Synthesis and their potential applications in advanced composite structures. *Compos. Part B Eng.* **37,** 437–448 (2006).

232. Choi, Y. C. & Choi, W. Synthesis of Y-junction single-wall carbon nanotubes. *Carbon N. Y.* **43,** 2737–2741 (2005).

233. Wei, B. Q. *et al.* Microfabrication technology: organized assembly of carbon nanotubes. *Nature* **416,** 495–6 (2002).

234. Vajtai, R. *et al.* Building carbon nanotubes and their smart architectures. *Smart Mater. Struct.* **11,** 691–698 (2002).

235. Kang, C. *et al.* Three-dimensional carbon nanotubes for high capacity lithium-ion batteries. *J. Power Sources* **299,** 465–471 (2015).

236. Gabay, T. *et al.* Electro-chemical and biological properties of carbon nanotube based multi-electrode arrays. *Nanotechnology* **18,** 35201–35201 (2007).

237. Nakanishi, W. *et al.* Bioactive nanocarbon assemblies: Nanoarchitectonics and applications. *Nano Today* **9,** 378–394 (2014).

238. Wildgoose, G. G., Banks, C. E. & Compton, R. G. Metal nanoparticles and related materials supported on Carbon nanotubes: Methods and applications. *Small* **2,** 182–193 (2006).

239. Kim, K. *et al.* Efficient Field Emission from Highly Aligned, Graphitic Nanotubes Embedded with Gold Nanoparticles. *Adv. Mater.* **15,** 1618–1622 (2003).

240. Chen, W., Loh, K. P., Xu, H. & Wee, A. T. S. Nanoparticle dispersion on reconstructed carbon nanomeshes. *Langmuir* **20,** 10779–10784 (2004).

241. Pham-Huu, C. *et al.* Large scale synthesis of carbon nanofibers by catalytic decomposition of ethane on nickel nanoclusters decorating carbon nanotubes. *Phys. Chem. Chem. Phys.* **4,** 514–521 (2002).

242. Bera, D. *et al.* In situ synthesis of carbon nanotubes decorated with palladium

nanoparticles using arc-discharge in solution method. *J. Appl. Phys.* **96,** 5152–5157 (2004).

243. Xue, B., Chen, P., Hong, Q., Lin, J. & Tan, K. L. Growth of Pd, Pt, Ag and Au nanoparticles on carbon nanotubes. *J. Mater. Chem.* **11,** 2378–2381 (2001).

244. Banerjee, S. & Wong, S. S. Formation of CdSe nanocrystals onto oxidized, ozonized single-walled carbon nanotube surfaces. *Chem. Commun.* 1866–7 (2004). doi:10.1039/b404204b

245. Zhang, H. *et al.* A novel approach to Co/CNTs catalyst via chemical vapor deposition of organometallic compounds. *Catal. Letters* **101,** 211–214 (2005).

246. Tessonnier, J. P., Pesant, L., Ehret, G., Ledoux, M. J. & Pham-Huu, C. Pd nanoparticles introduced inside multi-walled carbon nanotubes for selective hydrogenation of cinnamaldehyde into hydrocinnamaldehyde. *Appl. Catal. A Gen.* **288,** 203–210 (2005).

247. Trogadas, P., Fuller, T. F. & Strasser, P. Carbon as catalyst and support for electrochemical energy conversion. *Carbon N. Y.* **75,** 5–42 (2014).

248. Srivastava, a, Srivastava, O. N., Talapatra, S., Vajtai, R. & Ajayan, P. M. Carbon nanotube filters. *Nat. Mater.* **3,** 610–4 (2004).

249. Ishigami, N. *et al.* Microreactor utilizing a vertically-aligned carbon nanotube array grown inside the channels. *Chem. Commun. (Camb).* 1626–1628 (2007). doi:10.1039/b617356j

250. Kinoshita, H., Yamakawa, A. & Ohmae, N. Development of microreactors made of vertically aligned carbon nanotube films. *Carbon* **47,** 3374–3377 (2009).

251. Meysami, S. S., Koos, A. A., Dillon, F. & Grobert, N. Aerosol-assisted chemical vapour deposition synthesis of multi-wall carbon nanotubes: II. An analytical study. *Carbon N. Y.* **58,** 151–158 (2013).

252. Liu, W. W., Chai, S. P., Mohamed, A. R. & Hashim, U. Synthesis and characterization of graphene and carbon nanotubes: A review on the past and recent developments. *J. Ind. Eng. Chem.* **20,** 1171–1185 (2014).

253. Ohshima, T. & Soda, K. in *Stereoselective Biocatalysis* (ed. Patel, R.) 877–902 (Marcel Dekker, 2000).

254. Benck, J. D., Hellstern, T. R., Kibsgaard, J., Chakthranont, P. & Jaramillo, T. F. Catalyzing the hydrogen evolution reaction (HER) with molybdenum sulfide

nanomaterials. *ACS Catalysis* **4,** 3957–3971 (2014).

255. Chhowalla, M. *et al.* The chemistry of two-dimensional layered transition metal dichalcogenide nanosheets. *Nat. Chem.* **5,** 263–275 (2013).

256. Wang, Q. H., Kalantar-Zadeh, K., Kis, A., Coleman, J. N. & Strano, M. S. Electronics and optoelectronics of two-dimensional transition metal dichalcogenides. *Nat. Nanotechnol.* **7,** 699–712 (2012).

257. Wu, S. *et al.* Electrochemically reduced single-layer MoS_2 nanosheets: Characterization, properties, and sensing applications. *Small* **8,** 2264–2270 (2012).

258. Prabakaran, A. *et al.* WS_2 2D nanosheets in 3D nanoflowers. *Chem. Commun.* **50,** 12360–12362 (2014).

259. Choi, B. G., Huh, Y. S., Hong, W. H., Kim, H. J. & Park, H. S. Electrochemical assembly of MnO_2 on ionic liquid–graphene films into a hierarchical structure for high rate capability and long cycle stability of pseudocapacitors. *Nanoscale* **4,** 5394 (2012).

260. Jaramillo, T. F. *et al.* Identification of Active Edge Sites for Electrochemical H_2 Evolution from MoS_2 Nanocatalysts. *Science* **317,** 100–102 (2007).

261. Mahler, B., Hoepfner, V., Liao, K. & Ozin, G. A. Colloidal synthesis of 1T-WS_2 and 2H-WS_2 nanosheets: Applications for photocatalytic hydrogen evolution. *J. Am. Chem. Soc.* **136,** 14121–14127 (2014).

263. Ambrosi, A., Sofer, Z. & Pumera, M. Lithium intercalation compound dramatically influences the electrochemical properties of exfoliated MoS_2. *Small* **11,** 605–612 (2015).

263. Shi, J. *et al.* Controllable growth and transfer of monolayer MoS_2 on Au foils and its potential application in hydrogen evolution reaction. *ACS Nano* **8,** 10196–10204 (2014).

264. Tsai, C., Chan, K., Nørskov, J. K. & Abild-Pedersen, F. Rational design of MoS_2 catalysts: tuning the structure and activity via transition metal doping. *Catal. Sci. Technol.* **5,** 246–253 (2015).

265. Ma, C. *et al.* MoS 2 nanoflower-decorated reduced graphene oxide paper for high-performance hydrogen evolution reaction. *Nanoscale* **00,** 1–3 (2013).

266. Liang, L. & Meunier, V. First-principles Raman spectra of MoS_2, WS_2 and their heterostructures. *Nanoscale* **6,** 5394 (2014).

267. Berkdemir, A. *et al.* Identification of individual and few layers of WS_2 using Raman Spectroscopy. *Sci. Rep.* **3,** 1755 (2013).

268. Pomp, S. *et al.* Two-Dimensional Iron Tungstate: A Ternary Oxide Layer With Honeycomb Geometry. *J. Phys. Chem. C* **120,** 7629–7638 (2016).

269. Kuhness, D. Synthesis of low dimensional ternary oxide $FeWO_x$ and $MnWO_x$ nanostructures on single crystal metal surfaces. (PhD Thesis, University of Austria, 2015).

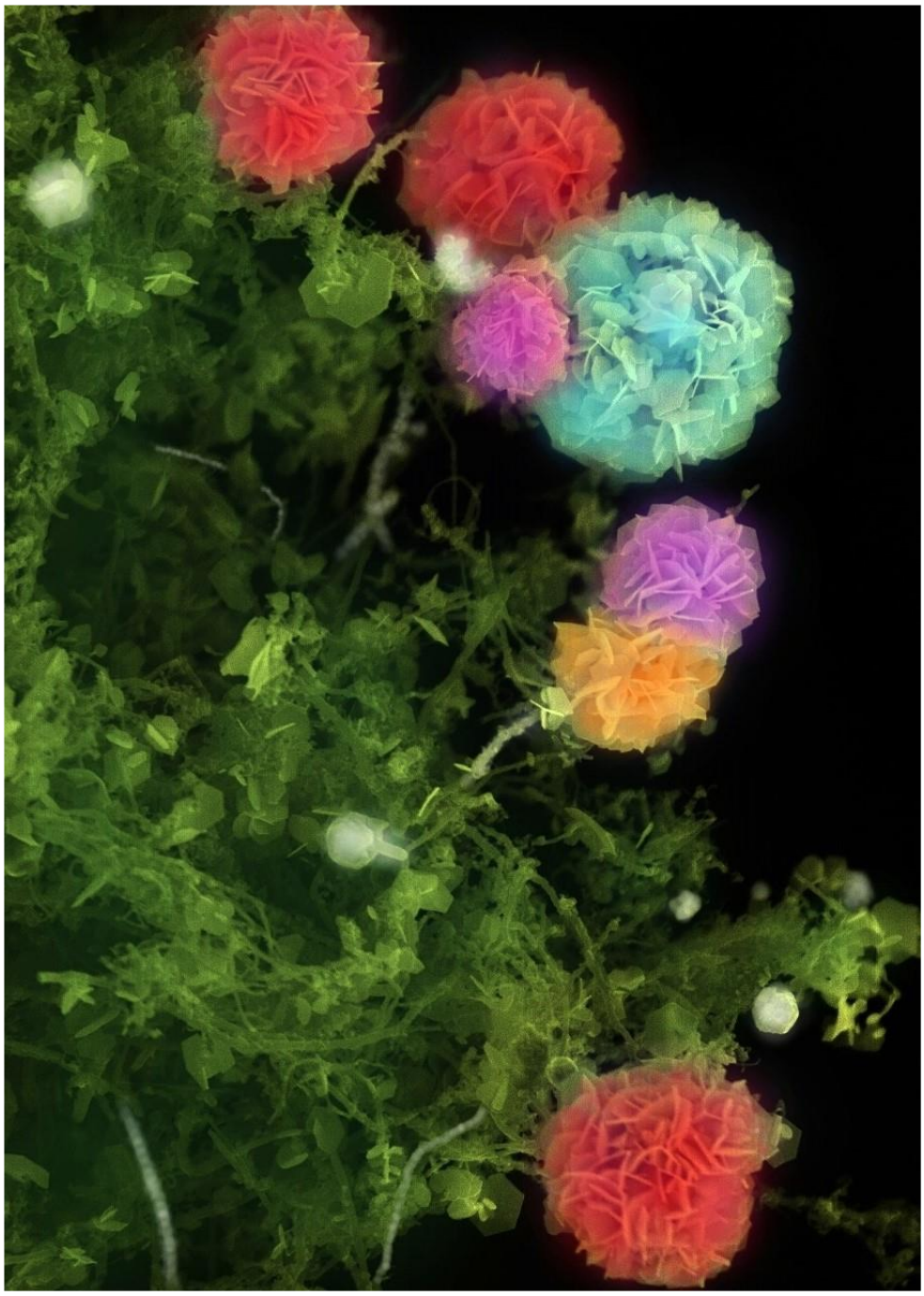
270. He, G. L. *et al.* Hydrothermal synthesis of $FeWO_4$-graphene composites and their photocatalytic activities under visible light. *Appl. Surf. Sci.* **351,** 474–479 (2015).

271. Li, X. *et al.* Carbon nanotube hybrids with MoS_2 and WS_2 synthesized with control of crystal structure and morphology. *Carbon N. Y.* **85,** 168–175 (2015).

272. Ksenevich, V. K. *et al.* Electrical properties of carbon nanotubes/WS_2 nanotubes (nanoparticles) hybrid films. *Nanosyst. Physics, Chem. Math.* **7,** 37–43 (2016).

273. Zou, M. *et al.* Controlled morphology evolution of electrospun carbon nanofiber templated tungsten disulfide nanostructures. *Electrochim. Acta* **176,** 255–264 (2015).

274. Conway, B. E. & Tilak, B. V. Interfacial processes involving electrocatalytic evolution and oxidation of H2, and the role of chemisorbed H. *Electrochim. Acta* **47,** 3571–3594 (2002).



Decorating the Christmas Tree – *WS_2 nanoflakes and nanoflowers on CNCs*

(The image won the Carbon at Christmas image competition organised by the British Carbon Group.)

APPENDICES

1. Specific Activity Calculation

eq-A 1

$$Specific\ activity = \frac{\frac{\Delta E}{\Delta t} \times V_{cuvette}}{\varepsilon_{340nm} \times V_{enzyme} \times C_{enzyme} \times d_{cuvette}}$$

$\Delta E/\Delta t$ = Slope in UV−vis spectrum in kinetic measurement (min^{-1})

$V_{cuvette}$ = Volume of the reaction mixture used in the cuvette

ε_{340nm} = Molar absorptivity ($mM^{-1}\ cm^{-1}$)

V_{enzyme} = Volume of the enzyme used in the reaction mixture (mL)

C_{enzyme} = Concentration of the enzyme used (mg/mL)

$d_{cuvette}$ = Path length of the cuvette (cm)

2. Surface Analysis For CC, CD, CP and BP

*Table A 1: Correlation factor for Langmuir and BET models used for analysis of carbon materials in **Chapter 2**.*

Material Abbreviation	Correlation factor for BET model	Correlation factor for Langmuir model
CC	0.997	0.999
CD	0.999	0.998
CP	0.998	0.999
BP	0.998	0.999

3. HPLC Calibration Curves

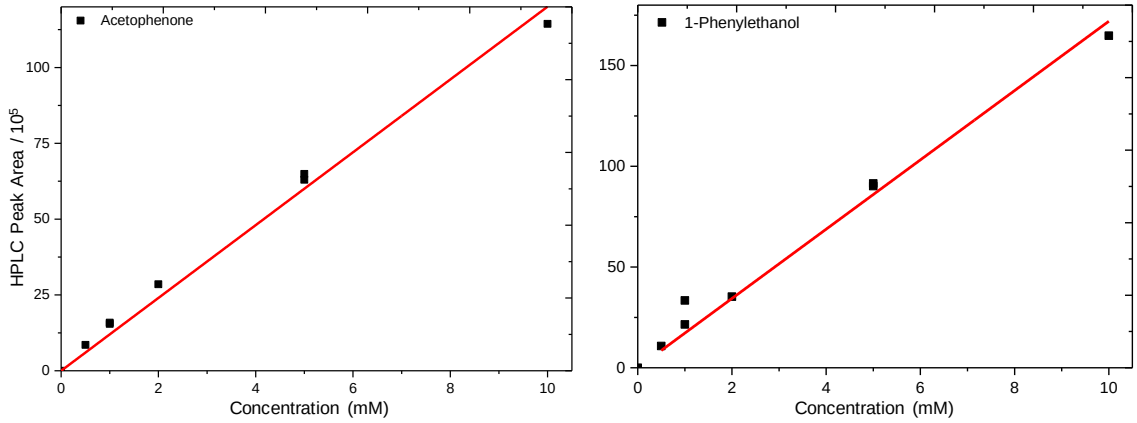


Figure A 1: HPLC calibration curves for acetophenone and 1-phenylethanol. R^2 value for acetophenone calibration curve is 0.994 and the line equation is $Y = 1.20 \times 10^6 X$. R^2 value for 1-phenylethanol calibration curve is 0.990 and, the line equation is $Y = 1.72 \times 10^6 X$.

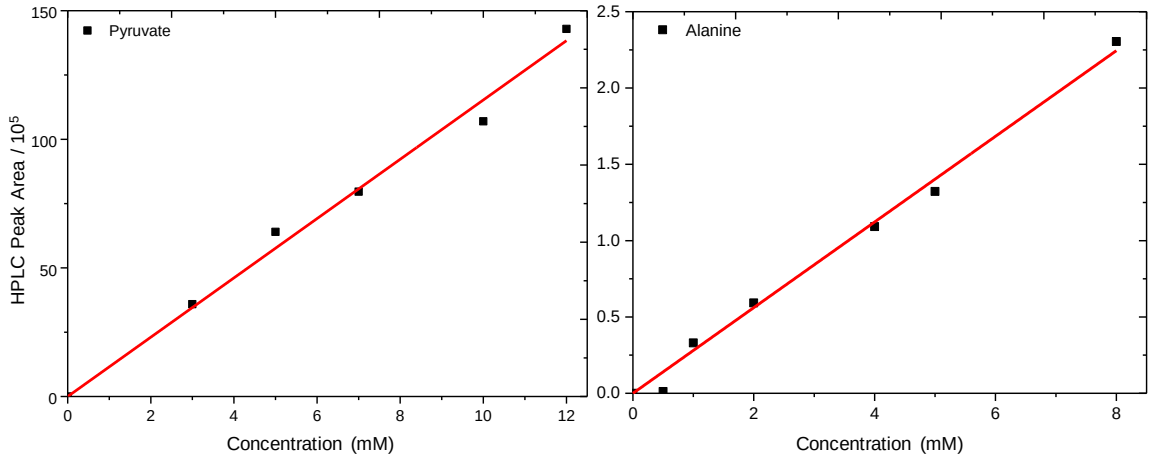
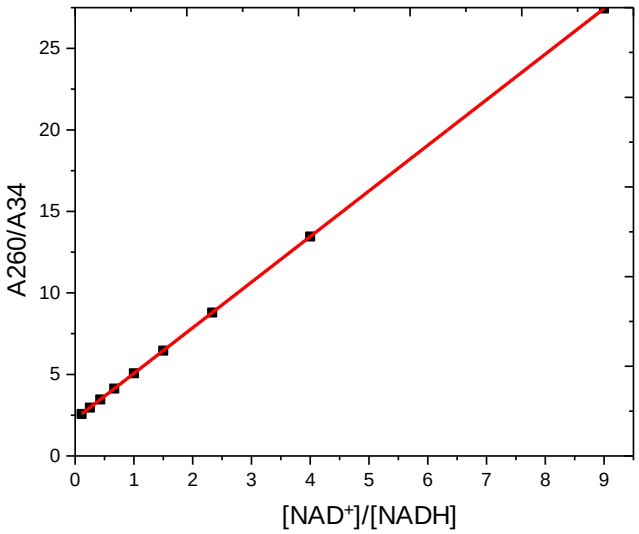


Figure A 2: HPLC calibration curves for pyruvate and alanine. R^2 value for pyruvate calibration curve is 0.996 and the line equation is $Y = 1.15 \times 10^6 X$. R^2 value for alanine calibration curve is 0.995 and, the line equation is $Y = 2.81 \times 10^4 X$.

4. UV-Vis for determination of NAD⁺/NADH ratio

Table A 2 Table showing the calculated values of [NAD⁺]/[NADH] and $A_{260\ nm}/A_{340\ nm}$ with the method and the extinction coefficients in the literature[215] for the plot in Figure A 3.

NAD⁺	NADH	A_{260}	A_{340}	NAD⁺/NADH	A_{260}/A_{340}
0.1	0.9	14.43	5.59	0.11	2.58
0.2	0.8	14.76	4.98	0.25	2.97
0.3	0.7	15.09	4.35	0.43	3.47
0.4	0.6	15.42	3.73	0.67	4.13
0.5	0.5	15.75	3.11	1.00	5.06
0.6	0.4	16.08	2.49	1.50	6.46
0.7	0.3	16.41	1.87	2.33	8.79
0.8	0.2	16.74	1.24	4.00	13.46
0.9	0.1	17.07	0.62	9.00	27.44



y= 2.79743 x + 2.26688

Figure A 3: A plot of [NAD⁺]/[NADH] vs $A_{260\ nm}/A_{340\ nm}$ that was graphed by using the calculated values with literature coefficients can be used to determine the concentration ratio of an unknown sample.

*Table A 3 Calculation of NAD^+/NADH ratio for 16 hr experiment in **Section 2.3.3** on carbon materials (CC, CD, CP, and BP).*

	Final A_{340nm}	Final A_{260nm}	y= A_{260nm}/A_{340nm}	x= NAD^+/NADH
CC	0.006	0.989	154.542	54.434
CD	0.073	0.988	13.547	4.032
CP	0.063	0.972	15.534	4.743
BP	0.318	0.889	2.798	0.190

Starting NAD^+ concentration = 0.96 mM

Conversion for BP:

$$x = \frac{NAD^+}{0.96 - NAD^+} = 0.1899$$

NAD^+ = 0.15 mM
NADH = 0.81 mM
% Conversion = 84

5. Temperature Profile of the Furnace Used In CNC Synthesis

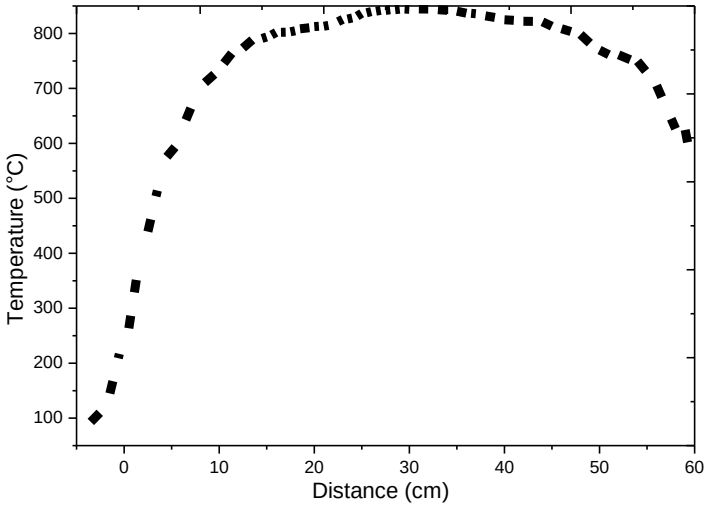


Figure A 4: Temperature profile of the 55 cm long single-zone horizontal tubular furnace used in CNC syntheses at 850 °C under 2.5 standard litre min^{-1} argon flow.

6. Specific surface area analysis based on Brunauer–Emmett–Teller (BET) theory

The surface area of the MWCNTs in CNCs were detected as 60 $m^2\ g^{-1}$.[1]

7. Blank CNC Flow Experiment

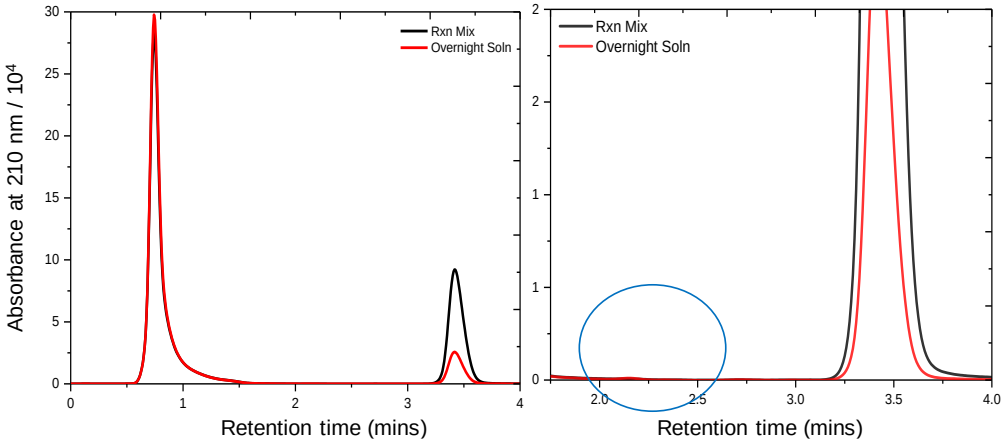


*Figure A 5: HPCL curves for H_2-driven biotransformations on CNCs without enzymes. Absence of a peak around 2.1 minutes shows that the CNCs do not catalyse the reaction. Following the same procedure in **Section 3.2.1.5.2**, 3 mL of reaction mixture containing 1 mM NAD^+ and 10 mM acetophenone was cycled through the CNCs. The samples were 10 times diluted with MilliQ water for HPLC analysis.*

8. NADH Generation in Flow on CNCs

*Table A 4 Calculation of NAD^+/NADH ratio for 5 hr experiment in **Section 3.3.3.1** on CNCs.*

	Final A_{340nm}	Final A_{260nm}	y= A_{260nm}/A_{340nm}	x= NAD^+/NADH
CNC	0.153	0.796	5.190	1.045

Starting NAD^+ concentration = 1 mM

Conversion for flow in CNCs:

$$x = \frac{NAD^+}{1.0 - NAD^+} = 1.045$$

NAD^+ = 0.51 mM
NADH = 0.49 mM
% Conversion = 49

9. Acetophenone Adsorption on MWCNTs of CNCs

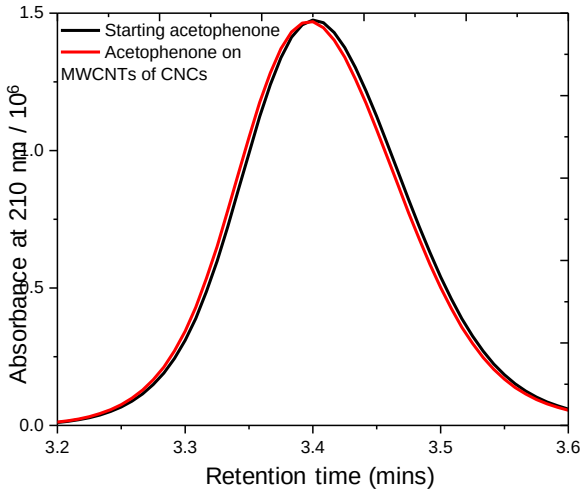


Figure A 6: HPLC curves for overnight adsorption of acetophenone on MWCNTs scraped off CNCs. 30 µL of 10 mg mL^{-1} MWCNT solution was used with 500 µL 10 mM acetophenone. The dispersion was not successful.

10. Batch NADH Generation on MWCNTs (of CNCs)

MWCNTs could not be dispersed well under the conditions for dispersing BP (10 mg mL^{-1} dispersion in Bis-Tris pH 6 buffer). Thus, the experiment is not exactly comparable with NADH generation on CD, CP, and BP.

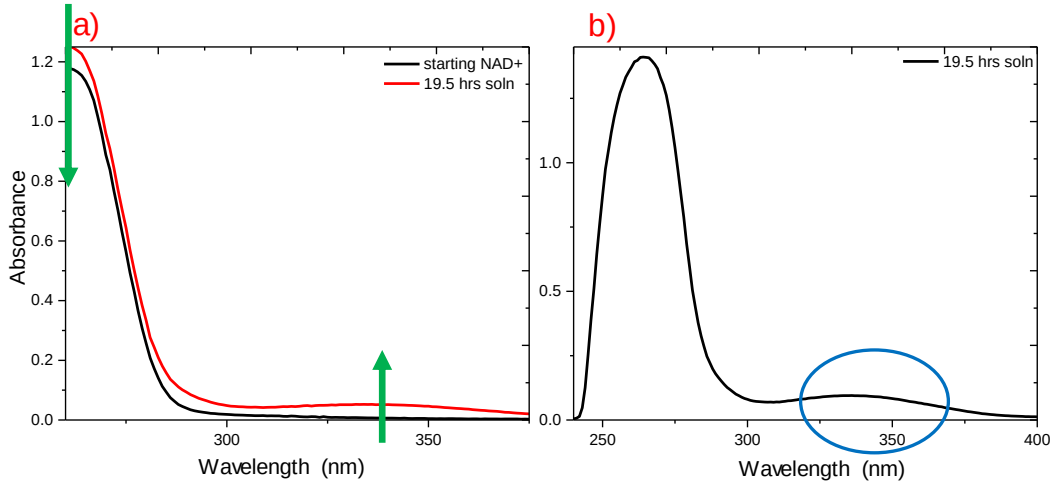


*Figure A 7: UV-Vis spectra for 19.5 hrs NADH generation on MWCNTs scraped off from a CNC. The same experimental conditions as NADH generation on carbon materials **Section 2.2.1.4** were used. However, the amount of the carbon used in the reaction was not the same due to the dispersion issues. a) spectra for 1:10 diluted NAD$^+$ starting solution and the 1:10 diluted 19.5 hrs reaction mixture. b) spectrum for 1:5 diluted 19.5 hrs reaction mixture.*

11. Batch Ketone Reduction on MWCNTs (of CNCs)

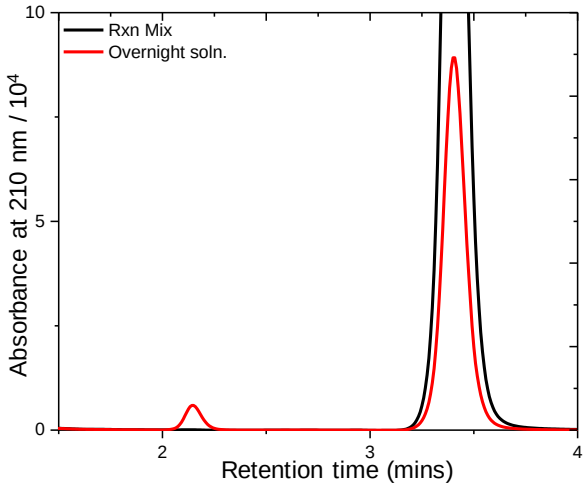


Figure A 8: HPLC chromatogram for acetophenone to 1-phenylethanol reduction on MWCNTs scraped off CNCs. The same conditions as the highest yield ketone reduction experiment conditions were used. The samples were 10 times diluted with MilliQ water for HPLC analysis. Conversion in batch is 10 times less than the conversion in flow. MWCNTs were not dispersed prior to the experiment.

12. Overnight Ketone Reduction in Flow Revisited

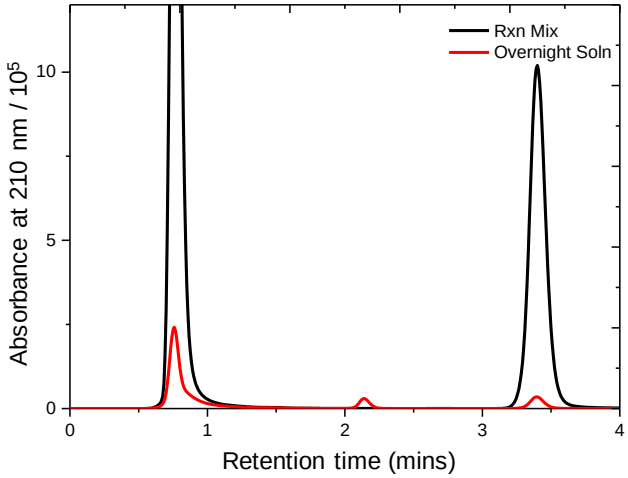


*Figure A 9: The overall HPLC chromatograms for overnight ketone reduction in **Chapter 3**.*

13. Overnight Reductive Amination In Flow Revisited

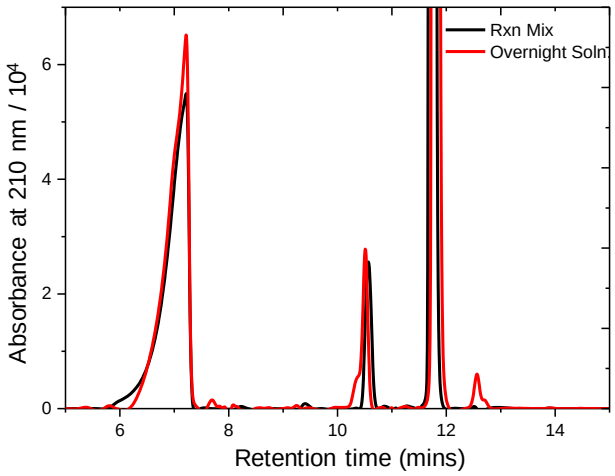


*Figure A 10: The overall HPLC spectra for reductive amination in **Chapter 3**.*

14. Temperature Profile of the Furnace Used in WS_2 Synthesis

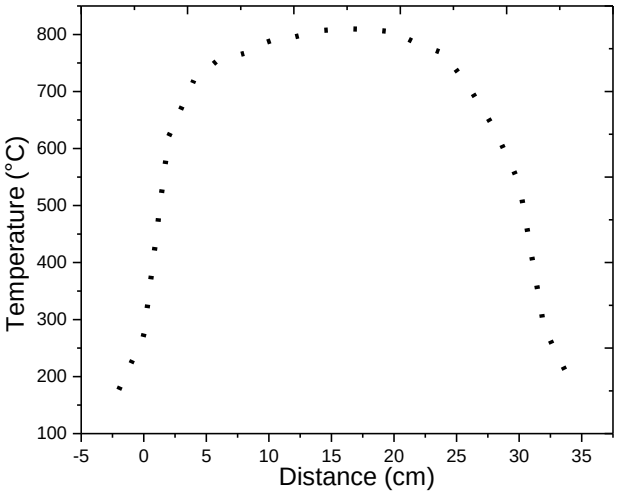


Figure A 11: Temperature profile of the 31 cm long single-zone horizontal tubular furnace used in WS_2 syntheses at 800 °C under 100 standard cubic centimetre per minute Ar flow.

15. Additional Raman spectra for WS_2-MWCNT assemblies

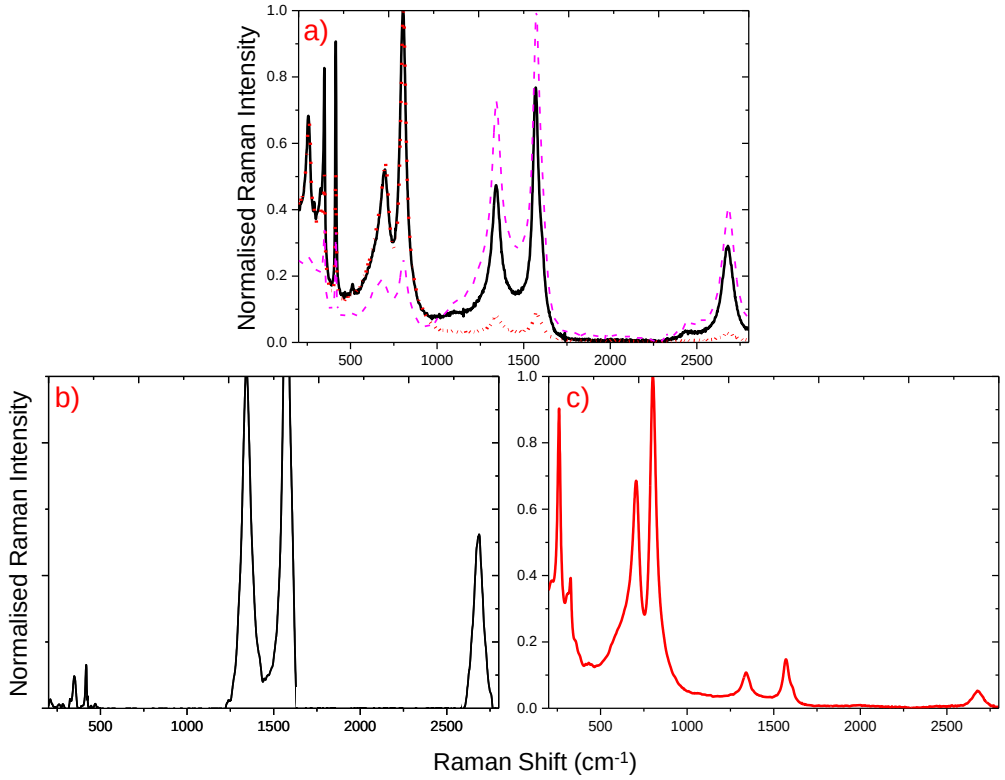


Figure A 12: Raman spectra of a) WS_2-WO_3-CNT b) WS_2-CNT c) WO_3-CNT

16. Additional voltammetry results

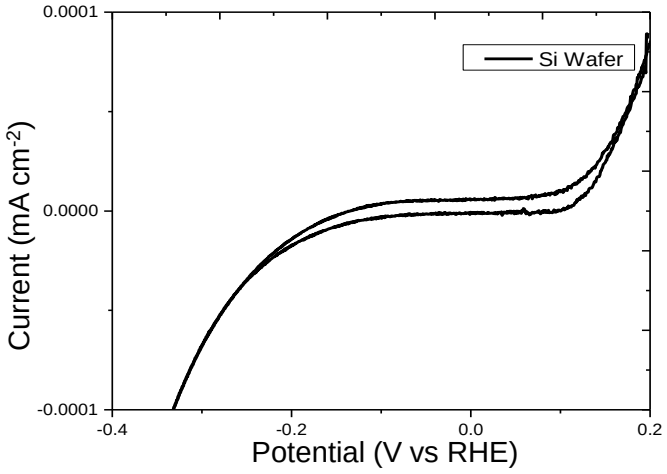


Figure A 13: Cyclic voltammogram of a blank Si wafer

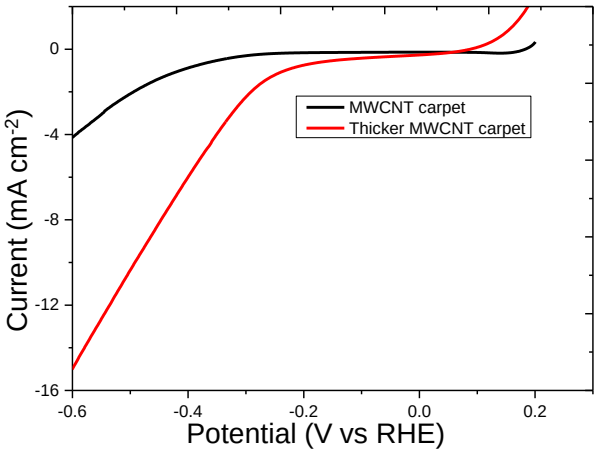
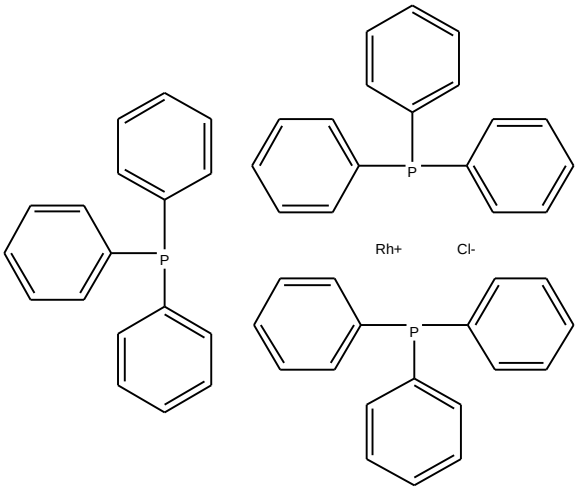


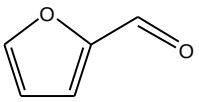
Figure A 14: Linear sweep voltammograms of an MWCNT carpet synthesised at 800 °C in 15 minutes (black) and an MWCNT carpet synthesised at 850 °C in 20 minutes (red).

17. Structures of the key chemicals mentioned in the Thesis

[a] Wilkinson's catalyst:



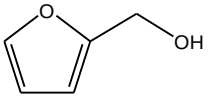
[b] Furfural:



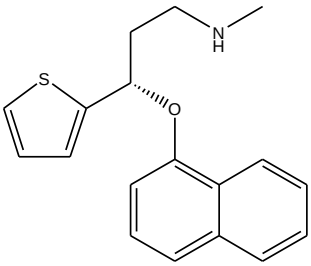
[c] Furan:



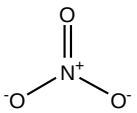
[d] Furfuryl alcohol:



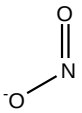
[e] (*S*)-Duloxetine:



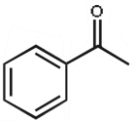
[f] Nitrate:



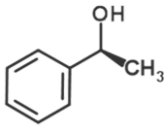
[g] Nitrite:



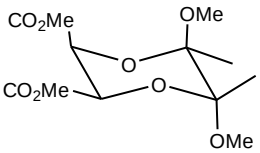
[h] Acetophenone:



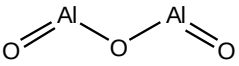
[i] (*S*)-1-phenylethanol:



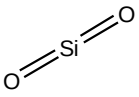
[j] Butane-2,3-diacetal protected tartrate:



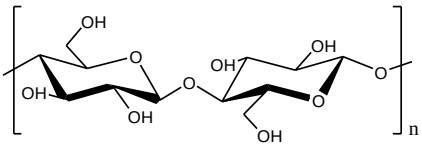
[k] Alumina:



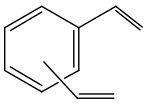
[l] Silica:



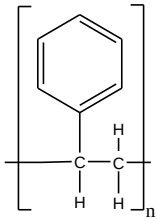
[m] Cellulose:



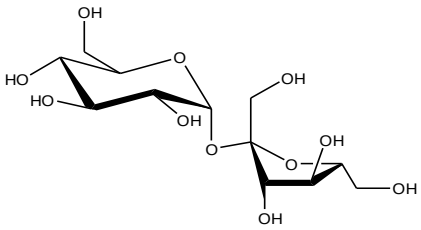
[n] Divinylbenzene:



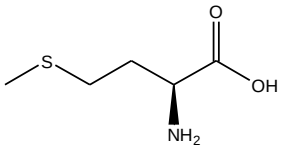
[o] Polystyrene:



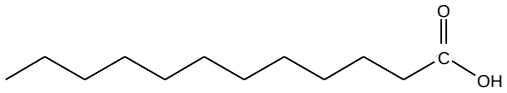
[p] Sucrose:



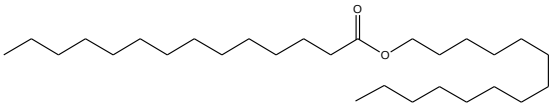
[q] L-methionine:



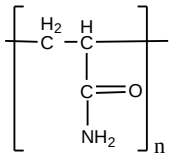
[r] Lauric acid:



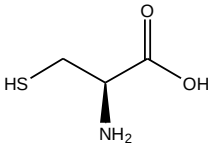
[s] Myristyl Myristate:



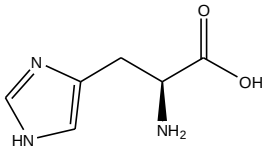
[t] Polyacrylamide:



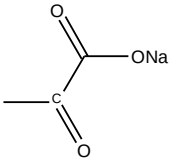
[u] Cystein:



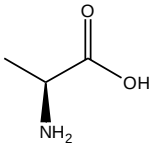
[v] Histidine:



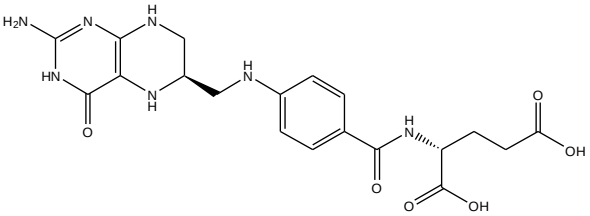
[w] Sodium pyruvate:



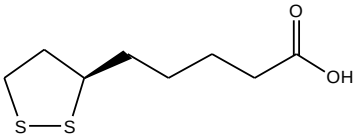
[x] L-alanine:



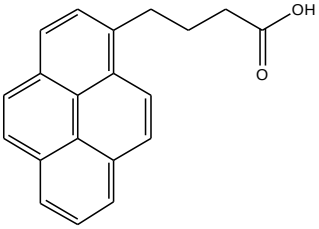
[y] Tetrahydrofolate:



[z] Lipoate:



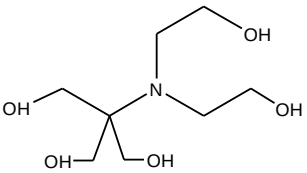
[aa] 1-pyrenebutyric acid:



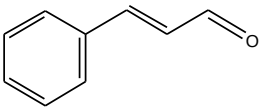
[bb] Acetonitrile:



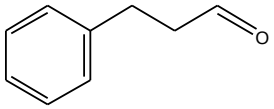
[cc] Bis-Tris:



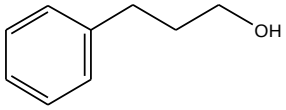
[dd] Cinnamaldehyde:



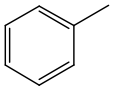
[ee] Hydrocinnamaldehyde:



[ff] Phenylpropanol:



[gg] Toluene:



[hh] Ferrocene:

